

Developing Novel Targeted Diagnostics and Therapeutics for Cholangiocarcinoma

Imeshi Umayanga Wijetunga

The University of Leeds
Leeds Institute of Medical Research
School of Medicine

May 2020

Submitted in accordance with the requirements for the degree of
Doctor of Philosophy

The candidate confirms that the work submitted is her own, except where the work was part of a collaborative publication as described below. Where expert technical help was required, the contribution of others has been explicitly described below and the candidate confirms that the appropriate credit has been given within the thesis where work of others has been included.

“Affimer proteins are versatile and renewable affinity reagents” Tiede C, Bedford R, Heseltine S, Smith G, Wijetunga I et al. Elife 2017;6

The candidate performed the experiments referred to in “Affimer binders for in vivo imaging” in the “Results” section of this paper and contributed Figure 5 C and D. The candidate authored the “In vivo work” section in the “Materials and methods”. She received technical help from Dr Nicola Ingram for the experimental work and all supervisors were involved in critical revision of the manuscript contribution.

“Development of orthotopic tumour models using ultrasound-guided intrahepatic injection. McVeigh LE, Wijetunga I, Ingram N, Marston G et al. Sci Rep 2019;9(1)

The candidate performed the experiments related to the orthotopic cholangiocarcinoma model including all the bioluminescent imaging and wrote the manuscript sections relating to this experiment. For the set-up of the pre-clinical minimally invasive orthotopic model of cholangiocarcinoma, expert technical skills were required to inject the murine liver under ultrasound guidance. Dr Gemma Marston performed this for all the experiments involving the orthotopic tumour model. Dr Gemma Marston and Dr Nicola Ingram performed the high-frequency ultrasound imaging for the longitudinal monitoring of tumour growth. All authors were involved in the critical revision of the manuscript.

Acknowledgements

My sincere thanks go out to my supervisors Dr Louise Coletta, Mr Raj Prasad and Dr Nicola Ingram for their support and guidance over the past six years.

In addition, I would like to express my gratitude to Mrs Sarah Perry and Dr Milene Volpato for the invaluable training on many aspects of lab research as well as technical assistance with *in vivo* experiments, Prof Mark Hull and the Molecular Gastroenterology research group for their constructive critique and the staff at the SBS for their technical support.

I would especially like to acknowledge Dr Gemma Marston and Dr Nicola Ingram who provided specialist technical skills in pre-clinical interventional radiology which were vital for this project. A heartfelt thank you to Dr Azhar Maqbool and the Cardiovascular Research Group at the University of Leeds, for the opportunity for collaborative research and funding through the British Heart Foundation grant NH/12/1/29832 as well as Dr Darren Tomlinson and his research group at the School of Molecular and Cellular Biology, who provided the affimers used in this project. I am very grateful to Dr Sunjie Ye and Dr Lucien Roach who synthesised the gold nanoparticles used in this project and assisted with the related experiments.

Dr Laura McVeigh and Dr Antonia Charalambous have my gratitude for their technical support, assistance with the systematic review as well as the much-needed moral support. I shall miss tea and tea cake breaks at the LImm café with the Level 9 team.

My husband Chean Yong, my father Kithsiri, my mother Sunanda, my brother Tharindu and innumerable friends (Hasini, Sook Cheng, Sonsoles and Marta, to name a few) have my eternal gratitude for their patience, support and love throughout this project, especially during the final write-up phase.

Abstract

Cholangiocarcinomas (CCAs) are a rare group of cancers with dismal prognosis. New therapeutic options are therefore warranted. Nanomedicine has the potential to improve cancer diagnosis and therapy (theranosis) but has infrequently been explored in CCA.

The aim of this study was to develop a targeted theranostic system for CCA. An orthotopic murine model of CCA to test these systems in a more accurate model of the disease was first generated. Potential biomarkers for theranosis were identified, one of which, tenascin C (TNC), was explored further.

To facilitate the development of orthotopic CCA models, bioluminescent extra-hepatic CCA cell lines were generated using lentiviral infection. Clone TFKluc2B2, was selected for the orthotopic model. These cells were injected under high-frequency ultrasound (HF-US) guidance into peri-cholecystic area of the murine liver. The optimised method yielded 90% success for tumour establishment with the ability to image tumour growth by longitudinal bioluminescent imaging and tumour volume measurement using HF-US.

Potential biomarkers for theranosis in cholangiocarcinoma were identified and evaluated using a systematic approach and a modified scoring system (TASC-T score). Matrix metalloproteinase 9, claudin 18, TNC, carbonic anhydrase 9 and epidermal growth factor receptor showed the highest theranostic potential. TNC was evaluated in 54 human CCA and paired para-cancerous normal liver specimens. Significantly higher TNC immunolabelling was observed in CCA tissue.

Fluorescent-labelled TNC affimers (peptide-based antibody mimetics), were evaluated for their ability to target TNC-positive murine tumours *in vivo*. A trend towards

increased fluorescence was seen in tumours of the TNC affimer group compared to control affimer. Gold nanoparticles and two chemotherapeutic agents (gemcitabine and irinotecan) were also evaluated as part of a potential theranostic system that would include photothermal therapy and targeted drug delivery.

This work provides the rationale for a nanoparticle-based theranostic system to be developed for improved therapeutics in CCA.

Table of Contents

Acknowledgements	iii
Abstract	iv
List of Figures	xi
List of Tables	xiv
List of Abbreviations	xv
Chapter 1	1
Introduction.....	2
1.1 Cholangiocarcinoma.....	2
1.1.1 Aetiology and classification.....	2
1.1.2 Diagnosis and staging.....	6
1.1.3 Management.....	7
1.1.4 Prognosis.....	17
1.2 Nanomedicine and potential applications in cholangiocarcinoma.....	18
1.2.1 Nanoparticles for diagnosis and therapy.....	20
1.2.2 Nanoparticles in clinical use in cholangiocarcinoma.....	22
1.2.3 Gold nanoparticles.....	24
1.3 Biomarkers for active targeting of gold nanoparticle delivery systems in cholangiocarcinoma	28
1.3.1 Theranostic biomarkers.....	28
1.3.2 Types of targeting ligands.....	31
1.3.3 Active targeting using gold nanoparticles.....	31
1.4 Tenascin C as a potential biomarker in cholangiocarcinoma.....	33
1.4.1 Structure and expression in normal tissues.....	33
1.4.2 Function.....	34
1.4.3 Expression in cholangiocarcinoma.....	36
1.4.4 Expression of tenascin C in other diseases.....	38
1.4.5 Tenascin C targeting in clinical trials.....	38
1.5 Pre-clinical models of cholangiocarcinoma for validation of nanoparticle-based delivery systems.....	40
1.5.1 <i>In vivo</i> imaging in pre-clinical models of human cancer.....	41
1.6 Thesis aim and objectives	43
Chapter 2 Materials and methods	44
2.1 Cell lines and culture	45

2.1.1	Extra-hepatic cholangiocarcinoma cell lines.....	45
2.1.2	Other cell lines.....	46
2.2	Luciferase transfection of TFK-1 and EGI-1 cell lines.....	47
2.2.1	Puromycin chemosensitivity assay	47
2.2.2	Transfection	48
2.2.3	Quantification of luciferase activity and clonal selection.....	50
2.2.4	Growth characteristics of selected TFK-1 and EGI-1 clones	50
2.3	Generation of <i>in vivo</i> mouse models	51
2.3.1	Subcutaneous xenograft models.....	51
2.3.2	Liver orthotopic model.....	52
2.4	Assessment of murine tumour and other tissues.....	52
2.4.1	Mechanical calliper measurement.....	52
2.4.2	Bioluminescence imaging.....	53
2.4.3	High-frequency ultrasound imaging.....	53
2.4.4	Fluorescence imaging.....	54
2.4.5	Confocal microscopy.....	56
2.4.6	Multispectral Optoacoustic Tomography (MSOT)	56
2.5	Identification of biomarkers with theranostic potential.....	57
2.5.1	Inclusion criteria	57
2.5.2	Exclusion criteria	58
2.5.3	Data extraction and analysis	58
2.6	Tenascin C as a candidate biomarker in cholangiocarcinoma	60
2.6.1	Immunohistochemistry.....	60
2.6.2	Immunoblotting.....	66
2.6.3	Immunofluorescence.....	69
2.6.4	Assessment of Tenascin C gene expression in cell lines	69
2.7	Evaluation of fluorescent labelled Tenascin C	70
2.7.1	Experimental setup.....	70
2.8	Assessment of cytotoxic effects of drugs and gold nanoparticles	71
2.8.1	Chemosensitivity to gemcitabine and irinotecan	71
2.8.2	Toxicity assays with selected gold nanoparticles.....	72
Chapter 3 Development of pre-clinical <i>in vivo</i> models of cholangiocarcinoma		74
Introduction.....		75
3.1	Generation of EH-CCA cell lines with bioluminescent properties.....	76

3.1.1	Characterization of EGI-1 and TFK-1 clones	76
3.1.2	<i>In vitro</i> growth and culture characteristics.....	78
3.1.3	Assessment of tumour growth	81
3.2	Generation of an orthotopic CCA tumour model	89
3.2.1	Intra-cholecystic injection, no cystic duct ligation (Method 1)	90
3.2.2	Peri-cholecystic, intra-liver parenchymal injection (Method 2).....	91
3.3	Histopathology of murine tumours.....	97
3.3.1	Xenograft	97
3.3.2	Orthotopic model.....	97
3.4	Discussion	100
3.4.1	Bioluminescence imaging for tumour models	100
3.4.2	Orthotopic tumour models of cholangiocarcinoma.....	104
3.4.3	Summary	105

Chapter 4 Identification of potential theranostic biomarkers in cholangiocarcinoma using a systematic review approach 106

	Introduction.....	107
4.1	Systematic search for theranostic biomarkers in CCA	108
4.1.1	Included and excluded studies	108
4.1.2	Gene ontology of selected candidate biomarkers.....	109
4.1.3	Selection of biomarkers for theranosis.....	111
4.2	Selected biomarkers for theranosis in CCA.....	113
4.2.1	Matrix metalloproteinase 9	117
4.2.2	Claudin 18	117
4.2.3	Tenascin C.....	118
4.2.4	Carbonic anhydrase 9	118
4.2.5	Epidermal growth factor receptor	118
4.3	Discussion	119
4.3.1	Matrix metalloproteinase 9 for theranostic applications.....	120
4.3.2	Claudin 18 for theranostic applications	123
4.3.3	Tenascin C for theranostic applications	125
4.3.4	Carbonic anhydrase 9 for theranostic applications.....	127
4.3.5	Epidermal growth factor receptor for theranostic applications.....	130
4.3.6	Systematic review - challenges and limitations	132
4.3.7	Future directions.....	134

Chapter 5 Tenascin C as a biomarker for theranosis in cholangiocarcinoma.... 136

Introduction.....	137
5.1 TNC is present in human cholangiocarcinoma tissue.....	138
5.1.1 TNC immunolabelling in human cholangiocarcinoma and paired normal liver tissue	140
5.1.2 TNC immunolabelling and survival in cholangiocarcinoma	141
5.2 TNC is present in selected murine xenograft and orthotopic liver tumour tissue	150
5.2.1 TNC expression on xenograft tissue.....	150
5.2.2 TNC immunolabelling in orthotopic liver tumours	155
5.2.3 TNC immunolabelling in normal murine liver.....	155
5.3 TNC is present in selected cell lines	157
5.4 Discussion	164
5.4.1 Tenascin C in human cholangiocarcinoma tissue.....	164
5.4.2 Tenascin C in murine disease models	166
5.4.3 Tenascin C in selected cell lines	167
5.4.4 Tenascin C for theranosis in cholangiocarcinoma	168
5.4.5 Future directions.....	168

Chapter 6 Development of a tenascin C targeted theranostic platform using affimers 170

Introduction.....	171
6.1 Active targeting with TNC affimers <i>in vivo</i>	174
6.1.1. Sensitivity of detection of fluorescent TNC affimers.....	174
6.1.2. Biodistribution of fluorescent TNC affimers in healthy, non- tumour bearing animals.....	176
6.1.3. Biodistribution of fluorescent TNC affimers in SW620 xenograft model.....	178
6.1.4. Biodistribution of fluorescent TNC affimers compared to control affimers	181
6.2 Gold nanoparticles as carriers for theranosis.....	195
6.2.1 Cytotoxicity of gold nanoparticles on selected cell lines	195
6.2.2 Assessment of targeting of TNC affimer labelled gold nanoparticles	197
6.2.3 Photoacoustic imaging of unlabelled gold nanoparticles.....	200
6.3 Gemcitabine and irinotecan for targeted drug delivery in cholangiocarcinoma.....	203
6.4 Discussion	205

6.4.1 Active targeting of TNC in pre-clinical models	205
6.4.2 Gold nanoparticles for theranosis.....	209
6.4.3 Chemotherapeutic drugs for theranosis	212
6.4.4 Summary	213
Chapter 7 General discussion and future challenges	214
7.1 Final summary	215
7.2 Pre-clinical models of extra-hepatic cholangiocarcinoma.....	216
7.2.1 Limitations.....	217
7.2.2 Ideal characteristics of an animal model	218
7.3 Targeting Tenascin C for theranosis	219
7.4 Targeted nanoparticles for theranosis	220
7.5 Future challenges.....	221
<i>List of References</i>.....	224
<i>Appendix 1 Data extraction table</i>.....	255
<i>Appendix 2 Ethical approval</i>.....	271

List of Figures

Figure 1-1 Cholangiocarcinoma classification	4
Figure 1-2 Illustration of extended right hepatectomy with caudate lobectomy for perihilar cholangiocarcinoma	10
Figure 1-3 Schematic of cancer drug delivery	19
Figure 1-4 Examples of nanoparticle-based drug delivery platforms.....	21
Figure 1-5 Properties of gold nanoparticles and examples of pre-clinical applications.....	27
Figure 1-6 Target Selection Criteria (TASC) scoring system.....	30
Figure 1-7 Exon structure of TNC.....	35
Figure 1-8 Tenascin C STRING network	37
Figure 2-1 Lentivirus plasmid structure.....	49
Figure 2-2 Measurement of fluorescence intensity in tumour and organs	55
Figure 2-3 PRISMA flow diagram.....	59
Figure 2-4 TNC scoring.	65
Figure 3-1 Puromycin sensitivity assay of TFK-1 and EGI-1 cell lines.....	77
Figure 3-2 Quantification of luciferase activity of TFK-1 and EGI-1 clones.....	79
Figure 3-3 Morphology of TFK-1 parental cell line and TFKluc2B2 clone	80
Figure 3-4 Doubling times of TFK-1, EGI-1 and luciferase-transfected clones.....	82
Figure 3-5 Comparison of luciferase activity of CCA cell lines with MC38luc11A	83
Figure 3-6 Xenograft growth curves.....	86
Figure 3-7 Bioluminescence imaging of TFKluc2B2 and TFKluc1D1 xenografts.....	87
Figure 3-8 Correlation between xenograft volume and radiance	88
Figure 3-9 Preliminary study of orthotopic tumour model establishment using intra-cholecystic injection of TFKluc2B2 cells (Method 1).....	92
Figure 3-10 Longitudinal bioluminescence imaging of animals following intra- cholecystic injection of TFKluc2B2 cells (Method 1).	93
Figure 3-11 Longitudinal bioluminescence imaging of animals following peri- cholecystic injection of TFKluc2B2 cells (Method 2).	95
Figure 3-12 Comparison of <i>in vivo</i> HF-US and bioluminescence imaging with macroscopic orthotopic tumour appearance	96
Figure 3-13 Histology of a TFKluc2B2 xenograft compared to TFKluc2B2 orthotopic tumour.....	98
Figure 3-14 Representative images of four orthotopic tumours by macroscopic imaging (A) and histology (B)	99

Figure 4-1 PANTHER classification of selected genes.....	110
Figure 4-2 STRING network of top 5 selected candidate biomarkers for theranosis in CCA.....	115
Figure 4-3 Schematic structure of MMP9.....	121
Figure 4-4 Schematic structure of Claudin 18.2	124
Figure 4-5 Schematic structure of Tenascin C.....	126
Figure 4-6 Schematic structure of Carbonic anhydrase 9	129
Figure 4-7 Schematic structure of EGFR.....	131
Figure 5-1 TNC immunolabelled human PH-CCA tissue sections	142
Figure 5-2 TNC in para-cancerous normal human liver tissue	144
Figure 5-3 TNC histscore comparison between paired CCA tissue and matched control liver	146
Figure 5-4 Overall survival in PH-CCA cohort stratified by TNC expression	148
Figure 5-5 Representative sections of TNC immunolabelled SW620 and TFKluc2B2 xenografts.....	153
Figure 5-6 TFKluc2B2 and SW620 orthotopic liver tumours.....	156
Figure 5-7 TNC expression in normal murine liver tissue	158
Figure 5-8 TNC mRNA expression in selected human and murine cell lines by RT-PCR.....	159
Figure 5-9 TNC detection using immunofluorescence in selected cell lines.....	161
Figure 5-10 Detection of TNC protein by immunoblotting.....	163
Figure 6-1 Schematic of a potential TNC targeted delivery platform.....	172
Figure 6-2 Detection of TNC15C-Rh1 probe <i>in vivo</i> over time.	175
Figure 6-3 Biodistribution of TNC15C-Rh1 in healthy animals.....	177
Figure 6-4 Biodistribution of TNC15C-Rh1 probe in SW620 xenograft model.....	180
Figure 6-5 Biodistribution of TNC15C-Rh2 vs GFP32C-Rh2 in SW620 xenograft tumour, liver, kidney and lung.....	182
Figure 6-6 Biodistribution of TNC15C-Rh2 vs GFP32C-Rh2 in spleen, heart and brain.....	183
Figure 6-7 Biodistribution of TNC15C-Rh2 vs GFP32C-Rh2 in TFKluc2B2 orthotopic tumour model.....	186
Figure 6-8 Comparison of fluorescence between batches of fluorescent probe.....	187
Figure 6-9 SW620 xenograft tumour volumes.....	189
Figure 6-10 Biodistribution of TNC15C-Rh3 vs GFP32C-Rh3 in SW620 xenograft tumour, liver, kidney and lung.....	190
Figure 6-11 Biodistribution of TNC15C-Rh3 vs GFP32C-Rh3 in spleen, heart and brain.....	191

Figure 6-12 TNC15C-Rh3 and GFP32C-Rh3 in SW620 xenograft tissue.....	193
Figure 6-13 Toxicity of PSS-coated gold nanorods on selected cell lines	196
Figure 6-14 Cellular uptake of TNC-AuNPLs versus Sc-AuNPLs in SW620 and HCT116 cells.....	198
Figure 6-15 Physical properties of TNC-AuNPLs and dark field microscopy in SW620 and HCT116 cell lines	199
Figure 6-16 MSOT imaging of gold nanoplates in tissue mimicking agar phantoms	201
Figure 6-17 Multispectral optoacoustic tomography of gold nanorods.....	202
Figure 6-18 Evaluating TFK-1 and TFKluc2B2 sensitivity to irinotecan and gemcitabine.....	204

List of Tables

Table 1-1 Staging for perihilar cholangiocarcinoma	8
Table 1-2 Stage groupings for perihilar cholangiocarcinoma	9
Table 1-3 List of clinical trials in unresectable cholangiocarcinoma utilising biological agents.	15
Table 1-4 List of clinical trials in unresectable cholangiocarcinoma utilising nanotherapeutic technology.	23
Table 1-5 Summary of clinical trials of tenascin C inhibitor therapy	39
Table 2-1 Tenascin C Optimization	61
Table 4-1 Potential biomarkers for theranosis: (TASC-T) scoring criteria.....	112
Table 4-2 TASC-T scoring of 16 selected biomarkers validated in ≥ 2 studies.....	114
Table 4-3 Study characteristics of the top 5 selected candidate biomarkers for theranosis in CCA.....	116
Table 5-1 PH-CCA patient demographics and clinicopathological variables.....	147
Table 5-2 IH-CCA patient demographics and clinicopathological variables.....	149
Table 5-3 Comparison of mechanical calliper vs HF-US tumour volume measurement in temporal SW620 xenografts and their corresponding TNC histoscore	152

List of Abbreviations

AJCC	American Joint Committee on Cancer
ANGP2	Angiopoietin 2
AuNPs	Gold nanoparticles
AuNPLs	Gold nanoplates
AuNRs	Gold nanorods
BDL	Bile duct ligation
BTC	Biliary tract cancer
CAF	Cancer-associated fibroblast
CA9	Carbonic anhydrase 9
CCA	Cholangiocarcinoma
CLDN18	Claudin 18
CLDN18.2	Claudin 18.2
CRC	Colorectal cancer
CRLM	Colorectal liver metastasis
DMSO	Dimethyl sulfoxide
DMEM	Dulbecco's Modified Eagle's Medium
D-CCA	Distal cholangiocarcinoma
ECM	Extra-cellular matrix
EDTA	Ethylenediaminetetra-acetic acid disodium salt
EGF	Epidermal growth factor
EGFR	Epidermal growth factor receptor
EH-CCA	Extra-hepatic cholangiocarcinoma
EPR	Enhanced permeability and retention
ERCP	Endoscopic retrograde cholangiopancreatography
FDA	United States Food and Drug Administration
FFPE	Formalin-fixed paraffin-embedded
FLR	Future liver remnant

FCS	Foetal calf serum
GBC	Gallbladder carcinoma
GFP32C-Rh	GFP-targeted affimer labelled with rhodamine red C ₂ maleimide
HCC	Hepatocellular carcinoma
hENT1	Human equilibrative nucleoside transporter 1
HF-US	High-frequency Ultrasound
HIER	Heat-induced epitope retrieval
HRP	Horseradish peroxidase
IH-CCA	Intra-hepatic cholangiocarcinoma
IP	Intra-peritoneal
MMP9	Matrix metalloproteinase 9
MPS	Mononuclear phagocyte system
MRI	Magnetic resonance imaging
MTT	3-[4,5-Dimethylthiazol-2-yl]-2,5-diphenyl-tetrazolium bromide
NGAL	Neutrophil gelatinase-associated lipocalin
NIR	Near-infrared light
OS	Overall survival
PAI	Photoacoustic imaging
PDT	Photodynamic therapy
PEG	Polyethylene glycol
PET	Positron emission tomography
PH-CCA	Peri-hilar cholangiocarcinoma
PSC	Primary sclerosing cholangitis
PSS	Polystyrene sulphonate
PTC	Percutaneous transhepatic cholangiography
PTT	Photothermal therapy
PVE	Portal vein embolization
ROI	Region of interest
RT-PCR	Reverse transcription polymerase chain reaction
Sc-AuNPL	Silica coated gold nanoplates

SPECT	Single photon emission computed tomography
TGF β	Transforming growth factor β
TLR-4	Toll-like receptor 4
TMA	Tissue microarray
TNC	Tenascin C
TNC-AuNPL	TNC affimer coated gold nanoplates
TNC15C-Rh	TNC-targeted affimer labelled with rhodamine red C ₂ maleimide
VEGF	Vascular endothelial growth factor
VEGF-R2	Vascular endothelial growth factor receptor 2

Chapter 1

Introduction

Introduction

1.1 Cholangiocarcinoma

Cholangiocarcinomas (CCA) are a group of rare malignancies affecting the bile ducts of the liver (Patel, 2006; Razumilava and Gores, 2014). The crude incidence rate of CCA in England in 2010-2013 was 3.58 per 100,000 population with a crude mortality rate of 3.37/100,000 (Public Health England, 2015). Due to their rarity, CCAs are included in the group of rare and less common cancers by the UK National Cancer Intelligence Network.

Worldwide, incidence of CCA has been rising and this has been highlighted by several studies (Khan *et al.*, 2008; Khan *et al.*, 2012; Bergquist and von Seth, 2015). The highest incidence remains in Thailand where CCA is a significant national health burden (Kamsa-ard *et al.*, 2011). Recently, the World Cholangiocarcinoma Day collaborative attempted to bring together various global patient support groups to raise awareness about this uncommon but lethal group of cancers (World Cholangiocarcinoma Day, 2019).

1.1.1 Aetiology and classification

Carcinogenesis in CCA develops on a background of biliary inflammation and obstruction (Khan *et al.*, 2008; Wadsworth *et al.*, 2011). Although major risk factors such as primary sclerosing cholangitis (PSC) and liver fluke infestation have been identified, the pathogenesis of CCA remains poorly understood (Khan *et al.*, 2008; Kirstein and Vogel, 2016). There is also a significant geographical variation in the distribution of CCA, with the highest incidence rates in North East Thailand where the rate is >80 per 100,000 population (Kirstein and Vogel, 2016).

1.1.1.1 Anatomical classification

The most commonly used classification of CCA is anatomical and describes peripheral or intra-hepatic (IH-CCA), hilar or perihilar (PH-CCA) and extra-hepatic (EH-CCA) subtypes (Razumilava and Gores, 2014). This is illustrated in **Figure 1-1A**. PH-CCA which is a variant of EH-CCA includes CCA around the hepatic duct bifurcation from 2nd order bile ducts to the origin of the cystic duct. Distal CCA (D-CCA), which includes CCA arising distal to the origin of the cystic duct down to the ampulla of Vater, is also a variant of EH-CCA (Khan *et al.*, 2012; Razumilava and Gores, 2013).

PH-CCA is the commonest type of CCA accounting for over 50% of CCA (Patel, 2006; Mansour *et al.*, 2015) and is the main focus of this project. An anatomical subclassification of PH-CCA is based on the Bismuth-Corlette classification (**Figure 1-1C**) which takes into account the degree of ductal involvement (Suarez-Munoz *et al.*, 2013). This classification is also used for benign biliary strictures and bile duct injuries (Mercado and Dominguez, 2011).

The umbrella term biliary tract cancers (BTC) includes all anatomical subtypes of CCA as well as gallbladder cancer (GBC). This grouping together of this heterogenous group of BTCs is often used in clinical trials due to the relative rarity of these cancers. However, the distinction between these subtypes is essential as they have different clinical, radiological and biological characteristics (Oliveira *et al.*, 2017).

1.1.1.2 Histopathological classifications

Another classification of CCA includes stratification by macroscopic pathological differences into mass-forming, periductal-infiltrating and intra-ductal growth types (**Figure 1-1B**) The vast majority of CCAs are adenocarcinomas that are usually well-differentiated (Patel, 2006) but moderate or poor differentiation is also seen.

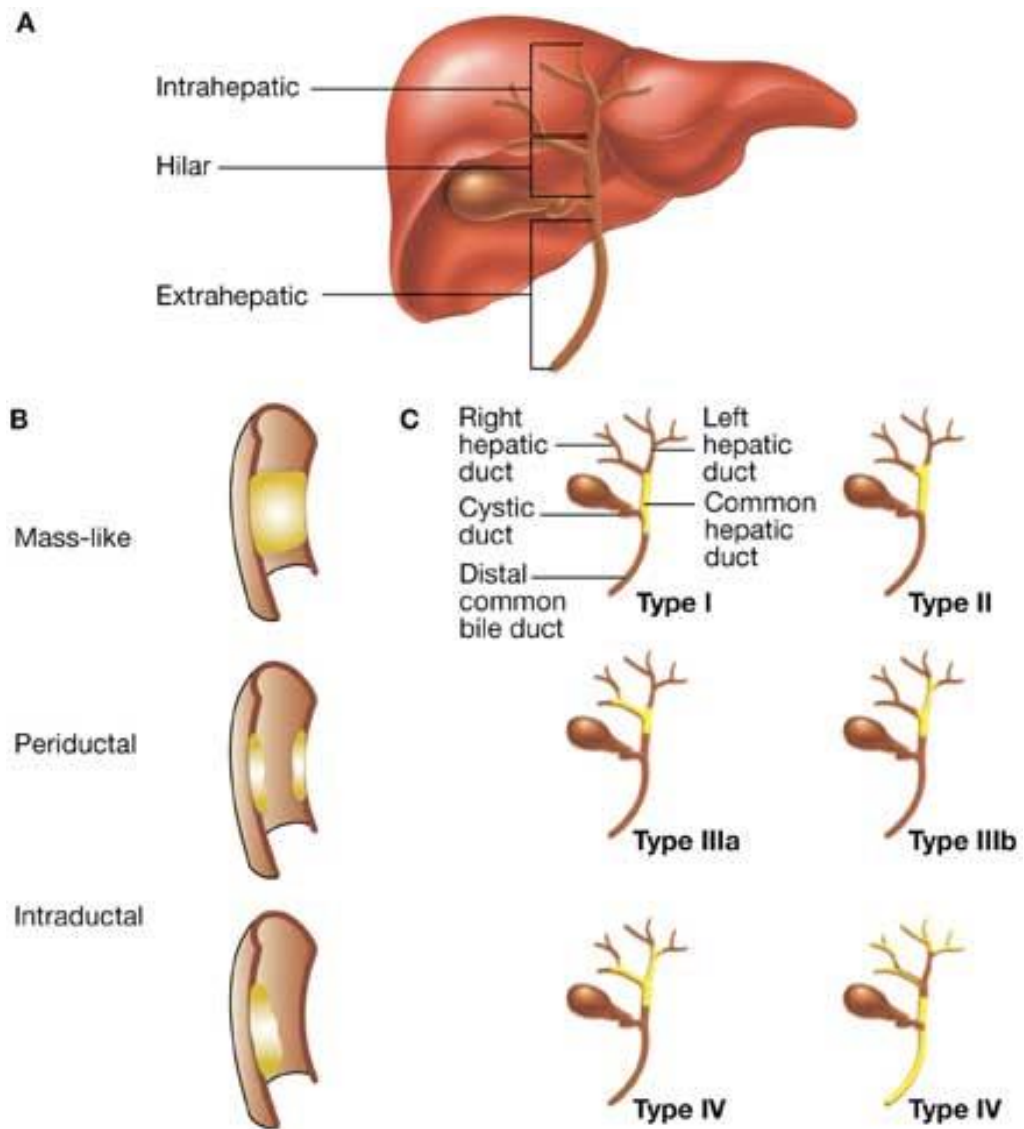


Figure 1-1 Cholangiocarcinoma classification.

Panel **A** shows the anatomical location of CCA variants in the biliary tree. Panel **B** shows the three main macroscopic pathological classifications. Panel **C** shows the Bismuth Corlette classification of PH-CCA - Type I: involvement of hepatic duct below the bifurcation; Type II: involvement of the bifurcation without invasion of second order ducts; Type IIIa: involvement of right sided ducts into second order, but with sparing of left second order ducts; Type IIIb: involvement of left sided ducts into second order, but with sparing of right second order ducts; Type IV: involvement of bilateral second order ducts and/or skip lesions.

Image taken from (Patel, 2006)

Histological classification of EH-CCA broadly includes mucinous adenocarcinomas and papillary tumours but IH-CCA are more varied (Kendall *et al.*, 2019). Other histological subtypes include rare variants such as combined hepatocellular carcinoma and cholangiocellular carcinoma which have a morphology that is a combination of typical hepatocellular carcinoma (HCC) and IH-CCA (Kendall *et al.*, 2019).

IH-CCA is also divided into large bile duct type and small bile duct type based on the predominant histological pattern whereas EH-CCA have a similar pattern to IH-CCA that have arisen from large bile ducts (Lendvai *et al.*, 2018).

These subtypes have distinct features (Oliveira *et al.*, 2017) and the heterogeneity of location and histological subtypes of this group of cancers makes it challenging for the development of therapeutic strategies that would be useful for all CCAs.

1.1.1.3 Molecular classification

An evolving field in CCA is its molecular classification. A vast number of identified molecular alterations in CCA have contributed to the better understanding of this varied group of cancers and paved the way for future more personalised treatments for patients based on the molecular profile (Kendall *et al.*, 2019). Alterations in genes such as *KRAS*, *TP53*, *IDH1*, *IDH2*, *BAP1*, *FGFR2*, *EGFR* and *ERBB2* are often detected in BTCs and some of these have drugs that target these alterations (i.e. 'druggable' molecular alterations)(Verlingue *et al.*, 2017b). However, the most common molecular targeted agents evaluated in clinical trials of BTC are epidermal growth factor receptor (EGFR) inhibitors in the absence of *KRAS* mutation (i.e. *KRAS* wild type) (Verlingue *et al.*, 2017a)

With the advent of next generation sequencing, high throughput genomics have made it possible for molecular profiling of cancers which the investigators of the MOSCATO-01 trial used to investigate patients who may benefit from specific targeted treatments

based on their molecular profile (Massard *et al.*, 2017). This umbrella study by Massard *et al.* (2017) included numerous types of cancers including the rare and difficult to treat ones like BTC. Of the 43 patients with BTC included in the MOSCATO-01 trial, 18 patients (14/18 IH-CCA, 2/18 EH-CCA, 2/18 GBC) were treated for a detected druggable genomic alteration using direct or indirect inhibition of the respective molecular target, the most common being *IDH1/IDH2* mutations and *FGFR1/FGFR2* translocations or mutations (Verlingue *et al.*, 2017b). In this small patient cohort, an improvement in median overall survival (OS) was seen with the targeted treatments (Verlingue *et al.*, 2017b).

Borger *et al.* (2012) have previously shown that *IDH1/IDH2* mutations are a feature of IH-CCA rather than EH-CCA or GBC. Sia *et al.* (2015) demonstrated that about 70% (79/114) of IH-CCA have druggable molecular alterations, the most common being *FGFR2* fusions which can be targeted with tyrosine kinase inhibitors targeting *FGFR2*.

In a systematic review Wiggers *et al.* (2014) highlighted the differences in immunohistochemical markers between IH-CCA and EH-CCA. They reported the expression of proteins such as EGFR, SMAD4, p27, BCL-2, VEGF-A as higher in IH-CCA whereas MUC1, MUC5AC, p53, AKT2 and HER2 were higher in EH-CCA (Wiggers *et al.*, 2014).

The molecular classification of CCAs is increasingly becoming important as these markers can aid differential diagnosis and molecular subtyping, give valuable information regarding the tumour biology and prognosis, predict response to therapy or even become the basis for novel treatments in the future.

1.1.2 Diagnosis and staging

Sporadic cases of CCA often present with jaundice, abdominal pain and weight loss. Majority of patients have advanced disease at presentation, with only 20-50% of

patients eligible for surgical resection, which is the only curative treatment option at present (Razumilava and Gores, 2013).

Patients with underlying primary sclerosing cholangitis (PSC) have a 10-15% lifetime risk of developing CCA and this risk is highest in the first year following diagnosis of PSC (Khaderi and Sussman, 2015). The diagnosis of malignancy in this group is often challenging due to the difficulties in distinguishing malignant changes from the underlying dysplastic changes of PSC, some of which may be premalignant (Harrison, 1999).

Disease staging in CCA is essential to assess resectability and predict outcomes. Several staging systems exist but the American Joint Committee on Cancer (AJCC) staging 8th edition for PH-CCA is shown in **Table 1-1** and **Table 1-2**. AJCC and other staging systems for IH-CCA (Yamamoto *et al.*, 2019) and D-CCA (Kang *et al.*, 2019) are also in routine use.

1.1.3 Management

1.1.3.1 Resectable disease

In cases of resectable (or operable) disease with curative intent, surgical management often includes major liver resection. For example, patients with PH-CCA often require a hepatic trisectionectomy with caudate lobectomy and local lymphadenectomy (**Figure 1-2**) to achieve complete resection and negative margins (Mansour *et al.*, 2015).

Potentially curative surgery is possible even for advanced T3/T4 disease (**Table 1-1**) if negative resection margins (R0 resections) can be achieved but curative surgery is not possible in the presence of metastatic disease.

Table 1-1 Staging for perihilar cholangiocarcinomaAJCC staging 8th edition. Taken and adapted from (Gaspersz *et al.*, 2019)

Stage	
Tumour (T) stage	
T _{is}	Carcinoma in situ / high grade dysplasia
T1	Tumour confined to the bile duct, with extension up to the muscle layer or fibrous tissue
T2a	Tumour invades beyond the wall of the bile duct to surrounding adipose tissue
T2b	Tumour invades adjacent hepatic parenchyma
T3	Tumour invades unilateral branches of the PV or HA
T4	Tumour invades main PV or its branches bilaterally, or the common hepatic artery, or unilateral second-order biliary radicals with contralateral portal vein or hepatic artery involvement.
Node (N) stage	
N0	No regional lymph node metastasis
N1	One to three positive lymph nodes typically involving the hilar, cystic duct, common bile duct, hepatic artery, posterior pancreaticoduodenal, and portal vein lymph nodes
N2	Four or more positive lymph nodes from the sites described for N1
Metastasis (M) stage	
M0	No distant metastasis
M1	Distant metastasis (includes lymph node metastasis distant to the hepatoduodenal ligament)

Table 1-2 Stage groupings for perihilar cholangiocarcinoma

AJCC staging 8th edition. Taken and adapted from (Gaspersz *et al.*, 2019)

Stage	T	N	M
0	is	0	0
I	1	0	0
II	2a-b	0	0
IIIa	3	0	0
IIIb	4	0	0
IIIc	Any	1	0
IVa	Any	2	0
IVb	Any	Any	1

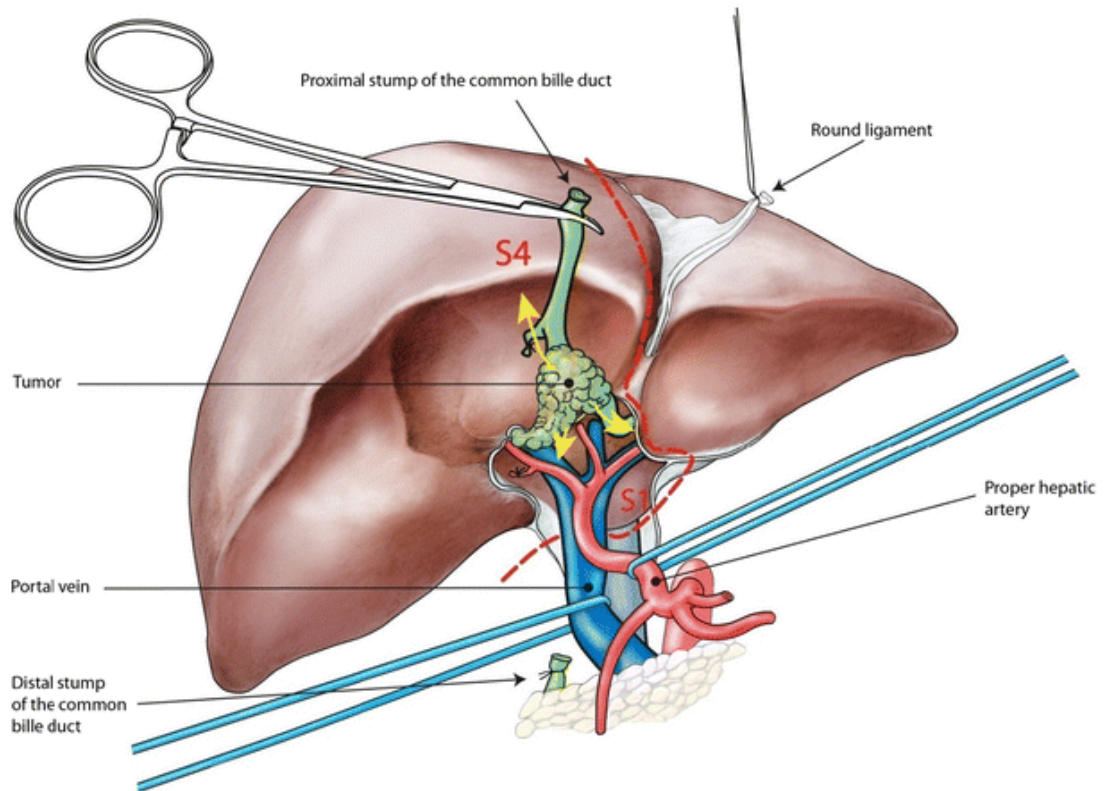


Figure 1-2 Illustration of extended right hepatectomy with caudate lobectomy for perihilar cholangiocarcinoma

An extended right hepatectomy and caudate lobectomy involves resection of all liver segments lateral to the red dotted line shown. The surrounding lymph nodes which follow the vasculature around the liver hilum (not shown in figure) are also excised. Occasionally, vascular resection and reconstruction is required. Biliary drainage is achieved by anastomosing the biliary duct(s) of the future liver remnant (segment 2 and 3) to a loop of jejunum (usually a Roux-en-Y hepaticojejunostomy).

Liver resection for PH-CCA often involves an extended right hepatectomy with caudate lobectomy (as shown in this figure) or an extended left hepatectomy depending on the side of the liver predominantly occupied by the tumour.

Taken from Rassam *et al.* (2018)

The presence of microscopic disease (R1 resections), macroscopic disease (R2 resections) or nodal involvement of disease are known poor prognostic indicators following curative intent resection (Young *et al.*, 2010).

Prior to surgery, biliary drainage either by endoscopic retrograde cholangiopancreatography (ERCP) or via a percutaneous transhepatic (PTC) route, may be required. In PH-CCA, biliary obstruction is often an early feature which may affect the function of the future liver remnant (FLR) (Mansour *et al.*, 2015; Tang *et al.*, 2017). Pre-operative portal vein embolization (PVE) is another strategy that is considered in the preparation for major liver resection. PVE can induce hypertrophy of the FLR and reduce risk of post-operative morbidity, especially liver failure (Mansour *et al.*, 2015; Cillo *et al.*, 2019).

IH-CCAs may be amenable to segmental liver resection but often major liver resection is required with reported median survival of 36 months and 5-year OS of 32% in a series of 163 patients with mass-forming IH-CCA (Farges *et al.*, 2011). D-CCA which require bile duct excision or pancreaticoduodenectomy (Schreuder *et al.*, 2019) are not the focus of this project and therefore not discussed further.

Limited experience from specialized centres has shown that there may be a role for liver transplantation in highly selected patients following neoadjuvant chemoradiotherapy (Gores *et al.*, 2013; Mansour *et al.*, 2015). Currently there is no evidence to support neoadjuvant therapy prior to upfront resection of resectable CCA (Grendar *et al.*, 2014).

Recently published outcomes of a large Japanese cohort of patients with PH-CCA (n=643) reported 41% 5-year OS in the octogenarians (≥ 80 years; n=40) undergoing major resection, which is promising given the aging populations worldwide (Akashi *et al.*, 2018). However, it is not known if these outcomes can be extrapolated to Western cohorts of patients.

1.1.3.2 Adjuvant therapy

Gemcitabine-based regimens remain the first-line agents despite scarce data from prospective randomised-controlled trials of adjuvant therapy in BTC (Anderson and Kim, 2009).

The recently concluded UK BILCAP trial randomised macroscopically completely excised BTC patients to adjuvant therapy with capecitabine versus observation alone. They reported an OS benefit with capecitabine (Primrose *et al.*, 2019). As capecitabine improved OS in these patients with acceptable chemotherapy-related adverse events, the trial concluded that adjuvant capecitabine should become the standard of care as opposed to observation alone (Primrose *et al.*, 2019). The ACTICCA-1 trial investigated adjuvant gemcitabine and cisplatin (Stein *et al.*, 2015) but in light of the results of the BILCAP trial, modified the control arm to capecitabine instead of observation alone. Two other phase III trials, BCAT (Ebata *et al.*, 2018) and PRODIGE (Edeline *et al.*, 2019), investigated adjuvant gemcitabine monotherapy and gemcitabine plus oxaliplatin respectively, but did not report a significant benefit of adjuvant chemotherapy.

In a meta-analysis of BILCAP, BCAT and PRODIGE trials, Messina *et al.* (2019) reported only modest improvement in recurrence-free survival (hazard ratio 0.83, 95% C.I 0.69-0.99) with 42% (183/435 patients) grade 3 or grade 4 adverse events in the adjuvant chemotherapy groups.

There are no prospective trials comparing radiotherapy following resection despite some encouraging results from retrospective studies especially in IH-CCA (Zheng *et al.*, 2018).

1.1.3.3 Unresectable disease

The current standard of care for locally advanced or recurrent CCA is systemic chemotherapy using gemcitabine and cisplatin regimens, with or without radiotherapy and photodynamic therapy (PDT), to achieve local control of symptoms and prolong survival (Okusaka *et al.*, 2010; Valle *et al.*, 2010).

PDT has been associated with a significant survival advantage in patients with unresectable CCA (Moole *et al.*, 2017) and improvement in 5-year OS compared to systemic chemotherapy (17.6% vs 3.8%; hazard ratio 0.72; 95%CI, 0.52-0.998; P = .048) has shown in a recent study (Wu *et al.*, 2019).

Radioembolization with Yttrium-90 glass microspheres evaluated in non-randomised studies have shown some benefit especially in IH-CCA and success in downstaging disease to enable surgical resection in BTC (Bourien *et al.*, 2018).

There are no standard second-line chemotherapeutic regimens for advanced BTC. Results of randomised controlled clinical trials such as the ABC-06 trial (NCT01926236) of 5-FU and oxaliplatin regimens (mFOLFOX) are awaited (Clinicaltrials.gov, 2019a). Combination chemotherapeutic regimens with agents such as nab-paclitaxel (nanoparticle formulation of paclitaxel that consists of albumin-bound drug) with gemcitabine have been evaluated with no survival benefit (Sahai *et al.*, 2018). A trial of triple regimens including nab-paclitaxel, gemcitabine and cisplatin (NCT02392637) is ongoing (Clinicaltrials.gov, 2019b).

New drugs such as NUC-1031 (acelarin), a nucleotide analogue which has been designed to overcome the drawbacks of gemcitabine (Sarr *et al.*, 2019), have also entered clinical trials (ABC-08 trial; NCT02351765) in advanced and metastatic BTC (Clinicaltrials.gov, 2019b). This drug, unlike gemcitabine is independent of the hENT1 transporter for uptake into cells, achieves higher intracellular levels of active drug

compared to gemcitabine and is not metabolised by cytidine deaminase which in the case of gemcitabine, results in toxic metabolites (Sarr *et al.*, 2019). For unresectable CCA where first line chemotherapy involves gemcitabine regimens, this drug offers promise of improved outcomes.

Selumetinib, a mitogen-activated protein kinase 1 and 2 inhibitor, is another new drug that has been in advanced BTC clinical trials but has thus far shown little benefit either as monotherapy (Bekaii-Saab *et al.*, 2011) or in combination (Bridgewater *et al.*, 2016).

Biological agents have also been trialled in CCA but the efficacy of these are yet to be reported (Morizane *et al.*, 2018). Clinical trials involving biological agents in unresectable CCA are summarized in **Table 1-3**.

Of the trials of biological agents in CCA, only one has published results to date. This phase II trial evaluating the vascular endothelial growth factor A (VEGF A) inhibitor bevacizumab in combination with an EGFR inhibitor erlotinib, reported 12% response rate and a median survival of 9.9 months in advanced BTC (Lubner *et al.*, 2010).

Reported outcome rates for standard gemcitabine and cisplatin regimens include a response rate of 26.1% and median survival of 11.7 months (Valle *et al.*, 2010).

Targeted therapy with bevacizumab and erlotinib may therefore provide an alternative therapeutic strategy, although it has not been shown to be superior to existing chemotherapy. The more recent trials have involved antibody-based immune checkpoint inhibitors against programmed cell death protein 1 (PD-1) and programmed cell death ligand 1 (PD-L1) but results of these trials are still awaited.

Table 1-3 List of clinical trials in unresectable cholangiocarcinoma utilising biological agents.

Table compiled following a search for “cholangiocarcinoma non-resectable”, “unresectable Bile duct cancer”, “Cholangiocellular carcinoma” in the Clinical Trials database (ClinicalTrials.gov, last accessed November 2019). References not available (N/A) or results not published.

Year	Trial number / Stage	Biological agent (target)	Phase	Results Reference
2006	NCT00356889 / Completed	Bevacizumab (VEGF-A)	II	(Lubner <i>et al.</i> , 2010)
2007	NCT00478140 / Terminated	Trastuzumab (HER2)	II	N/A
2008	NCT00624182 / Suspended	Peptide vaccine for URLC10 (URLC10)	I	N/A
2013	NCT01825603 / Completed	ADH-1 (N-cadherin)	I	N/A
2015	NCT02495896 / Active, not recruiting	Recombinant EphB4-HSA fusion protein (Ephrin-B2)	I	N/A
2017	NCT03250273 / Recruiting	Nivolumab (PD-1)	II	N/A
2017	NCT03201458 / Active	Atezolizumab (PD-L1)	II	N/A
2017	NCT03149549 / Recruiting	PROCLAIM-CX-2009 (ALCAM)	I / II	N/A
2018	NCT03473574 / Recruiting	Durvalumab (PD-L1) and Tremelimumab (CTLA-4)	II	N/A
2018	NCT03779100 / Suspended	PD-1 antibody (PD-1)	II	N/A
2018	NCT03257761 / Recruiting	Durvalumab (PD-L1)	I	N/A
2019	NCT03951597 / Recruiting	PD1 antibody JS001 (PD-1)	II	N/A
2019	NCT03942328 / Recruiting	Pneumococcal 13- valent Conjugate Vaccine; Therapeutic Autologous Dendritic Cells	I	N/A
2019	NCT03898895 / Not yet recruiting	Radiotherapy+antiPD-1 (PD-1)	II	N/A

In patients with unresectable disease, there is some evidence from specialized centres to suggest that neoadjuvant therapy could downstage disease to the extent that R0 resections can be achieved and improve survival (Frosio *et al.*, 2019).

1.1.3.4 Neoadjuvant therapy followed by liver transplantation

Limited experience from specialized centres has shown that there may be a role for liver transplantation in highly selected patients following neoadjuvant chemoradiotherapy (Gores *et al.*, 2013; Mansour *et al.*, 2015; Machairas *et al.*, 2019). Comparison of liver resection with liver transplantation for unresectable but not disseminated PH-CCA showed that in the selective cases of liver transplantation, this option was non-inferior in combination with neoadjuvant chemoradiotherapy (Moris *et al.*, 2019). The main arguments against liver transplantation in this cohort of patients is the risk of recurrent disease in the immunosuppressed patient and the scarcity of donor livers on an already stretched liver transplant waiting list.

1.1.3.5 Limitations and challenges of systemic cytotoxic chemotherapy for cholangiocarcinoma

Multiple chemotherapeutic agents have been used in advanced BTC, but gemcitabine is the most commonly used agent. Systemic gemcitabine chemotherapy is usually administered in 21 day cycles (Gabriel *et al.*, 2017) to allow recovery between cycles and minimise toxic side effects. Most CCA trials use this pulsatile administration at the maximum tolerated dose of gemcitabine (Valle *et al.*, 2010; Stein *et al.*, 2015; Ebata *et al.*, 2018; Edeline *et al.*, 2019). This high dosing can cause severe toxicities which can lead to dose modifications, missed cycles or even termination, all of which limits efficacy of therapy (Mross and Kratz, 2011). Only a fraction of the administered dose actually reaches the tumour microenvironment to be of therapeutic benefit but off-

target activity is responsible for many side-effects and toxicities (Mross and Kratz, 2011).

Constant administration of low dose chemotherapy with no drug-free breaks (i.e. metronomic dosing) has shown benefits in pancreatic ductal adenocarcinoma pre-clinical studies (Cham *et al.*, 2010) and other cancers (Simsek *et al.*, 2019). However, this has not been reported for CCA.

Intrinsic or acquired resistance to cytotoxic chemotherapy has been reported to be the major cause of treatment failure in metastatic cancer (Longley and Johnston, 2005). In CCA for example, tumours with low human equilibrative nucleoside transporter 1 (hENT1) levels are inherently less responsive to gemcitabine chemotherapy (Fisher *et al.*, 2013; Sasaki *et al.*, 2014).

In desmoplastic tumours like CCA, there is concern regarding the ability of chemotherapeutic drugs to penetrate the tumour stroma which is dense and hypovascular. This can limit the therapeutic efficacy of systemically administered drugs (Sirica and Gores, 2014). The authors of this study recommended new drug delivery mechanisms including nanotechnology-based drug delivery systems to overcome these barriers in CCA (Sirica and Gores, 2014).

These limitations highlight the need to develop more targeted tumour-specific therapies that are better tolerated by patients to improve efficacy.

1.1.4 Prognosis

Prognosis has remained dismal despite advances in operative strategies. PH-CCA patients undergoing curative resection with localized disease and negative margins have the best prognosis; over 50% 5-year disease-free and OS (Mansour *et al.*, 2015; Komaya *et al.*, 2018). In unresectable disease, median OS remains under 12 months even with palliative chemotherapy (Valle *et al.*, 2010).

1.2 Nanomedicine and potential applications in cholangiocarcinoma

Development of new treatment strategies remains a crucial part of the quest for improving outcomes of CCA, hence exploring new emerging technologies are worthwhile. Over the last decade, significant advances have been made in the field of nanomedicine and its potential applications for the diagnosis and treatment of human diseases (Chen *et al.*, 2014; Chen *et al.*, 2016b; Pelaz *et al.*, 2017). This field has become an attractive area for further research (Estanqueiro *et al.*, 2015; Park and Na, 2015; van der Meel *et al.*, 2019).

Utilising nanotechnology in cancer therapy could help overcome some of the challenges of CCA chemotherapy such as drug delivery to the hypovascular stroma of CCA (**Section 1.1.3.5**). Another advantage is that previously discovered chemotherapeutic drugs that have shown promise *in vitro* but have had limited translational applications due to physical properties such as hydrophobicity, might be successfully be delivered using nanoparticle delivery systems (Mico *et al.*, 2017). Hence, effective anti-cancer drugs that were previously classed as ineffective could be reassessed once a successful delivery platform has been developed.

Drug delivery to solid tumours have five key stages namely, circulation in the blood, accumulation and penetration into the tumour, internalisation by tumour cells followed by release of drug (**Figure 1-3**). A nanocarrier drug delivery system could be designed to efficiently negotiate each of these five steps (Pelaz *et al.*, 2017). However, for this mechanism to be effective, the nanoparticle delivery system should meet certain criteria.

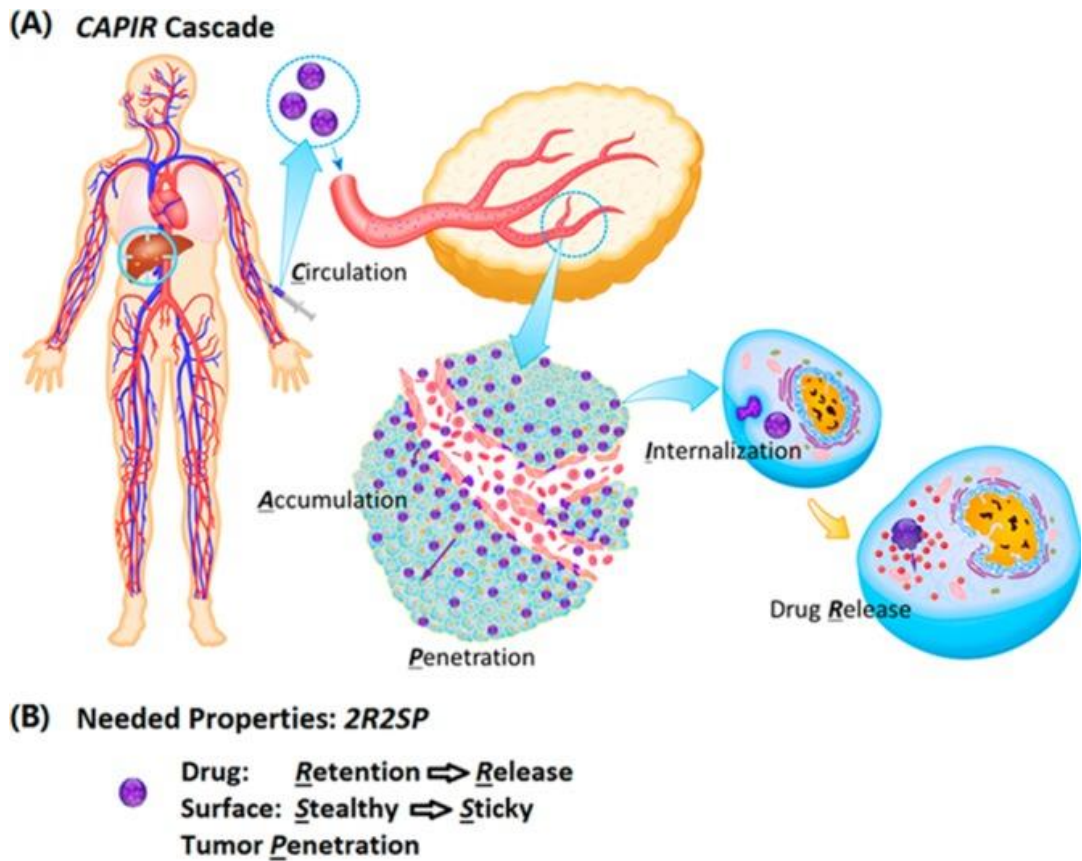


Figure 1-3 Schematic of cancer drug delivery

A shows the five step CAPIR cascade (circulation, accumulation, penetration, internalisation and drug release) of cancer drug delivery.

B summarises the properties required by a nanoscale carrier to efficiently navigate the CAPIR cascade and improve cancer drug delivery. These properties include drug retention and release at intended site, “stealth” to escape identification and sequestration by the immune system whilst in circulation and ability to bind to intended target.

Taken from (Sun *et al.*, 2014a)

It should have the ability to penetrate into the tumour and retain the drug until release at the tumour site (Sun *et al.*, 2012; Sun *et al.*, 2014a). The surface should not be immunogenic which could result in rapid sequestration from the circulation, but at the same time be able to accumulate at the tumour site either by passive or active targeting (Sun *et al.*, 2012; Sun *et al.*, 2014a). This can be challenging as features that favour one criteria, such as introduction of a targeting ligand on the nanoparticle to improve active targeting, may lead to a reduction in the circulation time and hence tumour accumulation (Sun *et al.*, 2014a).

1.2.1 Nanoparticles for diagnosis and therapy

Concomitant use of nanoscale particles for diagnostic and therapeutic applications, termed theranostics (Lammers *et al.*, 2011), has been evaluated in malignant and non-malignant conditions (Kelloff *et al.*, 2005; Wu *et al.*, 2013a; Kodiha *et al.*, 2015; Wu and Zhou, 2015a). Such a multifunctional theranostic particle would theoretically allow drug loading, imaging of drug delivery, active targeting of drug delivery to predetermined targets as well as assess tumour response to drug (Lammers *et al.*, 2011; Pelaz *et al.*, 2017). The use of targeted nanoparticles for drug delivery could improve the precision of drug delivery and therefore reduce off target toxicity (Huynh *et al.*, 2009).

A wide range of nanoparticles have been explored for theranostic purposes in human disease and some examples of these are summarised in **Figure 1-4**. Jokerst *et al.* (2011) described the ideal theranostic nanoparticle as one that is safe for humans, rapidly and selectively taken up by the target of interest, can efficiently deliver sufficient therapeutic agent with minimum off-site toxicity and quickly eliminated from the body or biodegraded into non-toxic by-products.

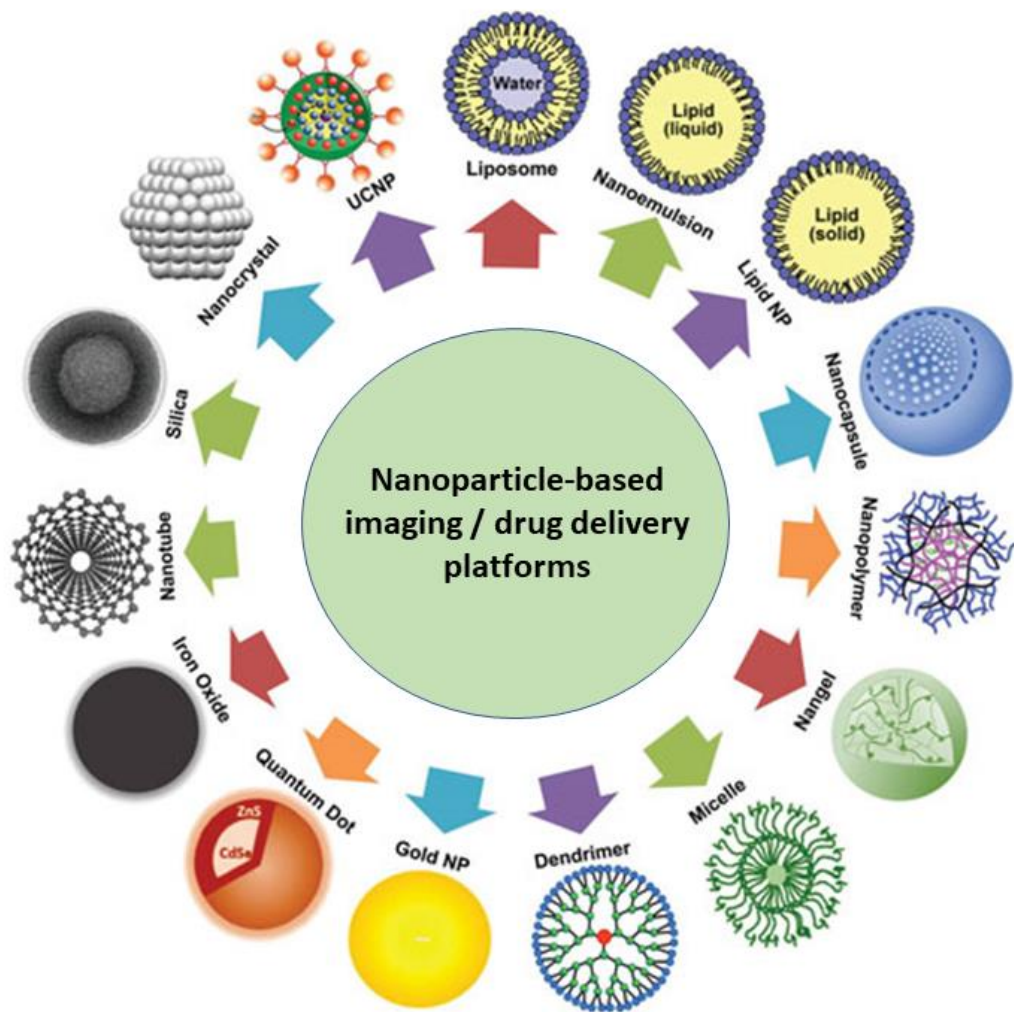


Figure 1-4 Examples of nanoparticle-based drug delivery platforms

Organic nanocarriers such as liposomes, nanoemulsions and lipid nanoparticles and inorganic nanocarriers such as gold nanoparticles, iron oxide and silica nanoparticles have all been utilised in pre-clinical studies of imaging and drug delivery.

Taken and adapted from Kumar *et al.* (2017). Not to scale

Surface functionalization of nanoparticles to recognise a 'target' in tumour tissue should improve the specificity of tumour targeting i.e. active targeting (Adair *et al.*, 2010), which should in turn allow targeted drug delivery to the tumour.

Other useful properties of nanoparticles include the potential for controlled drug release (Pelaz *et al.*, 2017). The triggers for drug release could be a change in pH or electrostatic charge which would enhance retention of drug in the nanoparticle until the correct conditions are met for drug release.

Nanoparticle-based delivery systems could extend diagnostic and therapeutic options in CCA. Firstly, development of a theranostic particle could improve diagnostic imaging, including detecting sites of occult disease and accurately mapping tumour margins. Secondly, targeted-drug delivery could enhance effectiveness of existing therapy but reduce systemic side effects including the undesirable chemotherapy-induced liver injury (Zorzi *et al.*, 2007). With targeted therapy, it is hoped that function of the normal liver will be preserved while delivering sufficient doses of therapeutic drugs to the liver tumour. Targeted-drug delivery in CCA could also include combinations of chemotherapeutic drugs that have proven efficacy in CCA.

Nanoparticles have also been applied in image-guided surgery (Pelaz *et al.*, 2017). Utilising this technology to accurately map tumour margins with real-time feedback to the operating surgeon would be a highly useful, practical application of this technology for CCA surgery as the poorer outcomes for margin positive resections has been well established (Messina *et al.*, 2019).

1.2.2 Nanoparticles in clinical use in cholangiocarcinoma

Liposomal irinotecan and nanoparticle formulation of paclitaxel (Nab-paclitaxel) are the only nanotherapeutic agents currently in CCA clinical trials (**Table 1-4**). These trials began recruiting within the last 5 years and are yet to publish their outcomes.

Table 1-4 List of clinical trials in unresectable cholangiocarcinoma utilising nanotherapeutic technology.

Table compiled following a search for “cholangiocarcinoma non-resectable”, “unresectable Bile duct cancer”, “Cholangiocellular carcinoma” in the Clinical Trials database (Clinicaltrials.gov, 2019b).

References not available (N/A) or results not published.

Year	Trial number / Stage	Nanotherapeutic drug	Phase	Results Reference
2015	NCT02495896 / Active, not recruiting	Palcitaxel Albumin-Stabilized nanoparticle formulation	I	N/A
2017	NCT03943043/ Recruiting	Nab-paclitaxel (Palcitaxel nanoparticle formulation)	I / II	N/A
2018	NCT03043547 / Recruiting	Nal-IRI (liposomal irinotecan)	II	N/A
2018	NCT03368963 / Recruiting	Nal-IRI (liposomal irinotecan)	I / II	N/A
2018	NCT03768414 / Recruiting	Nab-paclitaxel (Palcitaxel nanoparticle formulation)	III	N/A

Neither of these agents are actively targeted nor do these formulations have theranostic application.

Liposomes were the first nanomedicines that achieved United States Food and Drug Administration (FDA) approval for use in clinical trials in the mid-1990s and since then many more liposomal formulations have gained approval (Bobo *et al.*, 2016). These are among the most investigated and best established nanoparticles with formulations for improved circulation time and uptake by tumours being described over three decades ago (Gabizon and Papahadjopoulos, 1988). Liposomal irinotecan for example, has been shown to have a longer half-life with higher plasma levels of irinotecan and these modifications in irinotecan pharmacokinetics is associated with increased efficacy (Adiwijaya *et al.*, 2017; Lamb and Scott, 2017). Nab-paclitaxel is a albumin-bound paclitaxel which has demonstrated increased delivery efficiency and drug tumour penetration compared to solvent-based paclitaxel (Li *et al.*, 2018).

One of the disadvantages of liposomes is their accumulation in the mononuclear phagocyte system (MPS) after systemic administration, although conjugation of polyethylene glycol (PEG) to the liposome membrane decreases this risk (Sercombe *et al.*, 2015). Liposome interactions with plasma proteins can result in opsonisation and destabilisation of the liposome which can limit the drug efficacy as well as result in activation of complement proteins leading to an immunological response (Sercombe *et al.*, 2015).

1.2.3 Gold nanoparticles

A wide range of theranostic nanoparticles have been developed over the years (**Figure 1-4**). Lately, gold nanoparticles (AuNPs) for theranostic applications have gained popularity and have become the focus of intense research at the University of Leeds (Ye *et al.*, 2016; Roach *et al.*, 2018) and worldwide (Singh *et al.*, 2018).

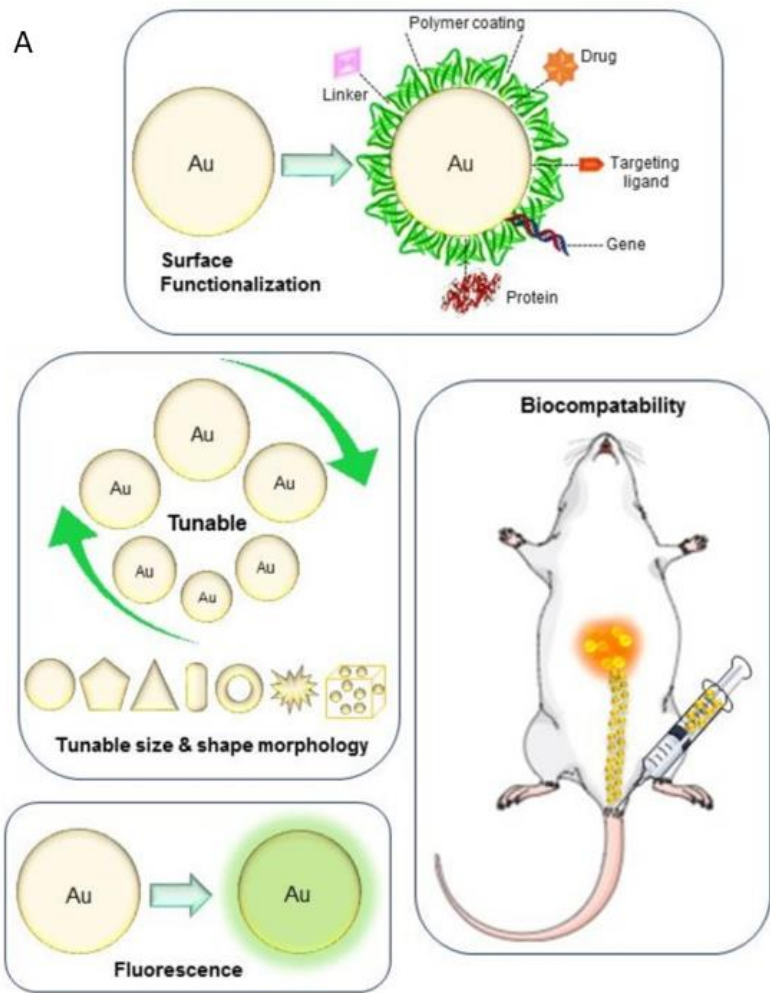
The properties of AuNPs (**Figure 1-5 A**) make them attractive candidates for theranostic delivery. These include their tunable size and shape depending on requirements, their ability to be surface functionalized with a variety of compounds (including drugs, targeting ligands and proteins) and their proven biocompatibility.

Figure 1-5 B shows examples of pre-clinical applications of multifunctional AuNPs, being used for tumour imaging, photothermal therapy (PTT) by generating heat in the presence of a laser of appropriate wavelength as well as PDT (where in the presence of a photosensitizer and laser of appropriate wavelength, reactive oxygen species are generated which causes cell death).

Preferential passive accumulation of AuNPs in tumour tissue due to the enhanced permeability and retention (EPR) effect was reported as one of their most useful properties (Fang *et al.*, 2011; Khawar *et al.*, 2014). This was thought to be due to leaky endothelium and poor lymphatic drainage that are characteristic of most fast-growing tumours. The small size of AuNP was thought to allow passive migration through tumour endothelium to reach the tumour microenvironment. This phenomenon has come under scrutiny lately as the usefulness of this property is yet to be proven in human trials. More recent studies have demonstrated that the dominant AuNP uptake mechanism (up to 97% in some tumours) is via an active transendothelial route rather than passive inter-endothelial EPR effect.

With the promise of improved diagnostics and therapeutics in cancer, some AuNPs have been FDA approved and are now in clinical trials (Singh *et al.*, 2018). However, many questions remain unanswered and further research is required in order to successfully translate this technology for theranostics in cancers such as CCA.

A



B

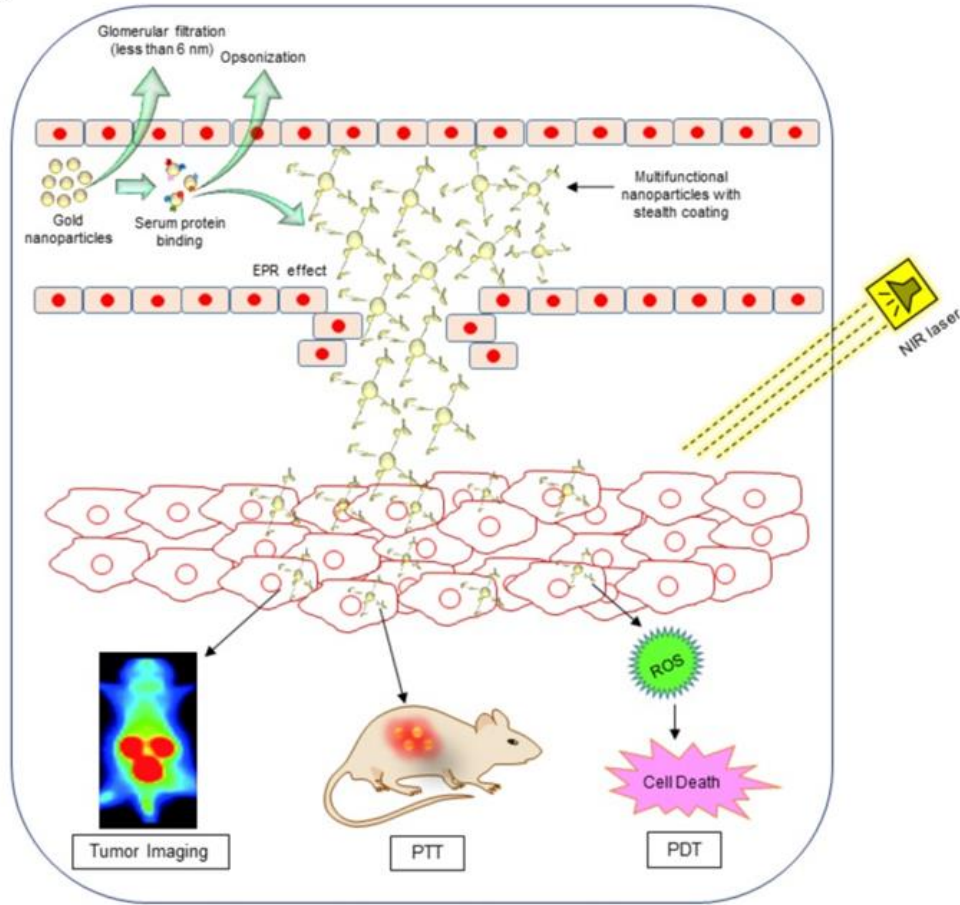


Figure 1-5 Properties of gold nanoparticles and examples of pre-clinical applications

A highlights useful properties of AuNPs. Tunable size and shape morphology; ability to be surface functionalized with a variety of compounds such as drugs, targeting ligands, proteins and genes; applications in imaging such as fluorescence; proven biocompatibility in pre-clinical models.

B shows examples of pre-clinical applications of multifunctional AuNPs. Tumour imaging; PTT (by generating heat in the presence of a laser of appropriate wavelength); PDT (where in the presence of a photosensitizer and laser of appropriate wavelength generates reactive oxygen species that result in cell death).

Taken and adapted from Singh *et al.* (2018)

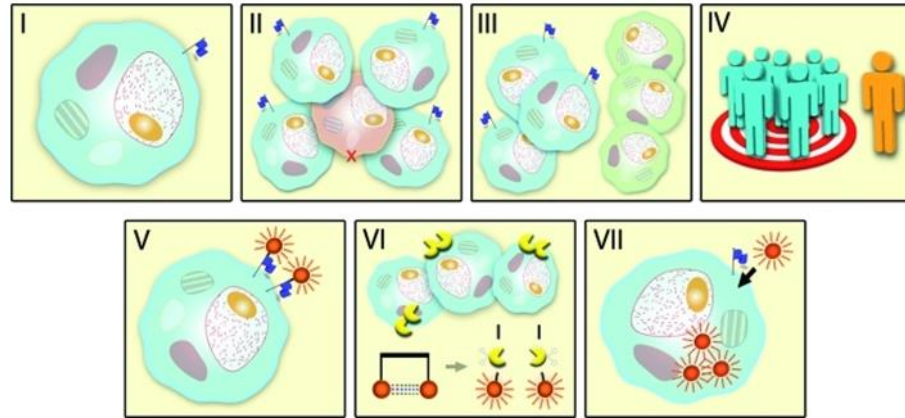
1.3 Biomarkers for active targeting of gold nanoparticle delivery systems in cholangiocarcinoma

A biomarker is defined as a characteristic that is objectively measured and evaluated as an indicator of normal biological processes, pathogenic processes, or pharmacological responses to a therapeutic intervention (Biomarkers Definitions Working Group, 2001).

A multitude of high-throughput biomarker discovery projects have reported on potential early diagnostic, prognostic and predictive markers in CCA (Silsirivanit *et al.*, 2014), but none have specifically reported on theranostic biomarkers. Active targeting of gold nanoparticles to EGFR has been investigated in pre-clinical models of cancers such as pancreatic and colorectal carcinoma with encouraging results (Patra *et al.*, 2008; Cherukuri and Curley, 2010; Fernandes *et al.*, 2017) but no similar studies in CCA have been reported.

1.3.1 Theranostic biomarkers

A tool for selection of biomarkers for targeted imaging using nanotherapeutic platforms has already been described by van Oosten *et al.* (2011)(**Figure 1-6**). However, no such tool exists for the selection of biomarkers for theranosis. Although there is overlap in the characteristics of an imaging biomarker and a theranostic biomarker, the latter requires low or negative expression in normal human tissues to limit the off-target binding. For an imaging biomarker, van Oosten *et al.* (2011) report a tumour to normal tissue ratio of >10 as acceptable. Normal tissue expression should be negligible for an ideal theranostic biomarker.



Characteristics			Score	
I	Extracellular protein localization	Bound to cell surface (receptor)	5	
		In close proximity of tumor cell	3	
II	Diffuse up-regulation through tumor tissue		4	
III	Tumour/normal tissue ratio > 10		3	
IV	Percentage up-regulation in patients	>90%	6	
		70%–90%	5	
		50%–69%	3	
		10%–49%	0	
V	Previously imaged with success <i>in vivo</i>		2	
VI	Enzymatic activity		1	
VII	Internalization		1	
Total: maximum			22	(Potential target ≥ 18)

Figure 1-6 TArget Selection Criteria (TASC) scoring system

Potential biomarker targets are assigned a score for displaying favourable criteria for targeting *in vivo*. The images above correspond to the characteristics described in the TASC score below. The blue flag represents the biomarker.

Points are allocated for the extracellular or membranous location of the biomarker, diffuse upregulation through tumour tissue, tumour to normal tissue expression ratio >10, percentage upregulation in patients, previous *in vivo* imaging application, enzymatic activity and internalisation of target. Biomarkers are considered to have theranostic potential if they score ≥ 18 .

Taken from (van Oosten *et al.*, 2011)

Highly expressed, CCA-specific biomarkers that have low or negative expression in normal human tissues are key to the development of theranostic platforms with active targeting capabilities.

Validated theranostic biomarkers combined with targeted NPs could have multimodal applications ranging from contrast-enhanced imaging, molecular-imaging, targeted drug delivery, assessing response to therapy and inferring prognosis.

1.3.2 Types of targeting ligands

Commonly used targeting ligands for active targeting include antibodies against selected biomarker (Byrne *et al.*, 2008; Foygel *et al.*, 2013). Despite their common use, antibodies have significant disadvantages including the need for an intact animal immune system for their production and cross-reactivity with other antigens (Baker, 2015; Bradbury and Pluckthun, 2015).

Antibody-mimetics have been recently developed to overcome the disadvantages of antibodies. Aptamers are small oligonucleotide chains (RNA or DNA) that have been designed to target specific molecules (Adachi and Nakamura, 2019). Some of these aptamers have been FDA approved (Adachi and Nakamura, 2019). Affimers, which are artificial binding proteins of less than 15kDa molecular weight, are novel non-antibody ligands that have the advantage over antibodies of being more reproducible, stable and scalable (Hughes *et al.*, 2017).

For this project, affimers as targeting ligands were explored as these novel reagents could be developed in-house at the University of Leeds.

1.3.3 Active targeting using gold nanoparticles

AuNPs have slowly navigated the translational pipeline with theranostic agents such as CYT-6091 (a PEG-coated AuNP targeted to tumour necrosis factor) passing phase I

clinical trials (Koonce *et al.*, 2015). CYT-6091 has also been investigated in combination with radiotherapy in a murine carcinoma model with promising results (Koonce *et al.*, 2015). Dziawer *et al.* (2019) have developed human epidermal growth factor receptor 2 (HER2) targeted AuNPs but these have only been evaluated *in vitro* in HER2 positive breast cancer cell lines.

A recent review of applications of active targeting using nanoparticle delivery systems in cancer therapeutics showed that the majority of published studies evaluated cell surface receptors (e.g.: integrin $\alpha_v\beta_3$, CD44 receptor, folate receptor) as active targets for targeted delivery using nanoparticles (Muhamad *et al.*, 2018). These studies highlighted by Muhamad *et al.* (2018) were all pre-clinical *in vitro* studies as these systems are not yet in human clinical use. Being 'visible' to the systemically administered theranostic agent is in theory, a requirement for a potential target for targeted delivery. Tumour extra-cellular matrix (ECM) proteins and tumour vascular endothelial markers would also meet this criterion and therefore could be considered theranostic targets. Cytoplasmic and nuclear receptors could also be considered but these would rely on cellular uptake of the systemically delivery theranostic agent prior to binding to target.

Ultimately, the success of any targeted AuNP system will depend on its ability to efficiently negotiate the CAPIR cascade for which the 2R2SP properties need to be fulfilled (**Figure 1-3**). Although AuNPs for cancer therapy have been a focus of intense research over the past decade, relatively few are clinically approved (Singh, 2019). Specific binding of an actively targeted AuNP system is yet to be proven in human clinical trials. More research efforts are still required to explore if targeted AuNPs could be used in anti-cancer theranostic systems.

1.4 Tenascin C as a potential biomarker in cholangiocarcinoma

The extra-cellular matrix protein Tenascin C (TNC) is frequently expressed in embryological tissues but expression in adult tissues is more restricted (Jones and Jones, 2000; Midwood *et al.*, 2016). It is of interest in cardiovascular research given the role it plays in post-myocardial infarction tissue remodelling and its associated value in prognosis following infarction (Maqbool *et al.*, 2016; Rienks and Papageorgiou, 2016). The presence of TNC in multiple different solid tumours and its association with poor clinical outcome has been reported (Orend and Chiquet-Ehrismann, 2006; Allen and Louise Jones, 2011). TNC as a biomarker in CCA has only been sparsely reported but suggest an increase in expression of TNC protein in the CCA ECM (Aishima *et al.*, 2003; Okamura *et al.*, 2005; Iguchi *et al.*, 2009).

1.4.1 Structure and expression in normal tissues

TNC is a multifunctional extracellular matrix glycoprotein that can exist in several different isoforms (Brosicke and Faissner, 2015; Giblin and Midwood, 2015). The basic structure of TNC comprises of four main domains: (Gulcher *et al.*, 1991; Jones and Jones, 2000; Pas *et al.*, 2006; Midwood *et al.*, 2016)

1. Tenascin assembly domain – This domain forms inter-molecular hydrophobic bonds and disulphide bridges.
2. Fibronectin type III repeats – This region is the most variable due to alternative splicing and post-translational modification. This region interacts with molecules such as transforming growth factor- β , fibroblast growth factor and platelet-derived growth factor.
3. Epidermal growth factor-like repeats – These act as ligands for EGF-R

4. Fibronectin globe – This binds to a range of extracellular factors which allows TNC to achieve a multitude of functions including the role it plays in cell adhesion, cell migration and synthesis of pro-inflammatory cytokines.

The exon structure of TNC is shown in **Figure 1-7**. Transcription of this could theoretically give rise to 511 human TNC splice isoforms although only around 100 isoforms have been discovered (Giblin and Midwood, 2015). The splice variants seen in embryological tissues are different to those seen in adult tissues, induced by conditions such as chronic inflammation and cancer (Brosicke and Faissner, 2015; Giblin and Midwood, 2015).

Expression of TNC in adult tissues is generally restricted to areas of wound repair and remodelling, fibrosis or neoplasia (Chiquet-Ehrismann *et al.*, 1986; Jones and Jones, 2000; Midwood and Orend, 2009; Brosicke and Faissner, 2015). Although expression in normal tissues of the central nervous system (Chiquet-Ehrismann and Tucker, 2011; Roll and Faissner, 2019) and liver sinusoids (Aishima *et al.*, 2003; Nong *et al.*, 2015) has been described, TNC is generally not detected in a wide range of normal tissues (Human Protein Atlas, 2019d).

1.4.2 Function

The role of TNC has been extensively investigated since the 1980s mainly by *in vitro* studies and experiments involving TNC knockout mice (Tucker *et al.*, 1993). TNC has a diverse range of functions in normal physiology as well as pathology. These have been well described by Midwood *et al.* (2016). The diverse range of TNC isoforms and its restricted but specific pattern of expression means that it exerts a multitude of physiological and pathological roles (Mackie and Tucker, 1999).

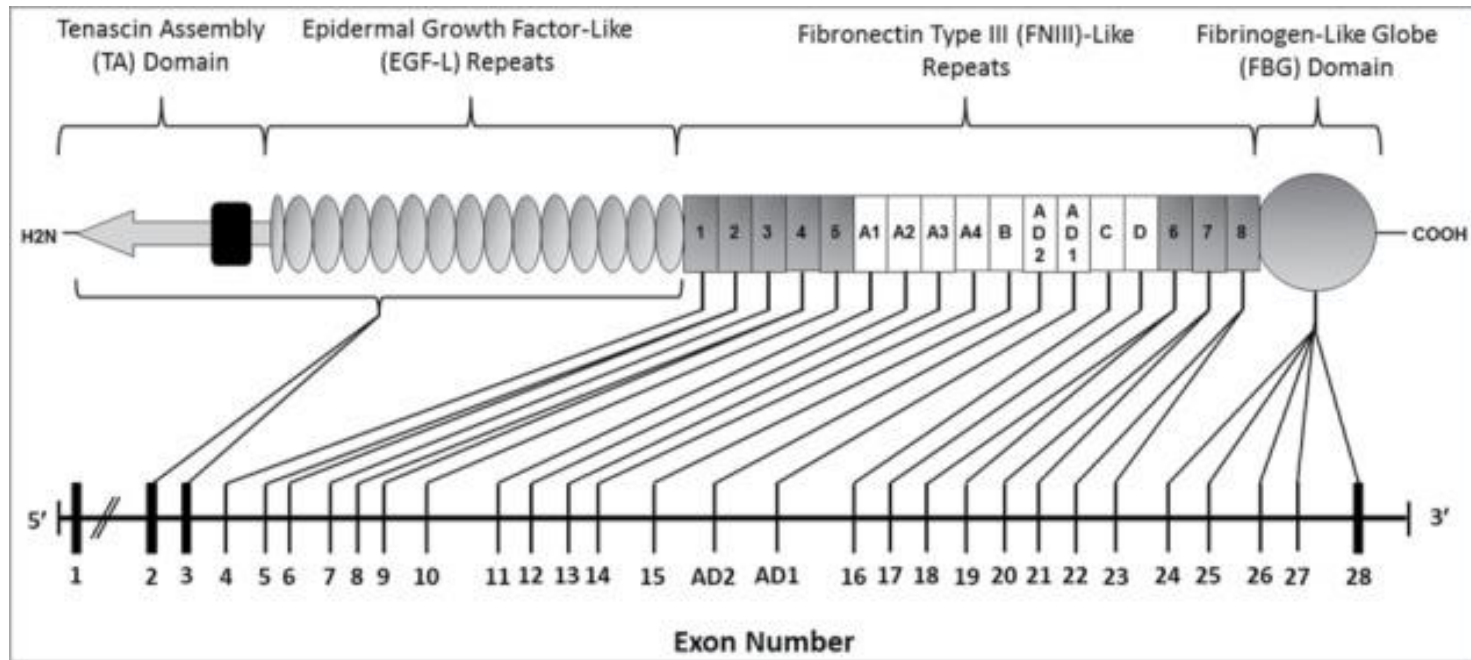


Figure 1-7 Exon structure of TNC.

TNC gene is located chromosome 9. This 30 exon structure codes for all the different alternate spliced variants of TNC. AD1 and AD2 are two exons that were discovered after the original 28 exon structure of TNC was described.

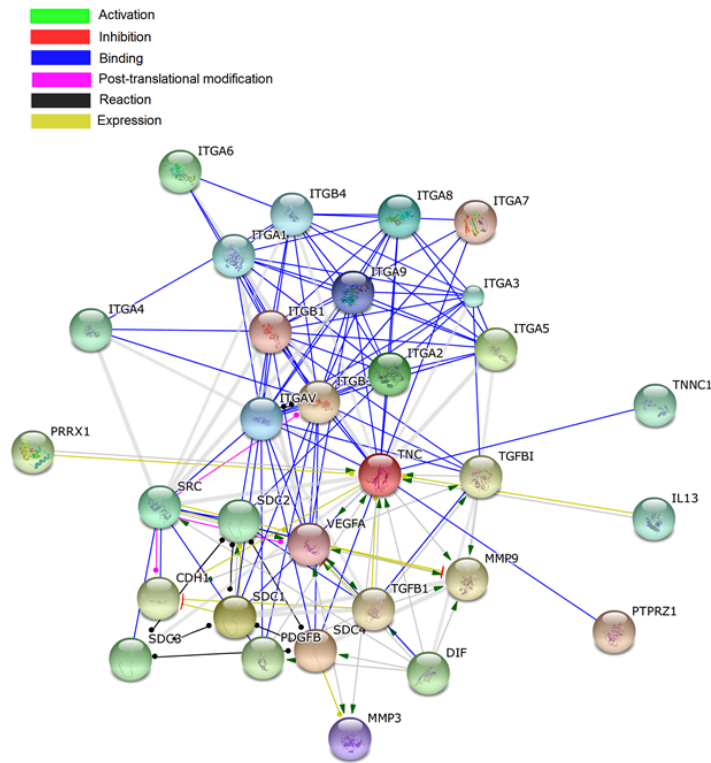
Image taken from (Giblin and Midwood, 2015)

A summary of the protein-protein interactions of TNC is shown in **Figure 1-8** (produced at my request by Dr Agne Antanaviciute using the STRING Network (STRING, 2014b)). The presence of several integrins on this network explains the role of TNC in cell adhesion, migration and signalling. Integrins are transmembrane receptors in the cytoskeleton of cells which function as links between the ECM and the cell (Alberts B, 2002). In addition to integrins, TNC binds to many other ECM proteins including fibronectin, collagen and periostin and has a structural role in the ECM (Giblin and Midwood, 2015). TNC also activates EGFR, toll-like receptor 4 (TLR4), transforming growth factor beta (TGF β), vascular endothelial growth factor (VEGF) and WNT signalling pathways as well as performing an immunological role in the defence against organisms such as *Streptococcus* sp. and human immunodeficiency virus (Giblin and Midwood, 2015). TNC also activates the function of matrix metalloproteases such as MMP9 and MMP3 that are ECM enzymes involved in tissue remodelling and wound healing (Nagase *et al.*, 2006).

1.4.3 Expression in cholangiocarcinoma

The presence of tenascins in CCA tissues was reported over two decades ago by Terada and Nakanuma (1994). It is now known that there are 4 types of tenascins, tenascin-W, -R, -X and -C (Chiquet-Ehrismann, 2004) and that it is TNC that is overexpressed in CCA tissue.

Aishima *et al.* (2003) evaluated the TNC expression in IH-CCA and showed 68% intra-tumoral expression and 31% expression at the 'invasive front'. Iguchi *et al.* (2009) also confirmed these findings (63.1% expression in intra-tumoral stroma out of 61 IH-CCA). Cancer-associated fibroblasts (CAF) express TNC as well as other markers associated with tumour growth. Therapeutic targeting of CAFs been shown to be effective in pre-clinical model of IH-CCA (Mertens *et al.*, 2013).



CDH1	Cadherin-1	ITGAV	RGD-motif binding integrins integrin-alpha-V
DIF	Protein dif-1	MMP3	Matrix Metalloproteinase 3
IL13	Interleukin 13	MMP9	Matrix Metalloproteinase 9
ITGA1	Integrin α 1	PRRX1	Paired related homeobox 1
ITGA2	Integrin α 2	PTPRZ1	Protein Tyrosine Phosphatase Receptor Type Z1
ITGA3	Integrin α 3	PDGFB	Platelet Derived Growth Factor Subunit B
ITGA4	Integrin α 4	SDC1	Syndecan 1
ITGA5	Integrin α 5	SDC2	Syndecan 2
ITGA6	Integrin α 6	SDC3	Syndecan 3
ITGA7	Integrin α 7	SDC4	Syndecan 4
ITGA8	Integrin α 8	SRC	Proto-oncogene tyrosine-protein kinase Src,
ITGA9	Integrin α 9	TNC	Tenascin C
ITGB1	Integrin β 1	TGFB1	Transforming Growth Factor Beta 1
ITGB3	Integrin β 3	TNNC1	Troponin C1
ITGB4	Integrin β 4	VEGFA	Vascular Endothelial Growth Factor A

Figure 1-8 Tenascin C STRING network

This STRING analysis of protein-protein interactions of TNC in humans (produced at my request by Dr Agne Antanaviciute using the STRING Network (STRING, 2014a). Index of abbreviations used in the STRING network is shown in the table. The line colour indicates the type of protein-protein interaction as shown above (top left corner)

There are no published immunohistochemical studies of TNC expression in EH-CCA and PH-CCA.

1.4.4 Expression of tenascin C in other diseases

TNC is also expressed in myocardium following myocardial infarction and has associated value in prognosis following infarction (Franz *et al.*, 2015; Maqbool *et al.*, 2016; Rienks and Papageorgiou, 2016). Kawakita *et al.* (2019) reported expression of TNC following ischaemic stroke and subarachnoid haemorrhage. Increased levels of serum TNC are observed in response to infection, inflammation (e.g. in chronic inflammation due to rheumatoid arthritis) or injury (Midwood *et al.*, 2016). In prostate cancer, TNC gene alteration (especially amplification) as well as an association with other genomic markers suggestive of aggressive tumour phenotype (e.g. NOTCH, SOX and WNT signalling pathway proteins) has been described.

1.4.5 Tenascin C targeting in clinical trials

Antibody-based TNC targeting has been trialled but the only published evidence of results are from trials of radioimmunotherapy in metastatic brain tumours (Reardon *et al.*, 2007). These and other trials are summarised in **Table 1-5**. Two of these trials were terminated early, one due to logistical reasons and the other due to negligible uptake of drug by the tumour and another trial has no published results. Despite the availability of TNC inhibiting antibodies, the outcome of TNC inhibition is still unclear.

Table 1-5 Summary of clinical trials of tenascin C inhibitor therapy

Year	TNC targeted agent	Disease	Phase	Trial number	Status/ Reference	Results summary
1991 - 1997	131I-monoclonal antibody 81C6 (TNC antibody I-81C6)	Primary or metastatic brain cancer	1 / 2	NCT00002752 NCT00002753 NCT00003478 NCT00003461 NCT00003484	(Reardon <i>et al.</i> , 2002; Reardon <i>et al.</i> , 2006a; Reardon <i>et al.</i> , 2006b; Reardon <i>et al.</i> , 2007; Reardon <i>et al.</i> , 2008)	Improvement in OS but dose limiting side effects observed
2008	Neuradiab (TNC antibody I-81C6)	Glioblastoma multiforme	3	NCT00615186	Terminated – Due to delay in site initiation and funding considerations	N/A
2009	Neuradiab (TNC antibody I-81C6)	Brain tumours	2	NCT00906516	Unknown status	N/A
2015	131I-Tenatumomab (radioiodine labelled TNC antibody)	TNC +ve cancer	1	NCT0260267	Terminated - Uptake of drug into the tumour lesion was negligible	N/A

1.5 Pre-clinical models of cholangiocarcinoma for validation of nanoparticle-based delivery systems

Animal models are a crucial step in the translation of novel cancer therapeutics to the clinic as they allow evaluation of tumour growth, response to treatment, drug resistance patterns and drug toxicity in a living organism prior to first-in-man clinical trials (Cheon and Orsulic, 2011).

Although several pre-clinical rodent models of CCA have been described, the majority in routine use are subcutaneous xenograft models. Orthotopic models of IH-CCA using chemotoxic agents such as thioacetamide or N-nitrosodiethylamine and gene knock-out techniques have been established (Praet and Roels, 1984; Farazi *et al.*, 2006). A syngeneic rat model of IH-CCA that employs BD Eneu cells (a rat-derived CCA cell line) surgically implanted into left hepatic duct followed by bile duct ligation (BDL) have reported successful development of tumours (Sirica *et al.*, 2008). A recent study (Yamada *et al.*, 2015) has also reported a human-like model of IH-CCA involving transduction of mouse biliary epithelium to express ectopic oncogenes (myr-AKT and Yes-associated protein) followed by unilobar BDL and administration of biliary mitogen IL-33. However, no orthotopic models of EH-CCA have been successfully established. (De Minicis *et al.*, 2013). An orthotopic model of gallbladder cancer involving surgical inoculation of cells into the gallbladder has been described but this has not been extrapolated to develop a similar model of CCA (Mita *et al.*, 2007).

The main disadvantage of a subcutaneous xenograft model is its inability to adequately model the tumour microenvironment. However, the relative ease of establishment of xenograft models as well as the convenience of tumour growth monitoring with mechanical calliper measurements make these models popular in pre-clinical research despite these limitations.

1.5.1 *In vivo* imaging in pre-clinical models of human cancer

The subcutaneous xenograft model is the most popular pre-clinical *in-vivo* model used for pharmacodynamic and pharmacokinetic studies of chemotherapeutic drugs. Using additional imaging techniques has the potential for improving existing models and developing new ones (O'Farrell *et al.*, 2013). For example, subcutaneous xenograft volume measurement by high-frequency ultrasound (HF-US) is more accurate compared to deriving volume from calliper measurements (Ingram *et al.*, 2013).

Other modalities such as optical imaging can add another dimension to pre-clinical evaluation of cancer therapeutics. Bioluminescent imaging relies on the detection of photons emitted by the conversion of luciferin to oxyluciferin by luciferase-expressing cells (Sato *et al.*, 2004) whereas fluorescent imaging requires cells expressing a fluorescent protein e.g. green fluorescent protein (GFP) (Martelli *et al.*, 2016). Although these imaging modalities require genetic modification of cancer cells, they can provide information regarding metabolic activity of cells and cell migration.

HF-US imaging is a convenient, non-invasive modality in the pre-clinical setting (Ingram *et al.*, 2013). Multispectral optoacoustic tomography (MSOT) is a relatively new but useful photoacoustic imaging (PAI) modality for imaging nanoparticles such as AuNPs and magnetic nanoparticles in the pre-clinical setting (Anani *et al.*, 2019; Wang *et al.*, 2019). MSOT imaging relies on image reconstruction using the ultrasound waves generated by the thermoelastic expansion of tissues heated with laser of appropriate wavelengths (Meng *et al.*, 2019). Endogenous contrast agents (e.g. oxy- or deoxyhaemoglobin, melanin) or exogenous contrast agents (e.g. AuNPs) can increase the signal to noise ratio with resultant images with strong contrast and high spatial resolution (Meng *et al.*, 2019).

Cross-sectional imaging techniques such as magnetic resonance imaging (MRI), computed tomography (CT), positron emission tomography (PET) and single photon emission computed tomography (SPECT) are exceedingly useful in pre-clinical imaging. Radiolabelled SPECT probes for example, are feasible imaging agents (Aalbersberg *et al.*, 2017) and could be used to image novel nanoparticle-based theranostic agents.

All these imaging modalities have advantages and disadvantages and as in clinical practice, several imaging modalities may be required to optimally investigate any novel theranostic agents.

1.6 Thesis aim and objectives

The aim of this research was to develop a novel targeted theranostic delivery system for cholangiocarcinoma.

The objectives to achieving this overall aim were:

- To establish an orthotopic model of CCA to evaluate novel theranostic systems
- To identify potential biomarkers in CCA with theranostic potential by systematic review of the literature
- To evaluate TNC as a candidate biomarker in CCA for active tumour targeting
- To develop a novel TNC targeted delivery platform using AuNPs

Chapter 2

Materials and methods

2.1 Cell lines and culture

2.1.1 Extra-hepatic cholangiocarcinoma cell lines

The EH-CCA cell lines TFK-1 (Saijyo *et al.*, 1995) and EGI-1 were purchased from DSMZ, Germany under a material transfer agreement. Both cell lines were authenticated in-house on arrival by short tandem repeat (STR) DNA analysis. Regular screening for mycoplasma was undertaken.

TFK-1 cell lines were grown in Roswell Park Memorial Institute 1640 medium (RPMI, Life Technologies, UK) with 10% (v/v) foetal calf serum (FCS). EGI-1 were grown in Dulbecco's Modified Eagle Medium (DMEM, Life Technologies, UK) with 10% (v/v) FCS.

75cm² or 150cm² flasks with vented caps (Corning Life Sciences, Massachusetts, USA) were used to grow both cell lines with incubation at 37°C, 5% carbon dioxide (standard conditions). At 70-80% confluence, both cell lines were sub-cultured by first washing with sterile phosphate-buffered saline (PBS, Invitrogen, UK) before incubating in 0.5mM ethylenediaminetetraacetic acid (EDTA) for 5-8min to loosen adherent cells followed by incubation with trypsin up to 12min. EGI-1 cells were more adherent than TFK-1 cells and often required longer trypsinisation which was in keeping with the cell line data sheet. Occasionally, gentle scrapping with a cell scraper (Greiner bio-one, Germany) was required to remove adherent cells. Scrapping was avoided when cell counting (performed using a haemocytometer) was required. Cells were centrifuged in Eppendorf™ 5810R centrifuge (Eppendorf™, Hamburg, Germany) at 400 g and trypsin-containing culture media discarded prior to re-suspending the cells in fresh culture media in fresh flasks at 1:5 – 1:10 dilution.

2.1.2 Other cell lines

2.1.2.1 Metastatic colorectal carcinoma cell line (SW620)

SW620 cells were originally obtained from European Collection of Authenticated Cell Cultures (ECACC), then maintained in house. SW620 cells were grown in RPMI media (Life Technologies, UK) with 10% (v/v) FCS. 75cm² or 150cm² flasks with vented caps (Corning Life Sciences, Massachusetts, USA) were used to seed cells prior to incubation under standard conditions. At 70-80% confluence, cells were sub-cultured. First a sterile PBS (Invitrogen, UK) wash was performed, followed by incubation with trypsin for 3-5min and then reintroduction of culture media to inactivate trypsin. Cells were harvested, centrifuged (Eppendorf™ 5810R centrifuge, Hamburg, Germany) at 400 g for 5min and trypsin-containing media discarded. After discarding the supernatant, cells were resuspended in fresh culture media placed in fresh flasks at 1:10 dilution.

2.1.2.2 Luciferase transfected murine colorectal carcinoma cell line (MC38Luc11A)

MC38Luc11A mouse syngeneic colorectal cancer cells were originally gifted by Professor D. Beauchamp, University of Virginia. These cells originated from the parent cell line MC38. MC38luc11A cells were known to have high luciferase activity and successfully established in animal tumour models (Dr M Volpato, personal communication). These were cultured using the same method described in **Section**

2.1.2.1.

2.2 Luciferase transfection of TFK-1 and EGI-1 cell lines

2.2.1 Puromycin chemosensitivity assay

To determine the concentration of puromycin for selection of lentiviral-transfected cells, the parent cell lines TFK-1 and EGI-1 were tested.

TFK-1 and EGI-1 cells were seeded at 2×10^5 cells/well in a 96 well plate on day 0 and incubated overnight at standard conditions. Stock puromycin dihydrochloride from *Streptomyces alboniger* (Sigma-Aldrich, UK) was made up to a concentration of 10mg/mL with sterile PBS. RPMI media with 10% FCS were used for serial dilutions of puromycin ranging from 78ng/ml to 10 μ g/ml. Every 48-72hrs, Puromycin-containing media were replaced with fresh media at the appropriate concentration and incubated at standard conditions. On day 8, 25 μ L of 5mg/ml 3-[4,5-dimethylthiazol-2-yl]-2,5-diphenyl-tetrazolium bromide (MTT) was added to each well containing 100 μ L of media (final concentration of MTT 1mg/mL) and incubated in the dark under standard conditions for 3-4hrs. Media were then carefully removed without disturbing the insoluble formazan crystals. The crystals were fully dissolved in 100 μ L dimethyl sulfoxide (DMSO) and the absorbance measured via an optical spectrophotometer (Berthold Technologies, Germany) at 570nm.

The mean absorbance for each dilution and control well was determined from triplicate measurements. The adjusted values were then used to calculate cell survival as a proportion of the control. Percentage cell viability was then plotted against concentration of puromycin to determine the concentration that resulted in <5% cell viability.

2.2.2 Transfection

TFK-1 and EGI-1 cells were seeded from confluent 75cm² flasks at passage 10 and 9 respectively into 6-well plates (Corning Life Sciences, Massachusetts, USA) at 3.0x10⁵ cells/well (approximately, 30-40% confluence) and incubated overnight in standard conditions.

The next day, 2ml of thawed lentiviral supernatant (Applied Biological Materials (ABM) Inc, California, USA). (**Figure 2-1**), was added to each test well along with 20μL of 1,3-dibromopropane;N,N,N',N'-tetramethylhexane-1,6-diamine (polybrene) at 0.8mg/ml. Only fresh growth media was added to control wells. Plates were incubated overnight in standard conditions. On day 2, the viral supernatant and polybrene was removed and the cells were washed with PBS. Growth media was added, and the cells were incubated under standard conditions for 72hrs. On day 5, cells were sub-cultured into 10cm dishes (Corning Life Sciences, Massachusetts, USA), using Trypsin/EDTA. Growth media containing the selection agent puromycin at 0.6μg/mL was added to both test and control wells and incubated under standard conditions for 72hrs. Every 72hrs, puromycin containing media at 0.6μg/mL was replaced. On day 14, TFK-1 dishes required sub-culturing.

Once individual clones of sufficient diameter were seen, these were individually sub-cultured (using sterile, filter paper soaked in trypsin) into 24 well plates with selection media. Once 70-80% confluent, each well was individually sub-cultured into 25cm² flasks. At confluence, clones from each flask were trypsinised, pelleted and resuspended in 1mL FCS containing 10% DMSO for freezing in liquid nitrogen.

Lenti-PGK-Luc Control Lentivirus

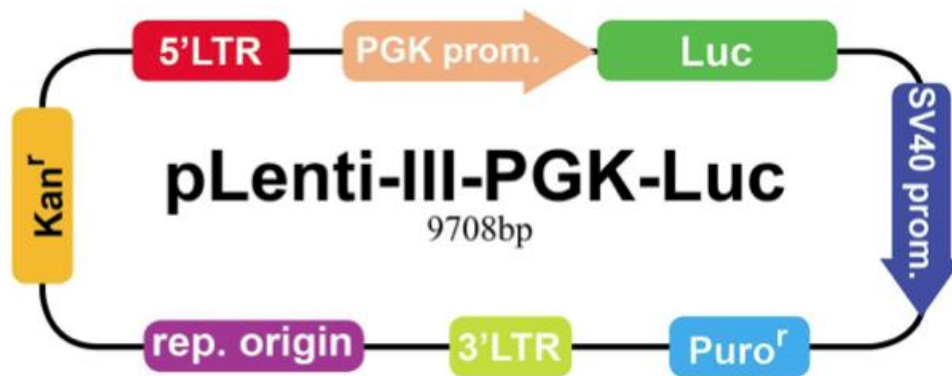


Figure 2-1 Lentivirus plasmid structure

This shows a schematic of lentiviral plasmid structure. The main components include Luc – firefly luciferase, Puro^r – puromycin resistance gene (to confer resistance of transfected cells to selection agent, puromycin) and PGK prom. – phosphoglycerate kinase promoter (to drive firefly luciferase expression)

Image from Applied Biological Materials ABM® <http://www.abmgood.com>

2.2.3 Quantification of luciferase activity and clonal selection

Frozen vials of each clone were thawed and resuscitated into T25 flasks containing growth media supplemented with 0.6µg/ml of puromycin. After 1 passage, cells harvested and seeded at 1×10^5 , 5×10^4 and 2.5×10^4 into Optical Btm PH Polymer base sterile 96-well black plates with clear bottoms (Thermo Scientific, UK) and incubated for 24-48hrs at standard conditions. Luciferase expression was determined using the luciferase assay system (Promega, UK) which included luciferase assay buffer, cell culture lysis reagent and the luciferase assay substrate, using the recommended method as summarized below.

Media were removed and each well was washed with sterile PBS. Cells were lysed for 5-10min with 1x cell culture lysis reagent (diluted 1:5 with ultra-pure water). Using a luminometer with auto-injectors (Berthold Technologies, Germany), 20µL of luciferase assay reagent was added to each well followed by a shake, 2s delay and then a count time of 2s. Control wells included media only and blank wells to ascertain background luminescence.

Selected clones of TFK-1 and EGI-1 were also plated at different seeding densities to compare luminescence to a known high luciferase-expressing colorectal carcinoma cell line, MC38Luc11A as well as the parent cell lines (negative control). This was done to compare relative light intensity at low cell numbers to ascertain the likelihood that these cells would be detectable to *in vivo* imaging modalities.

2.2.4 Growth characteristics of selected TFK-1 and EGI-1 clones

Growth characteristics of the transfected clones selected for *in vivo* experiments were compared to the parent cell line *in vitro* by MTT assay using the method described in **Section 2.2.1**. Cells (Clone(s) and parent at comparable passage number) were trypsinised, counted and seeded at 2,500 cells/well in 3 separate 96-well plates on day

0 and incubated overnight under standard conditions (8 technical replicates per condition). On day 1,2 and 3, MTT assays were performed to assess cell viability. Three biological replicates were performed for each cell line. Once absorbance versus time was plotted for each experiment, an exponential growth equation was applied to calculate doubling time. The doubling times obtained from biological replicate experiments were compared using Student's t-test assuming normal distribution of doubling time.

TFK-1 and its highest luciferase-expressing clone TFKluc2B2 were further evaluated in subsequent experiments instead of EGI-1 as the selected high-expressing EGI-1 clone failed to successfully establish as a xenograft tumour *in vivo*.

2.3 Generation of *in vivo* mouse models

All procedures were carried out in accordance with the Animals (Scientific Procedures) Act 1986. Animals were housed in a specific pathogen free (SPF) environment with food and drink available *ad libitum*. 6-10 week old BALB/c nude female and CD1 nude female mice (originally obtained from Charles River, UK then maintained in-house) were used for all animal experiments. For procedures under anaesthesia, inhalational anaesthesia with isoflurane in medical air (BOC, UK) was used for both induction (5% v/v) and maintenance (2-3% v/v) of general anaesthesia. Topical anaesthesia was used whenever possible for injection sites.

2.3.1 Subcutaneous xenograft models

For all xenograft models, 1×10^7 cells suspended in 100 μ L of serum-free media or PBS were injected subcutaneously in the right flank under topical anaesthesia. Mechanical callipers were used to monitor tumour growth over time. Generally, xenografts were allowed to grow and establish for 10-14 days prior to any intervention, with the

exception of xenografts grown from luciferase-transfected cell lines. These were imaged under anaesthesia as per the method described in **Section 2.4.2** up to 2 times a week beginning on day 5 post-injection. Animals were sacrificed by cervical dislocation by a competent individual at specified experimental time points or if the tumours reached the maximum diameter threshold of 17mm in any axis.

2.3.2 Liver orthotopic model

For the minimally invasive liver orthotopic model, two injection targets were used – Initially, the intra-cholecystic injection with no cystic duct ligation (method 1) and latterly the peri-cholecystic, intra-liver parenchymal injection (method 2).

6-10 week old BALB/c nude female mice were anaesthetised and an abdominal scan performed using the VisualSonics Vevo770 HF-US system (FUJIFILM VisualSonics Inc, Ontario, Canada). Once the liver and gall bladder were identified, 5×10^6 TFKluc2B2 cells suspended in 50 μ L of PBS were carefully injected using HF-US guidance into the appropriate targets by Dr Gemma Marston. Tumour growth was monitored using bioluminescence imaging and HF-US imaging as described in **Sections 2.4.2** and **2.4.3**.

2.4 Assessment of murine tumour and other tissues

2.4.1 Mechanical calliper measurement

All subcutaneous xenografts were measured with mechanical callipers twice weekly and tumour volume calculated according to the formula (shown below) described by Ingram *et al.* (Ingram *et al.*, 2013) which showed better correlation with tumour volume measured *in vivo* by HF-US. Graphs of tumour volume versus time were plotted.

$$\text{Tumour volume} = \pi/6 \times (\text{length} \times \text{width})^{3/2}$$

2.4.2 Bioluminescence imaging

In addition to mechanical calliper measurements, bioluminescent imaging technique was used to evaluate the growth of tumours comprised of luciferase-transfected cells. Subcutaneous xenografts and orthotopic models were imaged using the IVIS pre-clinical bioluminescence imaging system (PerkinElmer Inc, Massachusetts, USA) up to 2 times a week during the course of the experiment. Following induction of inhalational anaesthesia, the animals underwent intra-peritoneal (IP) injection of 1.2mg of beetle D-luciferin (Promega, UK) in 100 μ L. All images were obtained 5min following IP injection. Images were analysed using LivingImage Software Version 4.2 (PerkinElmer Inc, Massachusetts, USA) and results were presented graphically as average radiant efficiency (in photons/s/cm²/sr) of the standardized region of interest (ROI) versus time.

For the *in vivo* bioluminescence imaging, the ROI was a rectangular shape that included the abdomen of an animal. The size of this ROI was kept consistent throughout all experiments. For the *ex vivo* bioluminescence imaging, a circular ROI was used to incorporate the area of the tumour, and the size kept consistent throughout all experiments.

2.4.3 High-frequency ultrasound imaging

The Vevo 770 HF-US system (Fujifilm VisualSonics Inc, Ontario, Canada) was used to perform tumour imaging according to the method described by Abdelrahman *et al.* (2012). HF-US imaging was performed weekly by Dr N Ingram or Dr G Marston.

The Vevo 770 version 3 software (Fujifilm VisualSonics Inc, Ontario, Canada) was used to perform 3D reconstruction of the tumour images to ascertain the tumour volume according to the method described by Ingram *et al.* (2013).

2.4.4 Fluorescence imaging

IVIS imaging system (Perkin Elmer, USA) was used to capture fluorescent images *in vivo* under anaesthesia and following sacrifice by cervical dislocation, images of tissue (tumour, liver, kidney, spleen, heart, lung and brain) *ex vivo*. The fluorophore used for the experiments was rhodamine-red C₂ maleimide and the optimum filters for image capture for this fluorophore were excitation 570nm and emission 620nm. For fluorescence measurements (radiant efficiency in p/s/cm²/sr/μW/cm²) a region of interest (ROI) of a defined unit area was placed over the region of maximal signal intensity using Living Image software (v4.3.1, Caliper Life Sciences, USA) on the tumour and organs as shown in **Figure 2-2** .

As tissues display different degrees of auto-fluorescence, mean background fluorescence for organs/tissues was determined by *ex vivo* imaging of SW620 xenograft tumour bearing animal tissues (n=3 animals; tumour, liver, kidney, spleen, heart, lung and brain tissues) under the optimum experimental filters. A fixed region of interest was utilised, the area of which was kept constant across all experiments/imaging sessions.

To enable graphical representation of results and comparison of tissues between imaging sessions and different experiments, fold change in average radiant efficiency for a given tissue was calculated using the following equation –

$$\text{Fold change in average radiant efficiency for tissue } x \text{ (p/s/cm}^2\text{/sr)} \\ = \frac{\text{Measured average radiant efficiency of tissue } x \text{ (p/s/cm}^2\text{/sr)}}{\text{Mean background average radiant efficiency of tissue } x \text{ (p/s/cm}^2\text{/sr)}}$$

Background auto-fluorescence values for TFKluc2B2 orthotopic tumours were determined by *ex vivo* imaging of TFKluc2B2 orthotopic tumour-bearing animal tissues (n=2 animals; liver tumour, non-tumour liver, kidney, spleen, heart, lung and brain tissues) under the optimum experimental filters.

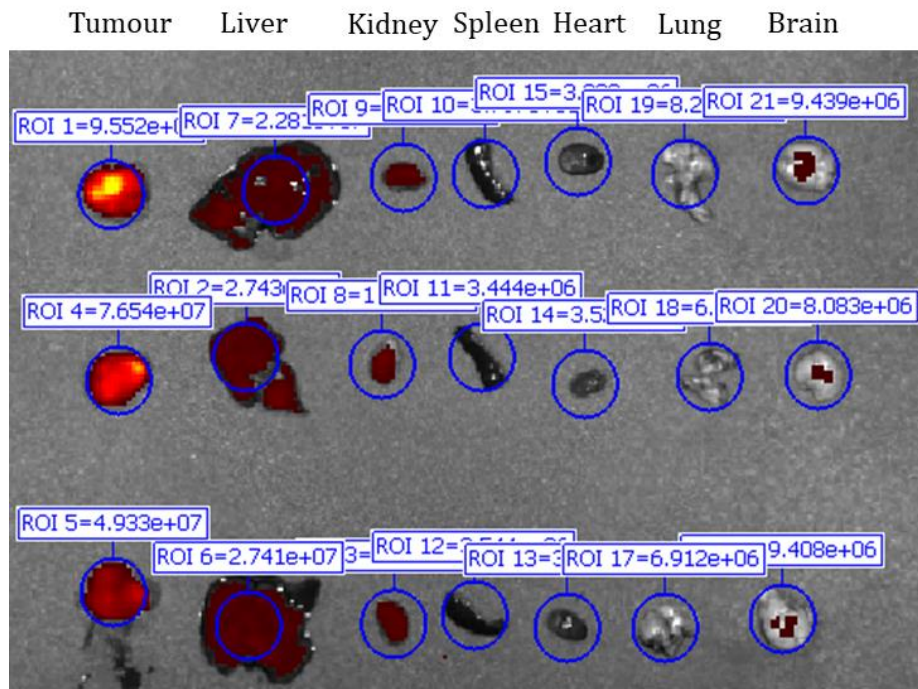


Figure 2-2 Measurement of fluorescence intensity in tumour and organs

Fluorescence intensity for each tissue was measured using a ROI of a standard area which was kept constant across tissues and imaging sessions. The figure shows xenograft tumour and organs of three animals at one experimental time point i.e. each row represents tissues of an individual animal.

For orthotopic tumours, the ROI for tumour was centred around the liver tumour while the non-tumour liver measurement was taken from the region away from the macroscopic tumour.

All images were captured under the optimum experimental filters (i.e. excitation 570nm/emission 620nm)

2.4.5 Confocal microscopy

Murine tissue embedded in optimal cutting temperature (OCT) compound (Thermo Fisher Scientific, Massachusetts, USA) and snap-frozen in liquid nitrogen were sectioned by Mr Mike Shires (Senior Laboratory Technician, Leeds Institute of Medical Research) using a Leica CM3050S research cryostat (Leica Biosystems, UK). Sections were then stained with DAPI nuclear stain and CellMask™ green plasma membrane stain (Thermo Fisher Scientific, Massachusetts, USA) according to the manufacturer's guidelines.

Confocal microscopy was performed by Dr Adam Davison (Flow Cytometry and Imaging Facilities Manager, Leeds Institute of Medical Research) using a Nikon A1R confocal microscope (Nikon, Tokyo, Japan). Exposure settings for DAPI, CellMask and Rhodamine-Red C2 maleimide were kept constant throughout the imaging sessions.

2.4.6 Multispectral Optoacoustic Tomography (MSOT)

The MSOT inVision 1286-TF (iThera Medical, Munich, Germany) hardware was set up according to the manufacturers' instructions. Nude mice were used for the experiments which negated the need for hair removal prior to imaging. While the water bath was warmed to 37°C, the mouse to be imaged was allowed to equilibrate to 38-39°C in a warming chamber for up to 10min prior to inducing anaesthesia with inhalational isoflurane. Subsequent procedures were all carried out under general anaesthesia, with constant monitoring of respiratory rate and titration of maintenance isoflurane. Tail vein cannulation using a 27-gauge needle connected to fine tubing (PE-20) was performed by Dr Gemma Marston or Dr Nicola Ingram. The needle was secured to the tail with tissue glue, lubricant applied to eyes, front teeth secured on the tooth bar of the nose cone delivering anaesthesia and the mouse placed in a cling film hammock surrounded by warmed ultrasound gel, taking care to exclude air bubbles.

The mouse was carefully placed in the water bath and the water-tight seal was checked on the cling film hammock by looking for bubbles. The patency of tail vein catheter was checked by injecting a few microliters of PBS.

Prior to imaging, the mouse was allowed to equilibrate in the water bath for 10min. Spectral data (obtained using UV-Vis by Dr Sunjie Ye and Dr Lucien Roach) for the gold nanoparticle being investigated was uploaded into the MSOT InVision software. The ROI to image was determined according to the experimental protocol. Generally, this included the region of the liver and/or the xenograft tumour. After a pre-injection scan was performed, the probe was injected under continuous imaging of a single pre-selected area within the ROI.

2.5 Identification of biomarkers with theranostic potential

In order to develop targeted theranostic platforms in CCA, biomarkers with theranostic potential require validation in CCA tissue. Therefore, the published literature was systematically searched for candidate biomarkers that have been validated in CCA tissue.

MEDLINE and EMBASE databases from 01 January 1996 to 30 September 2019 were searched for proteomic and immunohistochemical studies in CCA using the following inclusion and exclusion criteria.

2.5.1 Inclusion criteria

- All biomarkers discovered in bile or tissue from CCA patients by proteomic analysis or IHC studies that reported high expression (greater than 20% positive expression for the purpose of comparison).
- For IHC studies, inclusion of at least 30 CCA specimens was required for inclusion. A similar cut off was used by another systematic review on CCA

biomarkers (Wiggers *et al.*, 2014). For proteomic studies, only those with tissue validation in at least 30 CCA specimens were included.

2.5.2 Exclusion criteria

- Studies only involving cancer cell lines with no tissue validation.
- Circulating biomarkers in blood and urine were excluded unless they were also demonstrated to have high expression in the CCA tissue.
- High expression in normal bile ducts and liver tissue (>20% positive expression was used to exclude biomarkers highly expressed in normal tissue)
- Down-regulated biomarkers in CCA tissue
- Review papers, letters, editorials, conference abstracts and case reports.

2.5.3 Data extraction and analysis

The PRISMA flow diagram shown in **Figure 2-3** depicts the search strategy and the two main phases of this systematic review.

Evaluated biomarkers, site of tumour (IH-CCA, EH-CCA (which includes PH-CCA) or CCA when tumour site was not specified), geographical location of patients (Eastern or Western countries) and control group characteristics were recorded. For IHC studies, data extracted included the tissue compartment where staining was observed and whether whole slides or tissue-microarrays (TMA) were used. Where expression in normal tissues was not stated, the Human Protein Atlas (Uhlen *et al.*, 2015) was used to establish expression in a range of normal tissues.

Selected genes were subjected to gene ontology analysis using PANTHER classification system (Mi *et al.*, 2013) and categorized based on tissue compartment of expression. Biomarkers that were validated in 2 or more studies were included in the final analysis and interrogated in more detail. The STRING network (Szklarczyk *et al.*, 2019) was also used to further interrogate the final shortlist of biomarkers for theranosis.

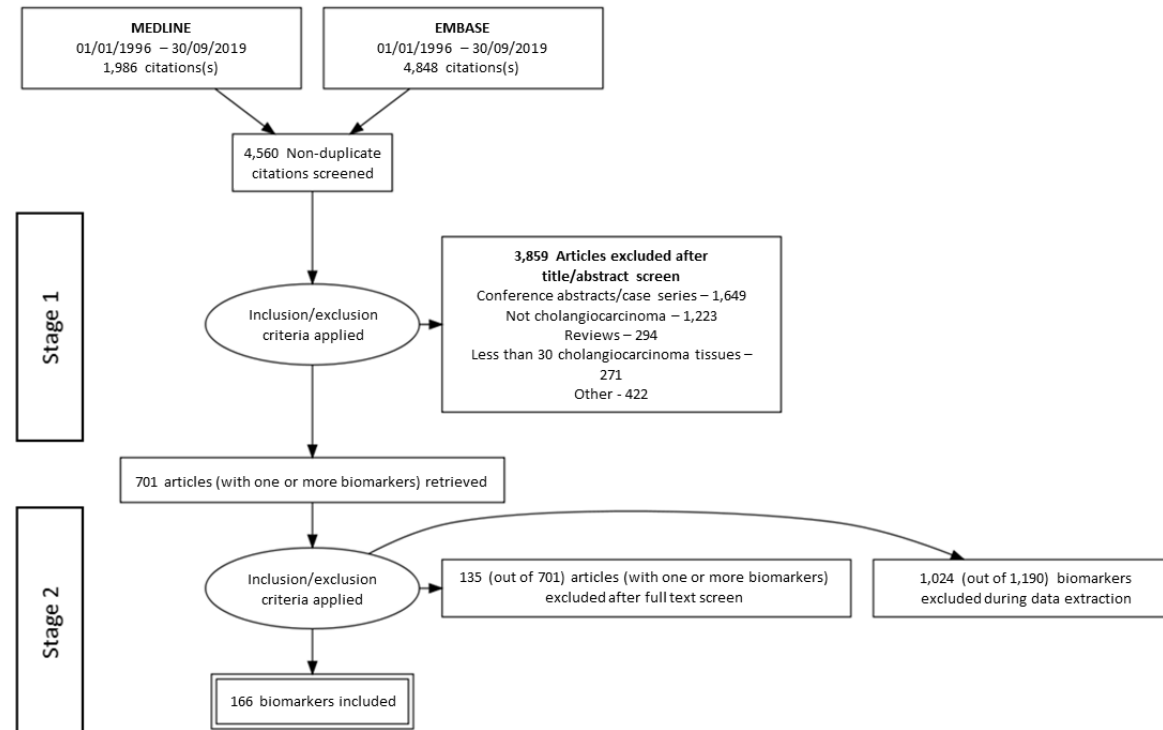


Figure 2-3 PRISMA flow diagram

This shows the search strategy for the systematic review of theranostic biomarkers in CCA. Stage 1 of the search involved title and abstract screen of 4,560 citations against the inclusion/exclusion criteria. Stage 2 involved full text reviews of 701 articles with one or more potential biomarkers. Data was extracted on 166 included biomarkers (details in **Appendix 1 Data extraction table**).

2.6 Tenascin C as a candidate biomarker in cholangiocarcinoma

TNC was further investigated as a candidate biomarker in CCA using human and murine tissues as well as selected cancer cell lines.

2.6.1 Immunohistochemistry

The protocols for immunohistochemical analysis of tissues were optimised for the three types of tissues, namely formalin-fixed paraffin-embedded (FFPE) murine tissue, snap-frozen murine tissue embedded in OCT compound (Thermo Scientific, Massachusetts, USA) and FFPE human tissue.

Ethical approval for the use of archival FFPE human PH-CCA tissue and matched control tissue from patients who underwent surgery at our institution for the purpose of validation of candidate biomarkers was already in place (REC 06/Q1206/136; 18/07/2011 – See *Appendix 2 Ethical approval*). Immunolabelling with TNC was optimized using the strategies described in **Table 2-1** on human and murine tissue.

2.6.1.1 Tissue fixation

Archival human FFPE tissues were processed according to the Leeds Teaching Hospitals NHS Trust protocol.

Retrieved murine tissues were fixed by immersion in 4% (w/v) paraformaldehyde (PFA) immediately after sacrifice by cervical dislocation. Following overnight immersion in PFA, tissues were washed in PBS and stored in 70% (v/v) ethanol until processing. All tissues were processed and paraffin-embedded by Mr Michael Shires (Senior Laboratory Technician, Leeds Institute of Medical Research).

Table 2-1 Tenascin C Optimization

This table lists the different methods assessed for optimization of TNC expression on tissue sections by immunohistochemistry

Antibody Manufacturer	Tissue type	Retrieval methods	Primary antibody dilutions	Blocking agents	Optimized protocol
Mouse monoclonal Anti-TNC Antibody 4F10TT, Immuno-Biological Laboratories Co. Ltd, Japan	FFPE Mouse xenograft	Heat-induced epitope retrieval (HIER) pH 6 Citrate buffer	1:50	0.3% H ₂ O ₂	HIER pH 6 Citrate buffer, 0.3% H ₂ O ₂ (Optimized by Dr Filomena Esteves and Dr Azhar Maqbool)
	FFPE Mouse liver	1. None 2. HIER pH 6 Citrate buffer	1:100, 1:150	0.3% H ₂ O ₂ , 3% H ₂ O ₂ 10% Casein	HIER pH 6 Citrate buffer, 10% Casein, 0.3% H ₂ O ₂
Rabbit polyclonal Anti-TNC antibody SC20932, Santa Cruz Biotechnology, USA	Fresh frozen Mouse (xenograft and liver)	None	1:50	0.3% H ₂ O ₂	No retrieval, 0.3% H ₂ O ₂ , 1:50 Ab dilution
Rabbit polyclonal Anti-TNC Antibody HPA004823, Sigma-Aldrich, UK	FFPE Human (PH-CCA and normal liver)	1. None 2. HIER pH 6 Citrate buffer	1:100, 1:200, 1:300	0.3% H ₂ O ₂ , 3% H ₂ O ₂ 10% Casein, Avidin/Biotin	No retrieval, 10% casein, 0.3% H ₂ O ₂ , 1:200 Ab dilution

For experiments that required cryopreserved tissue in addition to FFPE tissue, organs/tissues were cut in half following retrieval immediately after sacrifice. Half of the organs/tissues were then processed as described above and the other half were cryopreserved. For cryopreservation, the tissues were placed on a cork board wrapped in aluminium foil, immersed in OCT, cooled on dry ice then wrapped and snap frozen in liquid nitrogen. These were stored at -80°C. Cryosectioning was performed by Mr Michael Shires (Senior Laboratory Technician, Leeds Institute of Medical Research) Leica CM3050S research cryostat (Leica Biosystems, UK).

2.6.1.2 Reagents for immunohistochemistry

10mM Citric acid buffer pH 6.0 dH₂O, Tris-buffered Saline (TBS; 50mM Tris-Cl, pH 7.4; 150mM NaCl), Tris-buffered Saline with Tween (TBS-T; TBS with 10% v/v Tween-20) and 10% casein solution (Vector Laboratories Ltd, Peterborough, UK) were required for the immunohistochemistry protocols.

2.6.1.3 Formalin-fixed paraffin embedded tissue

immunohistochemistry

Five-micron thickness tissue sections were cut from FFPE tissue blocks using a Leica RM2235 microtome (Leica Biosystems, UK), fixed onto glass slides (Superfrost Plus®, Thermo Scientific) and allowed to dry overnight at 37°C. Sections were dewaxed using xylene and rehydrated using 100% ethanol followed by running water. Heat-induced epitope retrieval (HIER) was performed by placing the sections in pre-heated pH 6.0 citrate buffer and heated for 10min at full power in a 900W microwave. Although recommended for the TNC antibody, HIER was not performed on liver tissue due to non-specific background staining on all liver tissue if HIER was utilised. Slides were allowed to cool for at least 20min and rinsed briefly in running tap water prior to endogenous peroxidase blocking by immersion in 0.3% v/v H₂O₂ in methanol for

10min. 10% Casein (Vector Laboratories Ltd, Peterborough, UK; SP-5020) in PBS and antibody diluent reagent solution (Invitrogen, California, USA) were applied to each section for 20min.

The primary antibody used for human tissue sections was rabbit polyclonal anti-TNC primary antibody (Sigma-Aldrich, UK; HPA004823) at 1:200 dilution whereas for murine tissue sections, mouse monoclonal anti-TNC antibody (Immuno-Biological Laboratories Co. Ltd, Japan; 4F10TT) at 1:50 dilution was used. All antibodies were diluted in antibody diluent and applied to all but the no primary antibody control section. All sections were incubated at room temperature for 1hr. Sections were then washed with TBS-T twice for 3min and with TBS once for 3min. For human tissues, Dako Envision HRP-conjugated secondary antibody was applied to all slides for a 30min incubation at room temperature followed by TBS-T and TBS washes as described above.

For murine tissues, the mouse on mouse polymer IHC kit (Abcam, Cambridge, UK; ab127055) that included a rodent block for 30min and incubation with the secondary polymer for 30min was used according to the manufacturer's instructions.

DAB+ Substrate Chromogen System (Dako, CA) was applied for 10mins to all sections. Then, sections were counterstained with Haematoxylin and 'blued' with Scott's tap water before being dehydrated, cleared, mounted in DePex mounting adhesive (Sigma-Aldrich, UK) and allowed to dry overnight in a fume cupboard.

2.6.1.4 Scoring of TNC immunolabelling

Each tissue section was assigned a distribution score and an intensity score.

For the distribution score, each section was divided visually into 4 quadrants (**Figure 2-4B**) and each quadrant inspected carefully for any TNC-labelling. If none of the quadrants displayed any TNC-immunolabelling, the score assigned was 0. If one

quadrant was positive, a score of 1 was assigned and so on until a maximum distribution score of 4. For the intensity score, a range of immunolabelling intensity standards were determined prior to scoring as illustrated in **Figure 2-4 A**. Each slide was assessed for the maximum immunolabelling intensity in any given area and an intensity score assigned accordingly.

The TNC-score assigned to any slide was the product of its intensity and distribution scores (**Figure 2-4 C**). The maximum score possible was 12 and the minimum 0.

2.6.1.5 Fresh frozen murine tissue immunohistochemistry

The protocol for snap frozen OCT embedded-murine tissue had two distinct differences from the FFPE murine tissue IHC protocol in that no epitope retrieval was utilized and 10% Casein block was not required. The protocol is shown in **Table 2-1**.

2.6.1.6 Haematoxylin and eosin staining protocol

FFPE tissues were processed and sectioned according to the method described in **Section 2.6.1.1**. 5µm thick tissue sections were cut from FFPE tissue blocks using a Leica RM2235 microtome (Leica Biosystems, UK), fixed onto glass slides (Superfrost Plus®, Thermo Scientific) and allowed to dry overnight at 37°C. Sections were dewaxed using xylene and rehydrated using 100% ethanol followed by running water. Tissue sections were then incubated in haematoxylin (Sigma, UK) for the recommended duration (at least 1min) followed by rinsing in tap water. The slides were then placed in Scott's tap water for 1min prior to rinsing in tap water. Following this, the sections were placed in 1% eosin (Sigma, UK) for 1min and then washed in tap water. Subsequently, the slides were dehydrated through three 1min incubations in 100% ethanol followed by three 1min rinses in xylene. Coverslips were then mounted over the tissue sections with DePex (Sigma, UK) and allowed to dry overnight in a fume cupboard.

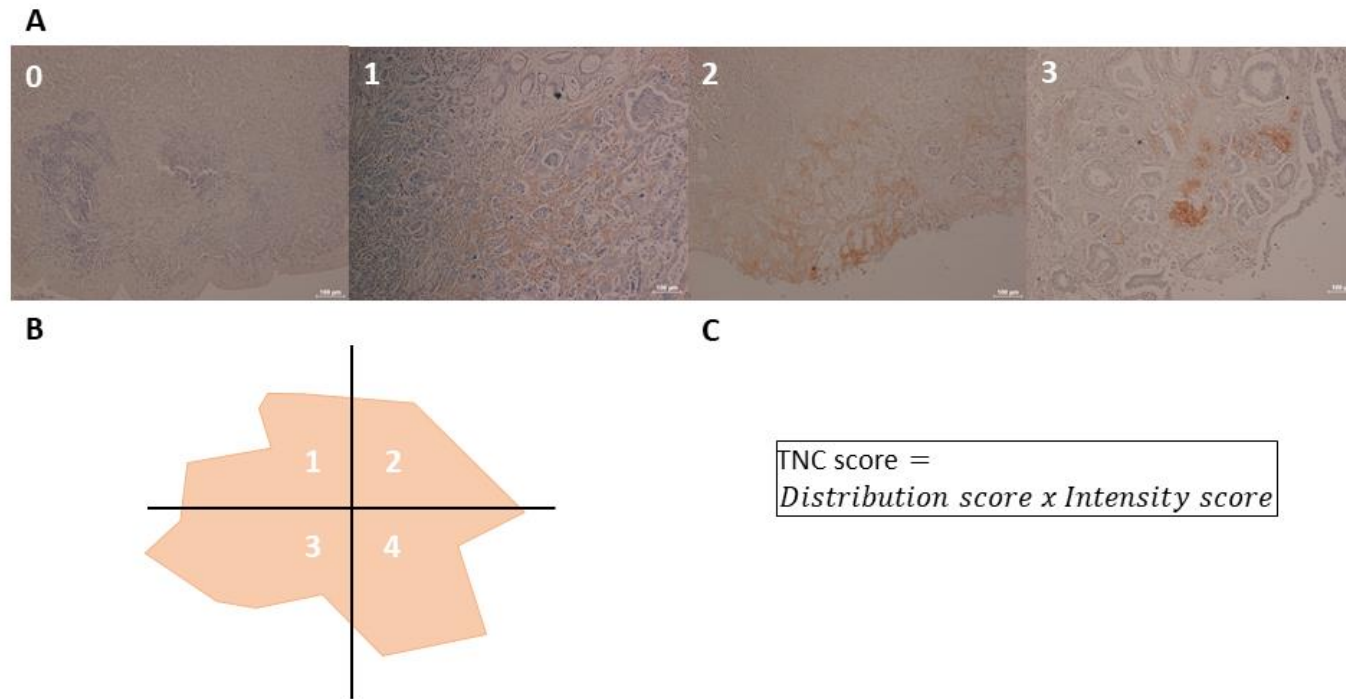


Figure 2-4 TNC scoring.

A. This shows representative images of intensity score with 0 showing no TNC immunolabelling to 3 showing the highest immunolabelling intensity. 1 shows mild intensity while 2 shows moderate intensity TNC immunolabelling. **B.** This is a schematic of the division of a tissue section into quadrants. Each quadrant was assessed for TNC immunolabelling. **C.** This shows how the TNC score was derived from the distribution score and intensity score for each tissue section.

2.6.2 Immunoblotting

2.6.2.1 Preparation of whole cell lysates

Whole cell lysates were made from cells grown as described in **Section 2.1**. Cell pellets were lysed on ice with 200-300 μ L of radioimmunoprecipitation assay (RIPA) buffer with protease inhibitor cocktail (Sigma-Aldrich, UK). After 15min, these were transferred to QIAshredder (Qiagen Ltd, UK) tubes and centrifuged at 1600 g for 2min at 2°C. The resulting lysates were stored in aliquots at -80°C.

2.6.2.2 Quantification of protein

Protein quantification was performed according to the Bio-Rad DC (Bio-Rad Laboratories, USA) protein assay kit instructions. Briefly, protein standards from 2mg/ml to 0.1mg/ml concentrations were made from bovine serum albumin. Cell lysate dilutions of 1:5, 1:10 and occasionally 1:20 were used to compare concentrations to standard protein curve. 5 μ L of cell lysates were pipetted into a clean, dry microtiter plate. 25 μ L of working reagent A solution was added to each well (Working reagent A was made by adding 20 μ L reagent S to 1ml of reagent A). Then 200 μ L of reagent B was added and gently agitated for 5s. After 15min, the absorbance was read at 620nm using a luminometer (Berthold Technologies, Germany,). GraphPad Prism version 7.00 for Windows (GraphPad Software, La Jolla, California USA) was used to plot standard protein curves to determine the slope-intercept formula, which was then used to determine concentrations of the unknown proteins, considering the dilution factor used in the assay.

2.6.2.3 Gel electrophoresis

Sodium dodecyl sulphate polyacrylamide gel electrophoresis (SDS-PAGE) method was utilized for separation of proteins. Protein samples were standardised to 50 μ g per cell line. Whole cell lysate samples were prepared in x4 NuPAGE® SDS sample buffer and

boiled on a hot block at 100°C for 5min. Tubes were centrifuged for 30s at 8,000 g, gently re-suspended and cooled on ice until loading onto gel. Running buffer was prepared from NuPAGE® MOPS SDS x20 running buffer by diluting in deionized water. A NuPAGE® tank was set up with NuPAGE® Novex 12% Bis-Tris precast gel (1.0mm, 10 lanes, Invitrogen), filled with running buffer. The prepared protein standardised whole cell lysate samples in NuPAGE® SDS sample buffer as well as protein standard ladder were loaded onto the lanes and electrophoresed at 180V for 45min-1hr in an ice bath.

2.6.2.4 Protein Transfer

Transfer buffer was made from x20 NuPAGE® transfer buffer (Invitrogen, UK) by mixing 25ml with 425ml deionised water and 50ml 100% methanol. HybondP membrane (G.E.Healthcare, Illinois, USA) was activated by placing in 5-10ml 100% methanol for 10s before placing in transfer buffer.

Once the loading dye had reached the bottom of the gel, the cassette was dismantled, and the gel carefully removed with moistened gloves to prevent fracture of the gel.

The transfer module was loaded with 3 transfer buffer-soaked sponges and 2 pieces of filter paper prior to placing the pre-cast gel followed by another piece of filter paper, making sure to avoid air bubbles by smoothing out using a glass rod. Three further transfer buffer-soaked sponges were added, and the transfer module loaded onto the rig. The cassette was filled with transfer buffer and the outer tank filled with deionised water followed by overnight transfer at 15V at room temperature.

2.6.2.5 Hybridisation of antibodies and visualising proteins

The next day, 1% v/v skimmed milk solution was made from skimmed milk powder in TBS-T for blocking. The membrane was then removed from the module and placed in 5-10ml of Ponceau S solution (Sigma-Aldrich, UK) to visualise lanes. The membrane

was then washed in deionised water prior to blocking with 1% skimmed milk for 1hr at room temperature on a rocking platform.

Following this, the membrane was placed in 1% v/v skimmed milk containing 1:200 rabbit polyclonal Tenascin C antibody (Santa Cruz sc20932) and 1:20,000 mouse monoclonal beta actin antibody. This was incubated for 1hr at room temperature on a rocking platform followed by washes in TBS-T. Then, the membrane was placed in 1% skimmed milk containing 1:2000 swine anti-rabbit HRP conjugated secondary antibody (Dako, Denmark; P0217) and incubated for 1hr at room temperature on a rocking platform. This was followed by a wash in TBS-T.

Pierce™ ECL western blotting pico substrate (Thermo Fisher Scientific, Massachusetts, USA) working solution was made according to the manufacturer's instructions (50-50 mix of the two solutions). The membrane was placed on a clean flat surface and drops of ECL working solution added to ensure full coverage of the membrane. After a 5min incubation, lanes were visualised using a gel imaging system (Bio-Rad Gel Doc, Imaging System Bio-Rad, California, USA) and images captured using Image Lab software version 5.0 (Bio-Rad, California, USA).

Then, the membrane was placed in 1% skimmed milk containing 1:50,000 rabbit anti-mouse HRP conjugated secondary antibody (P0161; Dako, Denmark) and incubated for 30min on a rocking platform. After washing with TBS-T, lanes were visualised as previously described. Densitometry of ECL signal corresponding to loading control proteins as well as protein of interest was measured using the Image Lab software version 5.0 (Bio-Rad, California, USA) and expressed graphically using GraphPad software (GraphPad Software, La Jolla, California USA).

2.6.3 Immunofluorescence

Presence of TNC in cell lines was determined by immunofluorescence (IF). Cells were seeded into 6-well plates (Corning Inc, USA) containing sterile coverslips and incubated under standard conditions until 70-80% confluence. Coverslips were fixed with 4% PFA for 10min at room temperature or 100% ice cold methanol for 10min. Coverslips were then washed with PBS x2. Methanol-fixed coverslips were allowed to air dry, sealed with paraffin and stored at 4°C. PFA-fixed coverslips were stored in PBS at 4°C prior to antibody labelling.

100µL of antibody diluent was added to each coverslip followed by a 5 min incubation at room temperature. 100µL of rabbit polyclonal anti-TNC antibody (sc-20932; Santa Cruz Biotechnology, Inc, Texas, USA) was used at 1:50 and 1:500 dilutions. A no primary antibody control was included for each fixation method. Coverslips with primary antibody were incubated for 1hr at room temperature. After washes with TBS-T and TBS, Alexa Fluor anti-Rabbit IgG secondary antibody (Thermo Fisher Scientific, Massachusetts, USA) was added to all coverslips at 1:300 dilution and incubated in the dark for 30min. After washes, coverslips were carefully lifted and mounted on slides with 20µL of Prolong Gold + DAPI. Coverslips were sealed with nail varnish and stored in the dark at 4°C until imaging with Zeiss AxioImager.Z1 Apotome fluorescent microscope (Carl Zeiss, Thornwood, New York, USA). Exposure times were calibrated on the expected brightest slide for each cell line (based on antibody dilution and fixation method to compare relative staining intensities) using the Zeiss AxioVision Software (Carl Zeiss, Thornwood, New York, USA).

2.6.4 Assessment of Tenascin C gene expression in cell lines

Cells were grown according to the method described in **Section 2.1** and harvested during exponential growth phase. These were given to Dr Azhar Maqbool who

performed the real-time reverse transcription polymerase chain reaction (RT-PCR) assay to assess *TNC* mRNA expression according to an established protocol.

Briefly, this included three steps; RNA extraction from cell pellets using Aurum total RNA minikit (BioRAD, Hemel, Hempstead, UK), synthesis of complementary DNA (cDNA) using Promega reverse transcriptase system (Promega, UK), followed by amplification of cDNA by RT-PCR, using TaqMan® gene expression assay (Life Technologies, Paisley, UK) and specific primers/probes as described below. To avoid contamination, these steps were performed in a DNA-free environment.

To detect TNC of human origin, human GAPDH primers/probe Hs99999905_m1 and human TNC primer/probe Hs01115665_m1 (Life Technologies, Paisley, UK) were used. Similarly, to detect TNC of mouse origin, mouse GAPDH primer/probe Mm99999915_g1 and mouse TNC primer/probe Mm00495662_m1 (Life Technologies, Paisley, UK) were used. The difference in the signal obtained for the target gene (*TNC*) compared to the endogenous control gene (*GAPDH*) reflected the amount of *TNC* in comparison to control. This relative quantification of TNC mRNA was expressed graphically as a percentage of GAPDH.

2.7 Evaluation of fluorescent labelled Tenasin C

2.7.1 Experimental setup

6-10 week old SW620 xenograft-bearing BALB/c nude female mice were utilised for the experiments. After 10-14 days of tumour growth, animals were randomised based on tumour size to either receive TNC affimer or control GFP affimer, each conjugated with Rhodamine-red C₂ maleimide, via tail vein bolus injection in 100µL of buffer. The affimers were supplied by Dr Christian Tiede and the fluorescent labelling was performed by Dr Robin Bon and Ms Anna Tang.

Animals were sacrificed at pre-determined time points from injection and tissues imaged *ex vivo* as described in **Section 2.4.4**. As described in **Section 2.4.4**, LivingImage Software Version 4.2 (PerkinElmer Inc, Massachusetts, USA) was used to determine the fluorescent intensity. In the preliminary workup of the biodistribution of fluorescent labelled TNC Affimer, a control GFP Affimer group was not included.

2.8 Assessment of cytotoxic effects of drugs and gold nanoparticles

2.8.1 Chemosensitivity to gemcitabine and irinotecan

TFK-1 and the selected clone TFKluc2B2 were evaluated for their sensitivity to two chemotherapeutic agents, gemcitabine and irinotecan. Cells at comparable passage number were plated at 4,000 cells/well in 96-well plates on day 0 and incubated overnight under standard conditions (8 technical replicates per condition).

Irinotecan was reconstituted according to the manufacturer's instructions in 100% DMSO to a concentration of 5 mg/ml and serial dilutions ranging from 200 μ M to 1.56 μ M were made up in media. Gemcitabine powder was reconstituted in PBS to a concentration of 10 mg/ml prior to serial dilutions from 200 μ M to 0.76 nM in media.

On day 1, media was replaced with drug-containing media at the appropriate concentrations and incubated under standard conditions for 72 hrs. All plates were subsequently subject to the MTT assay described in **Section 2.2.1**. Cell viability compared to vehicle (DMSO or PBS)

2.8.2 Toxicity assays with selected gold nanoparticles

Gold nanoparticles of two different shapes were selected for toxicity assays on cells based on their differing photoacoustic properties on MSOT inVision 1286-TF (iThera Medical, Munich, Germany) imaging.

2.8.2.1 Gold nanorods

Gold nanorods (AuNRs) were synthesised and gifted by Dr Lucien Roach. Briefly, AuNRs coated with poly-4-styrene sulphonic acid-co-maleic acid (PSS) were synthesised at a concentration of 975 $\mu\text{g}/\text{ml}$ in sterile Milli-Q water using an established protocol optimised Dr Lucien Roach (Roach *et al.*, 2018). The protocol included multiple wash steps and a filter sterilization to make the solution suitable for *in vivo* use. The final concentration was confirmed by atomic absorption spectroscopy prior to use in *in vitro* or *in vivo* assays.

To determine the concentration that would impact cell viability, concentration of AuNRs tested *in vitro* at high doses. AuNRs at 975 $\mu\text{g}/\text{ml}$ were centrifuged at 9,000 g and an appropriate volume of Milli-Q supernatant discarded prior to re-suspension by mixing and sonicating in a water bath to make x2 and x1.5 concentrations of AuNR suspension in order to achieve 195 $\mu\text{g}/\text{ml}$ and 146.25 $\mu\text{g}/\text{ml}$ on cells, respectively. 1:2 dilutions of the stock solution were done to achieve concentrations ranging from 97.5 $\mu\text{g}/\text{ml}$ to 6.1 $\mu\text{g}/\text{ml}$.

Cells were seeded at 4,000 cells/well in 96-well plates on day 0 and incubated under standard conditions. On day 1, 10 μL of AuNR solution of each concentration were added to the respective wells. For each concentration, 5 technical replicates of cells treated with AuNRs and 3 technical replicates of AuNR with media only (control wells) were used. After 24hrs, 10 μL of CCK-8 reagent (Sigma-Aldrich, USA) were added to all wells and incubated under standard conditions for 4hrs prior to measurement of

absorbance at 450nm on an optical spectrophotometer (Berthold Technologies, Germany). Absorbance of the control wells were deducted from the test wells at each corresponding concentration and cell viability were calculated as a proportion to control wells as shown in the equation below. Experiments were repeated until 3 biological replicate data sets under the same conditions were achieved.

$$\% \text{ viability} = \frac{\text{absorbance of treated cells} - \text{absorbance of control cells}}{\text{absorbance of control cells}} \times 100$$

A normalized dose-response curve was used to calculate the concentration at which 50% inhibition occurred (the IC₅₀ value) along with their corresponding 95% confidence intervals.

Chapter 3

Development of pre-clinical *in vivo* models of cholangiocarcinoma

Introduction

Pre-clinical animal models of cancer are essential for the evaluation and validation of novel, emerging therapies prior to human clinical use (Cheon and Orsulic, 2011).

Mouse and rat models are the most frequently utilised animal models of human disease owing to their small size, relatively low maintenance costs, rapid reproduction and genetic manipulation to replicate human disease conditions (Cheon and Orsulic, 2011; De Minicis *et al.*, 2013).

Multiple models of CCA have been developed but an ideal model does not exist (Loeuillard *et al.*, 2019). In a recent review of animal models of CCA, Loeuillard *et al.* (2019) reported that the majority of existing models are for IH-CCA and that there is a need to develop specific models for the other subtypes of CCA.

An ideal model should allow time-efficient generation of tumours, high throughput screening and facilitate *in vivo* imaging. In addition, it must adhere to the National Centre for Reduction, Refinement and Replacement (NC3R) principles which provide a legal and ethical framework for *in vivo* studies in the UK (Burden *et al.*, 2015). Tumour models should also adequately replicate the tumour microenvironment but the most commonly used animal models of CCA, the subcutaneous xenograft models, do not achieve this (Loeuillard *et al.*, 2019). Although a syngeneic rat orthotopic model of CCA exists, this requires invasive surgery to establish (Sirica *et al.*, 2008) and an equivalent mouse model does not exist.

This chapter is focussed on the development of a novel, reproducible, orthotopic tumour model of CCA using EH-CCA cell lines, minimally invasive techniques and high throughput pre-clinical imaging.

3.1 Generation of EH-CCA cell lines with bioluminescent properties

Bioluminescence imaging has an established utility for longitudinal assessment of *in vivo* tumour growth in other animal models (Ritelli *et al.*, 2015). Therefore, for the facilitation of high throughput screening and *in vivo* imaging of a novel orthotopic model of EH-CCA, bioluminescent cell lines were generated and characterized.

EH-CCA cell lines TFK-1 and EGI-1 were transfected with a lentivirus (Lenti-PGK-Luc control lentivirus) containing a plasmid which coded for the luciferase enzyme (**Figure 2-1**). This was performed according to the method described in **Section 2.2.2**.

The plasmid used to transfect cells also contained a gene that conferred resistance to puromycin. Therefore, to select stably-transfected clones, cells were treated with puromycin. To investigate the minimum concentration of puromycin required for selection, the cell viability of the parent cell lines following treatment with a range of concentrations of puromycin (0.078 - 10 μ g/ml) was tested. TFK-1 cell line was more sensitive to puromycin compared to the EGI-1 cell line (**Figure 3-1**). The lowest concentration of puromycin that resulted in <5% viability for both cell lines was 0.6 μ g/ml and was therefore used as the selection concentration during the transfection process.

3.1.1 Characterization of EGI-1 and TFK-1 clones

Colonies of transfected cells grown in 10cm plastic dishes were carefully lifted using sterile filter paper and transferred to individual wells. 15 EGI-1 and 12 TFK-1 transfected clones were successfully established, expanded and stored in liquid nitrogen prior to quantification of luciferase activity.

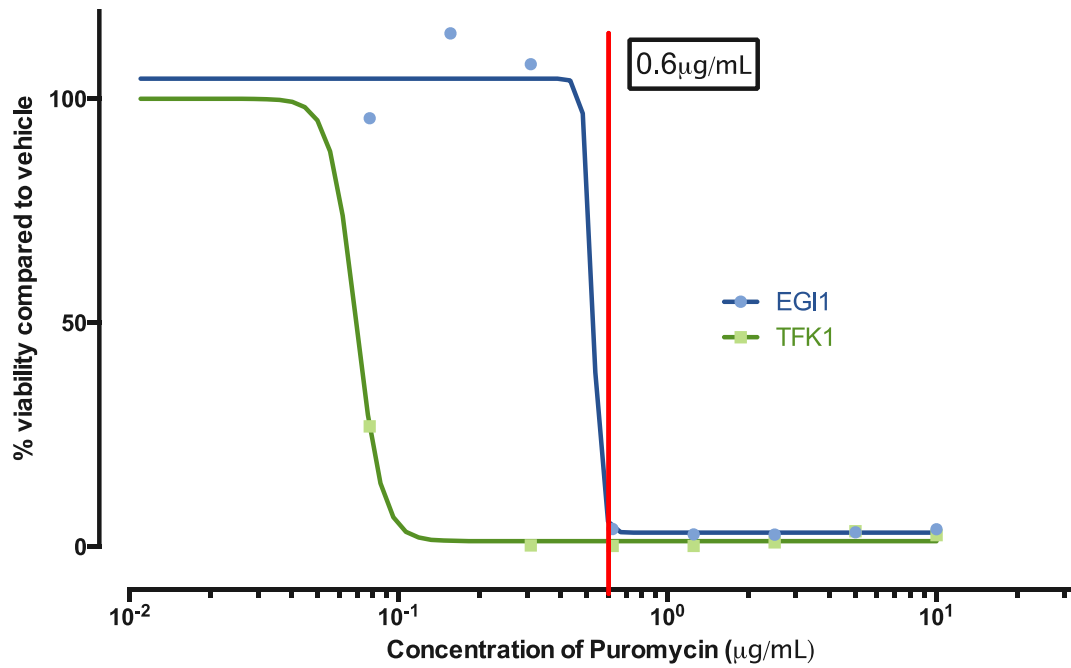


Figure 3-1 Puromycin sensitivity assay of TFK-1 and EGI-1 cell lines.

Cells were treated with puromycin for 7 days and then assayed for cell viability by MTT conversion. The red line indicates the concentration that caused >95% reduction in cell viability in both cell lines

Each point represents the mean cell viability of n=3 replicates from a single experiment.

Cell lysates of 12 TFK-1 clones were tested by *in vitro* luciferase assay according to the method described in **Section 2.2.3**. 1×10^5 cells per clone were tested and luciferase activity measured in relative light units (RLU). Of the 12 clones, 6 had no luciferase activity ($< 1 \times 10^2$ RLU), 1 had low activity (1×10^2 - 1×10^4 RLU), 2 had moderate activity (1×10^4 - 1×10^5 RLU) and 3 (TFKluc2B2, TFKluc1D1 and TFKluc2A4) had high activity ($> 1 \times 10^5$ RLU) (**Figure 3-2A**). The two clones with the highest activity (TFKluc2B2 and TFKluc1D1) were selected for further characterization.

15 EGI-1 clones were also tested using the same assay. Of these 15 clones, 1 had no luciferase activity ($< 1 \times 10^2$ RLU), 1 had low activity (1×10^2 - 1×10^4 RLU), 12 had moderate activity (1×10^4 - 1×10^5 RLU) and 1 (EGIlucD2) had high activity ($> 1 \times 10^5$ RLU) (**Figure 3-2B**). EGIlucD2 emerged as the EGI-1 clone with the highest luciferase activity and was selected for further characterization.

3.1.2 *In vitro* growth and culture characteristics

Light microscopy of parent cell lines compared to their transfected clones did not reveal any gross cellular differences. A representative image of TFK-1 and TFKluc2B2 is shown in **Figure 3-3**. Both cell lines grew as adherent epithelial-like monolayers. However, TFKluc2B2 and TFKluc1D1 clones were significantly less adherent to tissue culture plastic compared to the parent cell line TFK-1 and hence easier to harvest using trypsinisation. The same characteristic was not observed in EGIlucD2 compared to EGI-1.

The doubling times of the 3 selected clones compared to their parent cell lines were examined by MTT cell viability assay.

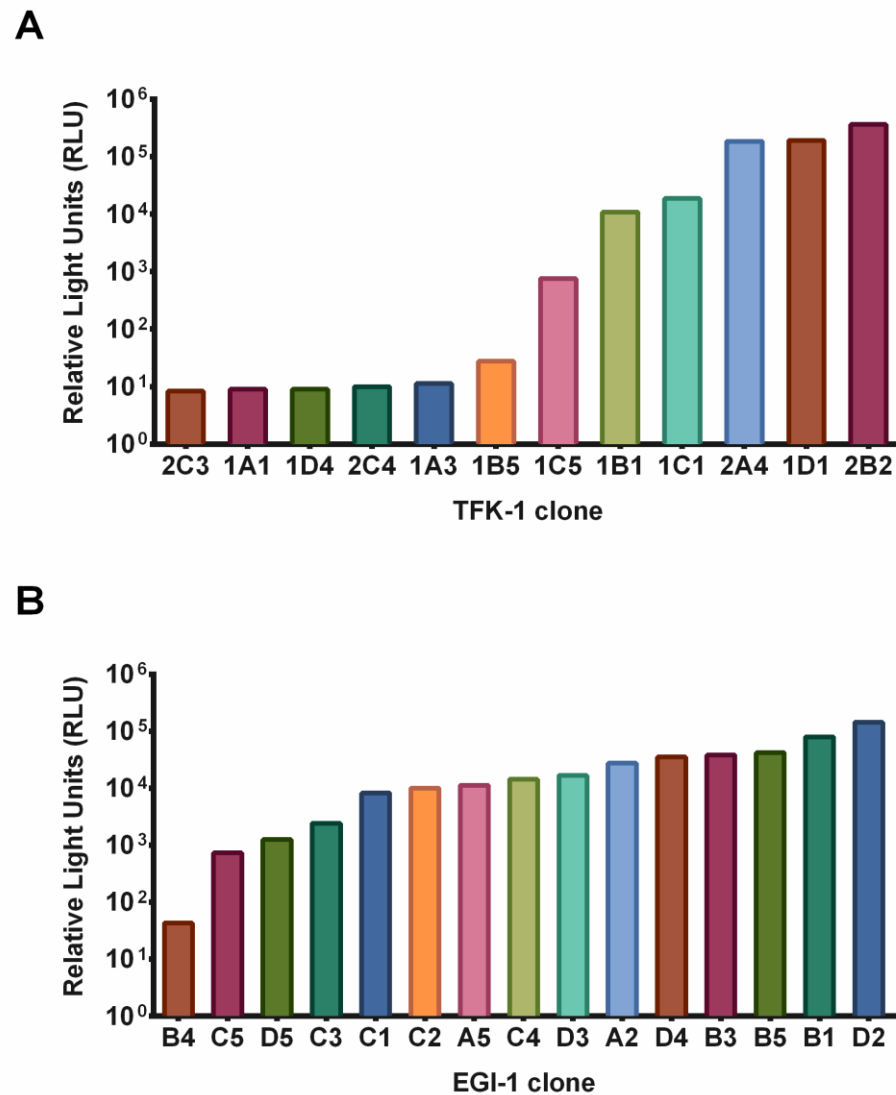


Figure 3-2 Quantification of luciferase activity of TFK-1 and EGI-1 clones.

Luciferase activity, expressed as relative light units was determined for 12 TFK-1 clones and 15 EGI-1 clones using a luciferase assay system (Promega, UK).

The values plotted are the means of n=3 technical replicates from a single experiment for each cell line (therefore no error bars shown). 1x10⁵ cells used for each cell line. The individual bars represent a single clone and the x-axis labels show the clone number.

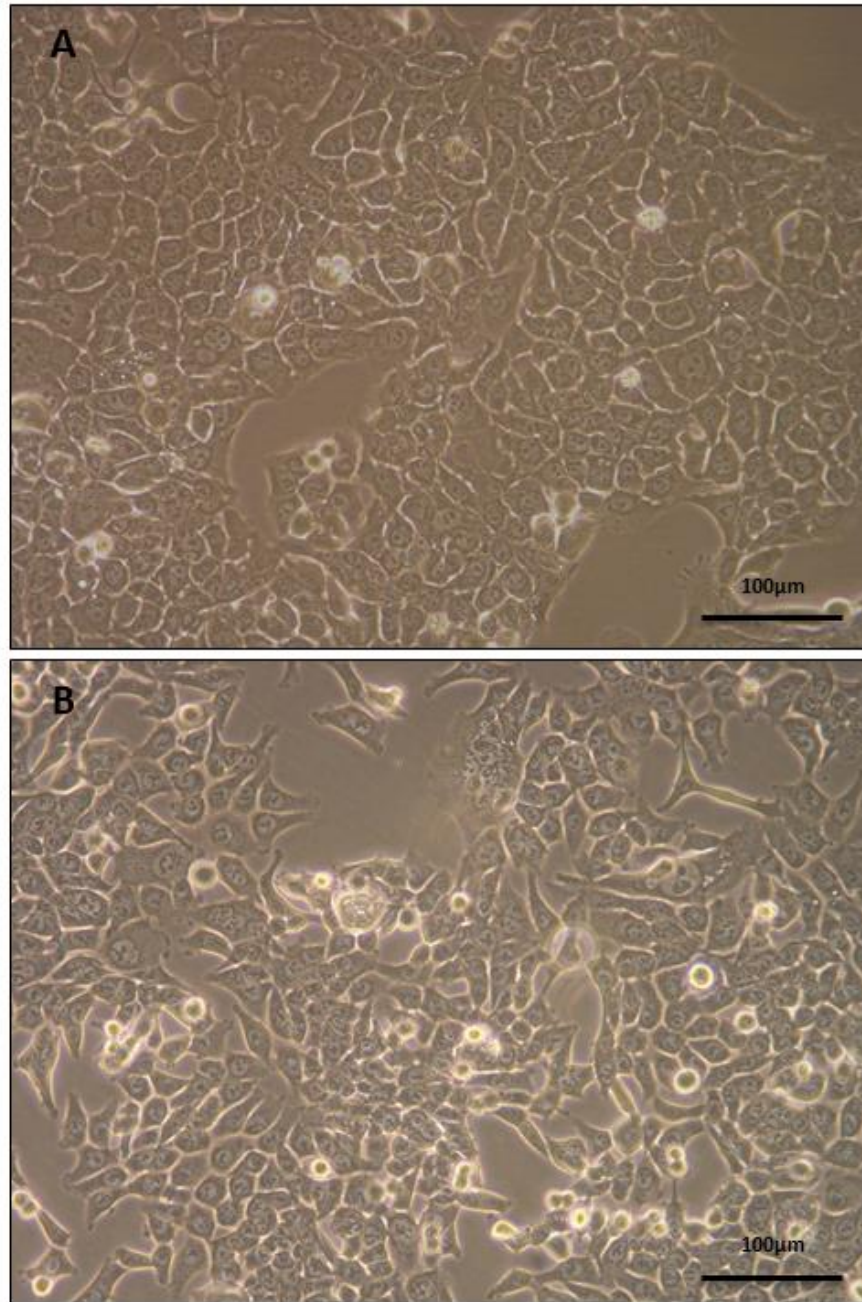


Figure 3-3 Morphology of TFK-1 parental cell line and TFKluc2B2 clone

Representative images of TFK-1 (A) and TFKluc2B2 (B) showed no significant gross cellular differences in the luciferase transfected clone TFKluc2B2 compared to the parent cell line TFK-1.

Images taken at comparable confluence and passage number. Scale bar shows 100µm.

The doubling time of TFKluc2B2 was significantly faster compared to the parent cell line TFK-1 (median 15.6h compared to 43.4h, $p=0.0036$; Kruskal-Wallis test, **Figure 3-4A**). However, TFK-1 doubling time compared to TFKluc1D1 was not significantly different (median 23.0h compared to 43.4h, $p=ns$, Kruskal-Wallis test). Median doubling time of the parent cell line EGI-1 (31.0h) compared to the clone EGIlucD2 (32.9h) was also not significantly different ($p=ns$, Kolmogorov-Smirnov test) (**Figure 3-4B**).

To investigate if the clones generated would emit adequate light for *in vivo* imaging, the luciferase-activity of TFKluc2B2 and TFKluc1D1 was compared to MC38luc11A (a cell line with high luciferase activity). MC38luc11A cells had previously been used successfully to generate an *in vivo* model of colorectal liver metastasis (Dr M Volpato, personal communication). As shown in **Figure 3-5A**, MC38luc11A cells (at passage 14) were more bioluminescent compared to TFKluc2B2 and TFKluc1D1 at all seeding densities (ranging from 7.8×10^2 - 1×10^5 cells). However, the bioluminescence was comparable between EGIlucD2 and MC38luc11A (at passage 20) (**Figure 3-5B**). This difference in MC38luc11A could be due to reduction in luciferase activity with increasing passage number or an error in cell count. Statistical comparison could not be performed as the results were obtained from a single experiment. As expected, TFK-1 and EGI-1 were negative for luciferase activity. Based on these findings, TFKluc2B2, TFKluc1D1 and EGIlucD2 were considered for *in vivo* tumour growth experiments.

3.1.3 Assessment of tumour growth

Prior to attempts at establishing an orthotopic tumour model, the ability of the selected cell lines to establish as subcutaneous tumour xenografts was tested. TFK-1 and EGI-1 parent cell lines as well as the selected luciferase-expressing clones were used to generate subcutaneous xenografts in CD1 nude mice. 1×10^7 cells suspended in 100 μ L PBS were used for each cell line.

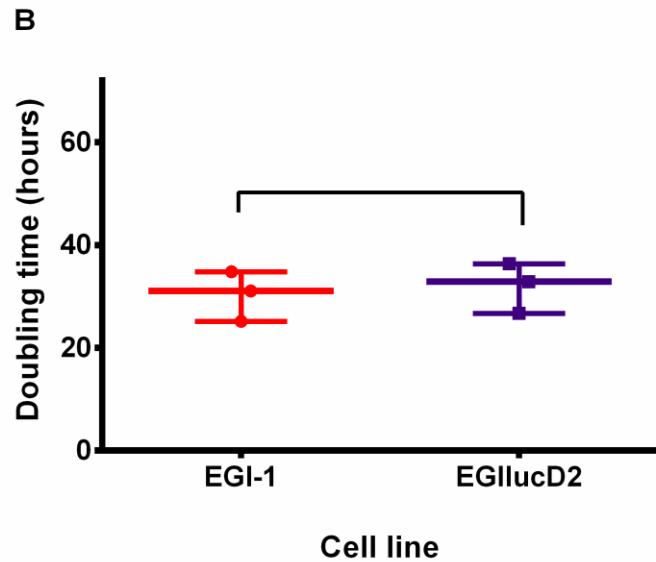
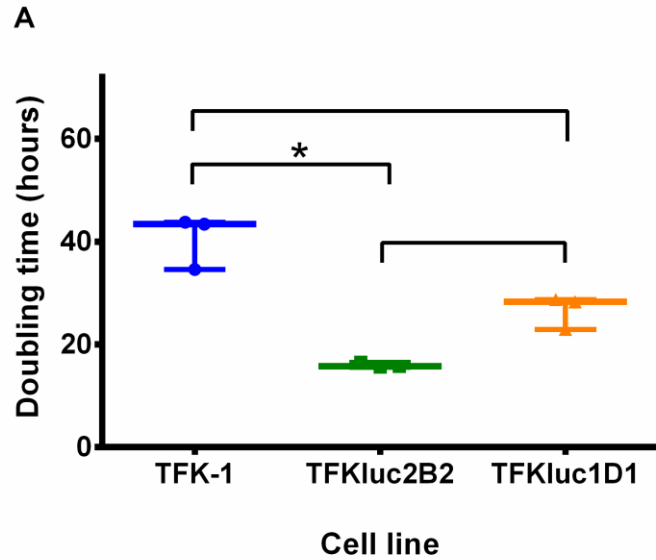


Figure 3-4 Doubling times of TFK-1, EGI-1 and luciferase-transfected clones

Median TFKluc2B2 doubling time (15.6h) was significantly faster than TFK-1 (43.4h; $p=0.0036$) but not significantly different compared to TFKluc1D1 (23.0h; $p=ns$) (Kruskal-Wallis test). Median doubling times of EGI-1 (31.0h) and EGIlucD2 (32.9h) did not show any significant difference ($p=ns$, Kolmogorov-Smirnov test).

The increase in viable cells over 72 hours was measured by MTT assay. Exponential growth equation was used to derive doubling time for each experiment. Median doubling time was determined using triplicate experiments. Graph shows median (solid horizontal line) and range (error bars).

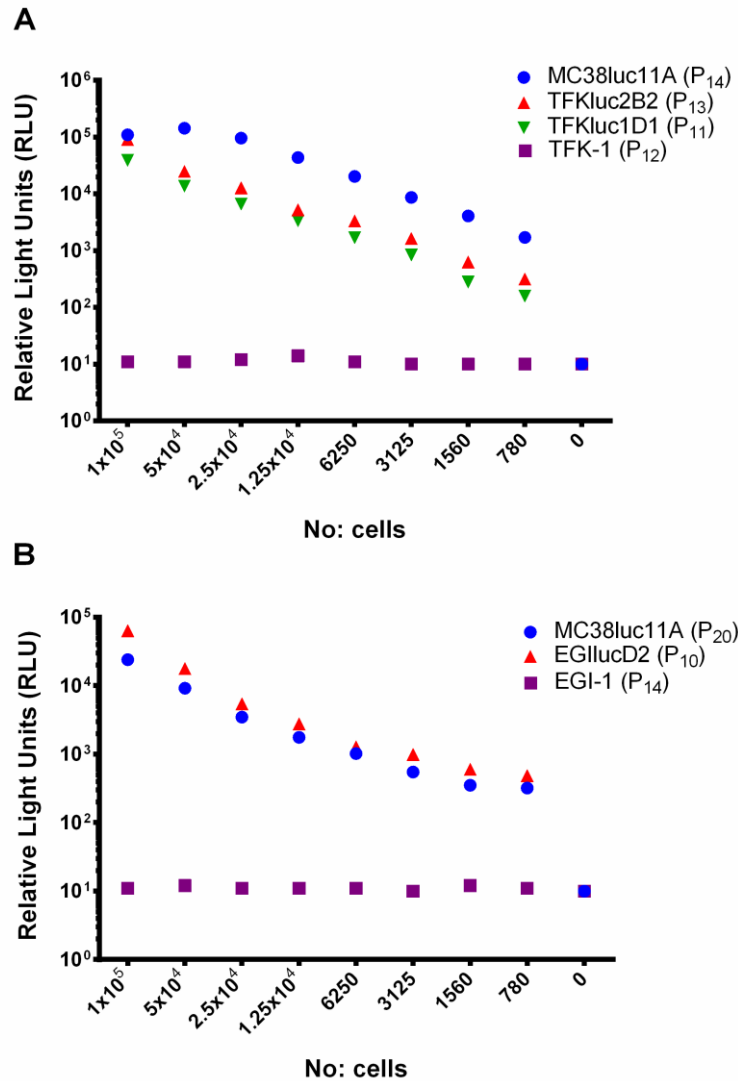


Figure 3-5 Comparison of luciferase activity of CCA cell lines with MC38luc11A

A. MC38luc11A (a high luciferase-expressing metastatic mouse colorectal carcinoma cell line), TFKluc1B2 and TFKluc1D1 were plated at decreasing seeding densities. After 24hrs, the luciferase assay system (Promega, UK) was used to measure the amount of light emitted. At comparable passage number and seeding density, MC38luc11A cells had higher luciferase activity compared to TKFluc2B2 and TFKluc1D1 clones.

B. In a separate experiment, MC38luc11A were compared with EGIlucD2. EGIlucD2 (passage 10) clone had higher luciferase activity compared to MC38luc11A (passage 20) at comparable seeding densities but lower passage number.

Each cell line or clone is shown in the graph legend with passage numbers shown in brackets. The values plotted are the means of n=3 replicates from a single experiment for each cell line. TFK-1 and EGI-1 cell lines included as controls.

Xenografts established from the TFK-1 and EGI-1 parent cell lines were monitored using mechanical calliper measurements, whereas for those established from luciferase-transfected clones (TFKluc2B2, TFKluc1D1 and EGIlucD2), bioluminescence imaging was performed in addition to mechanical calliper measurements.

3.1.3.1 Mechanical calliper tumour volume estimation

From day 10 post-injection, xenografts were measured twice weekly with mechanical callipers. Tumour volume was calculated as described in (**Section 2.4.1**) and plotted against time in days post-injection (**Figure 3-6**). Small tumours were visible by day 10 in all animals.

Two out of 3 TFKluc2B2 xenografts grew exponentially, reaching the maximum allowed tumour volume (according to UK Home Office regulations) of 1,500mm³ by day 16 and 20 (**Figure 3-6A** xenografts labelled A and B). One TFKluc2B2 xenograft, both TFKluc1D1 xenografts and the single TFK-1 xenograft followed a similar growth pattern, reaching a volume of <500mm³ by the final day of the experiment (day 28) (**Figure 3-6A** xenografts labelled C, D, E and F).

The three EGIlucD2 xenografts demonstrated some growth followed by a lag phase until day 20 (**Figure 3-6B** xenografts labelled J, K and L). Subsequently, three xenografts regressed and in one animal, there was no palpable xenograft on day 28 (**Figure 3-6B** xenograft labelled L). EGI-1 xenografts established successfully, reaching tumour volumes of 223, 663 and 709mm³ by day 28 (**Figure 3-6B** xenografts labelled G, H and I).

3.1.3.2 Bioluminescence imaging of xenograft tumours

Bioluminescence imaging of TFKluc2B2, TFKluc1D1 and EGIlucD2 xenografts (labelled A, B, C, J, K and L in **Figure 3-6A** and **Figure 3-6B**) was performed to determine

whether these xenografts were detectable by the IVIS imaging system. Representative images of TFKluc2B2 and TFKluc1D1 xenografts are shown in **Figure 3-7**.

As shown in **Figure 3-7 Panel 1**, xenografts A and C had detectable bioluminescence. The estimated tumour volumes of these xenografts on day of imaging using mechanical calliper measurements were 1,393 mm³ and 1,026mm³, respectively. Xenograft B which was much smaller (54mm³) appeared negative on this scale but demonstrated bioluminescence when imaged separately (**Figure 3-7 Panel 2**). The 2 TFKluc1D1 xenografts (E and D measuring 78 and 91mm³, respectively) shown in **Figure 3-7 Panel 3** demonstrated bioluminescence. However, compared to the TFKluc2B2 xenograft B (54mm³; radiance 5x10⁴ p/s/cm²/sr), the TFKluc1D1 xenograft of comparable tumour volume was less luminescent (78mm³; radiance 1.4 x10⁴ p/s/cm²/sr). Higher bioluminescence of TFKluc2B2 xenograft compared to TFKluc1D1 xenograft was in keeping with the *in vitro* findings for these two cell lines (**Figure 3-2**).

Longitudinal imaging of EGIlucD2, TFKluc2B2 and TFKluc1D1 xenografts was used to determine whether there was a relationship between xenograft volume and measured radiance. This was to ascertain if radiance could be used as a surrogate marker of tumour volume, as orthotopic liver tumours would not be measurable by mechanical callipers. A positive correlation between xenograft volume and radiance was observed in both EGIlucD2 xenografts (p=0.0001, Pearson correlation coefficient r = +0.829) as well as TFKluc2B2 and TFKluc1D1 xenografts. (p=0.011, Pearson correlation coefficient r = +0.787) as shown in **Figure 3-8A** and **B**. However, despite EGIlucD2 xenografts being significantly smaller (p=0.034, Mann-Whitney U test), they exhibited higher bioluminescence (p=0.015, Mann-Whitney U test) compared to TFKluc2B2 and TFKluc1D1.

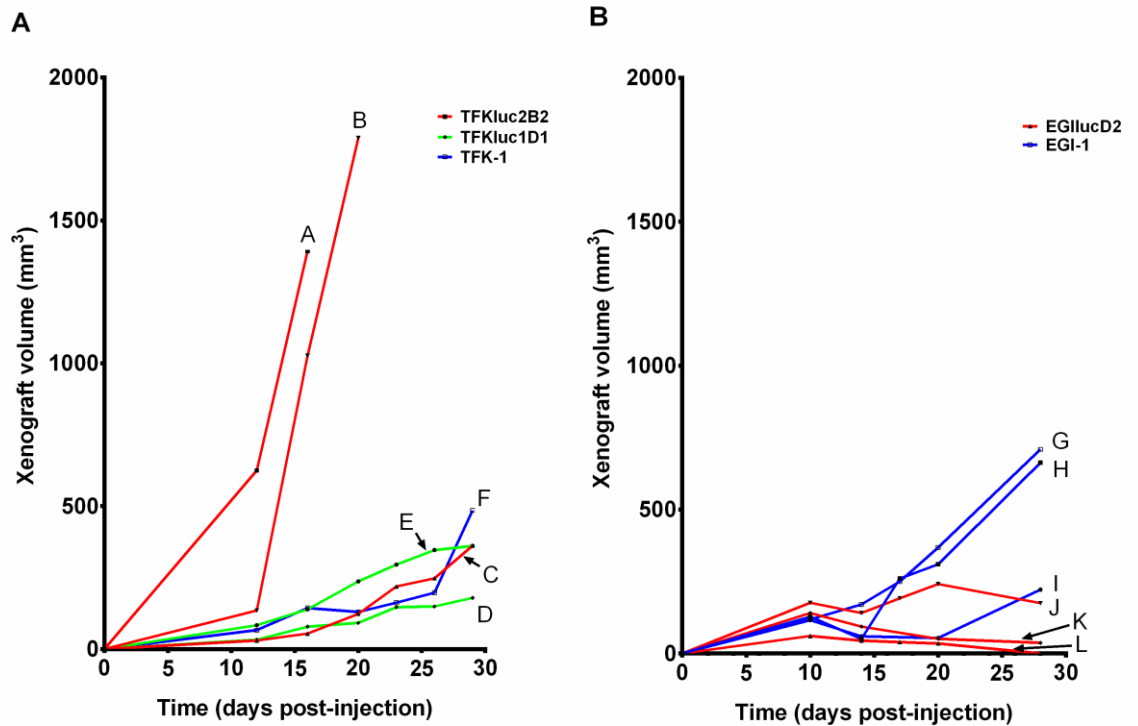


Figure 3-6 Xenograft growth curves

Graph **A** shows the xenograft volume over time of TFKluc2B2 (A, B and C), TFKluc1D1 (D and E) and TFK-1 (F) xenografts. Xenografts A and B grew exponentially and reached maximum tumour volume before the end of the experiment (day 28). Xenografts C, D and E had comparable growth rates to the parent cell line TFK-1 xenograft F.

Graph **B** shows the xenograft volume over time of EGI-1 (G, H and I) and EGI-lucD2 (J, K and L). Although xenografts J, K and L showed signs of initial growth, they regressed in size. The same pattern was not seen in xenografts G, H and I of the parent cell line EGI-1.

Each growth curve represents the growth of a single xenograft in an animal. 1×10^7 cells suspended in 100µL PBS was injected subcutaneously into the right hindquarters of CD1 nude female mice on day 0.

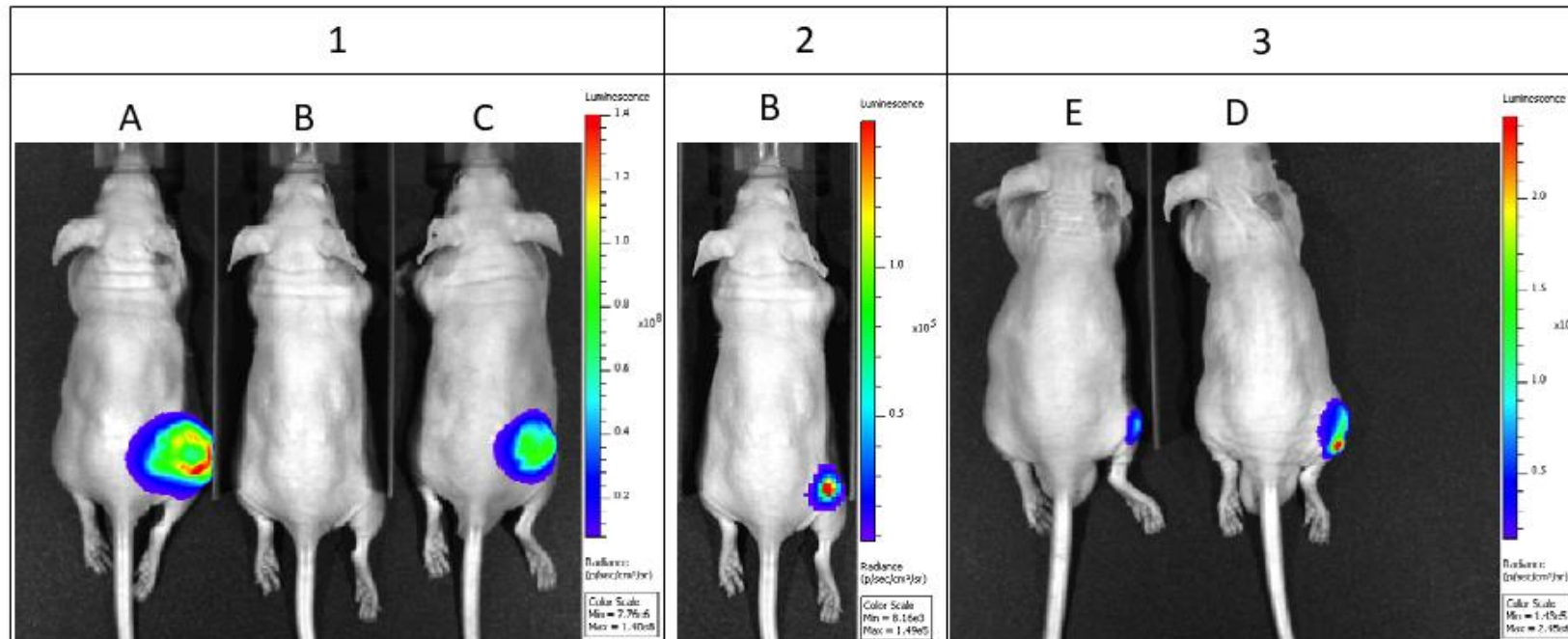


Figure 3-7 Bioluminescence imaging of TFKluc2B2 and TFKluc1D1 xenografts

Panel 1 shows all 3 TFKluc2B2 xenograft-bearing mice; A, B and C. The 2 large xenografts (measuring >1,000mm³) on day of imaging were highly luminescent. Xenograft B did not demonstrate visible bioluminescence on this scale. **Panel 2** shows the smaller TFKluc2B2 xenograft (B; measuring only 54mm³) which is visible on this scale, with luminescence several orders of magnitude lower (10⁵ compared to 10⁸) compared to the larger xenografts A and C shown in **Panel 1**. **Panel 3** shows the 2 TFKluc1D1 xenografts (E and D measuring 78 and 91mm³, respectively). The luminescent **scale** (in photons/second/square cm/steridan; p/s/cm²/sr) **is** shown to the right of each image. All xenografts included in figure obtained on day 16 post-injection.

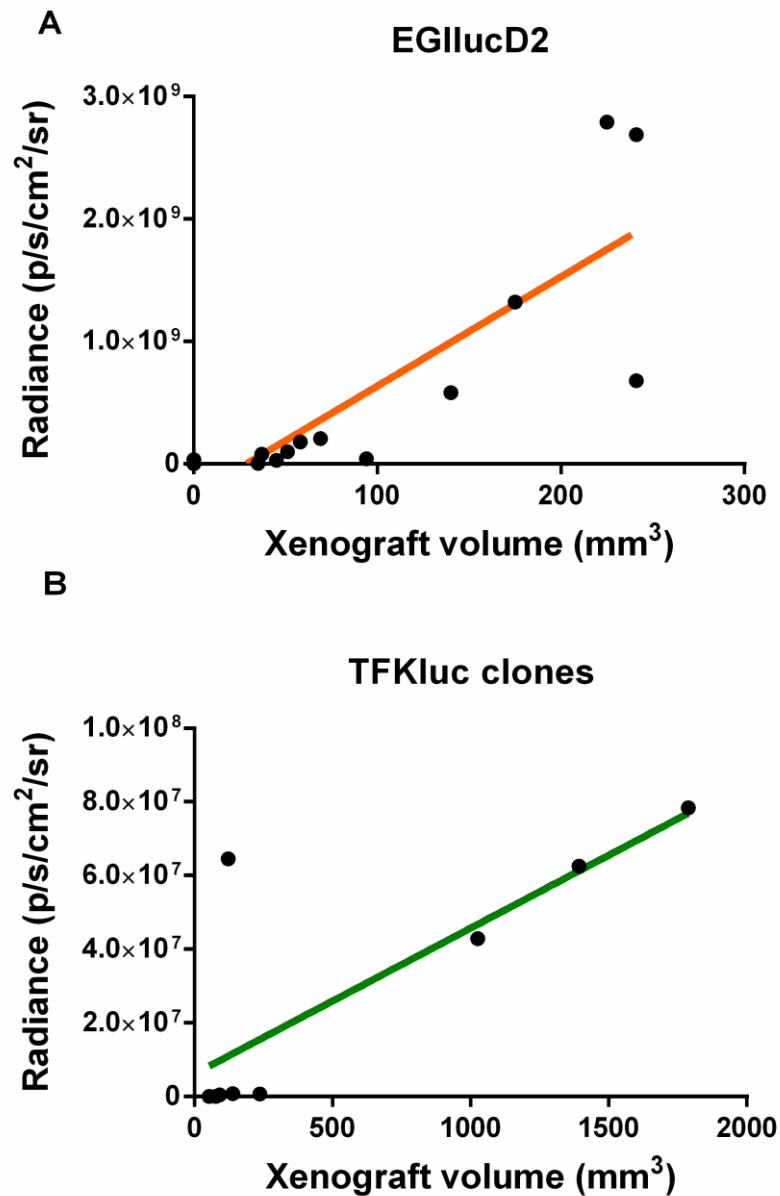


Figure 3-8 Correlation between xenograft volume and radiance

Tumour volumes determined using calliper measurements were compared to the measured tumour luminescence over time. This showed a positive correlation between tumour volume and radiance for EGIlucD2 xenografts, $r=0.904$; $p<0.0001$ (Graph A). Similarly, a positive correlation was seen between tumour volume and radiance of TKluc2B2 and TFKluc1D1 xenografts (included together as TFKluc clones), $r=0.800$; $p=0.014$ (Graph B).

Correlation determined using Spearman correlation coefficient. Linear regression used to draw line of best-fit.

IVIS imaging also established that the non-palpable EGIlucD2 xenograft (**Figure 3-6B** xenograft L) had metabolically active tumour cells. Such a xenograft would normally be regarded as completely regressed but the higher sensitivity of detection using bioluminescence imaging allowed the positive identification of active tumour cells.

3.2 Generation of an orthotopic CCA tumour model

Following the xenograft experiments with luciferase-transfected clones, TFKluc2B2 cell line was selected for the generation of the orthotopic CCA tumour model. The main characteristics of TFKluc2B2 that influenced this decision were that the cells established as xenograft tumours with no spontaneous regression (in contrast to EGIlucD2) and were detectable by bioluminescence imaging *in vivo*. TFKluc1D1 was not used as these xenografts were less luminescent compared to TFKluc2B2 xenografts at comparable xenograft volumes. TFKluc2B2 cells were used with the caveat that, compared to the parent cell line TKF-1, these clones had a significantly shorter doubling time (median 15.6h compared to 43.4h; **Figure 3-4A**).

A minimally invasive method of generating an orthotopic colorectal liver metastasis model has previously been described by Hawcroft *et al.* (2012). This method involved the HF-US guided injection of colorectal liver metastases cancer cells into the spleens of immunocompromised mice with subsequent single or multiple liver metastasis in all animals injected (Hawcroft *et al.*, 2012). Although specialist technical skill was required for the injection, this high take rate of tumours and the avoidance of major surgery in animals were significant advantages that could be applied for the generation of an orthotopic tumour model of CCA.

All procedures involving injection of tumour cells into the liver under HF-US were performed by a skilled operator (Dr Gemma Marston) and subsequent HF-US imaging was performed by trained operators (Dr G Marston, Dr N Ingram or Dr L E McVeigh).

As calliper measurements were not feasible for monitoring of tumour growth in orthotopic tumour models, bioluminescence and HFUS imaging were utilized.

3.2.1 Intra-cholecystic injection, no cystic duct ligation (Method 1)

This method was first attempted to generate a technically feasible and reproducible orthotopic model of CCA near the large bile ducts in a mouse liver. Three CD1 nude female mouse gallbladders were injected with 5×10^5 TFKluc2B2 cells suspended in 50 μ L of PBS under HF-US guidance. All animals were longitudinally monitored by twice weekly bioluminescence imaging and once weekly HF-US imaging.

Of the three animals, one (GB2) died unexpectedly on Day 18 but no macroscopic tumour was found on dissection. The cause of death could not be ascertained at necropsy and no evidence of jaundice or internal bleeding was seen.

Figure 3-9A shows average radiant efficiency of the three animals on serial bioluminescence imaging. Images were analysed on LivingImage software version 4.2 (PerkinElmer Inc, Massachusetts, USA) as described in **Section 2.4.2**. The average radiant efficiency measurements between the 2 tumours that established (GB1 and GB3) and the one that did not (GB2) were at least 2-3 orders of magnitude higher, suggesting that bioluminescent imaging could be used as a screening tool for identifying tumour growth. Based on this feasibility study, an average radiant efficiency greater than 5×10^6 p/s/cm²/sr should represent the presence of a tumour.

The macroscopic images of the tumours at endpoint in GB1 and GB3 animals are shown in **Figure 3-9B** and **Figure 3-9C**, respectively. GB1 showed an infiltrating tumour in the liver involving the gallbladder. GB3 revealed a subhepatic, intraperitoneal tumour adherent to small bowel and pancreas. This could have been the result of a mis-injection at the time of inoculation or seeding at these sites following passage of cells down the biliary system.

A further experiment was then carried out using the same method of HF-US guided injection. 10 CD1 nude female livers were inoculated with 5×10^5 TFKLuc2B2 cells in 50 μ L of PBS under HF-US guidance. They were monitored with bioluminescence imaging and HF-US imaging using the same protocol as the previous experiment. Only 2 developed tumours involving the liver and of these, one also had an intra-peritoneal tumour.

Figure 3-10 shows the serial bioluminescence imaging results for this cohort of animals. Only 1 animal (mouse no:5; **Figure 3-10**) had a recorded average radiant efficiency above the threshold (5×10^6 p/s/cm²/sr) determined by the preliminary experiment. This animal had a small orthotopic liver tumour. The maximum recorded average radiant efficiency for mouse 4 was 3.2×10^6 p/s/cm²/sr (**Figure 3-10**) and this animal too had a small orthotopic tumour although this was just below the predicted threshold. Due to the low success rate (2/10; 20%) of establishment of orthotopic liver tumours using this method, the technique was further refined.

3.2.2 Peri-cholecystic, intra-liver parenchymal injection (Method 2)

Due to the low success rate of method 1, several refinements were made to generate the Method 2 technique. BALB/c nude mice were used as they are a more inbred strain with less genetic variability compared to CD1 nude mice (Charlesriver, 2019). The number of cells inoculated in 50 μ L was increased to 5×10^6 from 5×10^5 cells. The injection site was changed to the liver parenchyma adjacent to gallbladder using the gallbladder as a sonographic landmark during injection.

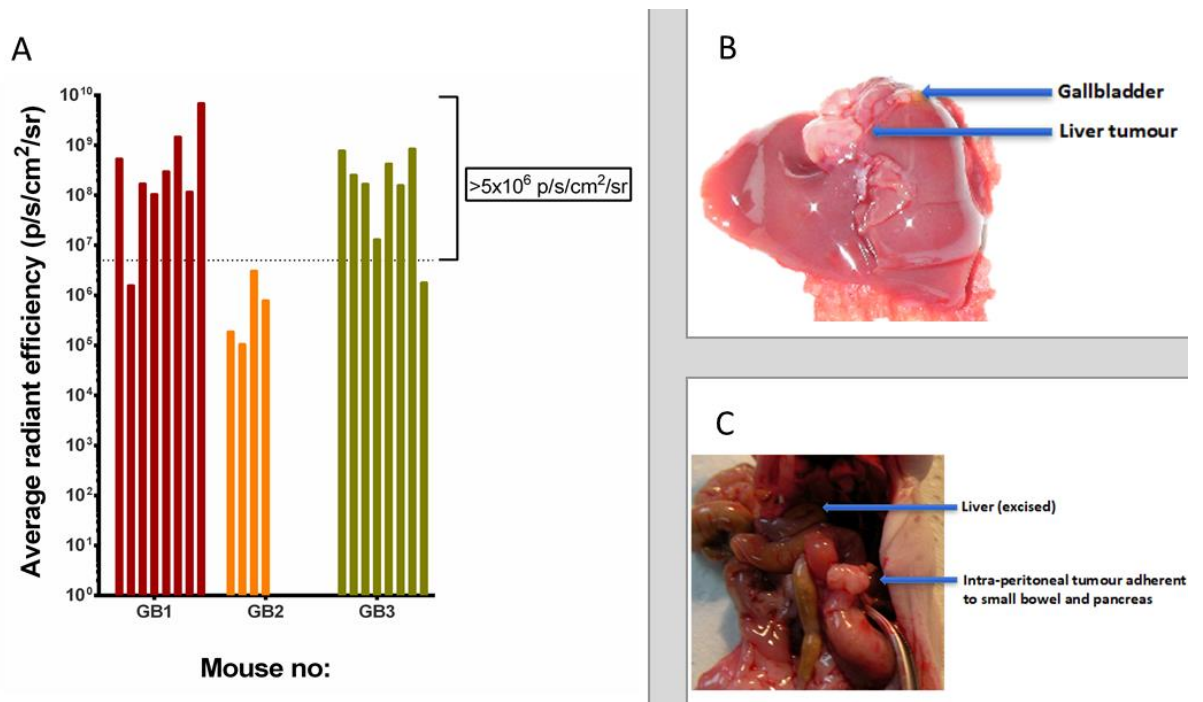


Figure 3-9 Preliminary study of orthotopic tumour model establishment using intra-cholecystic injection of TFKluc2B2 cells (Method 1)

Three CD1 nude female mice were injected with 5×10^5 TFKluc2B2 cells suspended in $50 \mu\text{L}$ PBS into the gall bladder (GB1, GB2 and GB3) and were imaged twice weekly on the IVIS Spectrum (PerkinElmer Inc, Massachusetts, USA). Imaging was performed 5 minutes following intra-peritoneal injection of D-luciferin. A standardized region of interest (ROI) over the abdomen of each animal was used to measure the average radiant efficiency. Each bar represents an imaging session.

A shows average radiant efficiency measured in each mouse during serial bioluminescence imaging. GB2 mouse unexpectedly died on day 18 but had no macroscopically-visible tumour upon dissection. GB1 had tumour involving liver. GB3 had an intra-peritoneal tumour adherent to small bowel and pancreas. Using these preliminary results, a threshold of 5×10^6 p/s/cm²/sr was set as the cut-off for identification of macroscopic tumour.

B shows GB1 showed tumour growth in liver with involvement of the gallbladder (denoted by arrows).

C shows GB3 had growth of an intra-peritoneal tumour with no liver involvement.

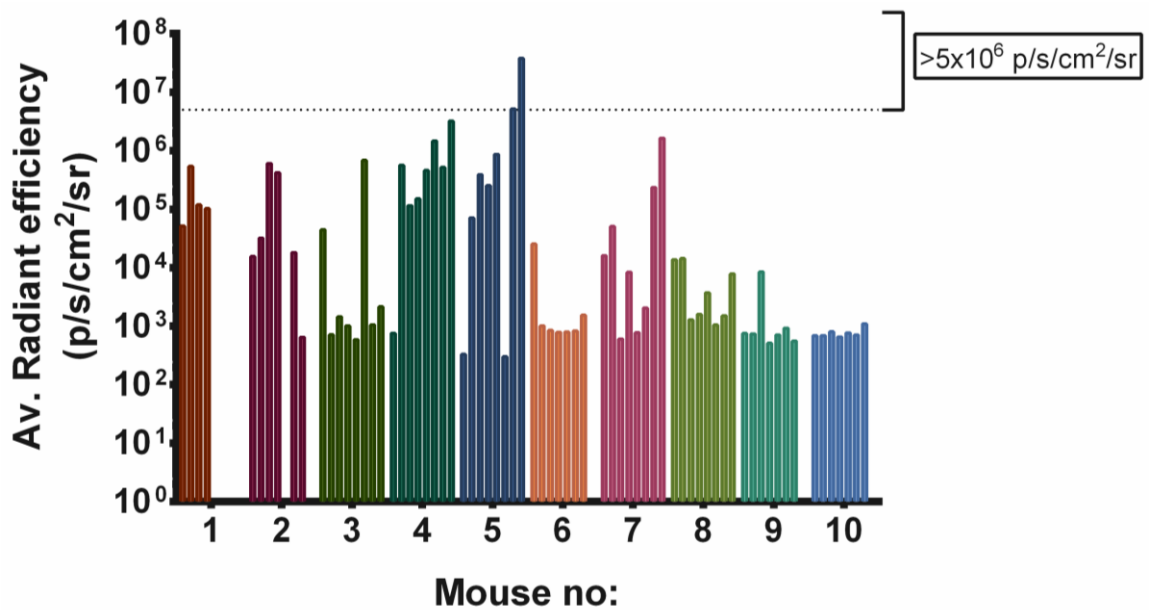


Figure 3-10 Longitudinal bioluminescence imaging of animals following intra-cholecystic injection of TFKluc2B2 cells (Method 1).

Ten CD1 nude female mice were injected with 5×10^5 TFKluc2B2 cells suspended in $50 \mu\text{L}$ PBS into the gall bladder and were imaged twice weekly on the IVIS Spectrum (PerkinElmer Inc, Massachusetts, USA). Imaging was performed 5 minutes following intra-peritoneal injection of D-luciferin. A standardized region of interest (ROI) over the abdomen of each animal was used to measure the average radiant efficiency.

Each bar represents the average radiant efficiency for an individual mouse at each imaging session. Mouse 1 (sacrificed on Day 15) had a small intraperitoneal tumour. Mouse 4 and 5 had macroscopic tumour involving the liver. The average radiant efficiency threshold determined by the preliminary experiment (5×10^6 p/s/cm²/sr; **Figure 3-9A**) for the identification of macroscopic tumour is denoted by the horizontal dotted line. This identified the successfully established orthotopic tumour in mouse 5. Mouse 4 had a final measurement of 3.2×10^6 p/s/cm²/sr which was just below the threshold. The other 7 animals (2, 3, 6, 7, 8, 9 and 10) did not have a macroscopic liver or intraperitoneal tumour on day of sacrifice (day 35).

10 BALB/c nude female mice were injected using this method and of these, 9 developed liver tumours. **Figure 3-11** shows the first four bioluminescence imaging timepoints for this cohort of animals with the radiant efficiency scale minimum set to 1×10^7 p/s/cm²/sr (i.e. above the cut-off where successful tumour establishment was expected). Two animals also developed a subcutaneous tumour at the injection site, one of which also had an intra-peritoneal tumour. On HF-US, median tumour volume was 21.23mm³ (Range 8.96 -32.48 mm³; n=6 measurements. n=2 had no HF-US images, n=1 – tumour too small for tumour volume measurement).

This method yielded a 90% (9/10) success rate inducing liver tumours without any demonstrable distant metastatic disease burden. The two subcutaneous tumours at injection site and the intra-peritoneal tumour were likely due to seeding during injection rather than metastatic spread.

Viability of tumour cells was determined by longitudinal bioluminescence imaging. Of the 8 animals that underwent HF-US prior to sacrifice, 7 tumours were positively identified and an animal with a negative signal by bioluminescence imaging was confirmed to have no demonstrable tumour on HF-US. **Figure 3-12A** shows the liver HF-US image of mouse no:19 (shown in **Figure 3-11**). This showed a liver tumour with estimated tumour volume of 32.48mm³. Bioluminescence imaging (**Figure 3-12B**) and gross pathology (**Figure 3-12C**) confirmed the successful establishment of an orthotopic tumour.

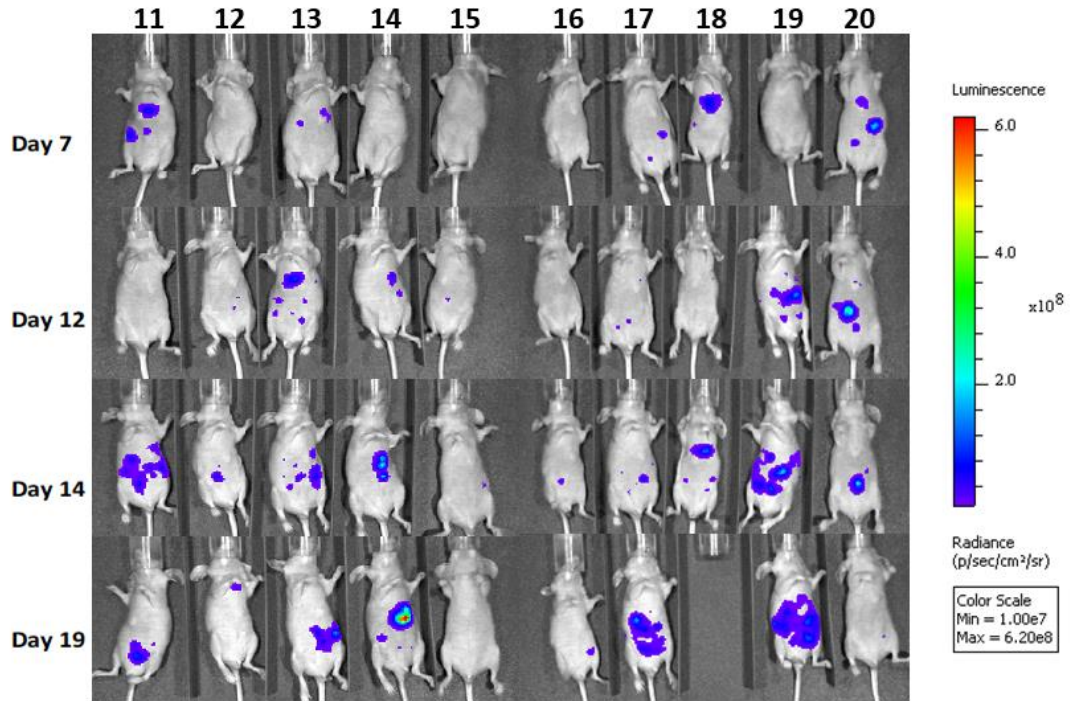


Figure 3-11 Longitudinal bioluminescence imaging of animals following peri-cholecystic injection of TFKluc2B2 cells (Method 2).

Images showing longitudinal bioluminescence imaging on days 7, 12, 14 and 19 of 10 BALB/c nude female mice injected with 5×10^6 TFKluc2B2 cells. The cells were suspended in $50 \mu\text{L}$ PBS and injected into the liver parenchyma near the gallbladder (peri-cholecystic, intra-liver parenchymal injection). The scale bar shows the standardized radiance across imaging sessions above the threshold expected for identification of liver tumours (range $1.0 \times 10^7 - 6.2 \times 10^8$). Each column represents the same animal. Each row represents an imaging session.

The animal shown in column 15 did not show any significant bioluminescence signal during longitudinal imaging sessions. It also had no demonstrable tumour by HF-US or post-sacrifice necropsy. Mice shown in columns 12, 16 and 20 had comparatively low signal which corresponded to smaller liver tumours. All other animals displayed strong bioluminescence signals and easily demonstrable liver tumours confirmed on gross pathology following sacrifice. Mouse 18 displayed abnormal behaviour and was sacrificed on day 16. A liver tumour was confirmed on gross pathology.

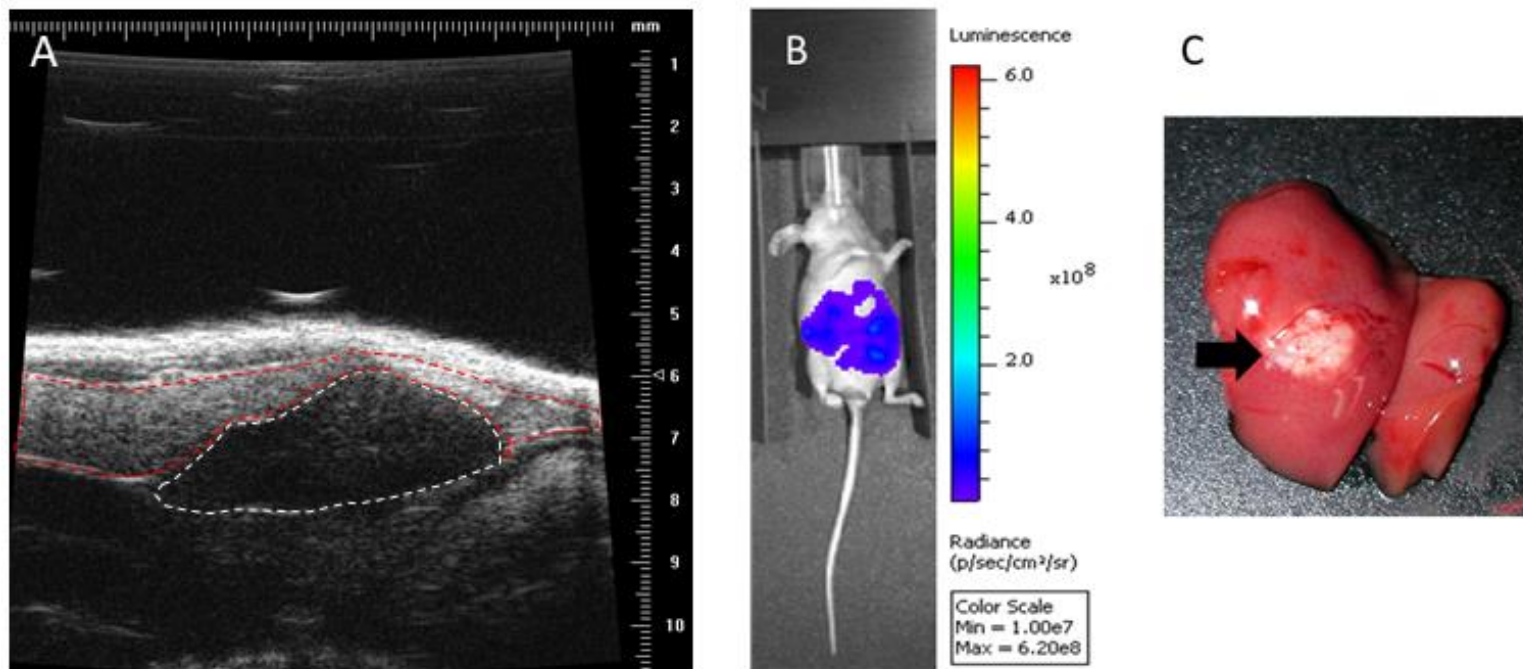


Figure 3-12 Comparison of *in vivo* HF-US and bioluminescence imaging with macroscopic orthotopic tumour appearance

A. HF-US image of the liver of mouse no: 19 (shown in **Figure 3-11**) obtained on day 19 post-injection of TFKluc2B2 cells into the liver parenchyma adjacent to the gallbladder. This confirmed the presence of a liver tumour. The hypoechoic region of tumour (white dotted line) was distinctly different in echogenicity from normal liver (red dotted line). **B.** Bioluminescence imaging of the same animal on day 19 showing light emission from viable tumour cells in the abdominal region. **C.** *Ex-vivo* macroscopic image of the liver showing same liver tumour on day of sacrifice (day 27) (black arrow).

3.3 Histopathology of murine tumours

In order to compare the xenograft model and the orthotopic model of CCA tumours, FFPE tissues of the TFKluc2B2 xenografts and orthotopic tumours were subjected to H&E staining.

3.3.1 Xenograft

H&E sections of xenograft tumours established from TFKluc2B2 cell line (described in **Figure 3-6**) showed sheets of tumour cells with occasional inflammatory cells and blood vessels (**Figure 3-13A and B**). The larger tumours had necrotic cores, but no areas of haemorrhage were observed. A pseudo-capsule was observed comprising of tumour cells and surrounding connective tissue. The larger tumours also frequently invaded into adipose tissue and muscle of the animal hindquarter and back (**Figure 3-13B**).

3.3.2 Orthotopic model

H&E sections from orthotopic tumours established from TFKluc2B2 cells appeared distinctly different to the subcutaneous xenograft tumours of the same cell line. Tumour cells infiltrating into the liver were seen (**Figure 3-13C**). The tumour core appeared much more vascular compared to their xenograft counterparts. Overall the appearances of the orthotopic tumour was that of a poorly differentiated adenocarcinoma characterised by highly atypical cells displaying nuclear pleomorphism with no discernible glandular features which are usually seen in well- to moderately-differentiated tumours. Areas of tumour stroma were much more prominent in orthotopic tumours (**Figure 3-13D**). This type of desmoplastic reaction is a feature of CCA. The macroscopic appearance of orthotopic tumours are shown in **Figure 3-14A**.

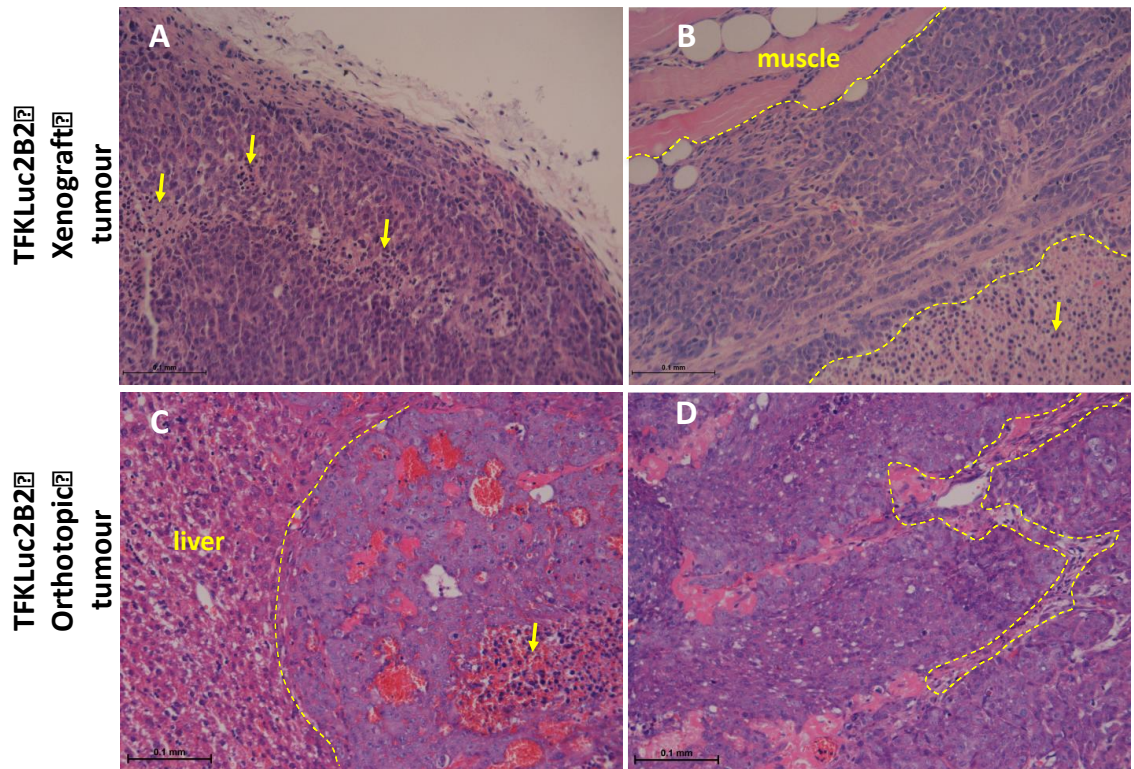


Figure 3-13 Histology of a TFKluc2B2 xenograft compared to TFKluc2B2 orthotopic tumour.

Representative images from H&E stained sections of TFKluc2B2 xenograft and orthotopic tumour tissue. Scale bar 0.1mm, except **D** (Scale bar 0.5mm)

A shows the typical appearance of a TFKluc2B2 subcutaneous xenograft showing areas of inflammatory infiltrate (arrows). A pseudo-capsule of tumour cells is seen on the tumour margin on the image superiorly. The tumour cells appear moderately-well differentiated. **B** shows a TFKluc2B2 xenograft invading into surrounding skeletal muscle tissue in the right flank of the animal. Inferiorly, a large area of inflammatory infiltrate and necrosis is seen (demarcated by dotted line and arrow).

In contrast, **C** shows a TFKluc2B2 orthotopic tumour invading into liver parenchyma which is typical of infiltrating or mass-forming types of cholangiocarcinoma. The tumour appears much more vascular (with obvious larger vessels within the tumour compared to xenograft tumours) and has the appearances of a poorly-differentiated adenocarcinoma. **D** shows areas of tumour stroma (area within dotted line) that are more prominent within the orthotopic tumours compared to xenograft tumours.

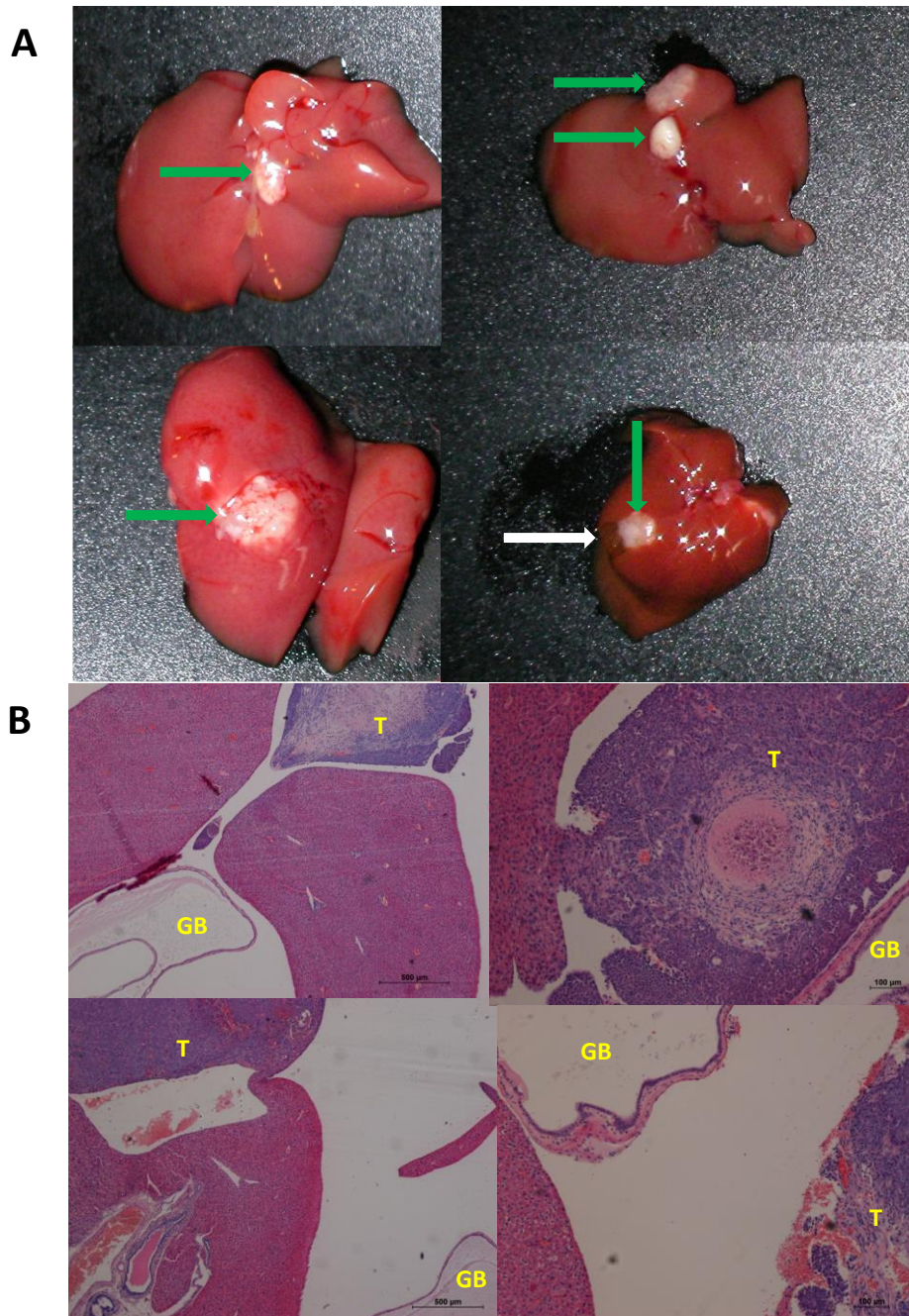


Figure 3-14 Representative images of four orthotopic tumours by macroscopic imaging (A) and histology (B)

Panel **A** shows 4 representative orthotopic liver tumours (green arrows). The white arrow on the bottom right image shows the gallbladder and demonstrates the proximity of the tumour to the gallbladder which was used as a landmark for injection under HF-US guidance.

Panel **B** shows 4 representative H&E stained paraffin-embedded 5µm sections of orthotopic tumours; images on the left of Panel **B** taken at x10 magnification and right at x20 magnification. Tumour (T) seen within 2mm of the Gallbladder (GB)

Where possible, the proximity of tumour to the gall bladder was identified on FFPE-sections of tumour as a surrogate marker of accuracy of initial injection site. This was not always possible as the delicate gall bladder was not always preserved intact after the fixation and embedding process to be accurately identified on histology. However, in these four cases, gall bladder was observed within 2mm of the tumour mass indicating that injections were relatively close (**Figure 3-14 B**).

3.4 Discussion

This chapter describes the development of a novel orthotopic CCA model from the *in vitro* lentiviral transfection of EH-CCA cells to express luciferase, through to the establishment, longitudinal bioluminescence imaging and histopathological examination of orthotopic CCA tumours.

3.4.1. Bioluminescence imaging for tumour models

Bioluminescence imaging is a form of optical imaging that has multiple pre-clinical applications, including *in vivo* tumour growth assessment in cancer research (Sadikot and Blackwell, 2005). Firefly luciferase gene is the most commonly utilized reporter for bioluminescence imaging and multiple pre-clinical tumour models of different cancer cell types have been developed (Sadikot and Blackwell, 2005; Hawcroft *et al.*, 2012; Ritelli *et al.*, 2015; Jones *et al.*, 2017). As the orthotopic model described in the present study utilises bioluminescence imaging, the advantages and disadvantages of this imaging modality are discussed in detail.

3.4.1.1. Advantages

Bioluminescence imaging has several advantages for *in vivo* imaging including the low intrinsic bioluminescence of tissues as well as low absorption and scattering of emitted light in small animals which allow detection by *in vivo* imaging systems

(Sadikot and Blackwell, 2005; de Almeida *et al.*, 2011). The high sensitivity of detection of light emitted from tumour cells was demonstrated when this was quantified for luciferase expressing clones in the present study (**Figure 3-5**). In addition, the non-palpable EGIIucD2 xenograft tumour displayed a detectable bioluminescence signal suggesting active tumour cells in a xenograft that would have otherwise been assumed to have completely regressed (**Section 3.1.3.2**). In an orthotopic model however, bioluminescence signal attenuation by overlying tissues would reduce the number of photons reaching the detector and therefore the limit of detection of viable cancer cells would be expected to be lower. Hence, it was important to select a clone with high luciferase-activity for the generation of the orthotopic tumour model.

The speed and ease of image acquisition of bioluminescence imaging as well as the minimal post-acquisition reconstruction and processing required for analysis, facilitated the high-throughput screening of these orthotopic tumour models. Acquisition times for bioluminescence imaging in this series of *in vivo* experiments were less than 30s per image and the imaging system allowed up to 5 animals to be imaged at once. The total anaesthetic time for animals was less than 10min per imaging session including the injection of D-luciferin which was required 5min prior to image acquisition. This enabled quick recovery of animals following the short anaesthetic and significantly reduced the imaging costs, both of which are advantageous for the planning of large-scale animal experiments.

3.4.1.2. Disadvantages

The level of resolution achieved is a disadvantage of bioluminescence imaging. Although organ level resolution *in vivo* is expected (Sadikot and Blackwell, 2005), in practice, this is challenging especially for abdominal imaging. For example, most of the animals shown in **Figure 3-11** had liver tumours (except two animals with subcutaneous tumours at injection site, one of which also had a peritoneal tumour) but

the light emission was not specific to the region of the liver. Although it is possible that this may have been due to microscopic intra-abdominal metastatic disease, it is more likely to be due to the scattering of photons emitted from the liver due to the surrounding tissues.

The quantitation of light emission showed variability during the imaging sessions over the course of the experiment and there was no predictable relationship between the serial measurements of light emission and time from injection of tumour cells (**Figure 3-9A, Figure 3-10, Figure 3-11**). Hence, bioluminescence imaging was only useful to ascertain a threshold average radiant efficiency which could predict the likelihood of a successfully established tumour.

None of the experiments described in this chapter investigated the tumour growth beyond day 35 from injection. The pattern of growth beyond this time period would be interesting as it may display an exponential growth phase of growth with locally advanced disease and possibly metastatic spread. These potential extra-abdominal metastatic sites could be identified by *in vivo* bioluminescence imaging.

Bioluminescence imaging for tumour growth and monitoring requires genetically modified, luciferase-expressing cells. Alteration in growth characteristics is one of the limitations of the transfection process used in the present study as the insertion point of the plasmid carried by the lentivirus is unpredictable. Investigation of the growth characteristics of TFKluc2B2 showed that it grew significantly faster compared to TFK-1 (15.6h vs 43.4h) (**Figure 3-4**). The reported doubling time of the parent cell line TFK-1 is 37h (Saijyo *et al.*, 1995). This difference in growth rate may have affected the luciferase screening assay result, emerging as brightest clone because this clone would have doubled prior to the assay being performed at 24h. In addition, TFKluc2B2 cells were less adherent to tissue culture plastic. As strongly adherent cells display less migratory behaviour (Fuhrmann *et al.*, 2017), this clone may have increased

metastatic potential compared to the parent cell line, TFK-1, from which it was derived. Thus, genetic modification of this cell line may have altered some cellular functions, the exact nature of which would be difficult to ascertain. The more these cells are altered, the less they resemble the tumour of origin which is a drawback as they may not be a good model of the disease of interest.

The other EH-CCA cell line used for the generation of luciferase-transfected CCA cells was EGI-1. Although this cell line did give rise to bioluminescent clones (**Figure 3-2B**), they did not establish successful xenografts (**Figure 3-6B**). This may also be due to an altered growth characteristic, potentially either favouring apoptosis or more vulnerability to the murine immune system, despite it being immunocompromised.

Another disadvantage of the CCA model described in this study is the requirement of an immunocompromised host for the successful growth of the bioluminescent cell line. Therefore, the utilisation of this model to investigate immunotherapies is not possible. To overcome this, a syngeneic mouse model of CCA could be derived and transfected to express luciferase prior to being implanted into an immunocompetent animal as an allograft. This may provide a good model for the investigation of targeted therapies as well as immunotherapies. However, this model is likely to be very time-consuming and expensive to establish.

Although the present model utilised the immortalised EH-CCA cell line TFK-1 to generate the luciferase-transfected cell line TFKluc2B2, luciferase-expressing patient-derived xenograft (PDX) models have been described for other cancers (Jones *et al.*, 2017). Using primary cells, Jones *et al.* (2017) were able to achieve stably transfected, luciferase-expressing cells to develop a PDX model of acute lymphoblastic leukaemia. Although PDX models of CCA have been successfully established (Cavalloni *et al.*, 2016; Garcia *et al.*, 2018) there are no reported luciferase-expressing CCA PDX models in the current literature.

3.4.2. Orthotopic tumour models of cholangiocarcinoma

In this chapter, two methods of orthotopic tumour establishment using a minimally invasive technique were investigated. A recent review by Erice *et al.* (2019) highlighted the complexity of CCA and the lack of an ideal model. The same authors and others have highlighted that the majority of existing models are those of IH-CCA with fewer EH-CCA models having been developed (Cadamuro *et al.*, 2018; Erice *et al.*, 2019; Loeuillard *et al.*, 2019).

In the present study, the success rate of establishing orthotopic CCA tumours using an EH-CCA cell line was higher with Method 2 (peri-cholecystic, intra-liver parenchymal injection under HF-US guidance; **Section 3.2.2**). Gross pathology and histology of these orthotopic tumours were examined to ascertain tumour proximity to the gallbladder. As described in **Section 3.3.2**, tumour tissue was noted within 2mm of the gall bladder which is an encouraging surrogate marker of accuracy of initial injection site and highlights the reproducible nature of this technique.

Histopathological examination of the orthotopic tumours highlighted the differences (as shown in **Figure 3-13**) compared to a subcutaneous xenograft using the same cell line (TFKluc2B2). The orthotopic tumours infiltrated into the liver, appeared more vascular with abundant stroma (**Section 3.3.2**). In a review, Cadamuro *et al.* (2018) highlighted that an orthotopic CCA tumour model better replicated the tumour microenvironment than the subcutaneous xenograft model. The authors had previously described abundant stroma of mouse origin in their orthotopic tumour which displayed areas of desmoplasia which is a hallmark of CCA (Cadamuro *et al.*, 2013). However, the method of injection involved a mini-laparotomy and surgical exteriorization of the spleen with direct injection of EGI-1 or TFK-1 cells into the spleen (Cadamuro *et al.*, 2013) compared to the minimally-invasive method of

injection (injection under HF-US guidance, thus avoiding surgery) described in this chapter (**Sections 3.2.1 and 3.2.2**).

3.4.3. Summary

The development of this orthotopic CCA model along with an orthotopic colorectal cancer liver metastasis model has now been published (McVeigh *et al.*, 2019). The use of minimally invasive techniques i.e. HF-US guided-injection of cells, have the advantages of reducing animal suffering and speeding up the process of establishment which will in turn enable large cohorts of orthotopic models to be set up. The realisation of this technique requires some technical expertise, but as yet, the standard practice still involves surgical injection (Magistri *et al.*, 2019).

This tumour model, although not ideal, could be used along with others for the assessment and validation of different CCA treatments, existing or novel. A more accurate CCA tumour model in this era of personalised medicine would be to establish orthotopic tumours from individual patient-derived CCA tissue, implanted into an immunocompromised animal liver followed by testing of the efficacy of targeted treatments prior to administration into the same patient. This hypothetical concept would be time-consuming, cost-prohibitive and often not practical for CCA patients and health professionals in a health service where the prognosis is poor and resources are finite.

Chapter 4

Identification of potential theranostic biomarkers in cholangiocarcinoma using a systematic review approach

Introduction

Over the last decade, significant advances have been made in the field of nanomedicine and its potential applications for the diagnosis and treatment of human diseases (Chen *et al.*, 2014; Chen *et al.*, 2016b; Pelaz *et al.*, 2017). Concomitant use of nanoscale particles for diagnostic and therapeutic applications, termed theranosis, have been evaluated in malignant and non-malignant conditions (Kelloff *et al.*, 2005; Wu *et al.*, 2013b; Kodiha *et al.*, 2015; Wu and Zhou, 2015b).

Active tumour targeting by nanoparticles that have been surface functionalized can potentially increase the specificity of nanoparticle-based therapy (Sun *et al.*, 2014a). At the University of Leeds, nanoparticles have been designed for *in vivo* fluorescent imaging as well as optoacoustic imaging in pre-clinical models of colorectal cancer. (Tiernan *et al.*, 2015; Ye *et al.*, 2015). Microscale particles such as microbubbles on the other hand, being several microns in size remain in the vascular space and can be engineered to target tumour vascular endothelium (Foygel *et al.*, 2013). Mechanisms for improving drug delivery using targeted, drug-loaded microbubbles have been further explored with promising results (McLaughlan *et al.*, 2013).

A recent systematic review on the application of active targeting nanoparticle delivery systems in cancer therapy did not show any pre-clinical studies in CCA (Muhamad *et al.*, 2018). This reflects the general scarcity of research efforts into novel therapeutics for this rare cancer. Active targeting relies on a 'target' or biomarker that is upregulated in tumour tissue compared to normal tissues to increase tumour specificity of the nanoparticle delivery system and reduce off-site toxicity (Patra *et al.*, 2010). As discussed in **Section 1.3**, a theranostic biomarker would form an integral part of a theranostic nanoparticle delivery system.

The aim of this chapter was to systematically interrogate the literature for published biomarker studies in CCA for the purpose of identifying validated biomarkers for *in vivo* testing of active tumour targeting as part of a theranostic delivery platform.

4.1 Systematic search for theranostic biomarkers in CCA

4.1.1 Included and excluded studies

The search strategy defined in **Section 2.5** identified 4,560 studies published between January 1996 and September 2019 on Medline and Embase databases. Stage 1 of the screening process involved title and abstract screen of these studies. 3,859 studies did not meet inclusion/exclusion criteria defined in **Sections 2.5.1** and **2.5.2**.

701 studies which included 1,190 biomarkers were selected for full text review in stage 2 of the screening process. This involved evaluating each reported biomarker against the inclusion/exclusion criteria as well as scrutiny of the human protein atlas annotated protein expression data for normal tissue expression of each biomarker (Human Protein Atlas, 2019c). 1,024 biomarkers were excluded for not meeting inclusion/exclusion criteria and the main reason for exclusion was the high expression of the biomarker in normal tissues.

From these studies, 166 candidate biomarkers that met the inclusion/exclusion criteria were identified and included in the data extraction table (***Appendix 1 Data extraction table***). In cases where no annotated protein expression data was reported in the human protein atlas, tissue expression data of biomarker(s) were extracted unless the study reported high expression in normal tissues. Once replicate biomarkers were excluded, 83 different biomarkers were identified of which only 47 had annotated protein expression data reported in the Human Protein Atlas. Of these 47 biomarkers, 16 were evaluated in two or more biomarker validation studies and

therefore selected for further interrogation. These 16 biomarkers included angiopoietin 1 (ANGPT1), angiopoietin 2 (ANGPT2), carbonic anhydrase 9 (CA9), cadherin 17 (CDH17), caudal type homeobox 2 (CDX2), Claudin 18 (CLDN18), epidermal growth factor receptor (EGFR), matrix metalloproteinase 7 (MMP7), matrix metalloproteinase 9 (MMP9), alpha-1 antitrypsin (SERPINA1), secreted frizzled related protein 1 (SFRP1), solute carrier family 2 member 1 (SLC2A1), trefoil factor 1 (TFF1), transforming growth factor beta-1 (TGFB1), tenascin C (TNC) and p53 (TP53).

4.1.2 Gene ontology of selected candidate biomarkers

Figure 4-1 shows the PANTHER GO-Slim (Mi *et al.*, 2019a) classification of the 16 genes coding for the selected proteins into the three gene ontology domains; molecular function, cellular component and biological process.

Figure 4-1A categorises the molecular function of the product of these genes. 12/16 are involved in binding such as protein binding, chromatin binding, heterocyclic compound binding or ion binding. 4/16 have catalytic activity either hydrolase (MMP9, MMP7, SERPINA1) or transferase (EGFR). Others such as SERPINA1 and TGFB1 are molecular function regulators.

In terms of cellular compartment of expression, the majority of gene products in the gene set are expressed in the extracellular region (**Figure 4-1B**). EGFR, CDH17, SFRP1 and CLDN18 are expressed in the plasma membrane. TP53 and CDX2 are transcription factors and are expressed in the nucleus.

12/16 are involved in cellular processes (**Figure 4-1C**) such as SERPINA1 and TGFB1 in cellular macromolecule metabolic processes, MMP9 and MMP7 in cellular component organisation, ANGPT1, ANGPT2, EGFR and TP53 in signal transduction.

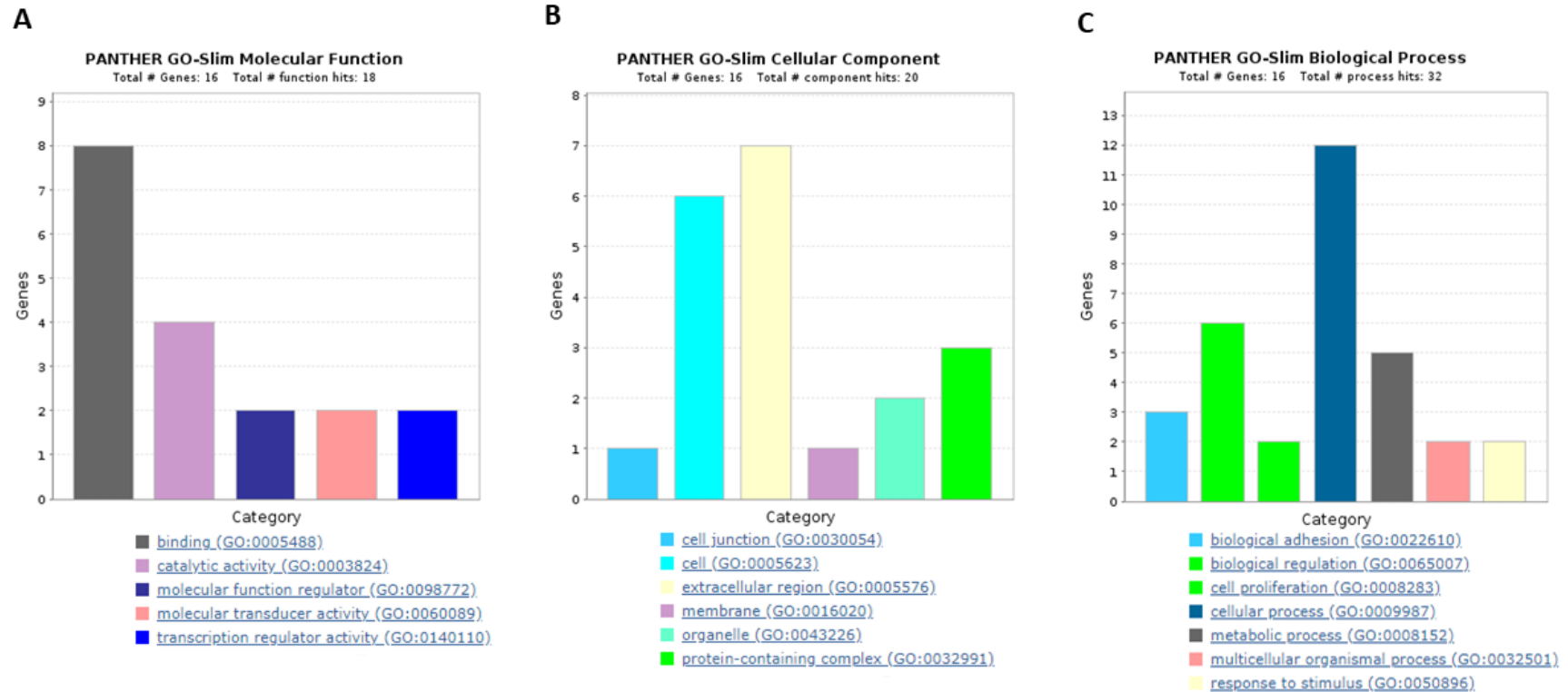


Figure 4-1 PANTHER classification of selected genes

PANTHER gene ontology classification of 16 selected genes based on (A) molecular function, (B) cellular component of expression and (C) involvement in biological processes. Large-scale gene function analysis protocol for PANTHER Version 14 classification system (Mi *et al.*, 2019b) used for this analysis (Mi *et al.*, 2019a).

The PANTHER Version 14 Go-Slim categorisation (Mi *et al.*, 2019a) which is a curated form of the entire gene ontology database did not include CA9, SLC2A1 and TNC. These were interrogated from the PANTHER complete gene ontology database. In summary, CA9 has carbonate dehydratase activity, is involved in bicarbonate transport and has membrane localisation. *SLC2A1* gene codes for GLUT1, which is a transmembrane glucose transporter involved in response to hypoxia and has a membrane localisation. TNC is an extracellular matrix structural protein that negatively regulates cell adhesion and is involved in extracellular matrix organisation.

4.1.3 Selection of biomarkers for theranosis

A scoring system for the selection of potential targetable biomarkers for imaging in colorectal cancer (TASC score) has been reported by van Oosten *et al.* (2011). However, there are no published scoring tools for the selection of theranostic biomarkers which despite overlap with imaging biomarker characteristics, have the additional requirement of very low or absent expression in normal tissues. A theranostic biomarker scoring system, which is a modified version of the TASC score (van Oosten *et al.*, 2011) named TASC-theranosis score (TASC-T) was therefore developed.

The 16 selected candidate biomarkers were evaluated using TASC-T scoring criteria as shown in **Table 4-1**. Briefly, points of different weighting were awarded to each biomarker for the following criteria; extracellular location, >20% positivity in tumour tissue, tumour to normal tissue expression ratio >10, reported percentage positivity or high expression, previous application as imaging or theranostic biomarker either in pre-clinical or clinical studies and if a targeting antibody (or antibody-mimetic ligand) for the biomarker was available for clinical use. All selected biomarkers scored 4 points as >20% positive expression was a selection criterion. Maximum score was 22. Biomarkers were considered to have theranostic potential if they scored 17 or higher. This arbitrary cut-off score was analogous to that used by van Oosten *et al.* (2011).

Table 4-1 Potential biomarkers for theranosis: (TASC-T) scoring criteria

	Parameter	Score
1	Extracellular or membrane localisation of biomarker	5
2	>20% positivity in tumour tissue	4
3	Tumour to normal tissue ratio >10	3
4	Percentage positivity or high expression in tumour tissue	
	>90%	6
	70-90%	5
	50-69%	3
	<49%	0
5	Previous application to imaging	
	Preclinical	1
	Clinical	2
6	Targeting ligand in human trials	1
	TOTAL	22

This cut-off allowed the higher scoring biomarkers with the greatest predicted theranostic potential to be evaluated in more detail.

Table 4-2 shows the TASC-T scoring for the 16 selected candidate biomarkers. A score of 17 or higher was awarded to MMP9, CLDN18, TNC, CA9 and EGFR.

The STRING database (Szklarczyk *et al.*, 2019) was used to ascertain any protein-protein interactions between the top 5 selected proteins as shown in **Figure 4-2**. This revealed associations between MMP9, CA9 and EGFR as well as TNC and EGFR in terms of being reported together in published studies (**Figure 4-2**). There was also evidence of co-expression of TNC and EGFR as well as CA9 and EGFR (**Figure 4-2**). An experimentally determined association between TNC and EGFR has also been established but CLDN18, on the other hand, did not have any known associations with the other 4 proteins being investigated (**Figure 4-2**).

4.2 Selected biomarkers for theranosis in CCA

The biomarkers scoring 17 or higher on the TASC-T score, namely, MMP9, CLDN18, TNC, CA9 and EGFR were selected for in depth analysis of their potential as theranostic biomarkers in CCA. The study characteristics of the selected published studies of protein expression of these 5 biomarkers in CCA are summarised in **Table 4-3**. Studies were regarded as low bias if two or more blinded investigators independently scored the tissue sections.

Three of these candidate biomarkers have only been previously evaluated in 2 studies. CA9, CLDN18, and TNC were evaluated in 548 Eastern tissue specimens, 76% (417/548) of which were IH-CCA tissues. MMP9 and EGFR have been evaluated in multiple studies, and a wide range of positive expression has been reported. Over 50% (936/1,793) of the tissue validation of TNC and EGFR involved IH-CCA tissues.

Table 4-2 TASC-T scoring of 16 selected biomarkers validated in ≥2 studies

	Tumour biomarker	Extracellular	Membrane	Highest % positive/ high expression reported in CCA	Targeting ligand in human trials	Previous use in pre-clinical/ clinical imaging	Reference	TASC-T (max 22)
1	ANGPT1	Yes	No	43.7	No	No	N/A	9
2	ANGPT2	Yes	No	57.6	No	No	N/A	9
3	CA9	No	Yes	85	Yes (Iodine-124 labelled cG250)	Yes	Divgi <i>et al.</i> , 2007	17
4	CDH17	No	Yes	52.9	No	No	N/A	15
5	CDX2	No	No	60	No	No	N/A	7
6	CLDN18	No	Yes	90	Yes (Claudiximab, Zolbetuximab)	No	N/A	19
7	EGFR	Yes	Yes	75	Yes (Cetuximab, Panitumumab)	Yes	McKnight <i>et al.</i> , 2018	17
8	MMP7	Yes	No	80	No	Yes	Scherer <i>et al.</i> , 2008	15
9	MMP9	Yes	No	67	Yes (Andecaliximab)	Yes	Hakimzadeh <i>et al.</i> , 2017	19
10	SERPINA1	Yes	No	57	No	No	N/A	12
11	SFRP1	Yes	Yes	60	No	No	N/A	12
12	SLC2A1	No	Yes	52	No	No	N/A	12
13	TFF1	Yes	No	98.4	No	No	N/A	15
14	TGFB1	Yes	No	47	Yes (Fresolimumab)	Yes	den Hollander <i>et al.</i> , 2015	15
15	TNC	Yes	No	63.9	Yes (Neuradiab, Tenatumomab)	Yes	Jacobson <i>et al.</i> , 2015	18
16	TP53	No	No	84	No	Yes	Li <i>et al.</i> , 2017	13

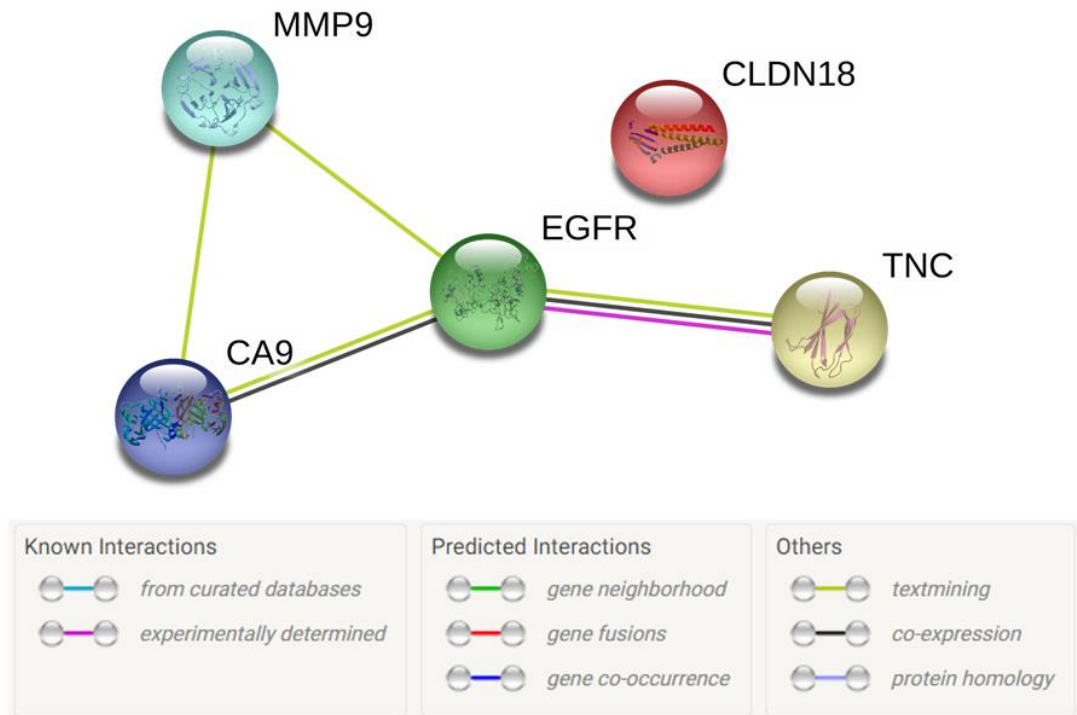


Figure 4-2 STRING network of top 5 selected candidate biomarkers for theragnosis in CCA

Green lines represent interaction between biomarkers as determined by text-mining (automated, unsupervised search of PubMed for proteins mentioned together). This shows that there are associations between MMP9, CA9 and EGFR as well as TNC and EGFR.

Black line represents co-expression of biomarkers (CA9 and EGFR; TNC and EGFR). Pink line represents experimentally determined association between TNC and EGFR.

There are no known associations between CLDN18 and the other 4 selected candidate biomarkers.

Table 4-3 Study characteristics of the top 5 selected candidate biomarkers for theranosis in CCA

NR – not reported; +ve – Positive; -ve - Negative. * Data amalgamated from multiple studies and range of expression for each CCA subtype.

Biomarker	Country	Site of tumour	No:	% high/+ve expression	Normal tissue control	Expression in normal tissues	Risk of bias	References
MMP9*	Multiple (mainly Eastern)	IH-CCA EH-CCA PH-CCA	302 214 120	45.6-62.5% +ve 47.3-58% +ve 67.2-67.7% +ve	Normal liver tissue	Weak or -ve	Low-High	8 studies (see paragraph 4.2.1)
CLDN18	Japan	IH-CCA EH-CCA	27 32	NR	Biliary epithelium	NR	High	(Keira <i>et al.</i> , 2015)
	Japan	IH-CCA EH-CCA	83 99	43% +ve 90% +ve	Biliary epithelium	-ve	High	(Shinozaki <i>et al.</i> , 2011)
TNC	Japan	IH-CCA	61	63.9% +ve	NR	NR	High	(Iguchi <i>et al.</i> , 2009)
	Japan	IH-CCA	48	37.5% high	NR	NR	High	(Soejima <i>et al.</i> , 2018)
CA9	China	IH-CCA	113	85.0% high	NR	NR	Low	(Bi <i>et al.</i> , 2019)
	Korea	IH-CCA	85	44.7% +ve	n=4 normal liver tissue	NR	High	(Gu, 2015a)
EGFR*	Multiple (mainly Eastern)	IH-CCA EH-CCA PH-CCA CCA	634 402 121 173	26.1-100% +ve 18-79% +ve 45.5% high 28.6-55% high	Normal liver tissue	+ve membrane	Low-High	15 studies, see paragraph 4.2.5)

4.2.1 Matrix metalloproteinase 9

MMP9 expression in CCA has been evaluated in 8 studies that met the inclusion/exclusion criteria (Itatsu *et al.*, 2009; Onodera *et al.*, 2009; Subimerb *et al.*, 2010; Shi *et al.*, 2013; Sun *et al.*, 2014b; Sun *et al.*, 2015; Tian *et al.*, 2015; Park *et al.*, 2018). 302 IH-CCA and 334 EH-CCA (including 120 PH-CCA tissues) have been evaluated with reported positive MMP9 expression ranges from 45.6-62.5% and 47.3-58% respectively. Only 2 studies commented on non-neoplastic biliary epithelium which they reported as faint or absent expression (Itatsu *et al.*, 2009; Onodera *et al.*, 2009). All 8 studies investigating MMP9 involve Eastern tissue specimens from Korea, China, Japan and Thailand. MMP9 scored 19/22 on TASC-T score.

4.2.2 Claudin 18

CLDN18 expression was reported in 2 Japanese studies which included a total of 110 IH-CCA tissues and 131 EH-CCA tissues, respectively (Shinozaki *et al.*, 2011; Keira *et al.*, 2015). Keira *et al.* (2015) reported CLDN18 positive expression on the basolateral surface of tissues with negative expression in the normal biliary epithelium. It was not possible to ascertain the percentage positivity or high expression in the 59 tissues included in this study. Shinozaki *et al.* (2011) reported 43% positive expression in 83 IH-CCA tissues and 90% positive expression in 99 EH-CCA tissues. The annotated protein expression of CLDN18 in normal tissues is reportedly restricted to the stomach with an 'enhanced' score for reliability which is the highest awarded¹ (Human Protein Atlas, 2019a). CLDN18 scored 19/22 on the TASC-T score.

¹ The Human Protein Atlas categorizes the reliability of normal tissue protein expression into four categories; enhanced, supported, approved and uncertain (in decreasing order of reliability). RNA sequencing data, immunohistochemical data from one or more antibodies and protein/gene characterization data are considered for the 44 normal tissues analysed prior to the award of a category.

4.2.3 Tenascin C

Similar to CLDN18, TNC was also reported in 2 Japanese studies but all 109 tissue samples were from IH-CCA patients (Iguchi *et al.*, 2009; Soejima *et al.*, 2018). Neither of these studies described TNC expression in normal liver tissue. The annotated protein expression of TNC is negative in all 44 tissues investigated by the human protein atlas (Human Protein Atlas, 2019a) although the reliability of this expression pattern is 'approved' which is one category higher than the lowest 'uncertain' category. Interrogating the primary data for the 2 TNC antibodies used by the human protein atlas, one (CAB004592, Santa Cruz Biotechnology) reported weak to moderate immunoreactivity in most tissues but pancreas, liver, central nervous system and lymphoid tissues were negative. Immunoreactivity with the second antibody (HPA004823, Sigma-Aldrich) reported strong positivity in seminiferous ducts and weak to moderate positivity in glandular epithelia. TNC scored 18/22 on TASC-T score.

4.2.4 Carbonic anhydrase 9

Two studies (Gu, 2015b; Bi *et al.*, 2019) have explored the CA9 expression in CCA tissue which included 198 IH-CCA tissue samples in total and reported 85% high expression in one study and 44.7% positive expression in the other (**Table 4-3**). Neither of these studies commented on CA9 expression in adjacent normal liver tissue. No studies that met the selection criteria for TASC-T scoring have evaluated CA9 expression in EH-CCA tissues. The annotated protein expression of CA9 in normal tissues display moderate to high expression in stomach, duodenum, small intestine and gall bladder (Human Protein Atlas, 2019a). CA9 scored 17/22 on TASC-T score.

4.2.5 Epidermal growth factor receptor

This systematic review included 15 different studies which report EGFR expression in CCA (Ogo *et al.*, 2006; Schmitz *et al.*, 2007; Yoshikawa *et al.*, 2008; Iguchi *et al.*, 2009;

Pignochino *et al.*, 2010; Shafizadeh *et al.*, 2010; Miyamoto *et al.*, 2011; Gu and Choi, 2012; Simbolo *et al.*, 2014; Yang *et al.*, 2014; Moon *et al.*, 2016; Padthaisong *et al.*, 2017; Gomes *et al.*, 2018; Xu *et al.*, 2019; Zhao *et al.*, 2019). 10/15 studies that investigated EGFR involved Eastern tissue specimens from Japan, China, Korea and Thailand with 5/15 originating from USA, Brazil, Italy and Germany.

In 402 tissue specimens of IH-CCA, the reported positive expression of EGFR ranged from 26-100%. Of the 634 EH-CCA specimens, 18-79% were reported as positive (**Table 4-3**). In 121 PH-CCA tissues and 173 CCA of unspecified subtype 28.6-55% of tissues were reported as positive. The proportion of CCA tissues positive for EGFR expression was higher in IH-CCA compared to EH-CCA in the studies included. This was also the case in the four studies that included both IH-CCA and EH-CCA tissues and reported EGFR expression results separately (Yoshikawa *et al.*, 2008; Pignochino *et al.*, 2010; Shafizadeh *et al.*, 2010; Simbolo *et al.*, 2014).

Of these 15 studies, only 1 study (Pignochino *et al.*, 2010) commented on normal liver and biliary tract tissue expression of EGFR as positive for EGFR immunoreactivity in all normal cholangiocyte and hepatocyte membranes. Low EGFR expression has been demonstrated in normal tissues such as liver, skeletal muscle and skin (Human Protein Atlas, 2019a). EGFR scored 17/22 on the TASC-T score.

4.3 Discussion

This systematic review has highlighted that there have been a vast number of biomarker discovery studies in CCA. This method of systematic review of literature and TASC-T scoring for the identification and selection of biomarkers for theranosis is also applicable to other cancers and diseases for which theranosis may be beneficial.

Although the five biomarkers MMP9, CLDN18, TNC, CA9 and EGFR have been highlighted by this systematic review as potential theranostic targets in CCA, most of them lack robust CCA tissue validation. CA9, CLDN18 and TNC have only been validated in 2 separate studies that met the inclusion criteria, whereas MMP9 and EGFR have been investigated by multiple research groups. Each of these biomarkers and their potential for theranostic applications are discussed here, including their basic structure as this is relevant for active targeting.

4.3.1 Matrix metalloproteinase 9 for theranostic applications

MMP9 is a type of collagenase present in the ECM which is involved in tissue remodelling such as in cardiac tissue following myocardial infarction (Lindsey, 2018) as well as other pathological states such as neoplasia (Vandooren *et al.*, 2013). The schematic structure of MMP9 is shown in **Figure 4-3**.

MMP9 overexpression and its negative association with prognosis in cancers such as gastric cancer has been reported and a monoclonal antibody aimed at MMP9 inhibition is currently in human trials (Kumar *et al.*, 2018). Results from a clinical trial commenced in 2016 comparing andecaliximab (also known as GS-5745), which is an MMP9 inhibitor, as monotherapy and in combination with anti-cancer agents in Japanese participants with gastric or gastroesophageal junction adenocarcinoma is currently awaiting results (ClinicalTrials.gov, NCT02862535). This is one of 5 completed trials that have evaluated andecaliximab in solid tumours but none have published results. None of these trials include patients with CCA.

Although a humanized monoclonal antibody is available, there are no published human studies using MMP9 as an imaging or theranostic biomarker.

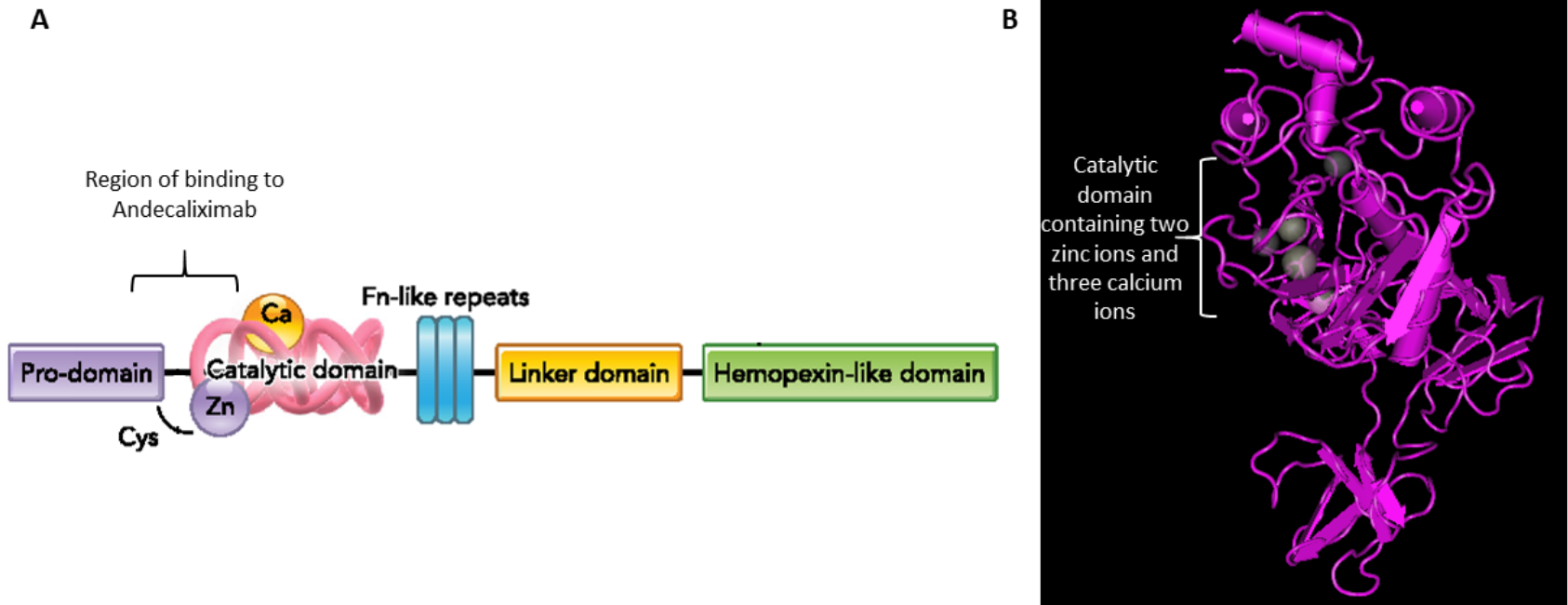


Figure 4-3 Schematic structure of MMP9

Panel **A** shows the different domains of the MMP9 protein and the binding site of the Anti-MMP9 monoclonal antibody andecaliximab. Taken and adapted from Yabluchanskiy *et al.* (2013)

Panel **B** shows the 3D crystal structure of MMP9 and demonstrates the catalytic domain containing two zinc ions and three calcium ions. Taken and adapted from Madej *et al.* (2014)

Recently, Hakimzadeh et al. (2017) developed a radiolabelled MMP9 and MMP2 targeted radioligand for the purpose of imaging atherosclerotic lesions. On *ex vivo* measurement of radioactivity, they demonstrated increased signal in mouse aortic tissue with atherosclerotic lesions and subsequently confirmed MMP9 and MMP2 immunoreactivity on these tissue sections. They described the labelling procedure as challenging with insufficient yield of radiolabelled product (Hakimzadeh *et al.*, 2017). This may be the reason the authors do not report any *in vivo* imaging. Although this radioligand maybe useful for imaging MMP9-expressing cancers, the lack of MMP9-specificity of the ligand could result in low signal-to-noise ratio as MMP2 expression in normal tissues is more widespread compared to MMP9 (Human Protein Atlas, 2019a).

None of the studies that met the inclusion/exclusion criteria for this systematic review included patients from Western cohorts. This is relevant due to the geographical variations and aetiological differences in the distribution of CCA (Khan *et al.*, 2019) which may reflect in expression of tissue biomarkers.

A study at our institution investigated MMP9 in 54 PH-CCA and paired adjacent non-cancerous control liver specimens from a Western cohort of patients but did not meet inclusion criteria for this study (Nair *et al.*, 2018). This was due to all adjacent non-cancerous liver controls being MMP9 positive to a lesser degree compared to tumour tissue, albeit just reaching statistical significance (Nair *et al.*, 2018). This is in contrast to the reported low or negative normal liver tissue expression reported by the human protein atlas (2019a) and the 2/8 studies that reported low or negative MMP9 expression in normal biliary epithelium (Itatsu *et al.*, 2009; Onodera *et al.*, 2009). Whether this is due to differences in tissue handling and immunohistochemical processing, non-specific background labelling from the antibody utilised or a genuine positive expression in normal liver requires clarification.

If normal liver is indeed truly positive, MMP9 is unlikely to be a good theranostic target despite being highlighted as a potential candidate in this review.

4.3.2 Claudin 18 for theranostic applications

CLDN18s are tight junction proteins that have two main alternate splice variants (Garcia-Hernandez *et al.*, 2017) of which variant 2 expression is mainly observed in gastric epithelium whereas variant 1 is expressed in lung tissue (Niimi *et al.*, 2001). Tight junction proteins exist in the lateral apical surface between two epithelial cells. The structure of CLDN18.2 (**Figure 4-4**) has two predicted extracellular loops, the first of which includes the binding site for claudiximab. Sahin *et al.* (2008) reported that CLDN18 splice variant 2, termed CLDN18.2 is expressed in several cancers including gastric (77% positive expression), pancreatic (80% positive expression) and oesophageal (78% positive expression) cancers.

CLDN18.2 has been identified as a target suitable for therapeutic antibody development (Sahin *et al.*, 2008) and CLDN18.2 inhibiting monoclonal antibodies (eg. claudiximab, zolbetuximab) are now in clinical trials for oesophageal, gastric and pancreatic adenocarcinoma. Two phase 3 trials using the addition of zolbetuximab or placebo to standard chemotherapeutic regimens are currently recruiting CLDN18.2 positive patients (ClinicalTrials.gov; NCT03504397, NCT03653507). However, a recent large immunohistochemical study of gastric cancer in a cohort of Caucasian gastric cancer patients only showed 42.2% (203/481) positive expression of CLDN18.2 (Dottermusch *et al.*, 2019).

Although published literature of CLDN18 expression in CCA is limited, one included study reported a difference in expression in CCA subtypes. Shinozaki *et al.* (2011) demonstrated 90% positive expression in EH-CCA compared to 43% in IH-CCA.

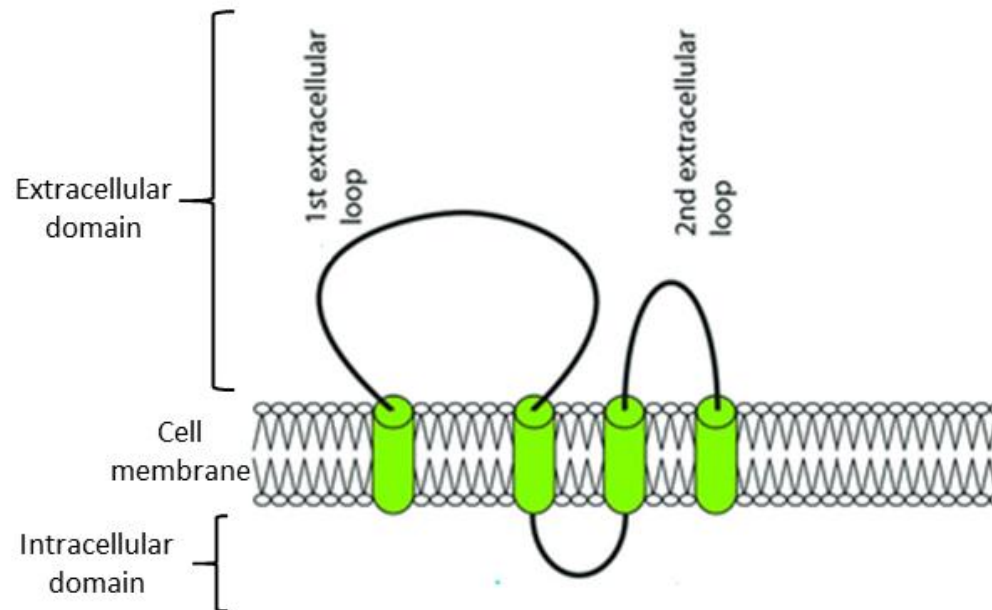


Figure 4-4 Schematic structure of Claudin 18.2

The first extracellular loop is the binding site for the monoclonal antibody claudiximab. Taken and adapted from Kumar *et al.* (2018)

Interestingly, expression of other biomarkers present in gastric epithelium such as mucin 5AC, mucin 6 and cytokeratin 20 have also been shown to be higher in EH-CCA compared to IH-CCA (Wiggers *et al.*, 2014).

Whether the extracellular domain of CLDN18.2 will be accessible to systemically delivered theranostic agents is not known. In favour of CLDN18.2 as a theranostic agent in terms of its cellular location is that it has been shown to be expressed throughout the gastric epithelial cell membrane in normal gastric mucosa (Niimi *et al.*, 2001) and not just restricted to tight junctions. This may also be the case in tumours as they are generally less adherent to neighbouring cells and have less organised cellular barriers compared to normal tissue.

4.3.3 Tenascin C for theranostic applications

TNC is a large protein that exists as a hexamer in the ECM (Chiquet-Ehrismann, 2004). Although expressed abundantly in embryonic development, its expression in adult tissues is limited to areas of inflammation, wound healing and tumour growth (Chiquet-Ehrismann *et al.*, 1986; Terada and Nakanuma, 1994; Midwood and Orend, 2009). This restricted pattern of expression and upregulation in tumour growth has made TNC an attractive biomarker for developing targeted theranostics (Chen *et al.*, 2016a). **Figure 4-5** shows a schematic of TNC structure as a monomer or hexamer as well as its spatial location within a tumour.

This review has highlighted two studies which report TNC expression in IH-CCA. TNC in EH-CCA has not been reported. However, TNC expression in pancreatic ductal (Xu *et al.*, 2015; Leppanen *et al.*, 2019), oesophageal (Leppanen *et al.*, 2017) and gastric (Qi *et al.*, 2019) adenocarcinoma have been described.

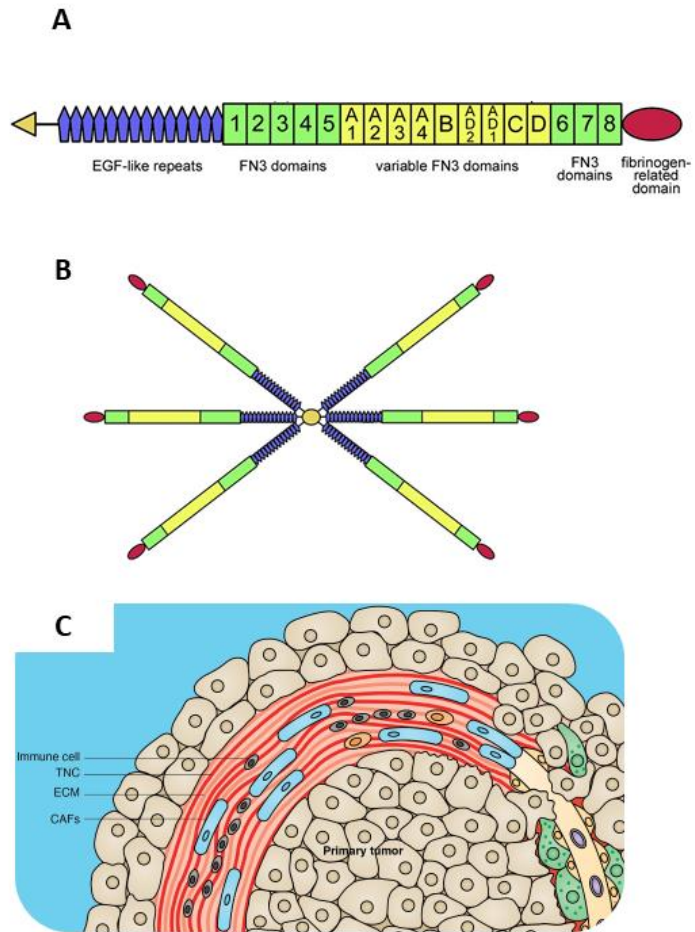


Figure 4-5 Schematic structure of Tenascin C

Panel **A** shows the 5 different domains of TNC from the N-terminus EGF-like repeats (left), fixed fibronectin domain, variable fibronectin domain, fixed fibronectin domain and C-terminus fibronectin head (right). Panel **B** shows the TNC hexamer, called a hexabrachion. Taken and adapted from Tucker and Chiquet-Ehrismann (2015)

Panel **C** shows the relationship of TNC to the tumour extracellular matrix and its constituents. Taken and adapted from Midwood *et al.* (2016)

With regard to TNC targeted imaging, Hicke *et al.* (2006) demonstrated tumour targeting in a glioblastoma xenograft model using a TNC-specific RNA aptamer. They were able to image U251 glioblastoma xenograft tissue *in vivo* with Technetium-99m labelled TNC aptamers using radionuclide imaging (Hicke *et al.*, 2006). He *et al.* (2018) developed a nanoparticle formulation of camptothecin prodrug conjugated with a cell penetrating peptide and TNC-targeted single-stranded DNA aptamer and evaluated this in a xenograft model of pancreatic ductal adenocarcinoma. They were able to demonstrate *in vivo* imaging of these particles and demonstrated a therapeutic response in a xenograft model (He *et al.*, 2018). These successful applications of TNC targeted theranostics by aptamers are promising as antibody mimetics have several advantages over antibodies including their lower cost, scalability and more ethical synthesis as they do not require an intact host immune system in their development (Tiede *et al.*, 2014; Yu *et al.*, 2017).

4.3.4 Carbonic anhydrase 9 for theranostic applications

CA9 belongs to a large group of carbonic anhydrase enzymes which act as catalysts for the reversible reaction of carbon dioxide with water to bicarbonate and hydrogen ion (Hilvo *et al.*, 2008; Alterio *et al.*, 2009). Although this family of enzymes are ubiquitously expressed in humans, CA9 expression is restricted mainly to the gastrointestinal tract and its overexpression is seen in several solid tumours such as gastric cancer (Driessen *et al.*, 2006; Alterio *et al.*, 2009). The role of CA9 in the regulation of pH in tumour microenvironment and induction of CA9 expression in response to tumour tissue hypoxia have been demonstrated (Swietach *et al.*, 2010).

Given the restricted expression in normal tissues and upregulation in solid tumours, CA9 has gained interest as a novel tumour target (De Simone and Supuran, 2010). Although pre-clinical data that support the use of CA9 inhibition as a therapeutic option for cancers exist, there are no human studies demonstrating clinical benefit

(Bayat-Mokhtari *et al.*, 2017). The results of a phase I clinical study of a CA9 inhibitor in solid cancers (ClinicalTrials.gov; NCT02215850) are awaited.

In addition to low normal tissue distribution and upregulation in cancer, as a potential theranostic target CA9 has several other key advantages. It is a membrane-bound protein with an extracellular catalytic component as shown in **Figure 4-6**. This makes it 'visible' to systemically delivered theranostic agents. In addition, it has previously been used as an imaging biomarker (Divgi *et al.*, 2007). Binding to CA9 and internalisation of positron emission tomography (PET) tracers labelled with CA9 antibody have been demonstrated in a mouse xenograft model of renal cell carcinoma (Cheal *et al.*, 2014).

The other feature that could be exploited is its enzymatic activity which is a desirable feature in an imaging (van Oosten *et al.*, 2011) as well as theranostic biomarker. A theranostic agent that is intended to target CA9 could be designed to be activated by CA9 thus releasing its drug payload only when it has reached the tissue target.

Although restricted mainly to gastric mucosa, CA9 is expressed in normal tissue and has a role in pH regulation (Pastorekova *et al.*, 1997) and hence consideration of the potential side-effects of CA9 as a theranostic target has to be considered. If this is to be explored in future *in vivo* studies, endpoint gastric mucosa histology should be assessed for potential off-target toxicity. Another disadvantage of CA9 as a theranostic target is the suggestion that its expression in tumour tissues is induced by tissue hypoxia (Supuran, 2018). If this is indeed the case in CCA as well, the delivery of a theranostic particle to the site of CA9 will be challenging as systemically administered agents are likely to have low tissue penetration to the areas of CA9 expression.

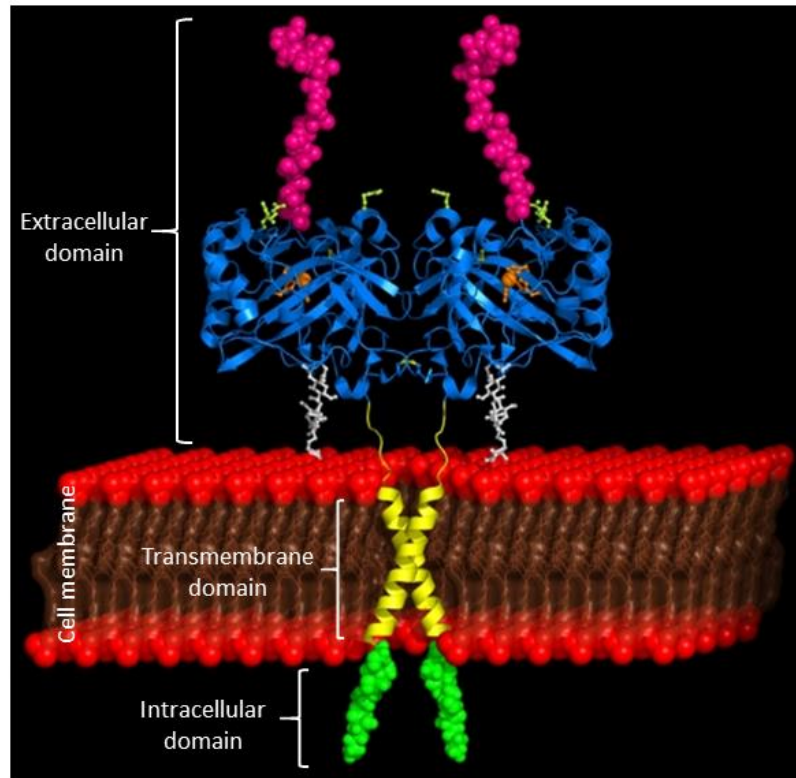


Figure 4-6 Schematic structure of Carbonic anhydrase 9

The extracellular domain of CA9 could be targeted by a theranostic agent. Image taken and adapted from Alterio *et al.* (2009)

4.3.5 Epidermal growth factor receptor for theranostic applications

Extensive research efforts have been focused on EGFR over the past two decades and anti-EGFR therapy in combination with conventional chemotherapy is now in routine practice for cancers such as metastatic colorectal cancer (Price *et al.*, 2018). Cetuximab which is a human/mouse chimeric monoclonal antibody, and the fully human monoclonal antibody panitumumab that inhibit EGFR were approved by FDA in 2004 and 2006, respectively (Corcoran and Hanson, 2014). Both cetuximab and panitumumab in combination with first-line chemotherapy have been evaluated in advanced BTC but neither have shown any significant improvement in progression free survival or overall survival (Merla *et al.*, 2015). This suggests that inhibiting the EGFR pathway alone may not be beneficial or that it may be beneficial only in a subset of BTC, a difference these clinical trials were not powered to detect.

A schematic structure of EGFR both in its inactive form and its dimerized active form is shown in **Figure 4-7**. Cetuximab and panitumumab work by binding to a site on the extracellular domain of EGFR that partly occludes the binding site for epidermal growth factor (EGF) (Li *et al.*, 2005; Sickmier *et al.*, 2016).

Non-invasive imaging of EGFR status has been investigated and several EGFR radiolabelled tracers have been developed for PET and single-photon emission computed tomography (SPECT) (Corcoran and Hanson, 2014; van Helden *et al.*, 2019). Van Helden *et al.* (2019) were able to image tumour uptake of cetuximab labelled radiotracer but this was not directly correlated with EGFR expression and did not predict treatment benefit with cetuximab. One confounding factor in this study was the pre-treatment of patients with unlabelled cetuximab to occupy non-malignant binding sites as invariably EGFR binding sites on the tumour could also be saturated which would have had an impact on subsequent imaging. This highlights the importance of a

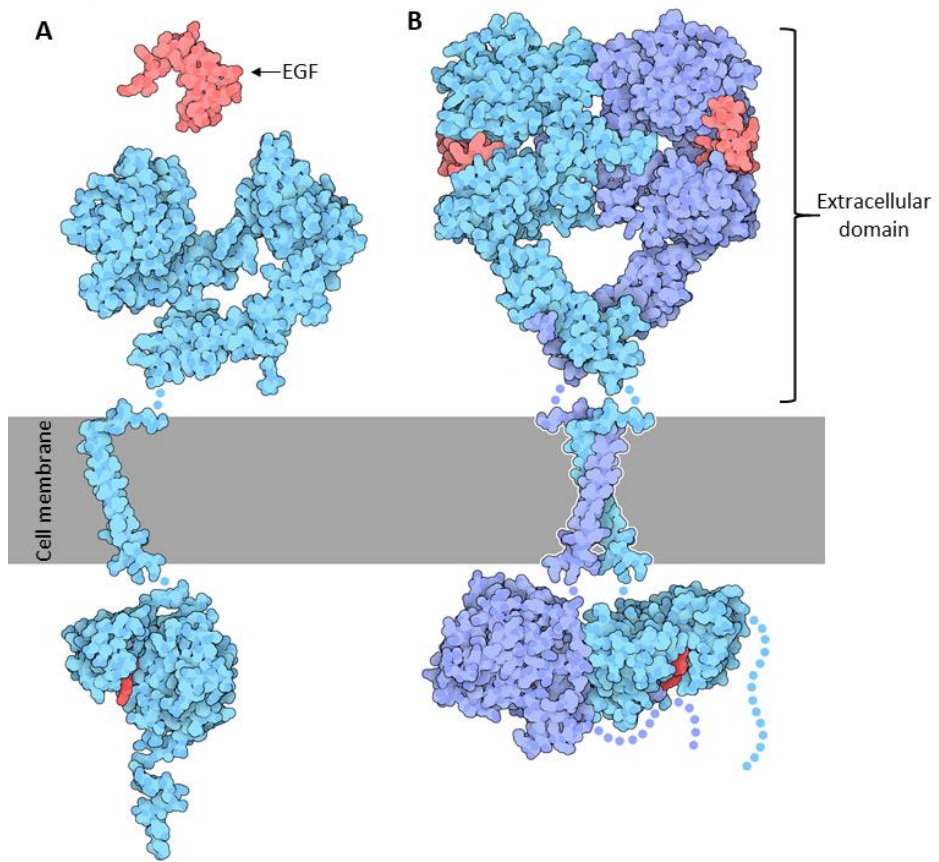


Figure 4-7 Schematic structure of EGFR

Panel **A** shows the inactive form of EGFR which dimerizes on binding of Epidermal growth factor (EGF) to its active form shown in Panel **B**. Bound EGF shown in red and cell membrane shown in grey.

Image taken and adapted from the protein data bank (Berman *et al.*, 2000)

theranostic biomarker having low or negative expression in normal tissues as pre-treatment should not be necessary if the expression of the biomarker of interest is truly negative in normal tissues.

This systematic review of theranostic biomarkers has identified 15 studies reporting expression of EGFR in CCA. Although the scoring methods differed between studies, there was a trend towards higher EGFR expression in IH-CCA compared to EH-CCA. This was still the case when only the four studies that reported on EGFR expression in both IH-CCA and EH-CCA were considered (Yoshikawa *et al.*, 2008; Pignochino *et al.*, 2010; Shafizadeh *et al.*, 2010; Simbolo *et al.*, 2014). This may suggest that EGFR may not be a useful theranostic marker in EH-CCA.

4.3.6 Systematic review - challenges and limitations

This systematic review had many challenges and several limitations. The heterogeneity of the CCA biomarker studies and the scarcity of biomarker validation in multiple centres confound the conclusions that can be drawn and make meta-analysis impossible. The studies encountered in this review were mainly aimed at biomarker discovery of diagnostic, predictive or prognostic biomarkers in CCA or those that could be direct therapeutic targets. These were not always suitable candidates as theranostic biomarkers.

The studies often discussed proteins using different aliases and therefore gene names had to be used to ensure that the data was being extracted for the correct gene product. This was not always well documented in the publications. Furthermore, there was significant variability in reporting of the results and scoring methods for the same marker that made comparison across studies very difficult. Often supplementary data was required to extract the necessary data and infrequently, studies had to be

excluded as the percentage positive expression or high expression in tissues could not be determined from the data provided.

The majority of studies involving histology specimens have been performed in Eastern countries such as Thailand and Japan where CCA has a higher incidence due to aetiological differences. Although this geographical difference reflects the relative disease burden of CCA worldwide, the scarcity of tissue from Western cohorts makes it difficult for conclusions to be drawn about the applicability of these biomarkers for CCA theragnosis worldwide. Hughes *et al.* (2006) explored the differences in cell phenotypes in a cohort of liver-fluke associated CCA (65 cases) in comparison to sporadic CCA (47 cases). They reported that liver-fluke associated CCA had more intestinal metaplasia phenotype and were also more likely to overexpress p53 in comparison to sporadic CCA. Whether other biomarkers expressed in liver-fluke associated CCA are comparable to those in sporadic cholangiocarcinoma seen in Western countries remains to be explored.

An attempt was made to assess the risk of bias of the studies including consideration of the criteria of the Newcastle-Ottawa Scale (Stang, 2010). However, due to significant heterogeneity the only measure of bias that was included in the data extraction was the assessment of tissue. Studies were regarded as low bias if two or more blinded investigators independently scored the tissue sections. A significant proportion of studies did not utilise control non-tumour tissues in parallel with CCA tissue biomarker expression analysis which was a significant deficiency.

Although the human protein atlas (2019a) was an exceedingly useful resource, 43% (36/83) of the potential candidate biomarkers did not have annotated protein expression data in normal tissues. Even for those proteins that did have annotated protein expression data, the reliability score for this was variable. The reliability score ranged from enhanced, supported and approved to uncertain reflecting the

immunohistochemical data available from one or more antibodies as well as the RNA sequencing data (Human Protein Atlas, 2019a). Despite this, no biomarker was excluded based on the reliability score in order to maximise the number of potential biomarkers identified for closer scrutiny in this study.

While guidance exists on reporting outcomes from tumour biomarker prognostic studies for IHC-based studies i.e. REMARK guidelines (Sauerbrei *et al.*, 2018), no such guidelines exist for tumour biomarkers in general. Hence, the studies included in this review display significant deficiencies of reporting. Such guidance for reporting of all biomarker studies would result in a more consistent data set and hence improve the likelihood that these studies will have a wider impact on translational research.

In conclusion, this study recommends that future studies on cancer biomarkers should concurrently report expression of those biomarkers in adjacent non-tumour tissue as well as report the cellular compartment where expression is observed. Another important aspect would be to report the subtype of CCA from which the tissues originate as immunohistochemical differences have been observed in IH-CCA and EH-CCA (Wiggers *et al.*, 2014). This should constitute a minimal data set for this type of study.

Good quality, detailed published data on cancer biomarkers would allow results from numerous studies to be analysed using bioinformatics techniques that would greatly accelerate and enhance the prediction of beneficial biomarkers for theranostic and other applications.

4.3.7 Future directions

The quest for ideal biomarkers that are specific to CCA tissue, which could then be actively targeted by drug-loaded nanoparticles is still in its infancy. Given the heterogeneity of biomarker expression and the various anatomical and histological

subtypes of CCA, individualising the treatment strategy to develop customisable theranostic agents may be the way forward.

Two out of the 5 biomarkers (CLDN18 and CA9) highlighted in this systematic review have also been reported as potential theranostic targets in gallbladder cancer (Espinoza *et al.*, 2019). EGFR and MMP9 have long been areas of research focus in cancer theranostics. TNC has also gained popularity as a biomarker for cancers as well as other conditions such as cardiovascular disease.

As demonstrated by this chapter, these 5 biomarkers with potential for theranosis in CCA have potential cross-specialty therapeutic applications. Each of these 5 biomarkers warrant further investigation in CCA but TNC was selected for pre-clinical validation which is explored in the next chapter.

TNC was selected for this purpose due to the option of collaborative research within the University of Leeds for the development of novel TNC targeted therapeutics. Considering the scale of resources required to develop, validate and translate biomarkers to clinical practice, collaborative efforts from different research groups will be essential for the development of novel CCA therapeutics in the future. The need for continued efforts to develop novel therapeutic strategies cannot be over-emphasized for this rare group of cancers that is rising in incidence globally.

Chapter 5

Tenascin C as a biomarker for theranosis in cholangiocarcinoma

Introduction

Development of a targeted theranostic platform for CCA using nanotechnology requires validation of a promising target. In this chapter, the feasibility of TNC as a candidate biomarker for theranosis in CCA was explored. TNC was one of the biomarkers with theranostic potential identified during the systematic search for biomarkers described in **Chapter 4**.

TNC is also a biomarker of interest in imaging myocardial remodelling following infarction (Imanaka-Yoshida, 2012; Maqbool *et al.*, 2016). This presented an opportunity for collaborative research with the cardiovascular research group at the University of Leeds who were developing gadolinium labelled TNC aptamers for MRI imaging which was funded by British Heart Foundation (Grant Number NH/12/1/29382 (Plein, 2012)). Multidisciplinary collaborations into novel therapeutics are likely to expedite translation compared to exclusive focus on one type of clinical application by a single research group.

The reported literature of TNC expression in CCA is sparse with no published studies evaluating TNC expression in PH-CCA or EH-CCA prior to the present study. An association between expression of tenascin proteins at the IH-CCA “invasive front” (i.e. border between normal liver tissue and tumour tissue) was first reported by Aishima *et al.* (2003). A recent meta-analysis showed high expression of TNC was associated with poor prognosis in 14 types of cancer including pancreatic, colorectal and lung cancer although it did not include CCA patients (Ming *et al.*, 2019). In desmoplastic tumours like CCA with abundant stroma and frequent inflammatory response (Castellano-Megias *et al.*, 2013; Sirica and Gores, 2014), the role of the ECM and its constituent proteins is an interesting topic of investigation.

TNC expression in normal tissues is restricted in adult human tissues with negative expression in most normal tissues (Human Protein Atlas, 2019b). This is described in more detail in **Section 1.4.1**. This pattern of high expression in cancer tissue and very low or negative expression in normal tissue are desirable qualities in a candidate biomarker for theranosis therefore further exploration into utilising TNC for this purpose is warranted.

In this chapter, the expression of TNC in a cohort of PH-CCA and IH-CCA tissues, selected murine xenografts and orthotopic CCA tumour tissue were evaluated using immunohistochemistry. Selected cell lines were also examined for the presence of TNC protein or mRNA using immunofluorescence, immunoblotting and RT-PCR.

5.1 TNC is present in human cholangiocarcinoma tissue

Archival FFPE specimens of both IH-CCA and PH-CCA with matched control liver tissue samples from our institution were first examined for the presence of TNC using immunohistochemistry. The hypothesis that TNC positivity could be a marker of poor prognosis was also investigated.

Immunohistochemistry was performed using the optimised method described in **Section 2.6.1**. The primary antibody (rabbit polyclonal Anti-TNC antibody HPA004823 (Sigma-Aldrich, UK)) was one of the antibodies used by the human tissue atlas to establish normal tissue expression patterns of TNC (Human Protein Atlas, 2019b).

Optimisation of the TNC IHC protocol for human tissue included several IHC batches using a pair of human CCA and liver tissue under different conditions (**Table 2-1**). Three primary antibody concentrations (1:100, 1:200, 1:300), two antigen retrieval methods (HIER using pH 6 citrate buffer and no retrieval) and four blocking agents to

reduce non-specific binding (0.3% H₂O₂, 3% H₂O₂, 10% casein with a avidin/biotin) were trialled.

HIER resulted in high background immunolabelling despite all three blocking steps and therefore was abandoned. There was no immunolabelling in the no primary antibody control even with HIER. The pattern of immunolabelling was similar between all three concentrations of antibody but the intensity was much higher in the 1:100 whereas 1:300 was faint. Therefore, 1:200 primary antibody dilution was selected for the optimised protocol.

No difference in pattern or intensity was observed with the 3% H₂O₂ compared to 0.3% H₂O₂ nor was there any improvement in non-specific labelling with avidin/biotin blocking step. The 0.3% H₂O₂ and 10% casein blocking steps were retained in the optimised protocol. The CCA tissue section used for protocol optimisation was included in subsequent IHC batches as an internal positive control.

Slides were scored by a single investigator (IW), blinded to clinical outcome. Slides were randomly numbered and not explicitly labelled as normal liver or CCA tissue prior to scoring. However due to the homogeneity of normal liver tissue and distinct tissue morphology of adenocarcinoma under microscopy, it was not possible to blind the investigator to tissue type.

Whole tissue sections were scored on distribution and intensity of immunolabelling. The minimum score possible was 0 and the maximum was 12. The location of the tumour tissue sections in relation to the anatomy of the tumour could not be determined on the available paraffin blocks and therefore the “invasive front” could not be scored separately.

No primary antibody controls in each batch were negative. Internal positive control (PH-CCA tissue section used for optimisation steps) was used as a positive control and to ensure batch consistency was maintained positive in each run.

5.1.1 TNC immunolabelling in human cholangiocarcinoma and paired normal liver tissue

TNC immunolabelling was detected in the extra-cellular matrix around CCA cells. Cytoplasmic staining was also seen occasionally but nuclear or membranous staining were not observed.

The distribution and intensity of TNC immunolabelling were variable. In cases where the TNC immunolabelling was restricted to an area of the tissue section, there was often an associated inflammatory infiltrate. Inflammatory cells themselves did not demonstrate TNC immunolabelling although the surrounding stroma was often positive. These features are shown in **Figure 5-1** which contrast with the para-cancerous normal human liver where only occasional weak immunolabelling was seen in the liver sinusoids and in some peri-vascular areas shown in **Figure 5-2**. Normal hepatocytes were negative.

Figure 5-3A shows the TNC histoscore comparison in 34 paired samples of PH-CCA and matched control liver. PH-CCA tissue had significantly higher TNC immunolabelling compared to control liver tissue ($p=0.002$). Most PH-CCA tissue was TNC-positive (25/34; 73.5%). The median (interquartile range, IQR) TNC histoscore for PH-CCA compared to paired normal liver tissue was 2 (4.5) and 0 (0), respectively.

Figure 5-3B shows the TNC histoscore comparison in 20 paired samples of IH-CCA and matched control liver. Significantly higher TNC immunolabelling was seen in IH-CCA tissue compared to control liver tissue ($p=0.0003$; Wilcoxon matched-pairs signed rank test). 75% (15/20) of IH-CCA tissue samples were TNC positive. The median (IQR) TNC

histoscore for IH-CCA compared to paired normal liver tissue was 4 (8.5) and 0 (0) respectively.

Figure 5-3C shows overall comparison of PH-CCA and IH-CCA tissue TNC histoscore with their respective control liver tissues. TNC histoscore was significantly higher ($p < 0.001$; Wilcoxon matched-pairs signed rank test) in CCA tissue samples compared to control liver tissues. The median (IQR) TNC histoscore for CCA tissues were 2.5 (6). 79.6% (44/54) of the paired normal liver tissue were negative for TNC expression. Of the positive normal tissue sections ($n=10$), only one normal had a TNC histoscore of 12, which was the only section with a score >6 . This tissue section (**Figure 5-2C**) also had areas of periportal inflammation and fibrosis and had diffuse TNC immunolabelling (**Figure 5-2D**).

5.1.2 TNC immunolabelling and survival in cholangiocarcinoma

Patient demographics and clinicopathological data for the PH-CCA and IH-CCA cohorts included in this study are shown in **Table 5-1** and **Table 5-2**, respectively. There was no difference in overall survival in this group of PH-CCA patients when dichotomised into TNC-positive and TNC-negative groups ($p=0.135$; Log-rank (Mantel-Cox); **Figure 5-2**).

There was also no difference in overall survival when the PH-CCA group was stratified into high- and low-expression of TNC using TNC histoscore of 6 as the cut-off (Log-rank (Mantel-Cox) $p=0.967$). This value was used as the cut-off value between high- and low-expression because only 2/54 normal liver tissue sections had a score higher than 6.

Overall survival outcomes were not investigated separately for the IH-CCA group due to the small sample size. Demographic and clinicopathological data for 1 IH-CCA patient was not available.

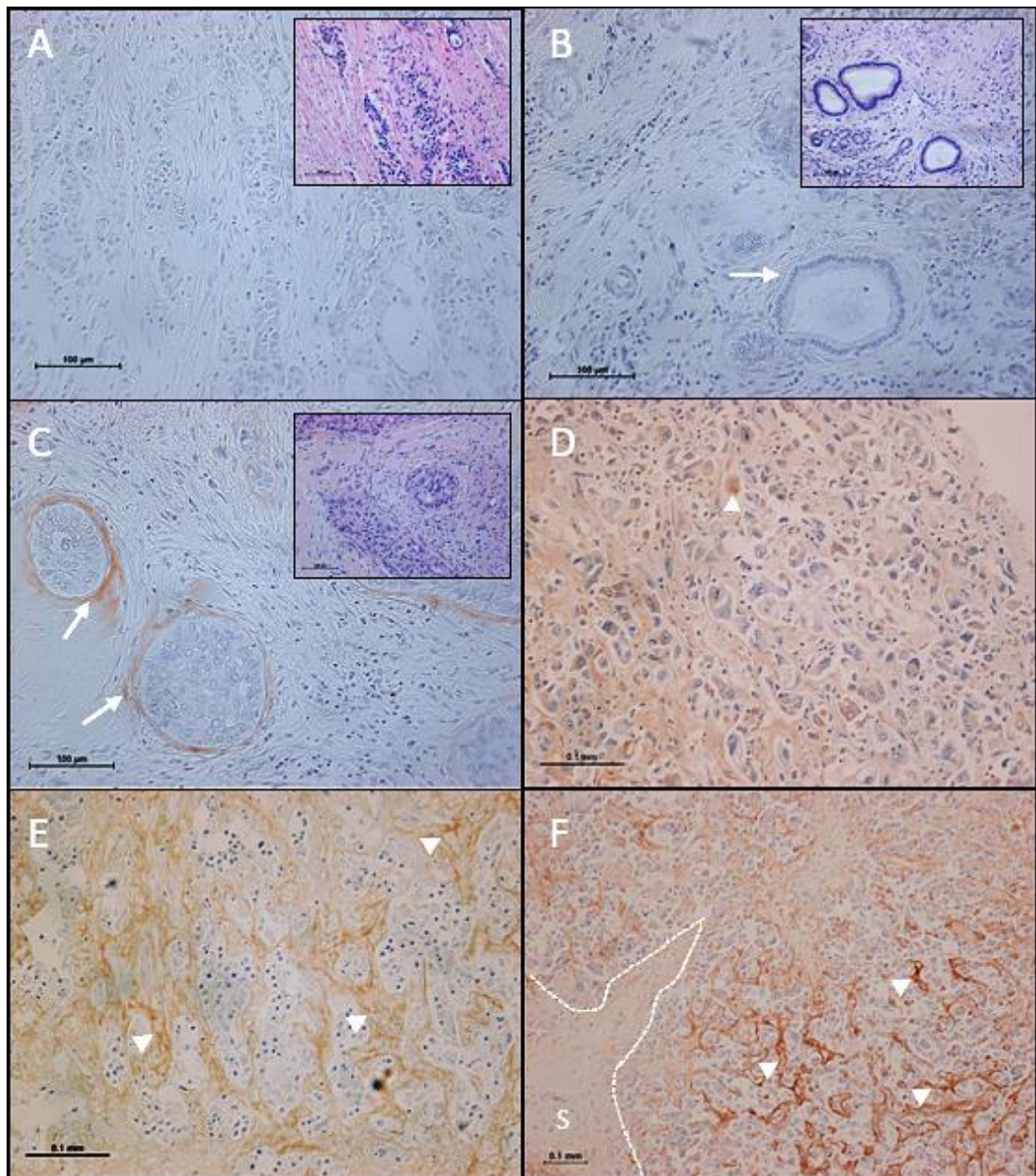


Figure 5-1 TNC immunolabelled human PH-CCA tissue sections

TNC immunolabelling was performed on 5 μ m thick FFPE tissue sections from 34 PH-CCA tissue blocks. Six representative tumour sections shown in this figure. Scale bar 100 μ m, x20 magnification except **F** (x10).

A & B. PH-CCA tumour sections showing no TNC immunolabelling. Inset **A & B** show corresponding H&E sections with abundant fibrotic stroma and glandular structures. White arrow shows in **B** shows a ductular structure with biliary-like epithelium (columnar epithelium with basal nuclei) and no TNC immunolabelling.

C. PH-CCA tumour section showing areas of TNC immunolabelling around nests of tumour cells (white arrows). Inset C shows a similar area from the corresponding H&E section that demonstrates abundant connective tissue surrounding tumour nests.

D. PH-CCA tumour displaying low intensity extra-cellular TNC immunolabelling. Occasional cytoplasmic positivity seen (white arrowhead).

E. PH-CCA tumour showing moderate intensity TNC immunolabelling which is widespread on this image (multiple white arrowheads)

F. PH-CCA tumour section showing high intensity TNC immunolabelling around tumour cells but low intensity labelling around the surrounding connective tissue stroma (labelled S, white dotted line)

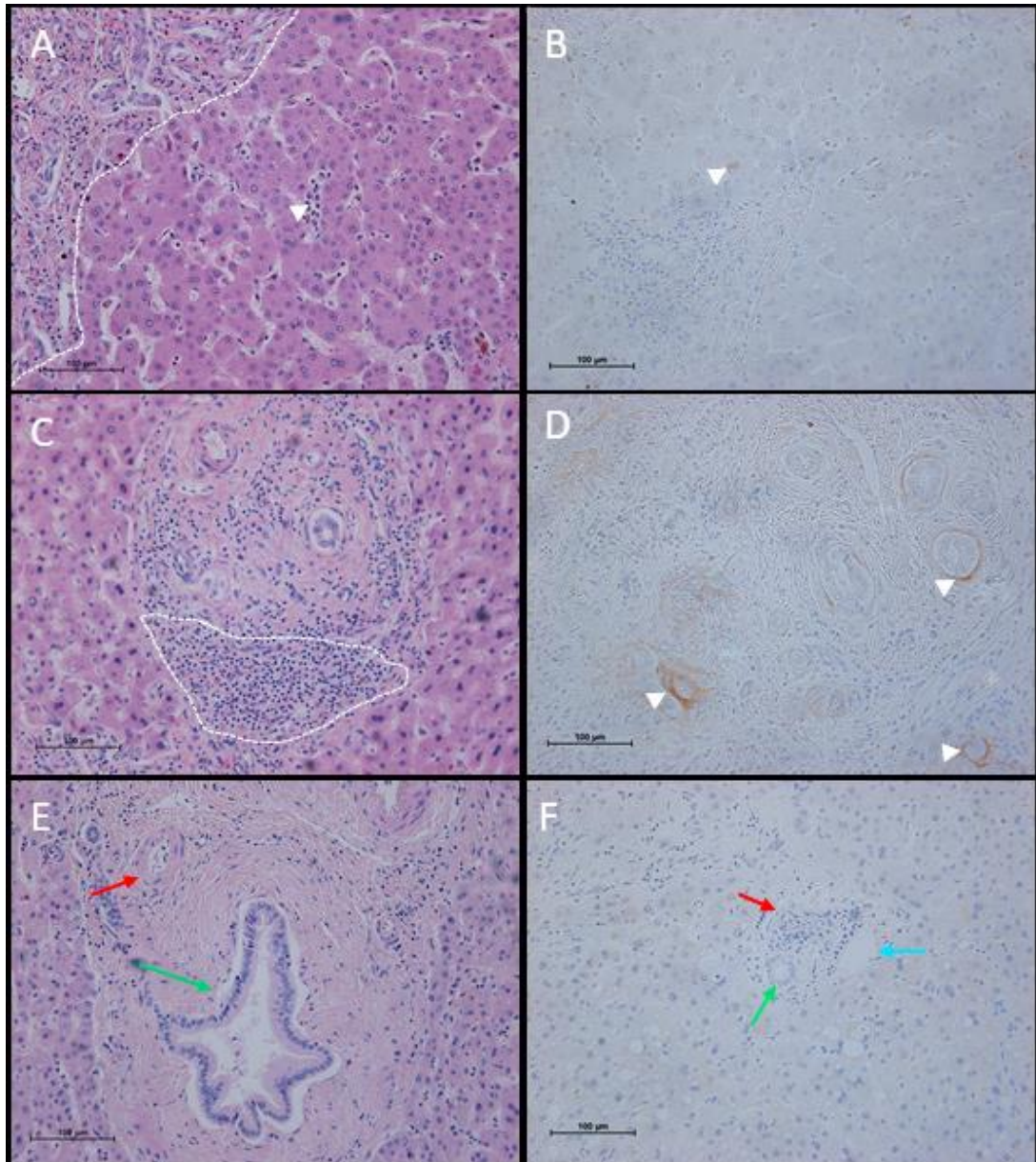


Figure 5-2 TNC in para-cancerous normal human liver tissue

TNC immunolabelling was performed on 5µm sections of FFPE para-cancerous normal human liver tissue from 54 tissue blocks. Three representative tumour sections shown in this figure; left panel H&E and right panel TNC immunolabelling of the same block. Scale bar 100µm, x20 magnification.

A shows a H&E stained section of para-cancerous normal liver showing fibrous periportal section of tissue (left top of image; boundary marked with white dotted line) distinct from the more homogenous hepatocyte architecture in the rest of the image. White arrowhead shows multiple Kupffer cells in the hepatic sinusoids. **B** shows negative TNC immunolabelling in the same liver tissue shown in **A**. Occasional brown staining was seen (white arrowhead) but this did not fit the pattern of TNC immunolabelling and is likely to be liver pigments.

C shows a periportal area with significant inflammatory cell infiltrate and fibrosis. This pattern of periportal fibrosis is likely due to underlying liver disease such as chronic hepatitis. **D** shows a section from the same tissue block that demonstrates focal TNC immunolabelling around perivascular and peri-glandular areas. This tissue section scored the maximum score of 12 on the TNC histoscore.

E&F shows H&E and TNC immunolabelled sections from the same control liver tissue block showing vascular and biliary structures. **E** shows a small intra hepatic bile duct (green arrow) with concentric fibrosis. Hepatic artery branch is also seen (red arrow). **F** shows negative TNC immunolabelling around portal structures (red arrow shows branch of hepatic artery; green arrow shows biliary radicle; blue arrow shows branch of portal vein)

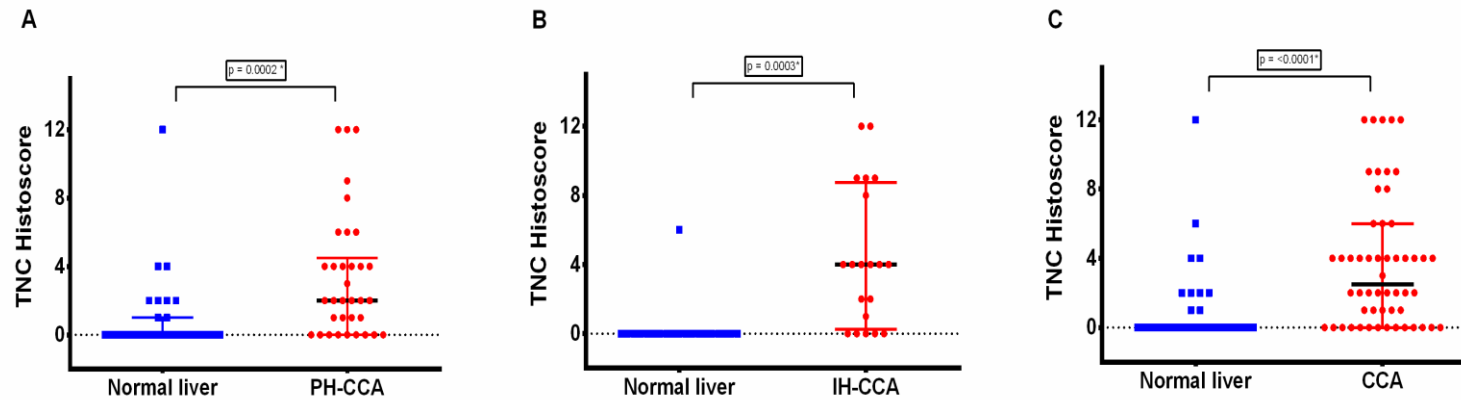


Figure 5-3 TNC histoscore comparison between paired CCA tissue and matched control liver

A. Comparison of TNC histoscore between PH-CCA tissue and paired control livers (n=34). PH-CCA tissue had significantly higher TNC score compared to matched control liver tissue (p=0.0002). **B.** Comparison of TNC histoscore between IH-CCA tissue and paired control livers (n=20). IH-CCA tissue was significantly more positive for TNC compared to matched control liver tissue (p=0.0003). **C.** Comparison of TNC histoscore between all CCA tissues with their respective paired normal liver controls (n=54; p<0.001).

5µm paraffin-embedded archival specimens of CCA tissue and matched control liver tissue were subject to TNC immunolabelling. TNC histoscore was the product of the TNC intensity score (0, none; 1, weak; 2, moderate; 3, high) and the distribution score (number of positive quadrants). Individual data points, median (horizontal black line) and IQR (error bars) shown.

Table 5-1 PH-CCA patient demographics and clinicopathological variables

Variable	Value
Age, years Median (range)	58.5 (33-81)
Gender Female % Male %	16 (47.1) 18 (52.9)
Surgical procedure, n (%) Left trisectionectomy Left trisectionectomy + caudate lobectomy +/- PV/HA resection Right trisectionectomy Right trisectionectomy + caudate lobectomy +/- PV resection / CBD excision Right trisectionectomy + caudate lobectomy + pancreaticoduodenectomy Right / Left hepatectomy +/- caudate lobectomy +/- PV resection Other (Orthotopic liver transplantation; Bile duct excision)	6 (17.6) 6 (17.6) 7 (20.6) 5 (14.7) 1 (2.9) 6 (17.6) 3 (8.8)
Tumour size, mm Median (range)	30 (10-75)
Tumour grade, n (%) G1 (Well differentiated) G2 (Moderately differentiated) G3 (Poorly differentiated)	19 (55.9) 10 (29.4) 5 (14.7)
Vascular invasion, n (%) Yes No or unknown	21 (61.8) 13 (38.2)
Perineural invasion, n (%) Yes No or unknown	28 (82.4) 6 (17.7)
T stage, n (%) 1 or 2 3 or 4	19 (55.9) 15 (44.1)
N stage, n (%) N0 N1 or N2	12 (35.3) 22 (64.7)
Resection margin, n (%) R0 R1	15 (44.1) 19 (55.9)
Tenascin C, n (%) Positive Negative	25 (73.5) 9 (26.5)

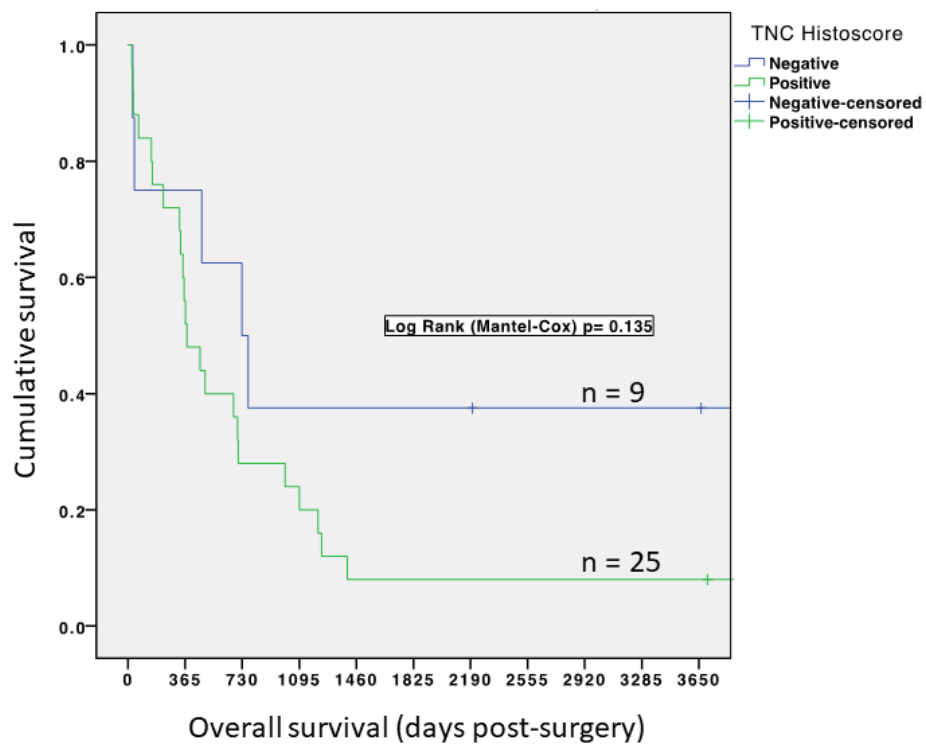


Figure 5-4 Overall survival in PH-CCA cohort stratified by TNC expression

The graph shows overall survival in days post-surgery of the PH-CCA cohort of patients stratified by expression of TNC (negative or positive). No statistically significant difference in overall survival was observed between the TNC positive (n=25) and negative (n=9) groups in the PH-CCA cohort (total n=34)

Table 5-2 IH-CCA patient demographics and clinicopathological variables

Variable	Value
Age, years Median (range)	63 (42-83)
Gender Female % Male %	15 (78.9) 4 (21.1)
Surgical procedure, n (%) Left trisectionectomy Left trisectionectomy + caudate lobectomy Right trisectionectomy Right / Left hepatectomy Left lateral sectionectomy Other (Left trisectionectomy + pancreaticoduodenectomy + distal gastrectomy + radical lymph node dissection; Segment 4b/5 resection; Segment 3/4 with gastric resection and transverse colectomy)	4 (21.1) 2 (10.5) 5 (26.3) 4 (21.1) 1 (5.3) 3 (15.8)
Tumour size, mm Median (range)	95 (13-190)
Tumour grade, n (%) G1 (Well differentiated) G2 (Moderately differentiated) G3 (Poorly differentiated)	3 (15.8) 12 (63.2) 4 (21.1)
Vascular invasion, n (%) Yes No	13 (68.4) 6 (31.6)
Perineural invasion, n (%) Yes No or unknown	7 (36.8) 12 (63.1)
T stage, n (%) 1 or 2 3 or 4	12 (63.2) 7 (36.8)
N stage, n (%) N0 or unknown N1 or N2	14 (73.7) 5 (26.4)
Resection margin, n (%) R0 R1	6 (31.6) 13 (68.4)
Tenascin C, n (%) Positive Negative	15 (78.9) 4 (21.1)

5.2 TNC is present in selected murine xenograft and orthotopic liver tumour tissue

The presence of TNC protein in murine tissue was investigated to establish the expression patterns in normal liver and two types of xenograft and orthotopic liver tumour tissue (TFKluc2B2 and SW620). These were the animal models set up to investigate active TNC targeting *in vivo* described in **Chapter 6**. SW620 colorectal cancer xenograft tissues were investigated as the SW620 cells are known to highly express TNC (Dr A Maqbool, personal communication). The TNC antibody used was a mouse monoclonal anti-TNC antibody 4F10TT (Immuno-Biological Laboratories Co. Ltd, Japan) with an anti-mouse IgG secondary polymer kit (ImmPRESS®, Vector laboratories, UK). The optimised method is described in **Table 2-1**.

Normal murine liver tissues were from non-tumour bearing BALB/c nude mice that had *in vivo* exposure to a fluorescent TNC affimer (TNC15C-Rh probe) as described in **Section 6.1**. The binding site of TNC affimer and the TNC antibody were expected to be different and therefore no competition for the TNC binding site was anticipated (Dr D Tomlinson, personal communication).

The TFKluc2B2 and SW620 xenografts were established in CD1 nude and BALB/c nude mice, respectively. The TFKluc2B2 and SW620 orthotopic liver tumour tissues were established in BALB/c nude mice.

5.2.1 TNC expression on xenograft tissue

10 SW620 xenograft tumours were investigated for TNC expression to ascertain any correlation between tumour size and TNC histoscore. These tissues were obtained from 10 BALB/c nude female mice bearing SW620 xenografts with no *in vivo* exposure to any treatments. The animals were sacrificed at four tumour size thresholds based on

calliper measurements on day 8 (Group A), 10 (Group B), 21 (Group C) and 28 (Group D) following injection of 1×10^7 SW620 cells in 100 μ L of PBS subcutaneously into right hind flank. The tumour volumes by mechanical calliper measurement, HF-US measurement and their corresponding TNC histoscores on xenograft tumour sections are shown in **Table 5-3**.

In Group A xenografts, HF-US measurement was lower compared to mechanical calliper measurement (Mean (mm³) 52.33 vs 113.67) but this was not statistically different ($p=0.25$; Wilcoxon matched-pairs signed rank test). In Group B, both modalities gave a similar tumour volume measurement. In group C, the tumour volume was higher in the HF-US group (1120.67 vs 973.0 mm³) but this was not statistically different ($p=0.5$; Wilcoxon matched-pairs signed rank test). Group D could not be compared as it included only one xenograft tumour.

The TNC histoscore was at maximum regardless of tumour size. Each xenograft scored the maximum for both distribution and intensity of TNC. As the tumour volume increased, more areas of tumour necrosis were observed. Necrotic areas were ignored for scoring as they tend to react with antibody non-specifically.

All FFPE SW620 tissue blocks from animals included in the TNC and GFP affimer experiments described in **Sections 6.1.4.1** and **6.1.4.4** were subject to TNC immunolabelling. These consistently scored the maximum TNC histoscore of 12. Four representative sections from these xenografts are shown in **Figure 5-5 A-D**.

Three TFKluc2B2 xenograft tissue sections were also examined for the presence of TNC and two representative sections are shown in **Figure 5-5 E-F**. The extracellular pattern of expression was similar to SW620 xenografts but more TNC immunolabelling was seen near the tumour cell interface with surrounding connective tissue. Overall, the distribution of TNC immunolabelling was restricted to focal areas as opposed to the diffuse distribution seen in the case of SW620 xenografts.

Table 5-3 Comparison of mechanical calliper vs HF-US tumour volume measurement in temporal SW620 xenografts and their corresponding TNC histoscore

In Group A xenografts, mean HF-US tumour volume (52.33mm³) vs mechanical calliper measurement (113.67mm³) was not statistically different (p=0.25; Wilcoxon matched-pairs signed rank test). In Group B, both modalities were comparable (201.67 vs 212.0 mm³). Group C tumour volumes were higher in the HF-US group (1120.67 vs 973.0 mm³) but this was not statistically different (p=0.5; Wilcoxon matched-pairs signed rank test). Group D could not be compared due to insufficient numbers.

The TNC histoscore for these xenografts did not vary with tumour size. (Mean TNC histoscore 12 in all groups).

	Calliper tumour volume (mm³)	HF-US tumour volume (mm³)	TNC histoscore
Group A			
1	125	79	12
2	118	51	12
3	98	27	12
Mean	113.67	52.33	12
Group B			
4	215	242	12
5	242	166	12
6	179	197	12
Mean	212.0	201.67	12
Group C			
7	973	1128	12
8	1060	909	12
9	886	1325	12
Mean	973.0	1120.67	12
Group D			
10	1,607	1092	12
Mean	N/A	N/A	N/A

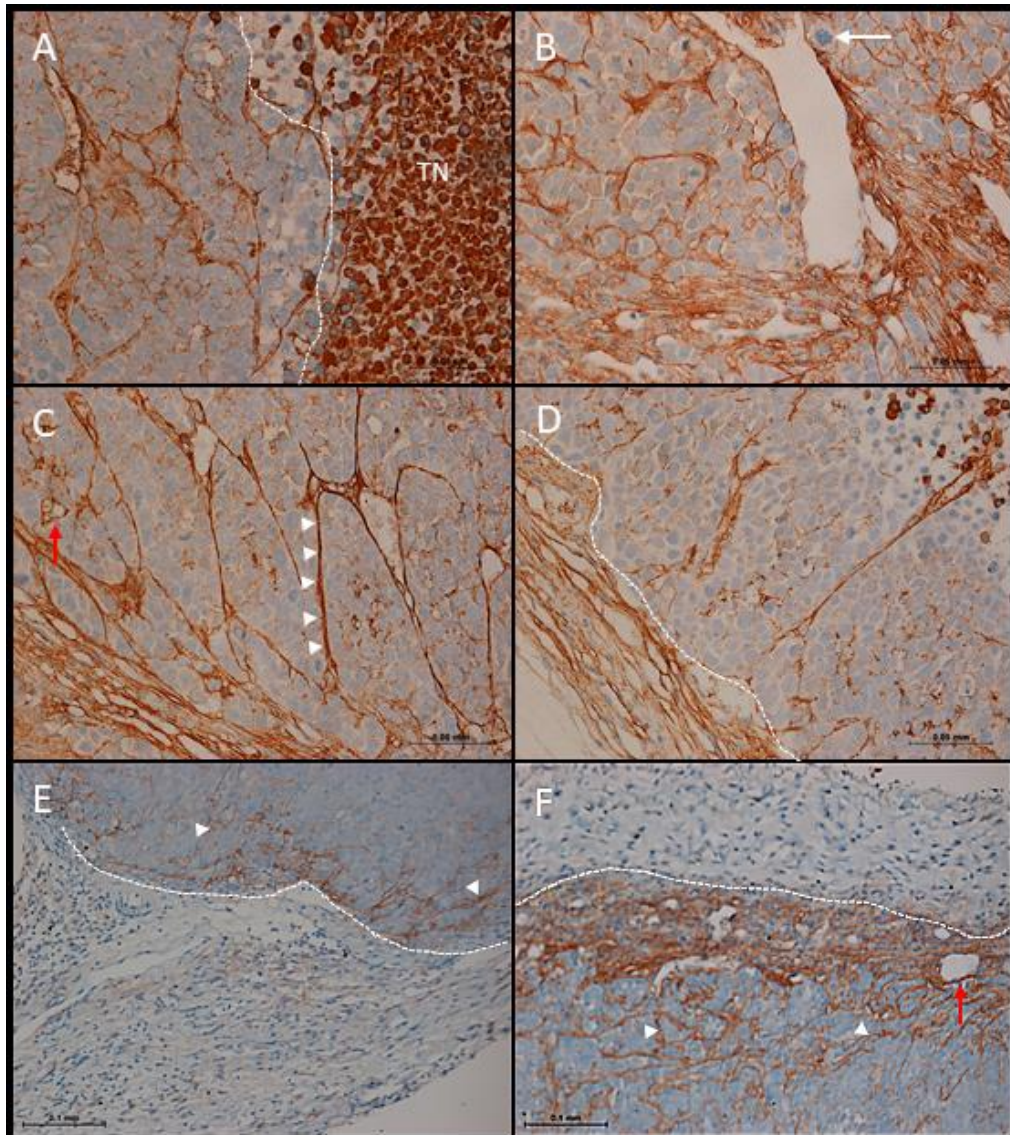


Figure 5-5 Representative sections of TNC immunolabelled SW620 and TKFluc2B2 xenografts

TNC immunolabelling was performed on 5µm sections of FFPE SW620 and TKFluc2B2 xenograft tissues. Images are from representative tumours. Tissue sections demonstrated mainly extra-cellular TNC immunolabelling in the connective tissue surrounding tumour cells. All SW620 xenografts investigated had diffuse TNC immunolabelling throughout the entire xenograft tumour cross-section. **A-D** Scale bar 0.05mm, x40 magnification. **E-F** Scale bar 0.1mm, x20 magnification.

A shows areas of tumour necrosis (to the right of white dotted line) were ignored for the TNC histoscore. A hypersegmented neutrophil is seen in **B**.

C clearly shows the linear pattern of TNC immunolabelling (white arrowheads). A small vessel is also seen (red arrow) with perivascular TNC immunolabelling.

D shows the boundary between xenograft tumour (white dotted line) and the subcutaneous tissue. Strong TNC positivity is also seen in the surrounding connective tissue.

E & F show two TFKluc2B2 xenografts demonstrating TNC positivity mainly in the extra-cellular matrix around tumour cells near the interface between tumour cells and the connective tissue (white dotted line) in the subcutaneous space. A blood vessel (red arrow) with strong TNC immunolabelling is seen in **F**.

5.2.2 TNC immunolabelling in orthotopic liver tumours

Twelve TFKluc2B2 orthotopic liver tumour tissue sections from tumours set up using the methods described in **Sections 3.2.1** and **3.2.2** were subject to TNC immunolabelling. The tumour area and peritumoral normal liver were scored separately on distribution and intensity. The median TNC histoscore for the liver tumour area was 10 (range 0-12) compared to peritumoral normal liver which consistently scored 4. **Figure 5-6 B** shows a representative image of TFKluc2B2 orthotopic liver tumour tissue with adjacent normal liver. This shows focal areas of less intense immunolabelling in the surrounding normal liver compared to the diffuse more intense immunolabelling within the tumour.

Six FFPE tissues from orthotopic liver tumours established using SW620 were kindly gifted by Dr L E McVeigh. These tumours were established using direct injection of SW620 cells into the liver under HF-US guidance. The tumour area and peritumoral normal liver were scored separately on distribution and intensity. 4/6 tumours scored 12 and 2/6 tumours scored 4 giving a median tumour TNC histoscore of 12 (range 4-12). In comparison, 5/6 peritumoral normal liver scored 4 and 1/6 scored 2 giving an overall median TNC histoscore of 4 (range 2-4). However, the distribution of the TNC positive areas in the adjacent normal liver was different to the tumoral areas (**Figure 5-6 E**). TNC immunolabelling in the normal murine liver was observed infrequently in focal areas in the extra-cellular spaces around liver sinusoids and some blood vessels compared to the more diffuse immunolabelling in the tumour tissue.

5.2.3 TNC immunolabelling in normal murine liver

TNC immunolabelling performed on FFPE liver tissue from the nine non-tumour bearing animals included in the experiment described in **Section 6.1.2** revealed weak positive (8/9 samples) or negative (1/9 liver samples).

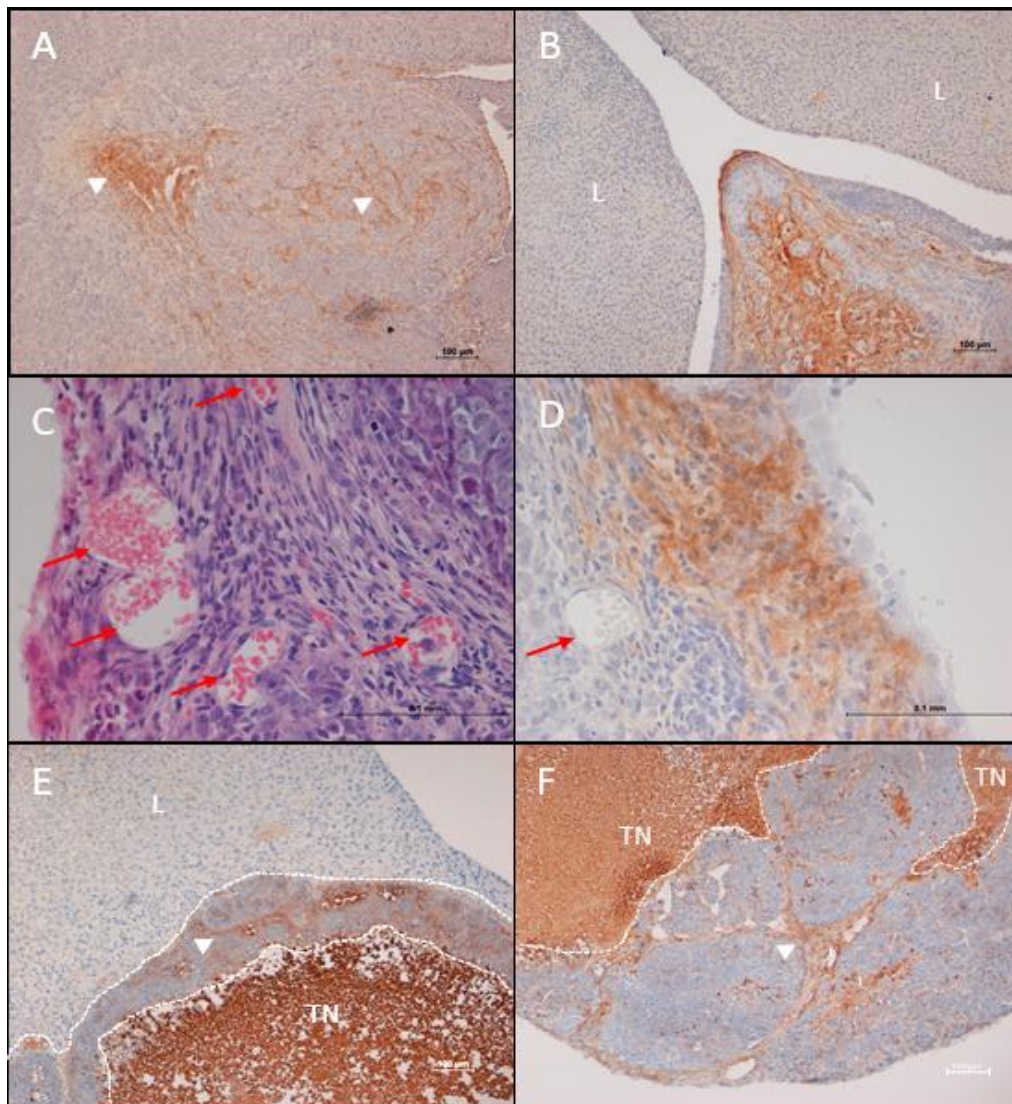


Figure 5-6 TFKluc2B2 and SW620 orthotopic liver tumours

A-D represent TFKluc2B2 orthotopic CCA tumours. Diffuse TNC immunolabelling is seen throughout the tumours shown in **A & B**. **B** shows adjacent normal liver (L) which show minimal TNC immunolabelling. **C** is an H&E image of a TFKluc2B2 orthotopic liver tumour showing several blood vessels (red arrows) surrounded by tumour cells and connective tissue stroma. **D** shows perivascular (red arrow shows blood vessel) TNC immunolabelling. This tumour only had focal areas of TNC positivity.

E-F represent representative sections from two SW620 liver tumours. Large areas of tumour necrosis (TN) were a feature of SW620 tumours. There were distinct areas of extracellular matrix TNC immunolabelling (white arrow heads) spread through the viable tumour areas. **E** shows the adjacent non tumour liver which had very little TNC immunolabelling except occasional positive sinusoids.

Scale bar 100µm, **A-B, E-F** x10 magnification, **C-D** x40 magnification.

The weak positive immunolabelling was seen mainly in the peri-sinusoidal spaces and occasionally around large blood vessels (**Figure 5-7 C & D**).

TNC immunolabelling was also performed on fresh-frozen liver tissue to clarify if the weak positive immunolabelling seen in paraffin-embedded liver tissue was an artefact due to the extensive tissue processing required for paraffin-embedded tissue. Five murine liver cryosections were investigated. 2/5 were negative and 3/5 demonstrated weak TNC immunolabelling. The pattern was similar (i.e. peri-sinusoidal) as observed in liver paraffin sections (**Figure 5-7 A & B**).

5.3 TNC is present in selected cell lines

A panel of cancer cell lines, fibroblast cell lines and a macrophage cell line were selected for the assessment of TNC protein expression. SW620, TFK-1 and TFKluc2B2 were included as they were the main cell lines being utilised for *in vivo* experiments in this project. THP-1, a human monocyte cell line derived from blood of a patient with acute monocytic leukaemia and RAW254.7 mouse macrophage cell line were also investigated. HCT116 human colorectal cancer cells, a type of normal human embryonal fibroblast cell HFF-2 and a cancer-associated fibroblast cell line from a luminal A breast cancer LA-CAF were also included. These cell lines were investigated to ascertain TNC expression by cell type and confirm findings reported in the literature. The purpose was to screen for cell lines for *in vitro* nanoparticle targeting assays.

SW620, TFK-1, TFKluc2B2, RAW264.7 and THP-1 whole cell lysates were used to quantitate TNC mRNA expression by RT-PCR. This experiment was carried out by Dr A Maqbool using a previously optimised method as described in **Section 2.6.4**. The results of this are shown in **Figure 5-8**. TNC mRNA was not detectable in RAW264.7 macrophages. TFK-1, TFKluc2B2 and THP-1 cell lines had much lower TNC mRNA compared to SW620.

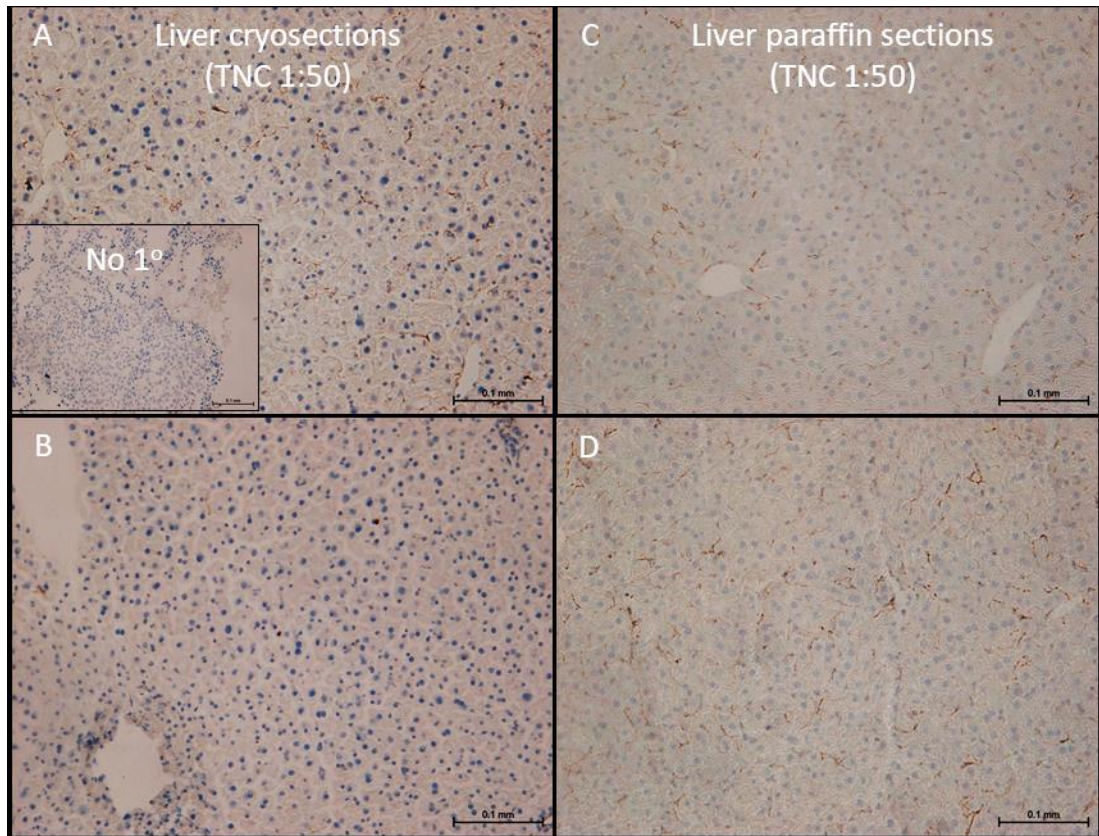


Figure 5-7 TNC expression in normal murine liver tissue

Liver cryosections in **A** & **B** and liver paraffin sections in **C** & **D** show occasional weak TNC immunolabelling in the liver sinusoids. Inset **A** shows the no primary antibody section which does not show any reactivity with the antibody.

Primary antibody dilution 1:50 for both cryosections and paraffin sections. No primary antibody section was clear (inset A). Scale bar 0.1mm, x20 magnification.

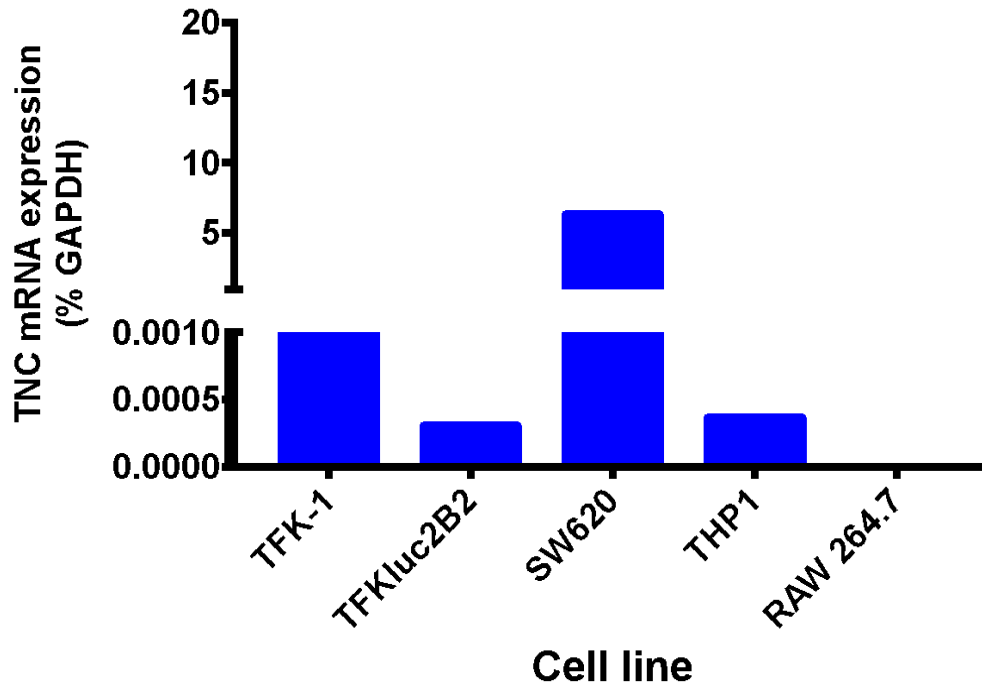


Figure 5-8 TNC mRNA expression in selected human and murine cell lines by RT-PCR

SW620 cell line had high TNC mRNA (5.467%) compared to TFK-1 (0.007%), TFKluc2B2 (0.0003%) and THP-1 (0.0003%). RAW 264.7 was negative for TNC mRNA expression.

Detection of TNC protein by IF was carried out in the panel of cell lines. HCT116 cells were known to be negative for TNC mRNA by PCR (Dr A Maqbool, personal communication). HFF-2 cells were included as it was both a fibroblast cell and an embryonal cell and hence expected to be positive for TNC. A review conducted by Giblin and Midwood (2015) reported abundant expression of TNC in embryonal tissues in developing mouse, chicken, rat and human. LA-CAF being a luminal A breast cancer-associated fibroblast was also expected. Multiple studies have shown that cancer-associated fibroblasts and angiogenic blood vessels are the main producers of TNC protein (Lowy and Oskarsson, 2015; Midwood *et al.*, 2016). The mouse macrophage cell line RAW264.7 was also assessed for TNC expression as tissue-associated macrophages are a component of the cancer stroma. The TNC-antibody used (Rabbit polyclonal Anti-TNC antibody SC20932, Santa Cruz Biotechnology, USA) was recommended for the IF detection of TNC of human or mouse origin.

As shown in **Figure 5-9**, SW620, TFK-1, TFKluc2B2, HFF-2 and LACAF cell lines were positive for TNC expression while HCT116 and RAW264.7 were negative. The fluorescence pattern appeared cytoplasmic in the TFK-1 and TFKluc2B2 cells but in SW620 and LACAF, fluorescence was not confined to the cell membrane, suggesting areas of protein secreted by the cells (**Figure 5-9 Row C**).

Presence of TNC protein in cell lysates was assessed by immunoblotting in selected cell lines (**Figure 5-10**). In the preliminary experiment with 30µg protein loading for each cell line, bands corresponding to that expected for TNC were visualised only in the SW620 cell line (**Figure 5-10 1B**). This experiment was repeated to include further cell lines (SW480, HCT116, RAW264.7-LPS, HFF-2 and LACAF) which revealed that TFK-1, TFKluc2B2, SW480, HCT116 and RAW264.7 cell lines were negative for TNC while SW620, RAW264.7-LPS (i.e. RAW264.7 cells stimulated with bacterial lipopolysaccharide), HFF-2 and LACAF cell lines were positive (**Figure 5-10 2B**).

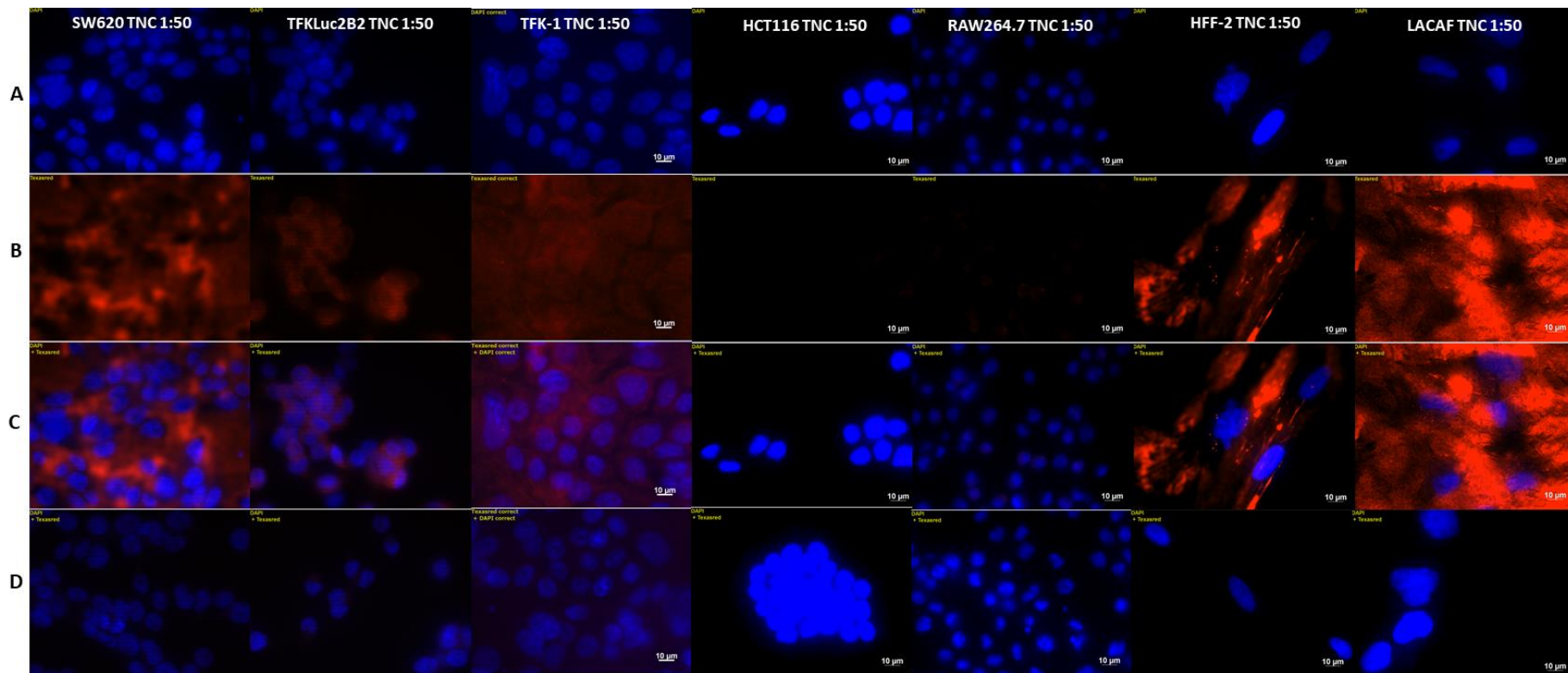


Figure 5-9 TNC detection using immunofluorescence in selected cell lines

SW620, TFKluc2B2, TFK-1, HFF-2 and LACAF were positive (denoted by the red fluorescence) for TNC while HCT116 and RAW264.7 were negative.

Row A DAPI filter; **Row B** TexasRed filter; **Row C** DAPI+TexasRed filters; **Row D** No primary antibody control DAPI+TexasRed filters.

Exposure settings kept constant for cell lines represented in columns 1-3 with the maximum exposure time for TexasRed filter set using the SW620 cell line. For the cell lines represented in columns 4-7, the TexasRed exposure time was set to the brightest LACAF cell line. HCT116 and RAW264.7 cells did not show any positivity even when the exposure time was manually increased (images not shown). Scale bar 10 μ m

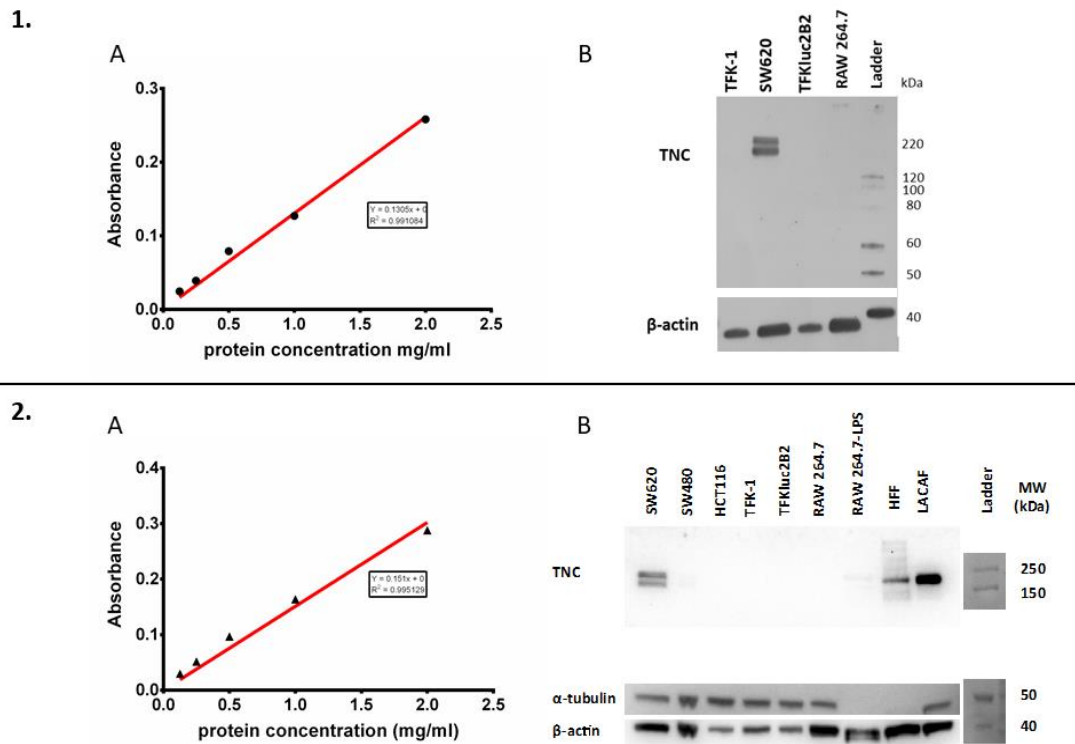


Figure 5-10 Detection of TNC protein by immunoblotting

1.A. and **2.A.** show the protein standard curves for each experiment. The standard curves were used to calculate 30 μ g protein loading for each cell line.

1.B This shows the TNC and β -actin bands for TFK-1, SW620, TFKluc2B2 and RAW 264.7 cell lines. Only SW620 cell line showed a detectable band around the expected 200kDa MW. TFK-1, TFKluc2B2 and RAW 264.7 were negative for TNC protein. β -actin band volumes were smaller in TFK-1 and TFKluc2B2 which suggested unequal protein loading or inherent differences in the cell lines.

2.B This shows the TNC, β -actin and α -tubulin bands for SW620, SW480, HCT116, TFK-1, TFKluc2B2, RAW 264.7, RAW 264.7-LPS, HFF-2 and LACAF cell lines. The highest band volume around 200kDa MW was detected in LACAF. SW620 showed two distinct bands which could represent two separate TNC isoforms. A faint band was detected in LPS stimulated RAW 264.7 macrophages (RAW-264.7-LPS) but this band was absent in the unstimulated RAW 264.7. The remainder of the cell lines were negative. Two housekeeping genes were used as loading controls in this experiment as initial experiment protocol consistently showed unequal β -actin loading despite equal amounts of protein loading. α -tubulin loading appeared much more consistent across cell lines but curiously absent in RAW 264.7-LPS and HFF-2 cells.

5.4 Discussion

In this chapter, TNC was explored as a potential theranostic biomarker in CCA. The expression of TNC was investigated in human and murine tissue as well as multiple different cell lines using different techniques.

5.4.1 Tenascin C in human cholangiocarcinoma tissue

Aishima *et al.* (2003), Iguchi *et al.* (2009) and Soejima *et al.* (2018) have reported TNC expression patterns in IH-CCA. TNC has also been reported as a marker of poor overall survival in IH-CCA (Aishima *et al.*, 2003). However, there are no published reports of TNC expression in PH-CCA. In the present study, IH-CCA and PH-CCA tissue frequently expressed TNC, 75% and 73.5% positive expression, respectively (**Section 5.1.1**). In contrast, the paired para-cancerous control liver tissue was only 18.5% positive. TNC histoscore was significantly higher in IH-CCA ($p=0.0003$) and PH-CCA ($p=0.0002$) tissues compared to their paired normal liver tissue controls (**Figure 5-3**).

The annotated protein expression for TNC in normal liver tissue is negative according to the human protein atlas (Human Protein Atlas, 2019b). However, the reliability score for TNC in normal tissues only has 'approved' status (as opposed to 'supported' or 'enhanced') which means that the staining pattern is only partly similar in the two antibodies used and that the RNA tissue location is different to the protein location (Human Protein Atlas, 2019a). For the antibody used in this study (HPA004823), the human protein atlas reports negative hepatocytes and bile duct cells, moderate positivity of glandular cells of the gallbladder and positivity in fibres of connective tissue in general (Human Protein Atlas, 2019b). However, it does not comment on TNC expression in normal liver sinusoids and peri-vascular areas of the liver which are the areas of the normal liver that demonstrated TNC immunolabelling in the present study (**Figure 5-2**).

The scoring method utilized by Soejima *et al.* (2018) classified tissues as TNC positive in >25% of tumour cells or tissue areas were positive regardless of staining intensity and reported 37.5% high expression of TNC in IH-CCA tissues. The study reported no significant difference in overall survival between the TNC high and low groups ($p=0.09$) and did not comment on adjacent normal tissue distribution of TNC. In contrast, the scoring method used by Aishima *et al.* (2003) considered sections to be TNC positive if >10% of intratumoral stroma had staining regardless of intensity. These differences in scoring make comparisons between them difficult. The scoring method (**Figure 2-4**) utilised for the present study incorporated a distribution score as well as an intensity score as diffuse staining at high intensity was considered beneficial for a theranostic biomarker.

Okamura *et al.* (2005) also reported TNC expression in 21 cases of IH-CCA and compared this to several subtypes of HCC. They concluded that TNC expression in IH-CCA was significantly higher (score 0.96 ± 0.40 compared to 0.27 ± 0.28) scirrhou HCC which is a rare variant of HCC. IH-CCA score was higher than the other HCC pathological subtypes compared (well-differentiated, moderately differentiated and poorly differentiated HCC) but no comparison was made with adjacent normal liver tissue nor was the overall number of positive tumours reported (Okamura *et al.*, 2005).

Overall survival in the present cohort of 34 PH-CCA patients was not significantly different when stratified by TNC positivity or by TNC high vs low expression (**Figure 5-4**). However, the low numbers of patients included could have resulted in type II error. A formal power-calculation was not performed prior to the study. If a power calculation is performed assuming 60% 2-year survival in TNC positive and 30% in TNC negative group (as reported by Aishima *et al.* (2003) for TNC expression at the IH-CCA invasive front) at 80% power and α of 0.05, the total sample size required to detect a difference in survival at 2 years post-surgery is 84 (Kane, 2016).

5.4.2 Tenascin C in murine disease models

The present study describes TNC expression in SW620 and TFKluc2B2 xenografts as well as orthotopic tumours. TNC expression was highest in SW620 xenografts, followed by the SW620 orthotopic model (**Section 5.4.2**). TFKluc2B2 xenografts and orthotopic tumour tissue were also positive for TNC but to a lesser degree compared to SW620. Given the higher expression, the SW620 model would be more practical for the pre-clinical validation of TNC targeted theranostic agents although it is not derived from a CCA cell line.

Mertens *et al.* (2013) used assessment of TNC expression in tissues as a surrogate marker of the effectiveness of drug (navitoclax) efficacy against cancer-associated fibroblasts (CAF). In a previous study of the syngenic rat model of IH-CCA used for this experiment, the authors had reported higher TNC expression in the liver tumour tissue compared to the adjacent normal liver (Sirica *et al.*, 2008). In this study, they reported a reduction in TNC positive stroma from 40% in the group treated with vehicle down to 10% in the group treated with navitoclax, a drug that induces apoptosis in myofibroblasts (Mertens *et al.*, 2013).

TNC expression in non-CCA murine models has been reported. A study on xenograft tissue from a metastatic mouse lung cancer cell line in GRS/A wild-type (TNC-expressing) and GRS/A TNC-knockout mice demonstrated the absence of TNC in the tumours of GRS/A TNC-knockout mice and showed a significant reduction in xenograft volume at 3 weeks in this group compared to the wild-type animals (Matsumoto *et al.*, 2017). This suggests that the TNC secreted by the stroma as opposed to the tumour cells themselves is the main driver of tumour growth, at least in the case of this cell line. This raises questions regarding the appropriateness of an animal xenograft model for TNC *in vivo* studies instead of an orthotopic tumour model as in the case of the latter, the CAFs would be recruited from the liver (Baglieri *et al.*, 2019) and are likely to

display a different phenotype to the CAFs recruited from subcutaneous tissue in the former. GRS/A mice are inbred, susceptible to mammary tumours and hepatomas but are immunocompetent (Bult CJ, 2019). A TNC-knock out immunocompromised mouse model maybe useful as a negative control in the pre-clinical validation of active TNC targeting. Another TNC knock-out mouse of C57BL/6 strain has been investigated in the context of subarachnoid haemorrhage (Fujimoto *et al.*, 2016) but not in carcinoma.

5.4.3 Tenascin C in selected cell lines

Several cell lines were investigated for the presence of TNC by RT-PCR, immunofluorescence and immunoblotting (**Section 5.3**).

TFK-1 and TFKluc2B2 cells showed low levels of TNC mRNA (**Figure 5-8**), were weakly positive on immunofluorescence for TNC (**Figure 5-9**) but negative for TNC protein expression by immunoblotting (**Figure 5-10**).

SW620 cell line was included in all three methods and was consistently positive for TNC. LACAF and HFF-2 were also positive (by immunofluorescence and immunoblotting) which was in keeping with expectations given their respective cells of origin. RAW264.7 cells stimulated with bacterial lipopolysaccharide expressed TNC protein by immunoblotting while unstimulated RAW264.7 cells were negative by both immunoblotting as well as RT-PCR for TNC mRNA expression.

The purpose of investigating TNC expression in a variety of cell lines was to ascertain the best *in vitro* model for the testing of targeted gold nanoparticles prior to their evaluation *in vivo*. Although a CCA cell line was preferable, the levels of TNC in TFK-1 and TFKluc2B2 cell lines were lower compared to SW620 cell line and therefore the SW620 cell line was selected for experiments evaluating TNC targeting *in vivo* (discussed in **Chapter 6**).

5.4.4 Tenascin C for theranosis in cholangiocarcinoma

As described in **Section 1.4.1**, TNC has low expression in normal adult tissues. This study (**Section 5.1**) and others have established TNC as an upregulated marker in cancers, often with a negative impact on prognosis (Ming *et al.*, 2019). The functional role of TNC in normal physiology and in tumour biology is now better understood (Midwood *et al.*, 2011; Midwood *et al.*, 2016). As highlighted in this chapter, several studies have investigated TNC in IH-CCA and this study confirms TNC expression in a small cohort of PH-CCA.

Studies have investigated targeting TNC with antibodies or antibody mimetics in Phase 0-Phase III clinical trials, mainly involving combination therapy with other drugs (Spence *et al.*, 2015) although none of these studies included BTCs.

A Korean group has investigated a multimodal nanoparticle with aptamers targeting nucleolin, $\alpha_v\beta_3$ integrin and TNC (Ko *et al.*, 2011). The *in vitro* data presented by the authors shows significantly higher uptake in five different cancer cell lines compared to control particles as well as single target labelled nanoparticles. The control cell lines (normal Chinese hamster ovarian cells and epithelial lung cells) did not show any difference. These multimodal particles also had the benefit of multimodal imaging properties as they could be used for MRI, fluorescence as well as radionuclide imaging due to their cobalt ferrite core, rhodamine in the silica shell and labelling with gallium-68 citrate, respectively. Despite promising *in vitro* data, no further pre-clinical validation studies nor first-in-man studies with this multimodal particle have been reported.

5.4.5 Future directions

At present, there is insufficient pre-clinical validation of TNC to justify clinical trials of TNC targeted therapy in CCA. More studies should focus on establishing TNC

expression in CCA, especially in PH-CCA which accounts for the majority of cases of CCA (Khan *et al.*, 2019).

Primary tumour TNC expression has been reported to be associated with lymph node metastasis in CCA (Aishima *et al.*, 2003) but TNC expression in positive lymph nodes (either macroscopic or microscopic) has not been investigated.

Another area of interest is TNC expression in the regenerating liver following liver resection as this would determine the feasibility of utilisation of TNC targeted agents in an adjuvant chemotherapeutic regimen following resection. The process of compensatory growth of the liver following liver resection is known to involve a complex interaction of cytokines, growth and metabolic factors (Fausto *et al.*, 2006) but a role for TNC and expression pattern of TNC in such cases has not been described.

Most studies including the present study explore TNC expression in the resected specimens of liver from patients deemed suitable to undergo curative-intent surgery.

This is a biased sample as most patients with CCA are not candidates for surgery.

Determination of TNC expression in biopsy specimens of patients deemed non-operable could extend the pool of patients for whom the CCA tumour expression of TNC is known and therefore are potential candidates for emerging novel treatments.

Mertens and colleagues (Mertens *et al.*, 2013) have demonstrated in pre-clinical studies that TNC expression could be used as a marker of effectiveness of treatment against CAFs in CCA. If a TNC targeted drug delivery platform is developed, effective anti-cancer therapy could be delivered directly to the CCA tumour microenvironment.

The opportunities for further research in CCA are vast, the pace of which is limited by adequate resources and networks of collaborations between CCA researchers which is fundamental to the translation of novel therapeutics for this rare group of cancers.

Chapter 6

Development of a tenascin C targeted theranostic platform using affimers

Introduction

AuNPs have demonstrated multiple properties that showcase their utility as theranostic particles and have been an area of extensive pre-clinical research in recent years (Jain *et al.*, 2012; Singh *et al.*, 2018). Given the role of gold nanoparticles in PTT and PTD (Singh *et al.*, 2018), this could be explored in cancers such as CCA where PTD is an established therapeutic option (Moole *et al.*, 2017; Wu *et al.*, 2019).

The concept of active targeting using AuNPs has also been explored (Patra *et al.*, 2010). An FDA approved AuNP carrying recombinant TNF- α protein was shown to be beneficial in a phase I clinical trial which enrolled patients with advanced solid tumours (Libutti *et al.*, 2010). Higher doses of recombinant TNF- α delivery without dose-limiting toxicity or immunogenicity was demonstrated (Libutti *et al.*, 2010).

Patra *et al.* (2008) also described active targeting in a pre-clinical orthotopic pancreatic adenocarcinoma model using a 5nm spherical AuNP carrying gemcitabine that was labelled with EGFR receptor targeting antibody (cetuximab). The authors reported higher tumour accumulation of gold in the EGFR-targeted AuNP compared to control as well as significant inhibition of tumour growth despite using a sub-therapeutic dose of 2mg/kg gemcitabine (Patra *et al.*, 2008). For this type of theranostic particle, a nanoscale carrier that serves as a delivery agent (that also provides contrast for imaging) which can be surface-functionalized to bind a specific target as well as carry an effective drug against the tumour of interest are required. All three components are evaluated in this chapter in the context of a novel theranostic particle in CCA, the concept of which is illustrated in **Figure 6-1**.

The nanoscale carriers evaluated in this chapter are gold nanoplates (AuNPLs) and gold nanorods (AuNRs) synthesised in-house at the University of Leeds by Dr Sunjie Ye and Dr Lucien Roach, respectively.

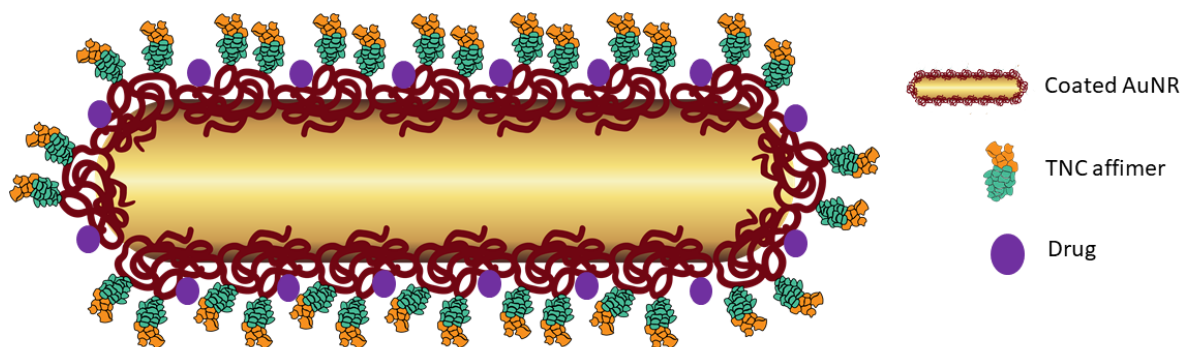


Figure 6-1 Schematic of a potential TNC targeted delivery platform.

This schematic illustrates a potential TNC targeted nanotherapeutic delivery platform with drug loaded, TNC affimer labelled coated AuNRs.

Schematic not drawn to scale. AuNR diameter can be varied; approximately 7-35nm diameter for the in-house synthesised AuNRs (Roach *et al.*, 2018). Drug and affimer attachment usually through thiol, amine or citrate bonds on the surface coating (various coating materials such as silica, polymers etc are available). Coating is required as the bare surface of gold with surfactant (usually cetrimonium bromide) used for the synthesis of these particles is inherently cytotoxic. Although AuNRs are shown in this figure, various shapes such as (plates, shells, tubes, wires etc) with specific properties can be synthesized.

TNC, the selected biomarker for active targeting in this chapter is one of the potential CCA theranostic biomarkers identified in the systematic review described in **Chapter 4**. Although the most commonly used targeting moieties in nanoparticle functionalization are antibodies, antibody replacement options such as peptides, aptamers (RNA and DNA) and affimers have been designed to overcome the limitations of antibodies (Baker, 2015; Bradbury and Pluckthun, 2015). TNC affimers are explored in this chapter as these are novel peptide scaffolds developed at the University of Leeds with several advantages over antibodies including smaller size, thermostability and relative ease of scaling up (Bedford *et al.*, 2017). Effective targeting of TNC affimers to TNC-expressing tumours is key to a TNC targeted delivery platform which could be translated clinically to deliver therapeutics.

TNC targeted affimer probes were synthesized by Dr D Tomlinson's group, School of Molecular and Cellular Biology, University of Leeds and fluorescent labelled with rhodamine red C₂ maleimide by Dr R Bon, School of Chemistry, University of Leeds. Three different batches of fluorescent labelled TNC affimers (TNC15C-Rh1, TNC15C-Rh2 and TNC15C-Rh3) were produced at three different time points and frozen in aliquots at -80°C. Alongside batches 2 and 3 of the TNC15C affimer probes, a control fluorescent labelled affimer probe targeting green fluorescent protein (GFP32C-Rh2 and GFP32C-Rh3) was also synthesized. These were all synthesised under sterile conditions to ensure they were safe for use in a pre-clinical animal model. The TFKluc2B2 orthotopic model (**Section 3.2.2**) and SW620 subcutaneous xenograft model and were utilised for the evaluation of these fluorescently labelled affimers. The TNC expression of these tumours is described in detail in **Section 5.2**.

Two model drugs, gemcitabine and irinotecan which are currently in clinical use in CCA therapy (Valle *et al.*, 2010; Sohal *et al.*, 2013), were also evaluated as part of the development of a TNC-based targeted drug delivery vehicle.

6.1 Active targeting with TNC affimers *in vivo*

TNC affimers have shown similar TNC specificity compared to TNC antibody during immunohistochemical applications (Tiede *et al.*, 2017) but their ability to target tumours *in vivo* was first explored in the present study. The aim was to assess the specificity of TNC affimer binding *in vivo* and to this end, fluorescent TNC affimers were evaluated.

6.1.1. Sensitivity of detection of fluorescent TNC affimers

The first batch of TNC affimers labelled with rhodamine red C₂ maleimide (TNC15C-Rh1; reported excitation/emission 560/580nm; concentration ~150µM) were supplied by Dr R Bon. To confirm that these fluorescent TNC Affimers were detectable on the IVIS Spectrum imaging system (PerkinElmer Inc. Waltham, MA, USA), 20µL of sample was placed in a small Eppendorf tube and imaged on the epi-illumination setting. Imaging was performed across a range of excitation (500nm, 535nm, 570nm) and emission (580nm, 600nm, 620nm and 640nm) wavelengths to detect optimum excitation/ emission wavelengths. Excitation 570nm/Emission 620nm was selected as the optimum wavelengths with the highest signal to background noise ratio. **Figure 6-2 A** shows detectable signal (green arrow) under these wavelengths.

Next, 100µL of TNC15C-Rh1 was injected subcutaneously into the left lower quadrant of a TFKluc2B2 liver orthotopic tumour bearing CD1 nude female mouse. The subcutaneous route of administration was selected over intravenous to slow systemic absorption and allow time for targeting. This animal had a positive signal over the abdomen on serial bioluminescence imaging (**Figure 3-10** (mouse 1)).

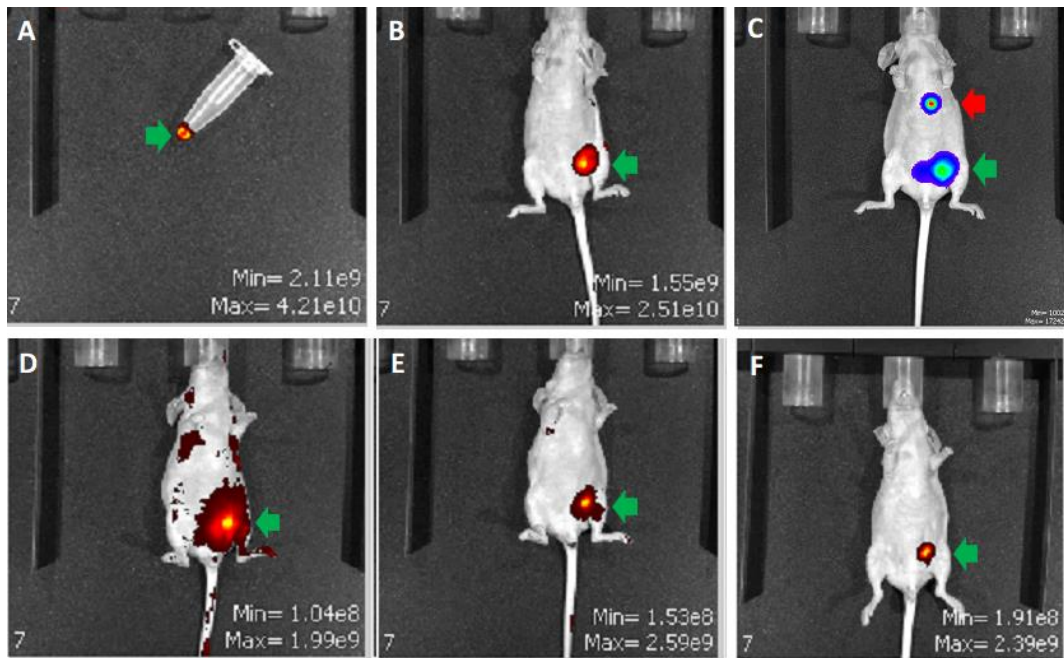


Figure 6-2 Detection of TNC15C-Rh1 probe *in vivo* over time.

A shows 20µL of TNC15C-Rh1 in an Eppendorf tube imaged at excitation 570nm/Emission 620nm. 100µL of probe was injected subcutaneously into left iliac fossa of a TFKluc2B2 liver orthotopic tumour bearing CD1 nude female mouse at 13 days post-tumour cell injection into liver and **B** shows an image under the same filters 1 min following this injection.

1.2mg of beetle D-luciferin was then injected intraperitoneally into right lower quadrant and **C** shows a bioluminescence image obtained 5 min following this injection. This confirms localization of tumour to the upper abdomen of the animal (red arrow) but also shows 'bleed through' (green arrow) of the fluorescence signals onto the bioluminescence filter.

D, E and **F** are images under the same filters taken at 6h, 24h and 48h post-injection of probe. Signal detected (green arrows) corresponds to the injection site. There was no detectable fluorescence signal localisation to orthotopic tumour.

Scale not included as signal decreases with time. Maximum/minimum radiance (p/s/cm²/sr) shown for each image.

Fluorescence imaging was first performed to confirm that the probe was detectable.

Figure 6-2 B shows the fluorescent signal detected at injection site (green arrow).

Figure 6-2 C shows the location of the orthotopic tumour (red arrow) as well as a signal at injection site (green arrow) with signal 'bleed-through' from the fluorescence emission onto the open bioluminescence filter. **Figure 6-2 D-F** shows fluorescence imaging of the same animal at 6h, 24h and 48h. A persistent signal at the injection site was noted but no localisation to the tumour site was visualised *in vivo*.

6.1.2. Biodistribution of fluorescent TNC affimers in healthy, non-tumour bearing animals

TNC15C-Rh1 was evaluated in healthy, non-tumour bearing mice (n=9) to ascertain the biodistribution of the probe in the absence of a TNC-expressing tumour. *Ex vivo* imaging of organs was utilised for biodistribution studies as *in vivo* fluorescence imaging lacked organ specificity. The murine gallbladder exhibited high auto-fluorescence signal and was removed from the liver specimens prior to imaging.

To compare across imaging sessions and subsequent experiments, the fold change in average radiant efficiency above background autofluorescence was calculated (**Section 2.4.4**). Background fluorescence of tissues for the non-tumour bearing animals was determined by *ex vivo* of organs from a sham injected (100µL PBS tail-vein injection before sacrifice) animal. Fold change in average radiant efficiency was calculated for each organ using its respective background fluorescence.

TNC15C-Rh probe was detected in the kidney and liver at all time points tested (**Figure 6-3**). Probe clearance in the first 48h was more rapid in the kidneys compared to the liver (median fold change in average radiant efficiency liver 10.9 at 24h post-injection to 6.6 at 48h vs kidney 16.3 at 24h to 8.4 at 48h). This is suggestive of a renal excretion route for the probe.

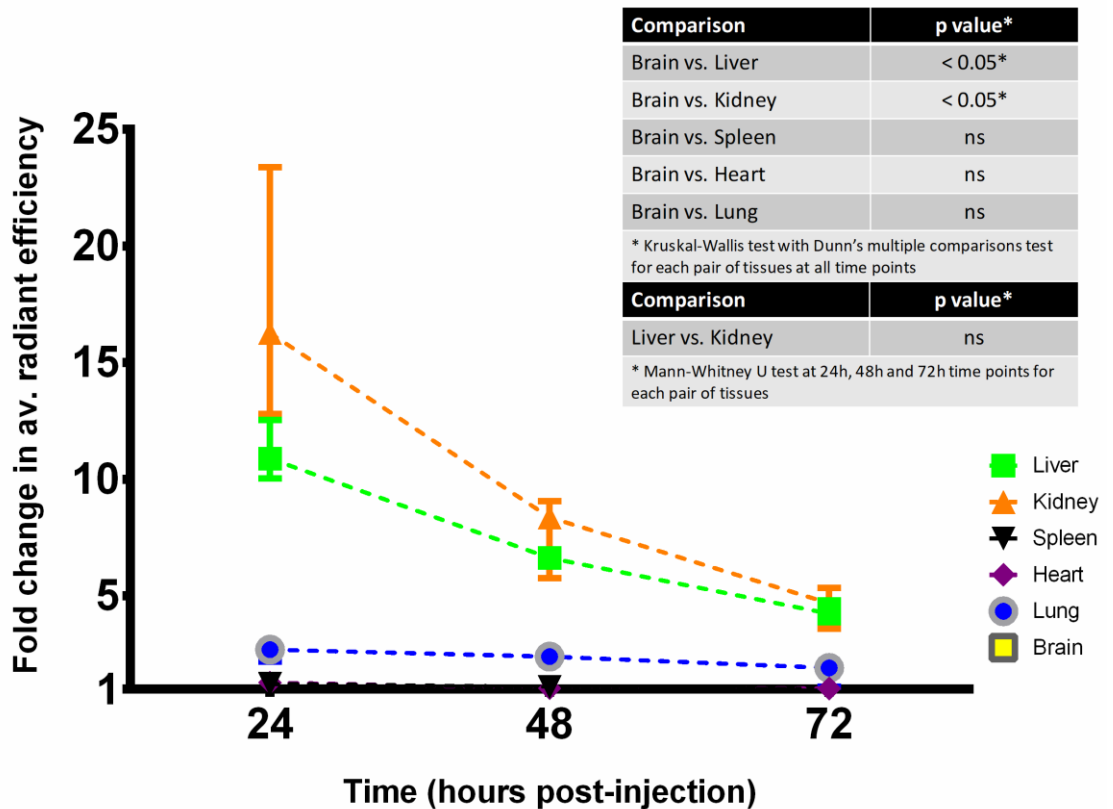


Figure 6-3 Biodistribution of TNC15C-Rh1 in healthy animals.

This graph shows the *ex vivo* fluorescence of organs at 24h, 48h and 72h time points following intravenous delivery of TNC15C-Rh1 (concentration ~150µM).

Significantly higher fluorescence was detected in the liver and kidney of animals at all time points compared to brain which showed the lowest rise in fluorescence ($p < 0.05$; Kruskal-Wallis test with Dunn's multiple comparison test). Increase in fluorescence in spleen, heart and lung was not significant compared to brain ($p = ns$; Kruskal-Wallis test with Dunn's multiple comparison test). No significant difference was observed in kidney and liver at 24h, 48h or 72h time points ($p = ns$; Mann-Whitney U test).

All values were corrected for each organ using background fluorescent values obtained from a sham injected mouse (tail-vein injection of 100µL PBS) and expressed as a fold change in average radiant efficiency. $n = 3$ animals at each time point, median and range plotted for each organ at each time point. Y axis starts at 1 as this is the lowest value for fold change in average radiant efficiency. Lines drawn to guide the eye and do not represent serial imaging of the same cohort of animals at different time points.

Brain tissue demonstrated the lowest rise in fluorescence and therefore was used for statistical comparison against the other organs. This showed a significant difference compared to the liver and kidney fluorescence at all time points tested ($p < 0.05$; Kruskal-Wallis test with Dunn's multiple comparison test). However, comparing liver and kidney fluorescence, there was no significance between these two organs at all time points tested ($p = \text{ns}$; Mann-Whitney U test at 24h, 48h and 72h time points).

Later time points beyond 72h were not investigated and therefore time for complete excretion of probe and return to background level of fluorescence could not be determined from this experiment. Earlier time points before 24h were also not included in this experiment but initial high fluorescence was expected in all tissues. Earlier and later time points would require testing in subsequent experiments.

6.1.3. Biodistribution of fluorescent TNC affimers in SW620 xenograft model

To determine active tumour targeting of TNC15C-Rh1, a high TNC expressing tumour model was required. The SW620 xenograft model was used to evaluate biodistribution of the TNC15C-Rh1 probe due to the relative ease of establishment compared to the TFKluc2B2 orthotopic model as well as the higher expression of TNC compared to the TFKluc2B2 xenograft model. TNC mRNA expression in SW620 cell lines and TNC immunolabelling in SW620 xenograft tissue are discussed in **Chapter 5 (Sections 5.4.3 and 5.4.2)**.

This preliminary experiment was required to inform future studies of useful imaging time-points. As with the previous experiment in healthy non-tumour bearing mice, differential tissue distribution of fluorescent probe could not be assessed *in vivo* and therefore images were obtained *ex vivo*. A control probe was not used for this

preliminary experiment. Each time point tested consisted of 3 animals except 72h where only 2 animals were included.

As shown in **Figure 6-4**, a high fold change in average radiant efficiency (background level = 1) was detected in all tissues imaged at 1h post-injection. Brain tissue showed the lowest increase in fluorescence throughout all time points tested and in comparison, tumour, liver and kidney fluorescence was statistically higher ($p < 0.05$; Kruskal-Wallis test with Dunn's multiple comparison test). Fold change in fluorescence for lung, spleen and heart were not statistically different to brain ($p = \text{ns}$; Kruskal-Wallis test with Dunn's multiple comparison test).

As shown in **Figure 6-4**, although higher fold change in fluorescence was observed in kidney at 1h (median 127.1, range 79.3-179.7) and 6h (median 85.9, range 76.6-121.5) time points, compared to liver and tumour this was not statistically different ($p = \text{ns}$; Mann-Whitney U test). The 72h time point was not statistically analysed due to insufficient numbers ($n = 2$).

Tumour fluorescence at the 48h time point (median 6.6, range 4.5-8.6) appeared the highest out of all organs but compared to kidney (median 2.6, 2.4-2.6) and liver (median 2.8, range 2.5-2.9), this was not statistically significant ($p = \text{ns}$; Mann-Whitney U test).

Tumour, liver and kidney tissue remained above background fluorescence level even at the final time point (72h) whereas spleen, heart, lung and brain returned to near background levels.

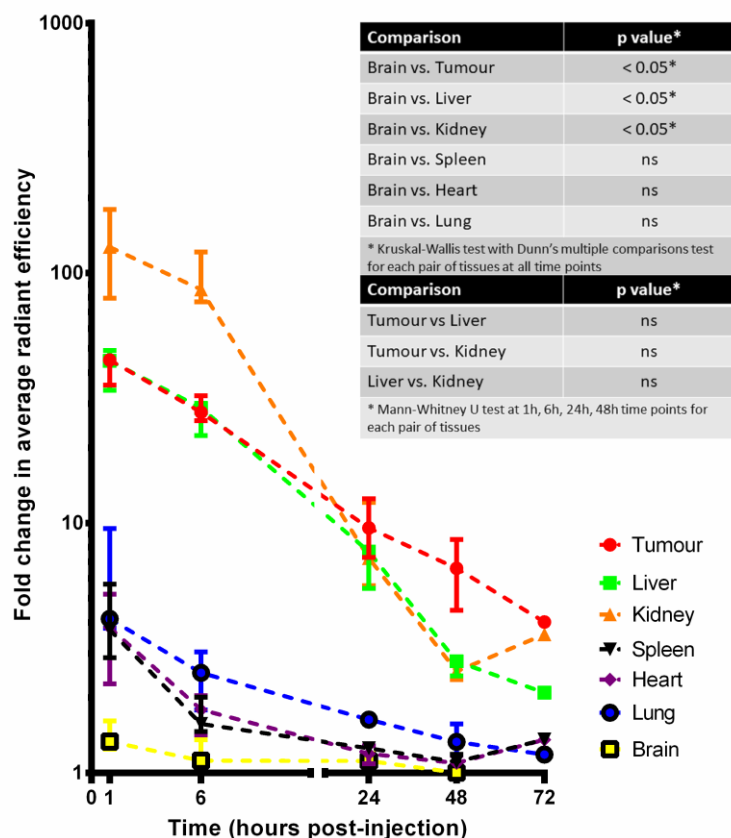


Figure 6-4 Biodistribution of TNC15C-Rh1 probe in SW620 xenograft model.

This graph shows the *ex vivo* fluorescence of tumour and organs at 1h, 6h, 24h, 48h and 72h time points following intravenous delivery of TNC15C-Rh1 (concentration ~150µM). Significantly higher fluorescence was detected in tumour, liver and kidney at all time points compared to brain which showed the lowest rise in fluorescence (p<0.05; Kruskal-Wallis test with Dunn's multiple comparison test). Increase in fluorescence in spleen, heart and lung was not significant compared to brain (p=ns; Kruskal-Wallis test with Dunn's multiple comparison test). No significant differences were observed in tumour, kidney and liver at 1h, 6h, 24h, 24h or 48h (p=ns; Mann-Whitney U test).

All values were corrected for each organ and tumour using background fluorescent values obtained from three sham injected mice (tail-vein injection of 100µL PBS) and expressed as a fold change in average radiant efficiency. n=3 animals at each time point except 72h (n=2). Median and range plotted for each organ at each time point. Y axis starts at 1 as this is the lowest value for fold change in average radiant efficiency. Lines drawn to guide the eye and do not represent serial imaging of the same cohort of animals at different time points.

6.1.4. Biodistribution of fluorescent TNC affimers compared to control affimers

To investigate if the difference (albeit not statistically different) in biodistribution of the TNC15C-Rh1 probe in the tumour at 48h (shown in **Figure 6-4**) was due to specific targeting, a control probe was required. Batch 2 of the fluorescent TNC affimer probe (TNC15C-Rh2) was supplied with a paired control probe with an affimer targeting green fluorescent protein (GFP32C-Rh2). Reported concentration for both probes was $\sim 200\mu\text{M}$ which was higher than TNC15C-Rh1 (concentration $\sim 150\mu\text{M}$). The fluorescent labelling was performed by Miss A Tang and Dr Robin Bon. These probes were evaluated in the SW620 xenograft model and the TFKluc2B2 orthotopic model. The preliminary experiment (**Figure 6-4**) suggested that at 24h and 48h, a higher fluorescent signal from the tumour was detected compared to signal from the liver and kidney. Therefore, in line with the NC3R principles (Kilkenny *et al.*, 2010), time points were limited to achieve at least $n=3$ at each time point of the experiment. Both probes were also evaluated in the TFKluc2B2 orthotopic model.

6.1.4.1. SW620 xenograft model

Figure 6-5 and **Figure 6-6** show the fold change in fluorescence of tumour and organs at 24h and 48h post-injection of TNC15C-Rh2 and GFP32C-Rh2 probes in the SW620 xenograft model. Three animals were included per group for each time point and the tumour volumes were not statistically different. Median xenograft tumour volumes at 24h were 482mm^3 (range 368-595) for TNC15C-Rh2 group and 394mm^3 (range 159-1,425) for GFP32C-Rh2 ($p=\text{ns}$; Wilcoxon-matched pairs signed rank test). Median xenograft tumour volumes at 48h were 577mm^3 (range 304-686) for TNC15C-Rh2 and 283mm^3 (range 168-753) for GFP32C-Rh2 ($p=\text{ns}$; Wilcoxon matched pairs signed rank test).

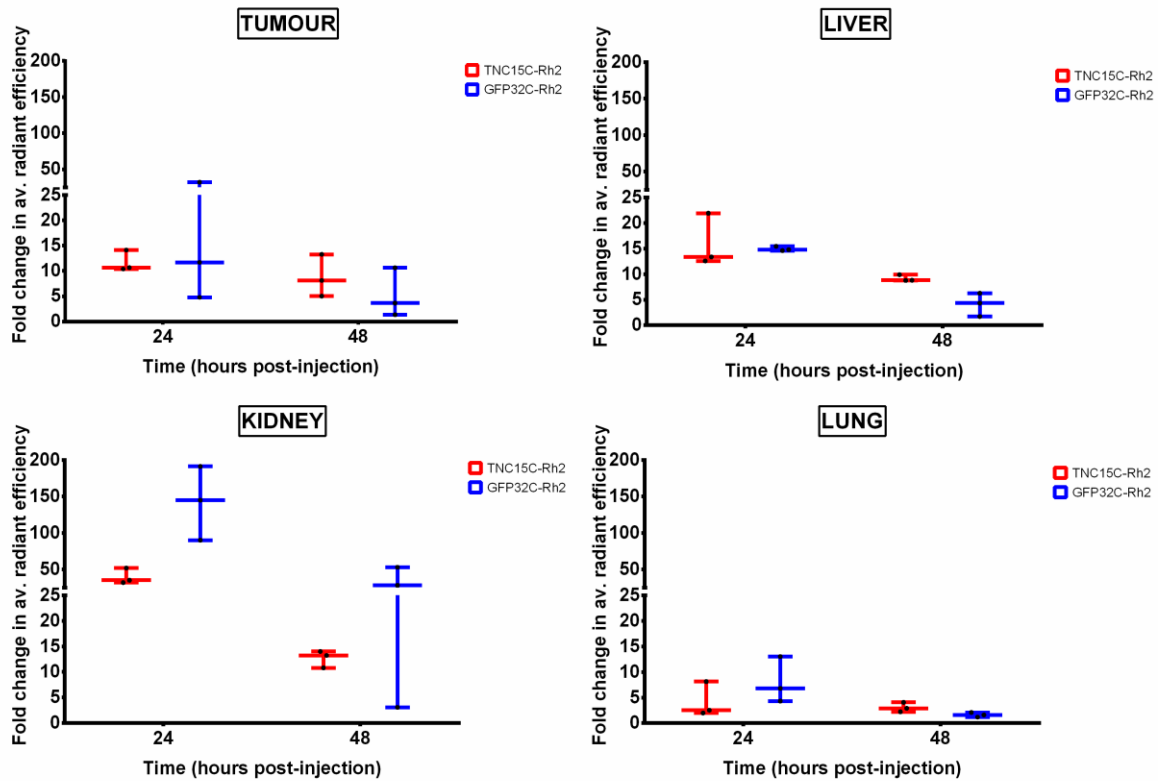


Figure 6-5 Biodistribution of TNC15C-Rh2 vs GFP32C-Rh2 in SW620 xenograft tumour, liver, kidney and lung.

Tissue fluorescence measured *ex vivo* at 24h and 48h time points following injection of TNC15C-Rh2 or GFP32C-Rh2 probe (concentration $\sim 200\mu\text{M}$) in the SW620 xenograft model. Comparison of the two probes did not show any statistically significant differences at 24h or 48h in any of the tissues.

Values normalised to sham injected animals ($n=3$) bearing SW620 xenograft tumours and expressed as fold change in average radiant efficiency; median and range plotted, $n=3$ animals per group at each time point. Wilcoxon matched pairs signed rank test used to compare the two groups at each time point.

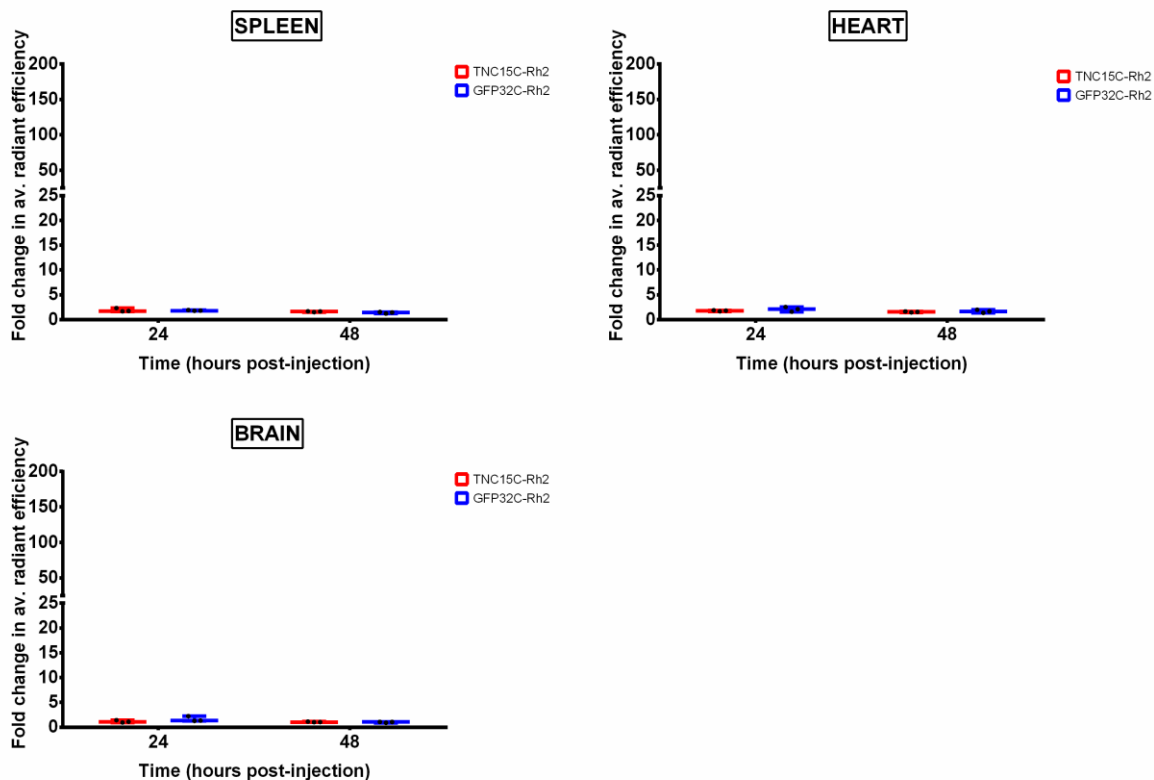


Figure 6-6 Biodistribution of TNC15C-Rh2 vs GFP32C-Rh2 in spleen, heart and brain.

Tissue fluorescence measured *ex vivo* at 24h and 48h time points following injection of TNC15C-Rh2 or GFP32C-Rh2 probe (concentration $\sim 200\mu\text{M}$) in the SW620 xenograft model. Comparison of the two probes did not show any statistically significant differences at 24h or 48h in any of the tissues.

Values normalised to sham injected animals (n=3) bearing SW620 xenograft tumours and expressed as fold change in average radiant efficiency; median and range plotted, n=3 animals per group at each time point. Wilcoxon matched pairs signed rank test used to compare the two groups at each time point.

Median tumour fold change in fluorescence at 24h was similar in TNC15C-Rh2 group compared to the GFP32C-Rh2 group (10.7 vs 11.7 respectively; $p=0.75$, Wilcoxon matched pairs signed rank test). At 48h fluorescence decreased to 8.1 in the TNC15C-Rh2 group but a more marked reduction to 3.6 was observed in the GFP32C-Rh2 group, although this difference was not statistically significant ($p=0.50$, Wilcoxon matched pairs signed rank test)

Median liver fold change in fluorescence followed a similar pattern of being comparable at 24h (TNC15C-Rh2 13.4 vs GFP32C-Rh2 14.8; $p=0.50$, Wilcoxon matched pairs signed rank test) but a more significant reduction at 48h (TNC15C-Rh2 8.8 vs GFP32C-Rh 4.3) although this was also not statistically significant ($p=0.25$, Wilcoxon matched pairs signed rank test).

Kidney fold change in fluorescence demonstrated the most variability compared to the other tissues. Median fold change in fluorescence at 24h and 48h was 35.2 and 13.2 in the TNC15C-Rh2 group but 144.9 and 28.2 in the GFP32C-Rh2 group. However, these differences were not statistically significant (24h $p=0.25$, 48h $p=0.50$, Wilcoxon matched pairs signed rank test). This suggests that overall the GFP32C-Rh2 probe was more fluorescent compared to the TNC15C-Rh2 probe and exhibited faster clearance through a likely renal route.

Median lung fold change in fluorescence at 24h and 48h were not statistically significant. As shown in **Figure 6-6**, fold change in fluorescence in spleen, heart and brain tissues were comparable between the two probes.

6.1.4.2. TFKluc2B2 orthotopic model

In the parallel experiment comparing TNC15C-Rh2 and GFP32C-Rh2, only one time point (24h) was included due to insufficient volume of fluorescent probes and numbers of successfully established TFKluc2B2 orthotopic models.

Figure 6-7 A shows a representative *ex vivo* fluorescence (**A1**) and bioluminescence (**A2**) imaging of the tissues of one animal injected with TNC15C-Rh2 probe. 1.2mg of beetle D-luciferin was injected intraperitoneally into right lower quadrant of the animal 5 minutes prior to sacrifice. Fluorescence imaging shown in **Figure 6-7 A1** demonstrates fluorescence in the liver tumour as well as the surrounding liver. **Figure 6-7 A2** clearly shows the liver orthotopic tumour which corresponds to the fluorescent hot spots on the previous image. However, 'bleed through' of the fluorescence emissions (peak emissions 560nm) onto the bioluminescence filter is likely. To quantitate the contribution of this 'bleed through' to the measured value would require control group with sham injected animals. This suggested that dual imaging of bioluminescence and fluorescence filters for rhodamine red C₂ maleimide in future experiments could be challenging.

Figure 6-7B shows the comparison of fluorescence between the tumour and tissues. Median kidney fold change in fluorescence was much higher in the GFP32C-Rh2 group compared to the TNC15C-Rh2 group (59.0 (range 40.5-104.9) vs 9.6 (5.9-10.6) respectively) but this was not significant (p=0.25, Wilcoxon matched pairs signed rank test). Similarly, no significant differences were observed in any of the other tissues.

6.1.4.3. *In vitro* dilution assay of fluorescent probes

Given the inconsistency in fluorescence in the control and test probe demonstrated in these experiments, fluorescence of the next batch of control (GFP32C-Rh3) and test (TNC15C-Rh3) probes synthesised by Miss A Tang were compared *in vitro* prior to *in vivo* assessment. **Figure 6-8 A** shows the comparison between TNC15C-Rh2 and GFP32C-Rh2 and **Figure 6-8 B** shows the comparison between TNC15C-Rh3 and GFP32C-Rh3. These graphs demonstrate that the GFP32C-Rh2 probe was 2.2 times more fluorescent at each dilution compared to the TNC15C-Rh2 probe but the GFP32C-Rh3 probe and TNC15C-Rh3 probes were of comparable fluorescence.

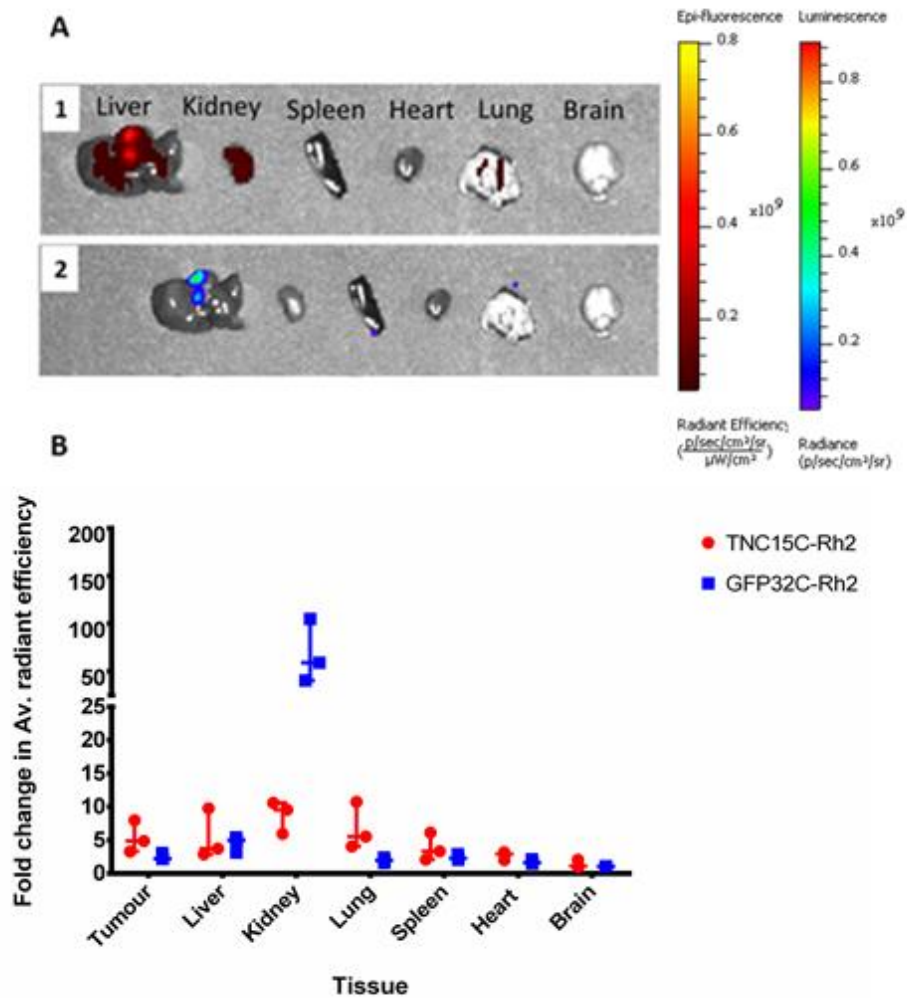


Figure 6-7 Biodistribution of TNC15C-Rh2 vs GFP32C-Rh2 in TFKluc2B2 orthotopic tumour model

A.1 *Ex-vivo* fluorescence imaging of 1 representative animal injected with TNC15C-Rh2 (concentration $\sim 200\mu\text{M}$) probe. Values were normalised to sham injected animals ($n=2$) bearing orthotopic tumours and expressed as fold change in average radiant efficiency. **A.2.** *Ex-vivo* bioluminescent imaging of tumour in the same animal confirming the site of tumour.

B. Comparison of *ex-vivo* fluorescence imaging of TNC15C-Rh2 and GFP32C-Rh2 probes shown with the median and range of fold change in average radiant efficiency plotted. Median kidney GFP32C-Rh2 fold change in fluorescence was higher (59.0) compared to TNC15C-Rh2 (9.6) but this was not significantly different ($p=0.25$, Wilcoxon matched pairs signed rank test) Fold change in fluorescence in other tissues were comparable between groups.

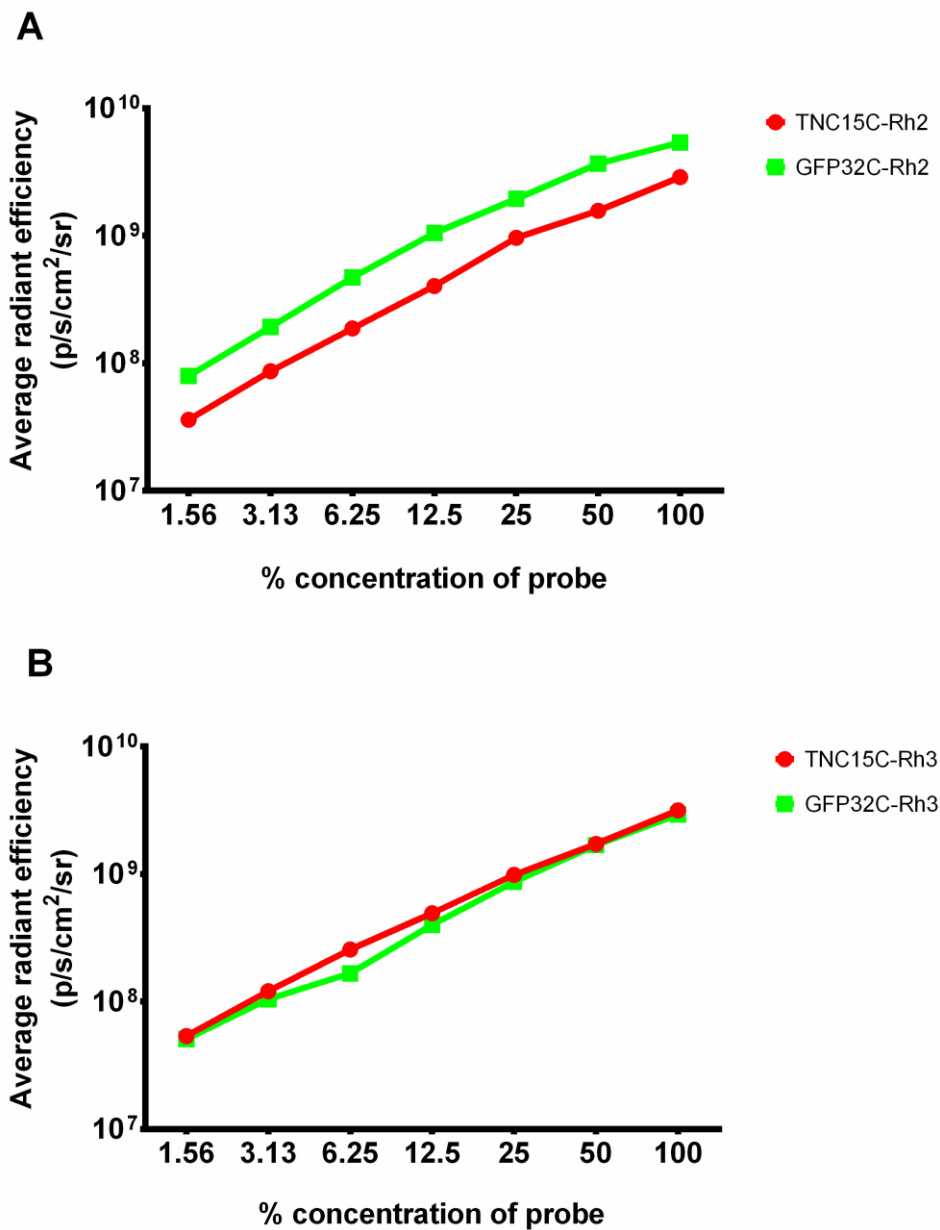


Figure 6-8 Comparison of fluorescence between batches of fluorescent probe

A. Comparison of TNC15C-Rh2 and GFP32C-Rh2 (concentration ~200 μ M) probes. This shows a 2.25 times higher fluorescence in the GFP32C-Rh2 probe across the range of dilutions compared to TNC15C-Rh2.

B. Comparison of TNC15C-Rh3 and GFP32C-Rh3 (concentration ~200-300 μ M) probes. This shows no significant difference between the fluorescence of the two probes.

n=1 data with only 1 technical replicate per dilution due to insufficient volume of probes.

6.1.4.4. Biodistribution in SW620 xenograft model with optimised probes

The experiment protocol was refined with the third batch of fluorescent probes, TNC15C-Rh3 and GFP32C-Rh3. Comparable fluorescence of the test and control probes was confirmed by *in vitro* dilution assay as shown in **Figure 6-8 B**. Miss A Tang and Dr R Bon confirmed an approximate concentration of ~200-300 μ M for both probes based on optical density measurement and an electrophoresis method (SDS-PAGE) but acknowledged difficulties with accurate estimation. A 96h time point was also tested to assess if the probes would be completely cleared by this time point.

Figure 6-9 shows that the pre-injection SW620 xenograft volumes were comparable between the two groups at each time point. However, tumours in both groups at the final time point were smaller than those in both groups at the first time point due to a selection bias for animals with larger tumours to be in the earlier time cohorts. This was to ensure that they did not reach maximum allowed tumour size prior to the end point of the experiment. Despite random assignment to the two groups, there was a general trend of the TNC15C-Rh3 injected group to be slightly smaller than GFP32C-Rh3 group, although this was not statistically significant.

Figure 6-10 shows the *ex vivo* fluorescence in tumour, liver, kidney and lung tissue at the time points tested while **Figure 6-11** demonstrates this for spleen, heart and brain. At 24h, higher median fold change in fluorescence was observed in the tumours of the TNC15C-Rh3 group (6.1 (range 4.7-8.0)) compared to those of the GFP32C-Rh3 group (2.2 (range 1.8-3.0)) but this difference was not statistically significant ($p=0.25$, Wilcoxon matched pairs signed rank test). Comparison of liver and kidney at the same time point for TNC15C-Rh3 and GFP32C-Rh3 also demonstrated differences (liver 10.2 (range 5.5-10.7) vs 2.6 (range 2.2-2.7); kidney 7.7 (range 7.1-14.3 vs 10.9 (range 5.7-11.1)) but these were not statistically significant.

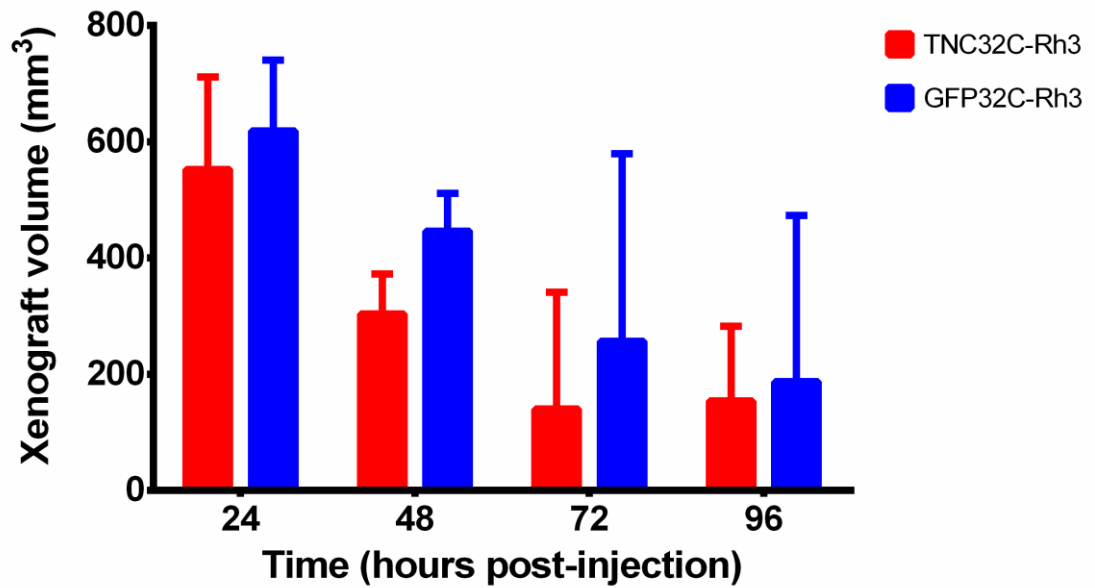


Figure 6-9 SW620 xenograft tumour volumes

The xenograft tumour volumes between the two groups at each time point showed no significant difference. (Mann-Whitney *U* test; 24h $p=0.90$, 48h $p=0.70$, 72h $p=0.40$, 96h $p=0.70$ between TNC15C-Rh3 and GFP32C-Rh3 groups); median and range plotted.

SW620 cells were injected into the right hind flank of 24 animals. Animals were randomised using stratified randomisation into injection groups with to obtain two groups with similar starting tumour volumes for each time point. Each bar represents $n=3$ animals i.e. 6 animals at each time point in the two groups. Serial measurements of tumour volume during the experiment was not undertaken.

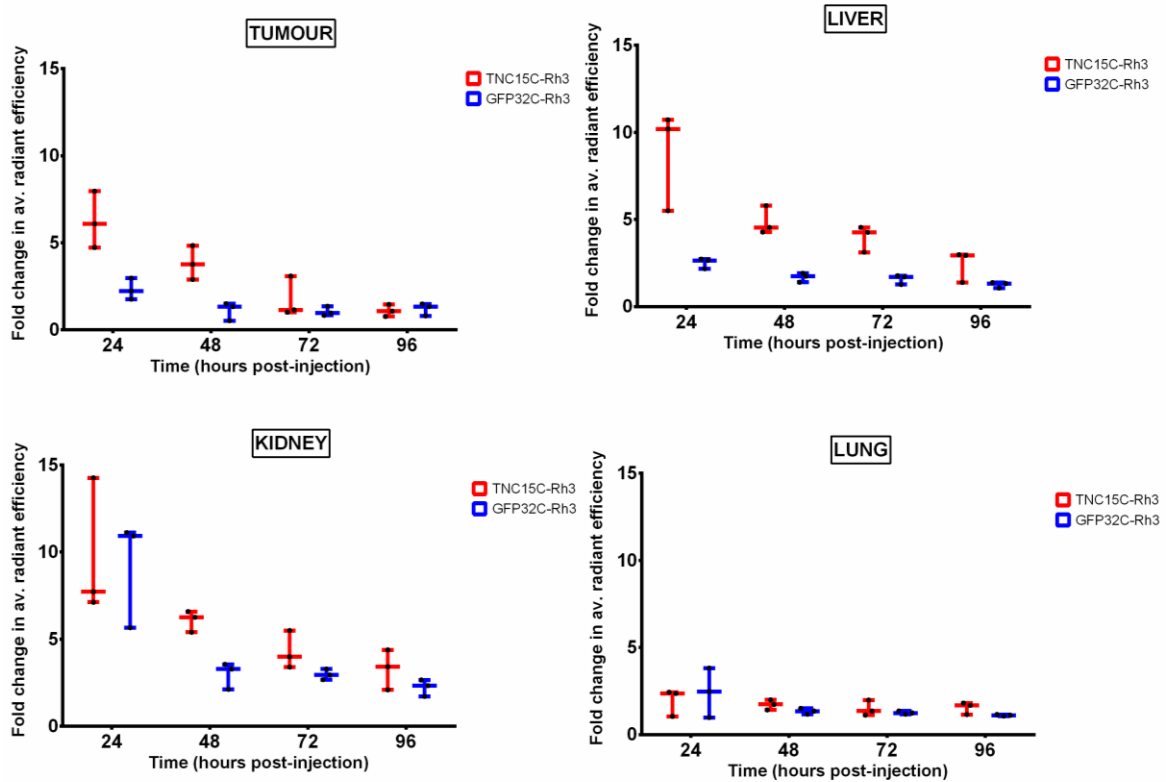


Figure 6-10 Biodistribution of TNC15C-Rh3 vs GFP32C-Rh3 in SW620 xenograft tumour, liver, kidney and lung.

Ex-vivo fluorescent imaging of tissues from mice injected with either TNC15C-Rh3 or GFP32C-Rh3 (concentration $\sim 200\text{-}300\mu\text{M}$). Comparison of the two probes did not show any statistically significant differences at 24h, 48h, 72h or 96h for any of the tissues ($p=\text{ns}$, Wilcoxon matched pairs signed rank test).

All values were normalised to sham injected mice and expressed as a fold change in average radiant efficiency. median and range plotted, $n=3$ animals per group at each time point.

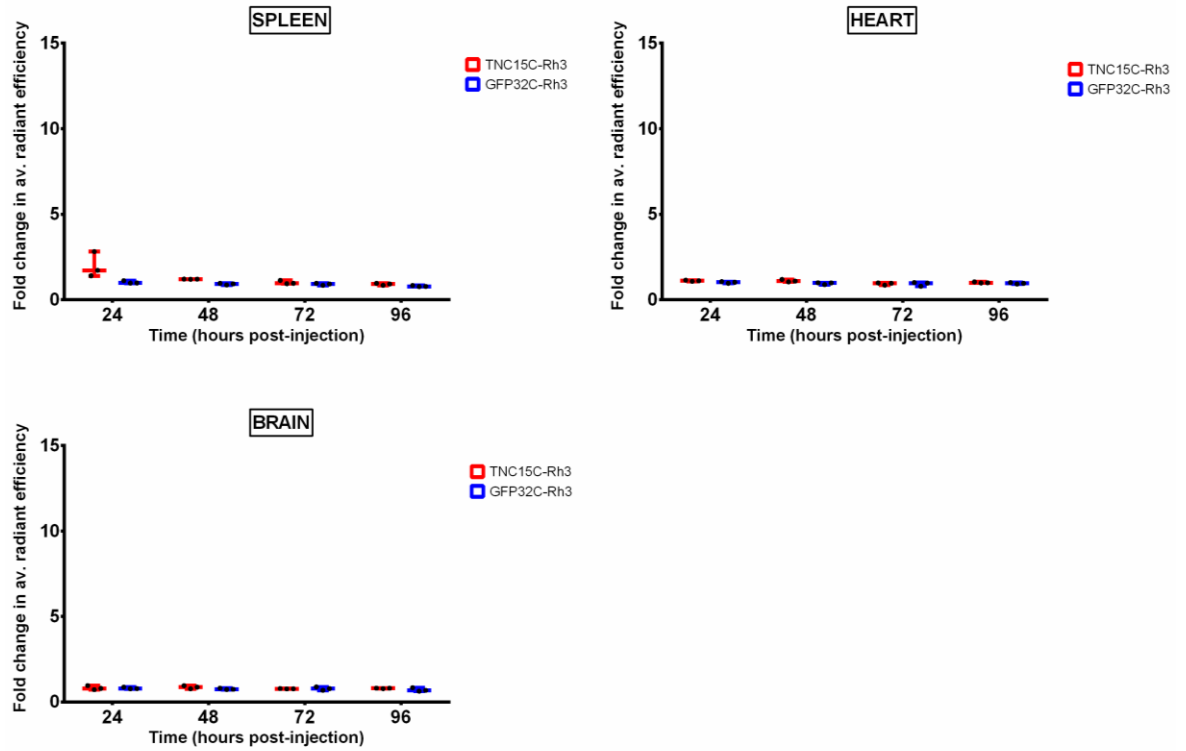


Figure 6-11 Biodistribution of TNC15C-Rh3 vs GFP32C-Rh3 in spleen, heart and brain

Ex-vivo fluorescent imaging of tissues from mice injected with either TNC15C-Rh3 or GFP32C-Rh3 (concentration $\sim 200\text{-}300\mu\text{M}$). Comparison of the two probes did not show any statistically significant differences at 24h, 48h, 72h or 96h for any of the tissues ($p=\text{ns}$, Wilcoxon matched pairs signed rank test).

All values were normalised to sham injected mice and expressed as a fold change in average radiant efficiency. median and range plotted, $n=3$ animals per group at each time point.

Interestingly, the fold change in fluorescence was higher in kidney (24h, median 10.9) compared to liver (24h, median 2.6) for GFP32C-Rh3 (**Figure 6-10**) whereas TNC15C-Rh3 fold change in fluorescence was high in both kidney (24h, median 7.7) and liver (24h, median 10.2). However, these changes were not statistically significant. The other tissues and time points did not show any statistical differences between the two probes.

Confocal microscopy (performed by Dr Adam Davison) was performed on fresh-frozen xenograft tissue to determine the presence and location of fluorescent affimers.

Tissues from the 48h time point after injection of TNC15C-Rh3 and GFP32C-Rh3 affimers were labelled with a fluorescent (green) cell membrane stain prior to confocal microscopy. **Figure 6-12** shows representative xenograft tissue sections from the xenografts in each group. Red fluorescence of rhodamine-labelled affimer was seen on some tissues (**Figure 6-12 A, B and D**; denoted with white arrows), but this was not observed across all tumours (no red fluorescence in **Figure 6-12 C, E and F**). There was no evidence to suggest specific TNC targeting by TNC15C-Rh3 affimer on confocal microscopy.

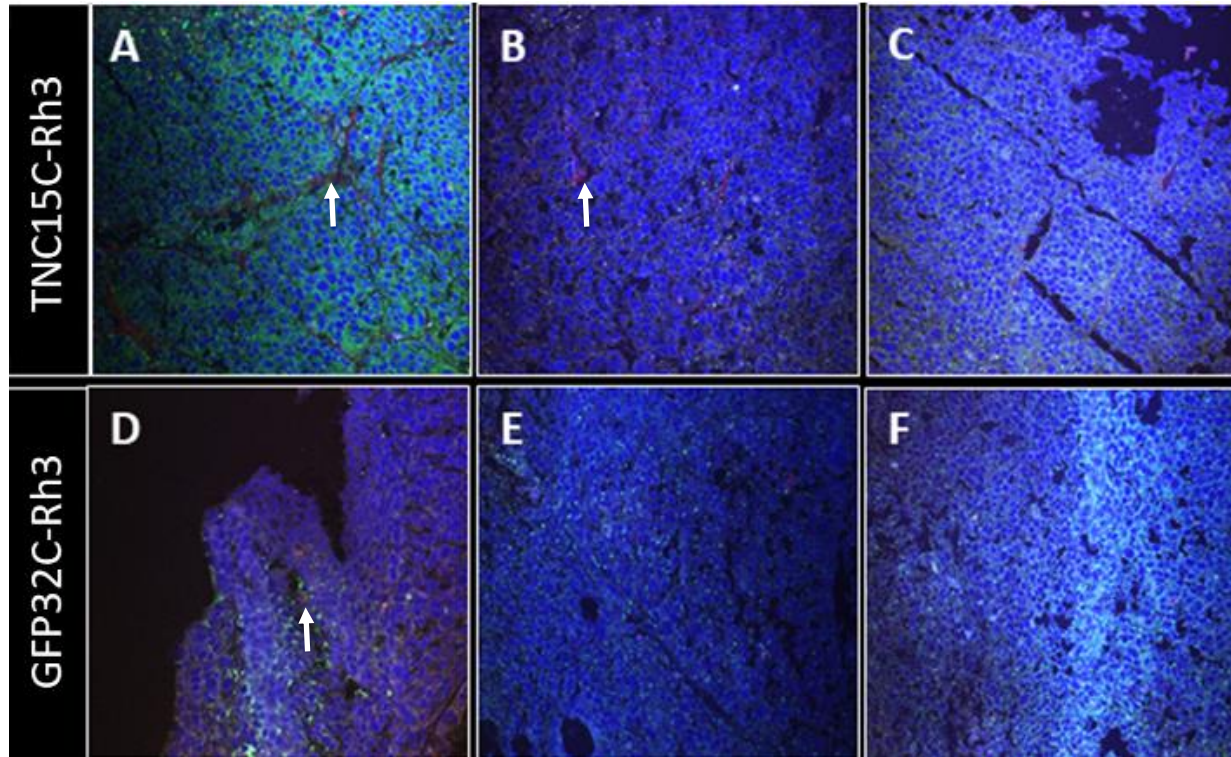


Figure 6-12 TNC15C-Rh3 and GFP32C-Rh3 in SW620 xenograft tissue

7µm fresh-frozen xenograft tissue sections from tumours at the 48h time point after injection of TNC15C-Rh3 and GFP32C-Rh3 affimers were labelled with a fluorescent (green) cell membrane stain according to manufacturer's instructions and subject to confocal microscopy. Exposure thresholds were set on control xenograft tissue with no exposure to *in vivo* fluorescent affimers. Red fluorescence indicates the presence of rhodamine-labelled affimer (A, B, D; denoted with white arrows), but this was not observed across all tumours (no red fluorescence in C, E and F).

6.2 Gold nanoparticles as carriers for theranosis

Fluorescent probes are useful for high throughput pre-clinical validation experiments, but they have limited clinical applications. Therefore, for the development of a TNC-targeted delivery vehicle, the application of AuNPs was explored. As some AuNPs are currently FDA-approved (Singh *et al.*, 2018), they show promise as a more translatable option for theranosis.

Although several AuNPs are commercially available, others with specific properties are the focus of research efforts at the University of Leeds (Ye *et al.*, 2016; Roach *et al.*, 2018; Ye *et al.*, 2018; Ye *et al.*, 2019). In this chapter, two shapes of in-house synthesised AuNPs, gold nanoplates (AuNPLs) and gold nanorods (AuNRs) were evaluated.

6.2.1 Cytotoxicity of gold nanoparticles on selected cell lines

The inherent cytotoxicity of polystyrene sulphonate (PSS) coated untargeted AuNRs synthesised by Dr Lucien Roach at 975µg/ml were first examined by *in vitro* cytotoxicity assays. Coating of AuNRs was required as the AuNRs were synthesised in the presence of the surfactant cetrimonium bromide (CTAB) which, although required for the production and stabilisation of AuNRs, is cytotoxic (Leonov *et al.*, 2008; Wan *et al.*, 2015). PSS was used as it improves dispersibility of AuNRs and allows multilayer assembly compared to silica-coating (Omura *et al.*, 2009).

As shown in **Figure 6-13**, the IC₅₀ for PSS-coated AuNR were 119.5-145µg/mL in SW620, TFK-1 and TFKluc2B2 cell lines.

AuNPLs were not investigated due to the low concentration (100µg/ml) and insufficient volume supplied. Cytotoxicity of AuNRs or AuNPLs on non-cancer cells was not examined.

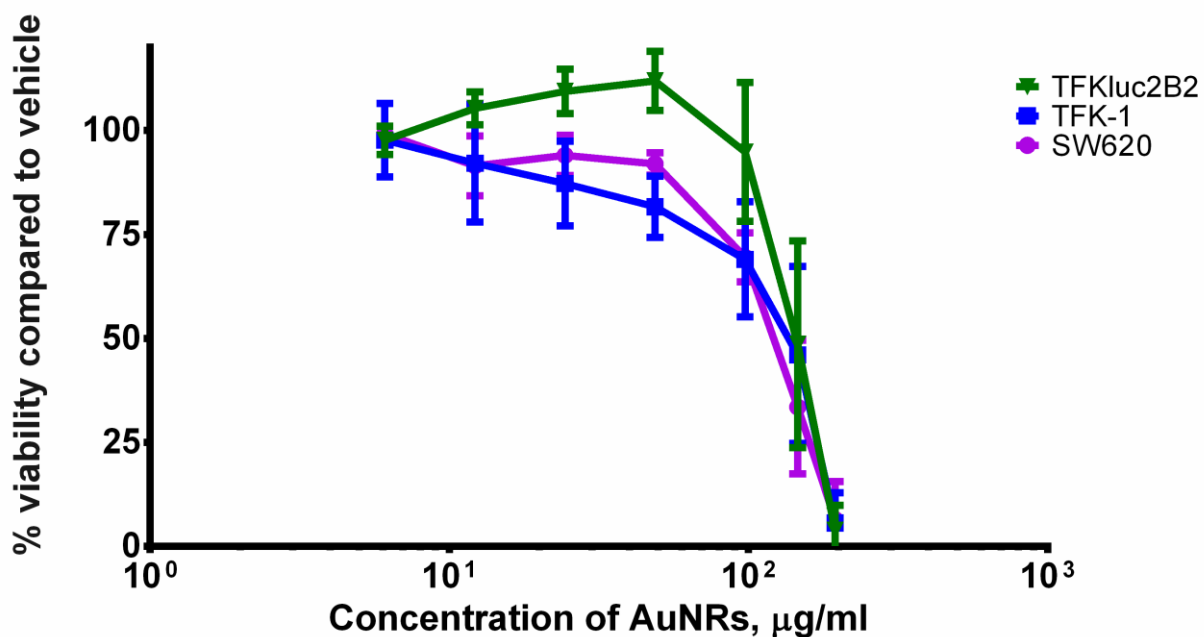


Figure 6-13 Toxicity of PSS-coated gold nanorods on selected cell lines

IC₅₀ (95% C.I) for each cell line was determined from the respective dose-response curves. TFKluc2B2 145µg/ml (132.9-154.6µg/ml); TFK-1 120µg/ml (93 - 143.5µg/ml); SW620 119.5µg/ml (108.5 - 130.2µg/ml)

Each point represents the mean of triplicate biological replicates under the same experimental conditions. Mean background absorbance of AuNRs at each concentration were subtracted from the mean of the corresponding test values.

CCK-8 assay was used to determine cell viability. % viability compared to vehicle plotted, mean±SD. IC₅₀ values for each cell line was determined from the corresponding dose-response curve.

6.2.2 Assessment of targeting of TNC affimer labelled gold nanoparticles

To assess the *in vitro* targeting ability of AuNPs labelled with TNC affimers, AuNPLs developed by Dr Sunjie Ye were utilised. The rationale was the convenience of labelling AuNPLs with TNC affimers using citrate bonds which was not possible with the PSS-coated AuNRs.

SW620, a high TNC expressing cell line (**Figure 5-8** and **Figure 5-10**) and HCT116, a TNC negative cell line were evaluated with AuNPLs which were TNC affimer coated (TNC-AuNPLs) or silica coated (Sc-AuNPL). Negative TNC expression of HCT116 cells was assessed by immunoblotting of cell lysates (**Figure 5-10**) and by RT-PCR performed by Dr Azhar Maqbool (personal communication) which was in keeping with the published literature (Li *et al.*, 2016).

TNC-AuNPLs fully coated with the TNC affimer were first assessed. This resulted in agglomeration (i.e. clustering) of the TNC-AuNPLs (**Figure 6-14**). No agglomeration occurred in the Sc-AuNPLs. To test the hypothesis that this was due to an alteration in the zeta-potentials of the suspension, the zeta-potential of TNC-AuNPLs were tested at different coverages. **Figure 6-15 A** shows that at 4/5th coverage of TNC-AuNPLs and above, the zeta potential increased above -10mV, creating an environment that favoured agglomeration. **Figure 6-15 B** shows the ultraviolet-visible spectroscopy (UV-vis) data that confirms the alteration of the absorption spectra between 850nm and 1,300nm at 4/5th coverage of TNC-AuNPLs and above.

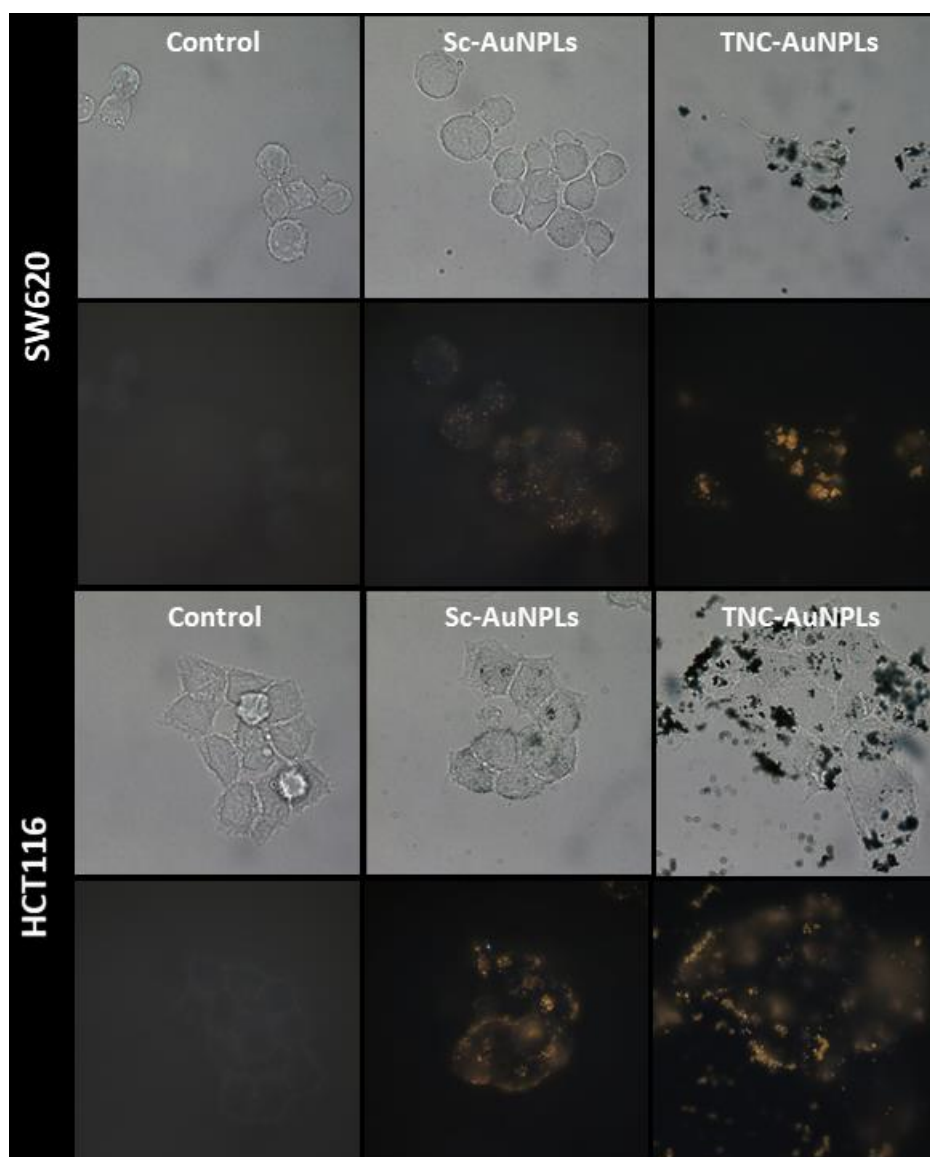


Figure 6-14 Cellular uptake of TNC-AuNPLs versus Sc-AuNPLs in SW620 and HCT116 cells

Both light (above) and dark field (below) images shown for each cell line.

For the SW620 cells, the control images (left column – no AuNPLs added) confirm absence of gold signal. Sc-AuNPLs were uptaken (middle column – light brown punctate signal). SW620 cells exposed to TNC-AuNPLs displayed cell wall distortion and agglomeration of particles intra-cellularly as well as extra-cellularly (right column).

In the HCT116 cells, the control images (left column) confirmed absence of gold signal. Sc-AuNPLs were uptaken (middle column – bright gold signal) by HCT116 cells. The TNC-AuNPL exposed HCT116 cells showed agglomerated particles with difficult to visualise cellular outlines.

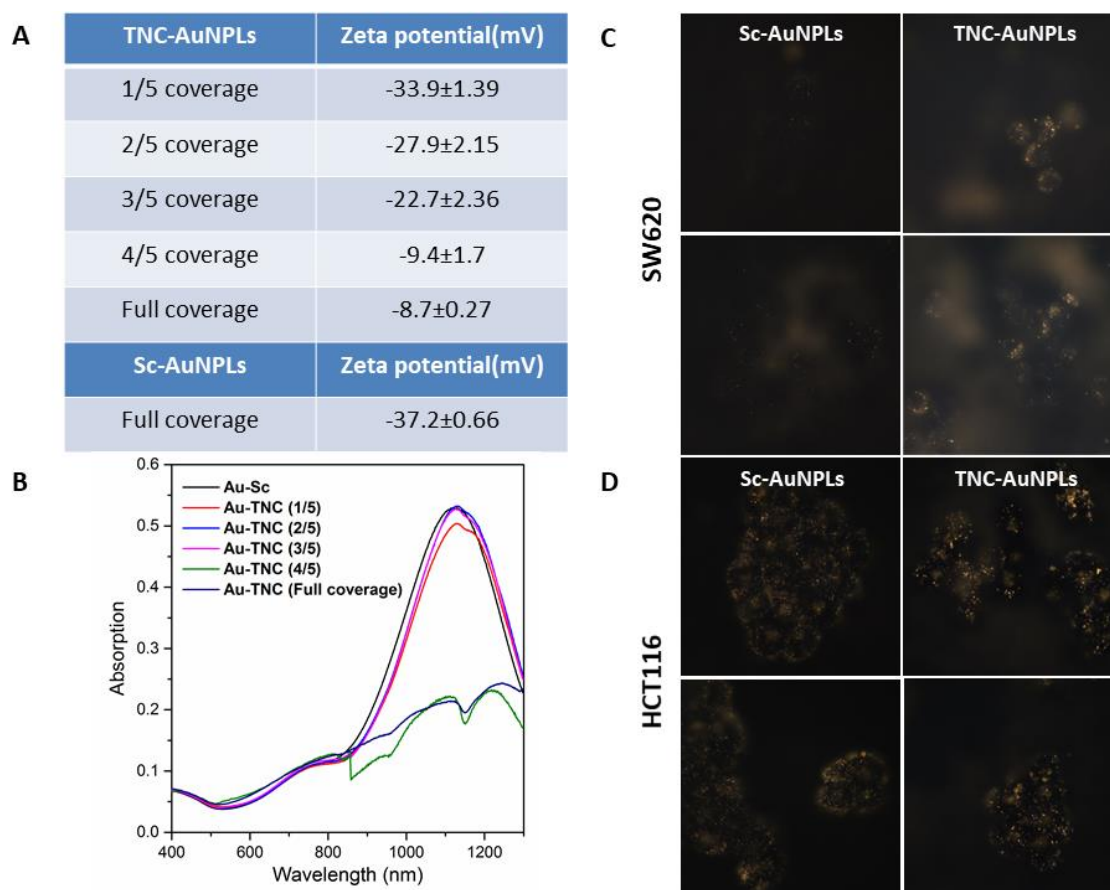


Figure 6-15 Physical properties of TNC-AuNPLs and dark field microscopy in SW620 and HCT116 cell lines

A. This table shows the Zeta potential measurements of TNC-AuNPLs at different coverage compared to Sc-AuNPLs. At 4/5th coverage or higher, the Zeta potential of TNC-AuNPL solution was higher than -10. **B.** This graph shows the UV-vis absorption spectra of TNC-AuNPLs at different coverage compared to full coverage of Sc-AuNPLs. This confirms the change in absorption spectra for the AuNPLs at 4/5th coverage or higher. **C.** This shows dark field microscopy of Sc-AuNPLs at full coverage (left column) & TNC-AuNPLs at 3/5th coverage (right column) on SW620 cells and demonstrates higher gold signal scattering (light brown background hue) in TNC-AuNPLs. **D.** This shows dark field microscopy of Sc-AuNPLs at full coverage (left column) & TNC-AuNPLs at 3/5th coverage (right column) on HCT116 cells displaying similar intra-cellular gold signal with less background scatter.

Hence, 3/5th coverage was utilized in the next experiment as a compromise between maximum possible surface coverage of the TNC affimer (i.e. maximum available binding sites for TNC) and reduction in likelihood of agglomeration of the colloid suspension.

In the SW620 cell line at 3/5th coverage of TNC-AuNPLs, higher signal scattering was noted on dark field microscopy compared to reduced signal from the Sc-AuNPLs as shown in **Figure 6-15 C**. However, in the TNC-negative control cell line, there was no difference between the TNC-AuNPL and Sc-AuNPL images (**Figure 6-15 D**). The amount of light scattering was not quantitated but all images were taken under the same exposure settings to ensure comparability. These experiments were performed with the assistance of Dr Sunjie Ye.

6.2.3 Photoacoustic imaging of unlabelled gold nanoparticles

As the AuNPLs and AuNRs were in-house synthesised, their utility as imaging agents for photoacoustic imaging had not previously been explored. Unlabelled AuNPLs were first evaluated in tissue-mimicking cylindrical agar phantoms and imaged on MSOT using the spectral data determined by UV-vis spectroscopy. **Figure 6-16** shows clearly visible signal from AuNPLs through a series of dilutions down to 6.25% (6.25µg/ml). At higher concentrations (100%, 50% and 25%), only circumferential signal was detected due to the laser absorption of the particles in the periphery. This prevented the penetration of the laser into the central core and therefore this region appears to show no signal despite the presence of AuNPLs of the same concentration.

A higher volume of AuNRs were synthesised compared to AuNPLs and hence, only AuNRs were evaluated *in vivo*. **Figure 6-17** shows pre- and post-injection images which show signal increase compared to baseline following injection of AuNRs. However, no signal increase was detected over the region of the xenograft. Subsequent imaging sessions at 4h and 24h did not reveal an AuNR signal in the region of the xenograft.

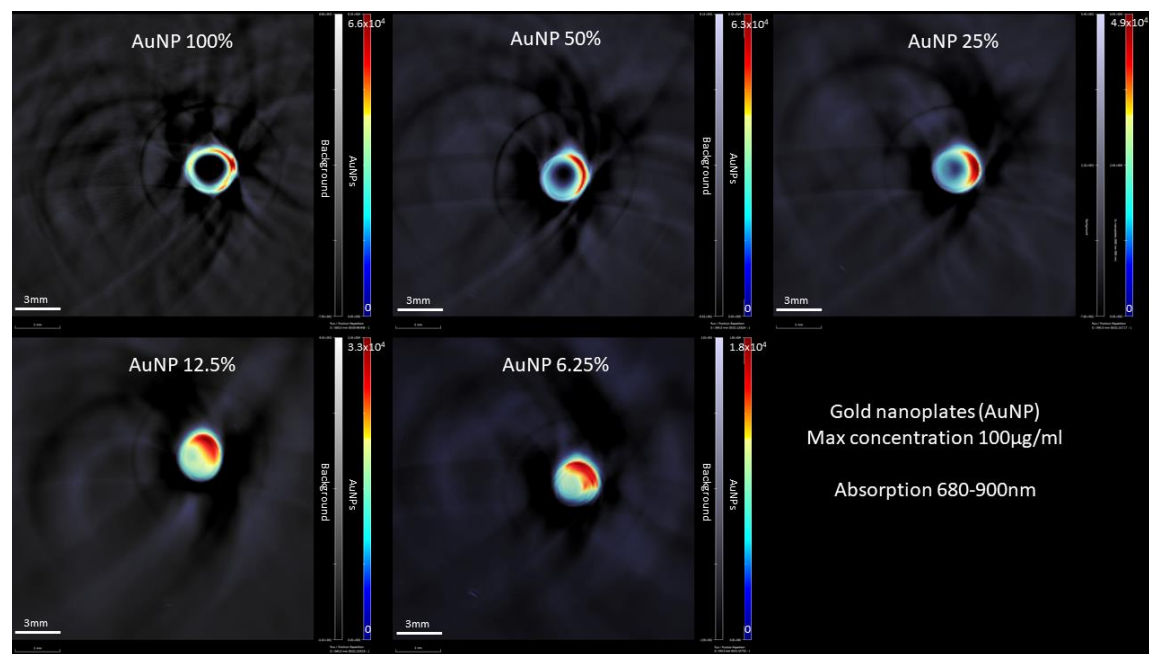


Figure 6-16 MSOT imaging of gold nanoplates in tissue mimicking agar phantoms

A clear visible gold signal was obtained from AuNPLs down to the lowest tested concentration 6.25% (i.e. 6.25µg/ml). At higher concentrations (100%, 50% and 25%), only circumferential signal was detected due to the laser absorption of the particles in the periphery that prevent penetration of the laser.

MSOT image reconstruction and UV-vis data measurement performed with the assistance of Dr L Roach and Dr Sunjie Ye. UV-vis spectroscopy measured absorption spectrum range for silica-coated AuNPLs was 680-900nm.

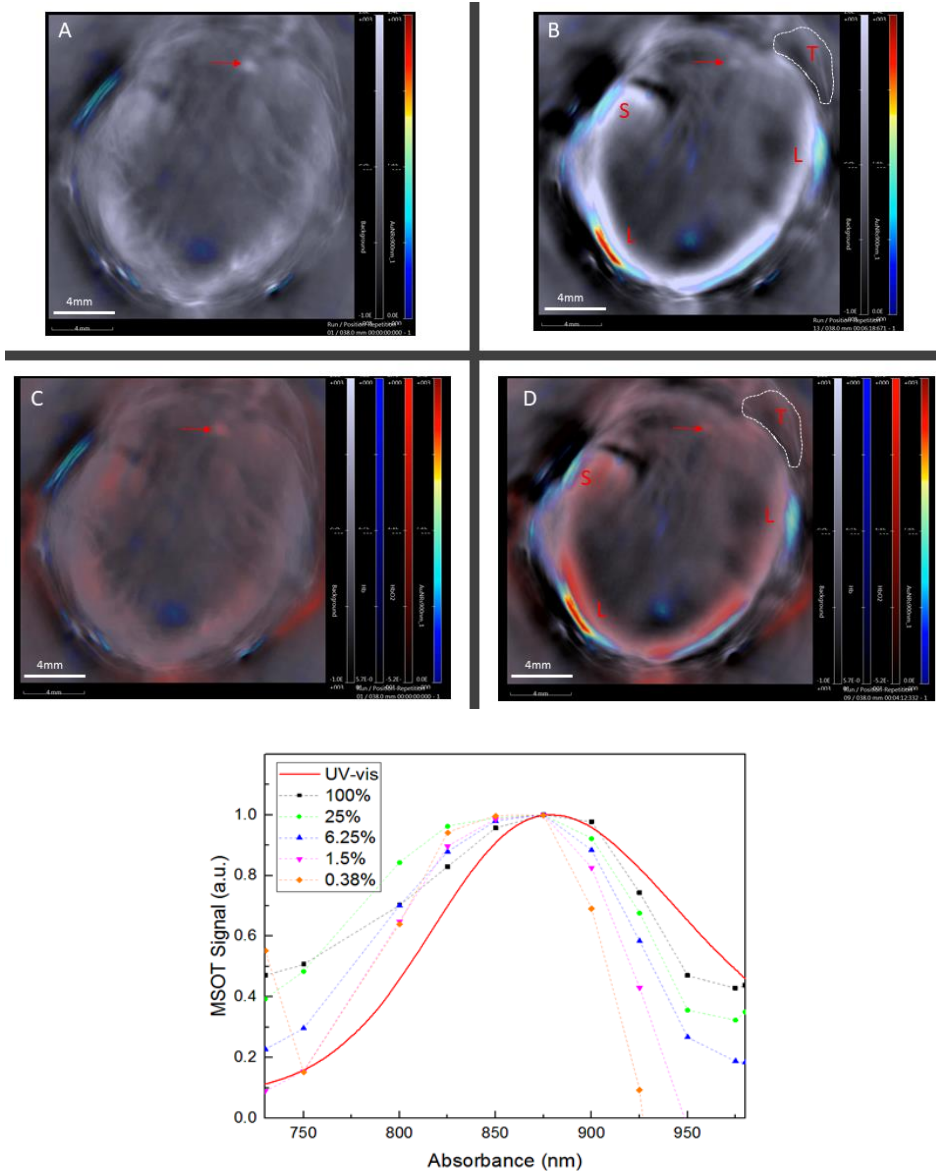


Figure 6-17 Multispectral optoacoustic tomography of gold nanorods

A-D shows AuNRs in SW620 xenograft model. Scale bar 4mm, red arrows denote aorta. S – spleen, L – liver, T – tumour.

A shows pre-injection image while **B** shows post-injection image (1 min following injection). Signal enhancement was visualised in liver and spleen. **C** and **D** shows the same pre- and post-injection images as **A** and **B** with further contrast-enhancement from oxygenated and deoxygenated blood. No contrast enhancement was observed in the region of the tumour (tumour not well visualised) during imaging sessions at immediately post-injection or at 4h and 24h following injection.

The graph shows the measured MSOT absorbance of AuNRs at different dilutions compared to the spectral data obtained by UV-vis spectroscopy (solid red line). This shows a left-shift of the peak absorbance with reducing concentration of AuNRs.

6.3 Gemcitabine and irinotecan for targeted drug delivery in cholangiocarcinoma

As part of the work up towards a TNC-targeted drug delivery vehicle, potential carriers (AuNPs) and active targeting to tumours using TNC-affimers have already been explored in this chapter. As the third main component of a TNC targeted theranostic particle (shown in **Figure 6-1**), effective chemotherapeutic agents against CCA were investigated. *In vitro* toxicity of two drugs used in the chemotherapy of biliary tract cancers, namely gemcitabine and irinotecan were examined. This was performed to determine the required concentration of drug that would need to be delivered to the target tissue to be effective.

Figure 6-18 shows the chemosensitivity assays for TFK-1 and TFKluc2B2. TFK-1 and TFKluc2B2 were sensitive to gemcitabine, with an IC_{50} of $0.93\mu\text{M}$ and $0.17\mu\text{M}$ respectively but required a higher concentration for equivalent cell death with irinotecan; $11.48\mu\text{M}$ and $5.61\mu\text{M}$, respectively. Cell viability did not reach 0% (i.e. complete cell death) even in the presence of much higher doses ($>100\mu\text{M}$ concentration) of both drugs.

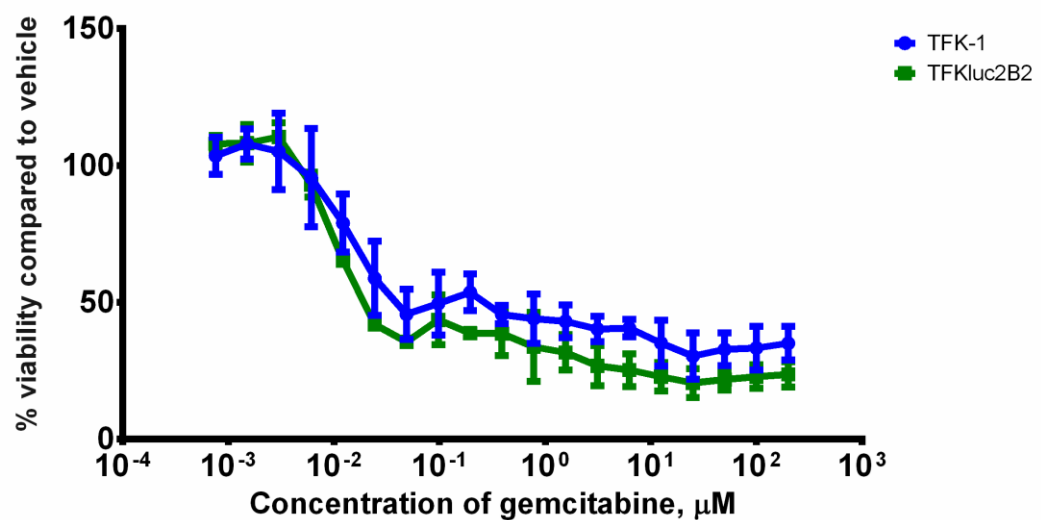
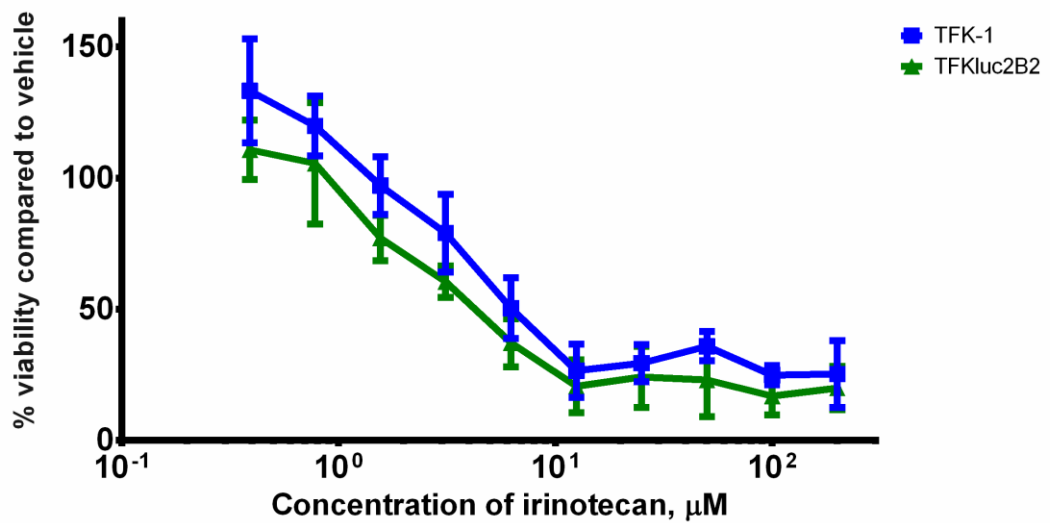


Figure 6-18 Evaluating TFK-1 and TFKluc2B2 sensitivity to irinotecan and gemcitabine

TFK-1 and TFKluc2B2 irinotecan IC_{50} values were $11.48\mu\text{M}$ (95% CI $6.69\text{-}19.72\ \mu\text{M}$) and $5.61\mu\text{M}$ (95% CI $4.02\text{-}7.83\ \mu\text{M}$) respectively (graph above) while gemcitabine IC_{50} values were $0.93\mu\text{M}$ (95% CI $0.44\text{-}1.98\ \mu\text{M}$) and $0.17\mu\text{M}$ (95% CI $0.09\text{-}0.34\ \mu\text{M}$) respectively (graph below).

Triplicate biological experiments were performed with at least 5 technical replicates for each concentration.

6.4 Discussion

6.4.1 Active targeting of TNC in pre-clinical models

In this chapter, TNC-affimers were evaluated for their ability to actively target TNC-expressing tumours. As affimers are novel peptides, these had not previously been evaluated *in vivo*. For proof of concept that TNC-expressing tumours can be targeted by this novel peptide, fluorescent TNC affimers were first evaluated. The final experiment with optimised probes (TNC15C-Rh3 and GFP32C-Rh3) did reveal higher tumour accumulation of the TNC targeted probe compared to test probe, although this difference was not statistically significant (**Section 6.1.4.4**). However, evaluation of active targeting of these fluorescent affimers had numerous challenges.

6.4.1.1. *In vivo* fluorescence imaging challenges

During the preliminary experiments with the TNC15C-Rh1 probe, the fluorescent signal was confirmed to be detectable by the *in vivo* fluorescence imaging system (**Section 6.1.1**). However, it lacked specificity to assess *in vivo* biodistribution in tumour and organs and thus, *ex vivo* imaging was utilised which made serial longitudinal imaging of animal cohorts impossible.

Following intravenous injection of TNC15C-Rh1 probe, a strong fluorescent signal above background was detected in liver, kidney and tumour when imaged *ex vivo* but there was a much lower signal in the other organs imaged (**Figure 6-4**). The fold change in average radiant efficiency measured for the tumour at the 48h time point was higher compared to the liver and kidney at the same time point. This is encouraging as this difference could be due to active tumour targeting by the TNC15C-Rh1 probe. However, a control probe was not used for this experiment to fully assess the observed phenomenon.

Autofluorescence of tissues was another challenge. The murine gallbladder fluorescence signal was high under the optimum excitation/emission filters used (**Section 6.1.1**). This is likely to be due to the autofluorescence of bile as this was detected in liver specimens of control animals with no exposure to any exogenous fluorophores. This background signal was subtracted from the experimental animals. Croce *et al.* (2014) reported excitation of bile at 366-465nm and although peak emissions were detected around 520nm, this fell to very low levels by 620nm (the emission wavelength used for detection in the present study). However, the clear detection of a fluorescent signal in the gallbladder at 620nm following excitation at 570nm suggests that fluorescence imaging would be challenging in liver orthotopic tumour models such as the one described in **Section 3.2.2** (where the gallbladder is used as a landmark for tumour cell inoculation). Fluorescence imaging using the near infrared (NIR) spectrum may avoid these drawbacks as the autofluorescence of normal tissues decrease with higher wavelengths (Frangioni, 2003).

Another challenge faced during fluorescence imaging was the unexpected difficulty with co-localisation of orthotopic tumour using bioluminescence and subsequent fluorescence imaging. Fluorescent signal “bleed through” into the bioluminescence filter or vice versa (**Figure 6-2** and **Figure 6-7**) could lead to inaccurate quantitation of both bioluminescence and fluorescence signals.

Previous work at our centre demonstrated successful *in vivo* fluorescence imaging using a carcinoembryonic antigen (CEA) antibody targeted fluorescent (containing NIR664 fluorescent dye) nanoparticle in a colorectal cancer xenograft model (Tiernan *et al.*, 2015). The excitation/emission wavelengths used by Tiernan *et al.* (2015) were 672nm/694nm compared to 570nm/620nm used for the rhodamine red C₂ maleimide in the present study and the targeting antibody was conjugated with a silica nanoparticle whereas the present study used a fluorescent targeting affimer without a

conjugated nanoparticle. Tiernan *et al.* (2015) demonstrated a significantly high tumour fluorescent signal in the tumour with CEA-targeted particles compared to control at 24h and 48h. In the present study, the differences between TNC targeted and control were not statistically significant. The shorter wavelengths used by Tiernan *et al.* (2015) were closer to the NIR spectrum which is better for optical imaging with lower background signal (Frangioni, 2003). Nanoparticles are known to alter biodistribution and the active CEA targeting combined with the EPR effect may have allowed the particles developed by Tiernan *et al.* (2015) to preferentially accumulate in the xenograft tumour.

6.4.1.2. Quality control of in-house synthesised fluorescent probes

Synthesis of fluorescent probes and estimation of concentration was performed by our collaborators Miss A Tang and Dr R Bon. Each attempt at labelling the affimers resulted in changes in concentration – TNC15C-Rh1 concentration $\sim 150\mu\text{M}$, TNC15C-Rh2 concentration $\sim 200\mu\text{M}$ and TNC15C-Rh3 concentration $\sim 200\text{-}300\mu\text{M}$). It was hypothesised that if the probe could be synthesised at high concentrations, it would be ‘bright’ enough to enable visualisation during *in vivo* imaging and hence efforts were made to increase the concentration of the fluorescent labelled affimers. Although this was intentional to increase the likelihood of detection *in vivo*, the difficulties of reproducibility between batches of labelled probe would have future implications for quality control.

The second batch of fluorescent affimer probes (TNC15C-Rh2 and GFP32C-Rh2) were not of equal fluorescence and therefore not comparable despite a similar estimated concentration. The control probe (GFP32C-Rh2) was brighter than the test probe (TNC15C-Rh2) which made interpretation of results challenging. After the *in vivo* experiments, the two probes were compared by *in vitro* dilution assay and the GFP32C-Rh2 confirmed to be 2.2 times brighter at comparable dilutions (**Figure 6-8A**).

Attempts were made to “correct” for this difference by adjusting the absolute value of detected fluorescence by a factor of 2.2 but this resulted in over manipulation of the data and was therefore abandoned. This highlighted the difficulties of quality control and synthesis of these probes and raised concerns regarding the scalability for larger scale studies.

A further batch of control and test probes (TNC15C-Rh3 and GFP32C-Rh3) were synthesised by the same team who ensured that the concentrations were comparable. This was confirmed on *in vitro* dilution assay using the IVIS imaging system prior to *in vivo* use. Higher levels were observed in the liver, kidney and tumour of the TNC15C-Rh3 group compared to predominantly kidney in the GFP32C-Rh3 group. Although visually tumour fluorescence appeared higher, when corrected for background fluorescence, the fold change in radiant efficiency was higher for the liver compared to tumour in the TNC15C-Rh3 group at all time points (**Figure 6-10**).

The GFP32C-Rh3 control probe behaved differently. Although the fluorescence was comparable in the kidney to the TNC15C-Rh3 probe, the fluorescence in the liver and tumour were comparatively low (**Figure 6-10**). This difference in biodistribution of the control probe compared to the TNC-targeted probe raised concerns regarding any inherent differences between probes such as surface charge which may result in a predominant renal excretion of GFP32C-Rh3 compared to TNC15C-Rh3. An alternative control probe could be considered for future experiments with further analysis of the physical properties of the colloidal solution to ensure comparability prior to *in vivo* use.

6.4.1.3. Limitations of the pre-clinical model

Although the TFKluc2B2 orthotopic model was intended for this series of experiments, the inability to obtain tumour and organ specific biodistribution of the TNC15C-Rh1 probe *in vivo* combined with the level of technical difficulty of model set up, made this challenging. An orthotopic model compared to a xenograft model is superior in terms of

replicating the tumour microenvironment (Loeuillard *et al.*, 2019) which is important especially in the case of an extracellular matrix protein such as TNC.

To achieve the aim of detecting TNC affimer binding to TNC expressing tumour, a xenograft model using a cell line (SW620) with high TNC expression (**Sections 5.2** and **5.3**) was utilised. It was hypothesized that a superficially located xenograft tumour would result in decreased attenuation of any fluorescent signal from the tumour compared to an orthotopic tumour model. TFKluc2B2 xenograft model was not used as tissue expression of TNC was lower compared to SW620.

6.4.2 Gold nanoparticles for theranosis

Fluorescent nanoparticles, although useful in pre-clinical research, have limited translational value outside of the intra-operative setting. Therefore, novel in-house synthesised AuNPs were evaluated as these could form the basis of future applications of molecular imaging with existing imaging modalities such as PAI, PET CT, SPECT or MRI.

Numerous different types of nanoparticles for targeted therapy have been developed (**Figure 1-4**) but AuNPs were selected as this was an active area of research by our collaborators (**Section 6.2**).

6.4.2.1. Toxicity and biocompatibility

AuNPs are usually regarded as biocompatible but Lopez-Chaves *et al.* (2018) have shown that AuNPs can accumulate in organs, mainly in spleen and liver with resultant oxidative stress. However, there is a lack of coherent data regarding AuNP toxicity (Singh *et al.*, 2018) and most studies only report short-term toxicity data.

CTAB, a surfactant commonly used in the synthesis of AuNPs is cytotoxic and therefore AuNPs usually surface coated (Leonov *et al.*, 2008). This surface modification increases

biocompatibility and reduces toxicity in cancer cell lines as demonstrated by Leonov *et al.* (2008) in HepG2 human HCC cell line. However, the authors also demonstrated higher sensitivity of normal cells; IC₅₀ for normal porcine kidney cells 1.1µg/ml compared to 33µg/ml for HepG2 cells (Leonov *et al.*, 2008).

This chapter investigated *in vitro* toxicity of PSS-coated AuNRs kindly gifted by Dr L Roach on three cancer cell lines, TFK-1, TFKluc2B2 and SW620. The IC₅₀ of AuNRs (119.5-145µg/mL, **Figure 6-18**) was higher than what would be realistically used for future *in vivo* applications. However, the inherent cytotoxicity on normal cells, especially normal hepatocytes and cholangiocytes would require future investigation.

6.4.2.2. Labelling and assessment of binding to tenascin C

Antibody labelling of AuNPs for therapeutic applications have been described (Karmani *et al.*, 2013; Li *et al.*, 2019) but affimers being novel peptide scaffolds, have no similar published studies.

AuNPLs were selected for labelling by with TNC affimers due to the ease of labelling (**Section 6.2.2**). Labelling and characterization were performed with the assistance of Dr Sunjie Ye. The initial labelling attempt with the aim of maximum surface coating of AuNPLs with TNC affimers resulted in agglomeration of particles and therefore for the next attempt, a range of surface coatings were tested, and zeta-potential of each solution measured. This allowed assessment of the coverage of AuNPLs with TNC affimer that was optimal for stability of the particles in colloidal dispersion.

Interpreting the images of the cells following fixation after application of nanoparticles was challenging due to the passive diffusion and/or endocytosis of these very small particles across the cell membrane. The control TNC negative cell line HCT116 demonstrated intracellular AuNPs (**Figure 6-15 D**). Proof-of-concept of active TNC-targeting was not demonstrated using this method, likely due to TNC being an ECM

glycoprotein rather than a membrane bound protein. The process of washing the cells after addition of AuNPLs to remove unbound particles could have also resulted in removal of any secreted TNC as well as any TNC-bound TNC-AuNPLs. In addition, the absence of other supporting ECM cells that also secrete/express TNC in the actual tumour microenvironment makes this *in vitro* experiment less translatable to the *in vivo* setting.

To refine this assay, TNC affimer labelled AuNPs could be compared to control affimer labelled AuNPs in a TNC expressing cell line with quantification of the amount of gold per field of view. Although, this would give a quantitative assessment of the difference in active targeting and passive uptake, it would still be a surrogate marker of TNC affimer binding.

6.4.2.3. Photoacoustic imaging

AuNPs have successfully been used for PAI (Li and Chen, 2015; Zhao *et al.*, 2018). With the assistance of Dr L Roach, AuNPLs were imaged on agar tissue-mimicking phantoms using MSOT. This confirmed that the particles gave a strong photoacoustic signal through a range of dilutions (**Figure 6-16**). The synthesised volume of TNC-AuNPLs were insufficient for PAI but detectable signal was expected.

In vivo assessment of unlabelled PSS-coated AuNRs was performed on a SW620 xenograft model. These were previously evaluated in agar phantoms and shown to elicit a strong PAI signal (Dr L Roach, personal communication). Although the AuNR signal was detected during and immediately following injection (**Figure 6-17**), it was not detected at the tumour site subsequently. This could have been due to insufficient passive accumulation of AuNRs due to EPR effect or quick elimination of the AuNRs resulting in insufficient time for accumulation. Further tissue analysis for biodistribution of gold was not performed for this experiment but this could be incorporated into future experiments using either inductively coupled plasma mass

spectrometry (Lopez-Chaves *et al.*, 2018) or imaging mass spectrometry (Muko *et al.*, 2019). These quantitative analyses would be necessary for comparison of targeted compared with untargeted AuNPs.

6.4.3 Chemotherapeutic drugs for theranosis

As the final component of the targeted delivery platform, two drugs were evaluated. The drugs of choice were gemcitabine and irinotecan which are existing therapies for CCA (Valle *et al.*, 2010; Sohal *et al.*, 2013). Both the parent TFK-1 cell line and the transfected luciferase-expressing clone TFKluc2B2 were investigated (**Section 6.3**). The chemosensitivity pattern of both cell lines to gemcitabine was similar across the range of concentrations used but the IC₅₀ for TFK-1 was higher compared to that of TFKluc2B2 (0.93 μM (95% CI 0.44-1.98 μM) vs 0.17 μM (95% CI 0.09-0.34 μM)). A similar pattern was observed for irinotecan for the two cell lines and again TFKluc2B2 was more sensitive to the drug; TFK-1 11.48 μM (95% CI 6.69-19.72 μM) and TFKluc2B2 5.61 μM (95% CI 4.02-7.83 μM). These differences may be explained by the shorter doubling time of TFKluc2B2 (<24hrs) which may have allowed these cells an opportunity to replicate and reach exponential phase prior to the addition of the cell-cycle inhibiting drugs (gemcitabine inhibits DNA synthesis and irinotecan inhibits topoisomerase I during S-phase which results in DNA double-strand breaks).

The measured IC₅₀ of these drugs on these cell lines will serve as a guide for calculating the dose of drug that would need to be delivered via this platform in order to have a therapeutic effect. Drug loading onto AuNPs can be achieved by techniques such as direct adsorption to the AuNP surface (Wang *et al.*, 2018) or drug loading into hollow AuNPs with triggered release using NIR (de Solorzano *et al.*, 2020) depending on the type of AuNP and drug used. Conjugating large amounts drug to AuNPs could be challenging and therefore, the lower the dose that needs to be delivered the better.

Promisingly, Patra *et al.* (2008) have shown that targeted delivery of low doses of gemcitabine can have therapeutic effect in pancreatic adenocarcinoma.

6.4.4 Summary

This chapter has investigated the three main components of a theranostic TNC targeted therapeutic platform for CCA, namely the target, carrier and drug. TNC affimers showed some specificity towards tumours *in vivo* compared to control affimers although high levels were detected in liver and kidney tissue. The two types of in-house synthesised AuNPs evaluated showed detectability on PAI and were not inherently toxic to the cancer cells tested. The two drugs evaluated were confirmed to be cytotoxic to the cell lines tested and the respective IC₅₀ values were determined.

A multimodal theranostic particle such as a gemcitabine-loaded, TNC-affimer labelled AuNR which could target deliver gemcitabine, act as an imaging tracer as well as have thermoablative capabilities, offers potential for improved therapeutics in CCA.

However, the technical challenges of developing reproducible, scalable particles with demonstrable biocompatibility will be significant rate limiting factors in the translational pipeline.

Chapter 7

General discussion and future challenges

7. General discussion and future challenges

7.1 Final summary

The aim of this project was to develop a novel targeted theranostic delivery system for CCA. Such a delivery system requires pre-clinical validation in a model that mimics the human CCA tumour microenvironment, and as such a novel orthotopic model of CCA was developed (**Chapter 3**). EH-CCA cell lines were used to establish this model as most existing models are of IH-CCA despite the majority of CCA being EH-CCA (Cadamuro *et al.*, 2018; Erice *et al.*, 2019; Loeuillard *et al.*, 2019). This mouse model took advantage of both HF-US and bioluminescence pre-clinical imaging systems and utilised a minimally invasive method of tumour cell inoculation (**Section 3.2.2**). The development of this CCA model along with an orthotopic tumour model of CRLM developed by Dr L E McVeigh has now been published (McVeigh *et al.*, 2019).

Another requirement to achieving the thesis aim was the identification of biomarkers that could serve as potential targets for molecular imaging and targeted drug delivery. Previous work at our institution had focussed on CCA biomarker discovery using biliary proteomics (Farid *et al.*, 2011) and validation of selected biomarkers for theranosis (Nair *et al.*, 2018). To identify other potential candidate biomarkers for theranosis, a systematic review of the literature was performed (**Chapter 4**). This search strategy identified multiple biomarkers and a scoring system, the TASC-T score, was developed to select those with greatest potential as theranostic biomarkers. The top 5 biomarkers according to the TASC-T score were MMP9, CLDN18, TNC, CA9 and EGFR.

TNC was selected as the candidate biomarker for further validation in CCA as this presented an opportunity for collaborative research with the cardiovascular research group at the University of Leeds who aimed to develop TNC targeted MRI imaging, funded by British Heart Foundation (Grant Number NH/12/1/29382 (Plein, 2012)).

To validate TNC as a potential theranostic target in CCA TNC expression in archival CCA tissues at our institution was explored (**Chapter 5**). This was found to be upregulated in CCA tissue with comparatively low expression in adjacent normal liver in both human (**Section 5.1.1**) and murine tissues (**Section 5.2**).

As part of the development of a novel theranostic platform, novel peptides (i.e. TNC affimers) with similar affinity to TNC protein compared to TNC antibody were investigated (**Chapter 6**). TNC affimers showed some specificity towards tumours *in vivo* compared to control affimers although high levels were detected in liver and kidney tissue (**Section 6.1.4.4**). The work up of this TNC affimer in an animal model has now been published along with other applications of affimer technology (Tiede *et al.*, 2017).

7.2 Pre-clinical models of extra-hepatic cholangiocarcinoma

Orthotopic models permit the investigation of biological behaviour of tumour cells and their interaction with the liver microenvironment and are superior to the subcutaneous xenograft model for the evaluation of drug efficacy (Huynh *et al.*, 2011). Orthotopic models of CCA and GBC described in the literature involve surgical inoculation of tumour cells into the biliary tree or liver (Horiuchi *et al.*, 2003; Cadamuro *et al.*, 2013; Jo *et al.*, 2013; Rizvi *et al.*, 2018). For example, the method described by Rizvi *et al.* (2018) involve a 1cm incision below the xyphoid process of the animal for the injection of tumour cells into the liver.

This thesis describes the development of an EH-CCA orthotopic tumour model utilising HF-US guided injection of luciferase-expressing CCA cell lines into murine liver (**Chapter 3**). The peri-cholecystic area was selected as the site of injection as the gallbladder is the only part of the biliary tree that can be easily identified on HF-US in a murine model. Fasting mice prior to injecting was an optimization strategy to distend

the gallbladder which resulted in easy identification on HF-US. This approach allowed cell injection into the liver adjacent to the gallbladder, avoiding invasive surgery and thus post-operative complications in the animal.

As the cell lines used for the orthotopic model expressed luciferase, longitudinal imaging for monitoring of tumour growth was sensitive, fast and comparatively cheaper than MRI or CT. Cadamuro *et al.* (2013) and Fabris *et al.* (2011) have also described orthotopic CCA models using luciferase-expressing EGI-1 and TFK-1 cell lines albeit not using a minimally-invasive technique.

7.2.1 Limitations

The optimised minimally invasive orthotopic CCA model described in the present study (**Section 3.2.2**) does have limitations. The inability to ligate the right or left hepatic duct following injection of cells to induce cholestasis, is one such limitation. Obstructive jaundice due to cholestasis is a presenting symptom in upto 90% of patients with PH-CCA (Blechacz, 2017). Orthotopic models such as the IH-CCA syngeneic rat model described by Sirica *et al.* (2008) induce hepatic injury due to cholestasis by bile duct ligation using an open technique. This syngeneic rat IH-CCA model does have the advantages of mimicking the tumour microenvironment with cholestasis in an immunocompetent host but is time-consuming and costly to generate (Sirica *et al.*, 2008). A novel orthotopic model of EH-CCA developed recently involves two invasive surgeries for model establishment (CBD ligation to induce dilataion followed by injection of tumour cells into the dilated duct) (Song *et al.*, 2019). This EH-CCA orthotopic model does feature cholestasis but the authors report 25% (5 out of 20) animal deaths (Song *et al.*, 2019).

Other disadvantages of the present model include the need for genetic modification of human CCA cell lines to enable bioluminescence imaging (**Section 3.4.1.2**) and the requirement for an immunocompromised host. The latter means that the model

developed in the present study (**Section 3.2.2**) cannot be used to assess efficacy of immunotherapies such as the newer immune checkpoint inhibitors (for example, PD-1 and PD-L1 inhibitors).

7.2.2 Ideal characteristics of an animal model

In a review of animal models of CCA, Loeuillard *et al.* (2019) described six ideal characteristics of an animal model. Ideally, a CCA model should originate from an immunocompetent host, display similar genetic aberrations and phenotypic expression to human CCA, exhibit desmoplastic stroma, mimic an anatomical subset of CCA and also model the metastatic phenotype of CCA (Loeuillard *et al.*, 2019). The method used by the authors of this review to evaluate CCA animal models used five criteria (Loeuillard *et al.*, 2019). The anatomical location of the tumour (ideally, an orthotopic tumour in the liver), liver injury or dysfunction, histological and genetic characteristics as well as animal consequences.

The model described in the present study (**Section 3.2.2**) does fulfil the ideal anatomical location criteria but does not model liver injury or dysfunction. Liver function tests were not routinely measured but this can be performed with future experiments using this model. Histologically, the orthotopic tumours did resemble an invasive adenocarcinoma (**Figure 3-14**).

The parent cell line TFK-1 was established from a patient with mid-CBD invasive papillary adenocarcinoma and TFK-1 subcutaneous xenograft histology has shown morphological similarities to the original resected specimen from the patient (Saijyo *et al.*, 1995). TFK-1 cells also express mucin 1 (MUC-1) and human epidermal growth factor receptor 2 (HER2) but are negative for *KRAS* mutation (Saijyo *et al.*, 1995). The expression of these markers and the recommended CCA markers by Loeuillard *et al.* (2019) such as SRY-Box 9 (SOX-9), cytokeratin 7 (CK-7) and cytokeratin 19 (CK-19),

were not formally evaluated in the TKFluc2B2 cells, xenograft or orthotopic tumour tissue. This could be an area for future investigation to further validate this model. Other criteria that have not been evaluated in the present model are the animal consequences (survival and metastasis) as all the experiments evaluated short-term tumour growth. However, these long-term outcomes can be considered in future experiments.

As no ideal orthotopic animal model of CCA exists, future research in this field is essential. Other areas that could be investigated include implantation of patient-derived xenografts (Cavalloni *et al.*, 2016; Garcia *et al.*, 2018) into murine liver or injection of CCA organoids (Broutier *et al.*, 2017) into the murine liver.

7.3 Targeting Tenascin C for theranosis

TNC is one of several biomarkers with theranostic potential in CCA (**Chapter 4**). The reported TNC expression in CCA (**Section 4.2.3**) and the theranostic potential of TNC (**Section 4.3.3**) are discussed in **Chapter 4**. Targeted molecular imaging using TNC aptamer (Hicke *et al.*, 2006) or TNC antibody (Song *et al.*, 2017) and TNC targeted drug delivery (He *et al.*, 2018) have been evaluated by other investigators but none of these pre-clinical studies involved CCA models.

The role of the tumour ECM and expression of TNC in the progression of cancers including CCA has been described (Neesse *et al.*, 2015; Sukowati *et al.*, 2015). Pre-clinical studies have shown that therapeutic targeting of CAFs (which secrete TNC) result in a reduction in TNC positive tumour ECM (Mertens *et al.*, 2013). A TNC targeted imaging agent could monitor the effectiveness of such anti-CAF therapy. TNC was present in the majority of CCA tissue ECM investigated in the present study compared to the paired normal liver which was generally negative or only weakly positive in the liver sinusoids (**Section 5.1**).

This thesis also investigated TNC affimers which are novel, antibody-mimicking targeting peptides (**Chapter 6**). Affimer technology is now commercially available and addresses the disadvantages of antibodies (Baker, 2015; Bradbury and Pluckthun, 2015; Bedford *et al.*, 2017; Adamson *et al.*, 2019). In time, novel reagents such as affimers should replace costly antibodies with smaller, physicochemically stable and a more ethical alternative to antibodies (Bedford *et al.*, 2017).

Developing nanotheranostic platforms targeted to TNC also has the benefit of translatability to other cancers such as melanoma where TNC is highly expressed (Shao *et al.*, 2015), as well as other benign diseases such as cardiovascular disease (Franz *et al.*, 2015; Song *et al.*, 2017).

7.4 Targeted nanoparticles for theranosis

Targeted nanoparticles for molecular imaging and therapeutic drug delivery in cancer have been an area of extensive research over the past decade (Morales-Cruz *et al.*, 2019; Raj *et al.*, 2019). Targeted drug delivery has the potential to revolutionize the current method of administration of chemotherapy (usually cyclical administration) and allow precision delivery of drug with sustained-release, metronomic dosing with greater therapeutic efficacy and fewer systemic side-effects (Cisterna *et al.*, 2016).

In addition to the potential benefits described in cancer research, targeted nanoparticles have favourable pre-clinical data in other disease such as Alzheimer's disease (Martin-Rapun *et al.*, 2017) and cardiovascular disease (Tan *et al.*, 2019).

A vast array of hypothetical formulations of targeted nanoparticles can be designed by varying the nanoparticle properties and the ligand to enable binding to a specified target. Whether one type of targeting ligand on a single nanoparticle delivery system or multiple types targeting ligands would improve active targeting would require in-depth evaluation. Drug-loading of targeted nanoparticles adds another layer of

complexity. Optimisation of nanoparticle drug loading, determination of amount of drug loading, confirmation of drug release on binding to target(s) as well as pharmacokinetics and pharmacodynamics of these complex drug-loaded nanoparticle delivery systems *in vivo* will require further investigation.

For theranostic AuNPs, successful molecular imaging is an important aspect for the translation of these novel therapeutics to clinical practice. Multiple modalities are available (Ehlerding *et al.*, 2018) but MRI (Sologan *et al.*, 2019), CT (Curry *et al.*, 2014) and PET CT (Simon *et al.*, 2020) have been effectively used with AuNPs. These imaging modalities are in routine use for imaging in CCA and therefore, these should be explored first to expedite translation.

7.5 Future challenges

Based on the current extensive research, a wide range of potential targeted nanoparticles for diagnostic and therapeutic use could be developed. Any variation in physical properties of the nanoparticle (material, size, shape, surface charge, surface coating etc.), the type of targeting ligand (antibody, aptamer, affimer etc.), the target (any promising theranostic biomarker) or type of encapsulated drug, would change the properties of the formulation and thus the theranostic efficacy *in vivo*.

This wide range of targeted nanoparticle formulations would seem advantageous and in theory, it could provide customisable therapy to an individual patient (i.e. personalised medicine). However, the pre-clinical validation of such formulations to gain FDA approval for clinical use and evaluation of therapeutic benefit in large scale clinical trials would be extremely challenging. Despite the range of formulations, perhaps only a handful may eventually be of clinical use. Prediction of which of these would have clinical application will be an immense challenge. A theranostic delivery

system with multiple functional components may only perform as well as its weakest link.

The majority of nanomedicines submitted for FDA approval over the past decade were liposomal formulations of chemotherapeutic agents (D'Mello *et al.*, 2017) with only 11% of submissions involving metallic nanoparticles (Clogston *et al.*, 2019) such as the gold nanoparticles used in this study.

For FDA approval, nanomedicines such as theranostic nanoparticle formulations would need to be pharmaceutical grade with appropriate quality control steps (Clogston *et al.*, 2019). Most pre-clinical studies such as the present study utilise in-house synthesised and labelled particles and as such have limited scalability for large studies. To enable clinical trials, large scale production of a reproducible product is required. Furthermore, the stability and shelf-life of these formulations would need to be established. It is perhaps difficulties in these areas that have hampered the translation of promising theranostic nanoparticles, such as the multimodal nanoparticle described by Ko *et al.* (2011) described in the published literature nearly a decade ago. Despite having shown promise in pre-clinical studies, these particles may have failed regulatory approval, large-scale application deemed cost prohibitive or lacked impetus from personnel involved to take forward to clinical trials.

Further pre-clinical research is essential to translate promising nanotechnology for the therapeutic benefit of patients with CCA, those with other cancers or even benign diseases to whom this technology would be beneficial. Researchers should be encouraged to publish negative results to avoid duplication and wastage of scarce resources. Research efforts would need to be collaborative and more streamlined. Nanoparticle testing would need standardisation and scale up requirements addressed from the outset with acknowledgement of the global health economics in order to

expedite the translation of this technology for clinical use (Anselmo and Mitragotri, 2019).

With multiple research avenues left to be explored for this promising technology, it may take over a decade before these theranostic applications are in routine use for the benefit of patients with CCA.

List of References

Aalbersberg, E.A., de Wit-van der Veen, B.J., Zwaagstra, O., Codee-van der Schilden, K., Vegt, E. and Vogel, W.V. 2017. Preclinical imaging characteristics and quantification of Platinum-195m SPECT. *Eur J Nucl Med Mol Imaging*. **44**(8), pp.1347-1354.

Abdelrahman, M.A., Marston, G., Hull, M.A., Markham, A.F., Jones, P.F., Evans, J.A. and Coletta, P.L. 2012. High-frequency ultrasound for in vivo measurement of colon wall thickness in mice. *Ultrasound Med Biol*. **38**(3), pp.432-442.

Adachi, T. and Nakamura, Y. 2019. Aptamers: A Review of Their Chemical Properties and Modifications for Therapeutic Application. *Molecules*. **24**(23).

Adair, J.H., Parette, M.P., Altinoglu, E.I. and Kester, M. 2010. Nanoparticulate alternatives for drug delivery. *ACS Nano*. **4**(9), pp.4967-4970.

Adamson, H., Nicholl, A., Tiede, C., Tang, A.A., Davidson, A., Curd, H., Wignall, A., Ford, R., Nuttall, J., McPherson, M.J., Johnson, M. and Tomlinson, D.C. 2019. Affimers as anti-idiotypic affinity reagents for pharmacokinetic analysis of biotherapeutics. *Biotechniques*. **67**(6), pp.261-269.

Adiwijaya, B.S., Kim, J., Lang, I., Csozsi, T., Cubillo, A., Chen, J.S., Wong, M., Park, J.O., Kim, J.S., Rau, K.M., Melichar, B., Gallego, J.B., Fitzgerald, J., Belanger, B., Molnar, I. and Ma, W.W. 2017. Population Pharmacokinetics of Liposomal Irinotecan in Patients With Cancer. *Clin Pharmacol Ther*. **102**(6), pp.997-1005.

Aishima, S., Taguchi, K., Terashi, T., Matsuura, S., Shimada, M. and Tsuneyoshi, M. 2003. Tenascin expression at the invasive front is associated with poor prognosis in intrahepatic cholangiocarcinoma. *Mod Pathol*. **16**(10), pp.1019-1027.

Akashi, K., Ebata, T., Mizuno, T., Yokoyama, Y., Igami, T., Yamaguchi, J., Onoe, S. and Nagino, M. 2018. Surgery for perihilar cholangiocarcinoma from a viewpoint of age: Is it beneficial to octogenarians in an aging society? *Surgery*. **164**(5), pp.1023-1029.

Alberts B, J.A., Lewis J, et al. 2002. Integrins. *Molecular Biology of the Cell*. [Online]. 4th edition ed. New York: Garland Science.

Allen, M. and Louise Jones, J. 2011. Jekyll and Hyde: the role of the microenvironment on the progression of cancer. *J Pathol*. **223**(2), pp.162-176.

Alterio, V., Hilvo, M., Di Fiore, A., Supuran, C.T., Pan, P., Parkkila, S., Scaloni, A., Pastorek, J., Pastorekova, S., Pedone, C., Scozzafava, A., Monti, S.M. and De Simone, G. 2009. Crystal structure of the catalytic domain of the tumor-

associated human carbonic anhydrase IX. *Proc Natl Acad Sci U S A.* **106**(38), pp.16233-16238.

Anani, T., Brannen, A., Panizzi, P., Duin, E.C. and David, A.E. 2019. Quantitative, real-time in vivo tracking of magnetic nanoparticles using multispectral optoacoustic tomography (MSOT) imaging. *J Pharm Biomed Anal.* p112951.

Anderson, C. and Kim, R. 2009. Adjuvant therapy for resected extrahepatic cholangiocarcinoma: a review of the literature and future directions. *Cancer Treat Rev.* **35**(4), pp.322-327.

Anselmo, A.C. and Mitragotri, S. 2019. Nanoparticles in the clinic: An update. *Bioeng Transl Med.* **4**(3), pe10143.

Baglieri, J., Brenner, D.A. and Kisseleva, T. 2019. The Role of Fibrosis and Liver-Associated Fibroblasts in the Pathogenesis of Hepatocellular Carcinoma. *Int J Mol Sci.* **20**(7).

Baker, M. 2015. Reproducibility crisis: Blame it on the antibodies. *Nature.* **521**(7552), pp.274-276.

Bayat-Mokhtari, R., Homayouni, T.S., Baluch, N., Morgatskaya, E., Kumar, S., Das, B. and Yeger, H. 2017. Combination therapy in combating cancer. *Oncotarget.* **8**(23), pp.38022-38043.

Bedford, R., Tiede, C., Hughes, R., Curd, A., McPherson, M.J., Peckham, M. and Tomlinson, D.C. 2017. Alternative reagents to antibodies in imaging applications. *Biophys Rev.* **9**(4), pp.299-308.

Bekaii-Saab, T., Phelps, M.A., Li, X., Saji, M., Goff, L., Kauh, J.S., O'Neil, B.H., Balsom, S., Balint, C., Lierseemann, R., Vasko, V.V., Bloomston, M., Marsh, W., Doyle, L.A., Ellison, G., Grever, M., Ringel, M.D. and Villalona-Calero, M.A. 2011. Multi-institutional phase II study of selumetinib in patients with metastatic biliary cancers. *J Clin Oncol.* **29**(17), pp.2357-2363.

Bergquist, A. and von Seth, E. 2015. Epidemiology of cholangiocarcinoma. *Best Pract Res Clin Gastroenterol.* **29**(2), pp.221-232.

Berman, H.M., Westbrook, J., Feng, Z., Gilliland, G., Bhat, T.N., Weissig, H., Shindyalov, I.N. and Bourne, P.E. 2000. The Protein Data Bank. *Nucleic Acids Res.* **28**(1), pp.235-242.

Bi, C., Liu, M., Rong, W., Wu, F., Zhang, Y., Lin, S., Liu, Y., Wu, J. and Wang, L. 2019. High Beclin-1 and ARID1A expression correlates with poor survival and high recurrence in intrahepatic cholangiocarcinoma: a histopathological retrospective study. *BMC Cancer.* **19**(1), p213.

Biomarkers Definitions Working Group. 2001. Biomarkers and surrogate endpoints: preferred definitions and conceptual framework. *Clin Pharmacol Ther.* **69**(3), pp.89-95.

Blechacz, B. 2017. Cholangiocarcinoma: Current Knowledge and New Developments. *Gut Liver.* **11**(1), pp.13-26.

Bobo, D., Robinson, K.J., Islam, J., Thurecht, K.J. and Corrie, S.R. 2016. Nanoparticle-Based Medicines: A Review of FDA-Approved Materials and Clinical Trials to Date. *Pharm Res.* **33**(10), pp.2373-2387.

Borger, D.R., Tanabe, K.K., Fan, K.C., Lopez, H.U., Fantin, V.R., Straley, K.S., Schenkein, D.P., Hezel, A.F., Ancukiewicz, M., Liebman, H.M., Kwak, E.L., Clark, J.W., Ryan, D.P., Deshpande, V., Dias-Santagata, D., Ellisen, L.W., Zhu, A.X. and Iafrate, A.J. 2012. Frequent mutation of isocitrate dehydrogenase (IDH)1 and IDH2 in cholangiocarcinoma identified through broad-based tumor genotyping. *Oncologist.* **17**(1), pp.72-79.

Bourien, H., Palard, X., Rolland, Y., Le Du, F., Beuzit, L., Uguen, T., Le Sourd, S., Pracht, M., Manceau, V., Lievre, A., Boudjema, K., Garin, E. and Edeline, J. 2018. Yttrium-90 glass microspheres radioembolization (RE) for biliary tract cancer: a large single-center experience. *Eur J Nucl Med Mol Imaging.*

Bradbury, A. and Pluckthun, A. 2015. Reproducibility: Standardize antibodies used in research. *Nature.* **518**(7537), pp.27-29.

Bridgewater, J., Lopes, A., Beare, S., Duggan, M., Lee, D., Ricamara, M., McEntee, D., Sukumaran, A., Wasan, H. and Valle, J.W. 2016. A phase 1b study of Selumetinib in combination with Cisplatin and Gemcitabine in advanced or metastatic biliary tract cancer: the ABC-04 study. *BMC Cancer.* **16**, p153.

Brosicke, N. and Faissner, A. 2015. Role of tenascins in the ECM of gliomas. *Cell Adh Migr.* **9**(1-2), pp.131-140.

Broutier, L., Mastrogiovanni, G., Verstegen, M.M., Francies, H.E., Gavarro, L.M., Bradshaw, C.R., Allen, G.E., Arnes-Benito, R., Sidorova, O., Gaspersz, M.P., Georgakopoulos, N., Koo, B.K., Dietmann, S., Davies, S.E., Praseedom, R.K., Lieshout, R., JNM, I.J., Wigmore, S.J., Saeb-Parsy, K., Garnett, M.J., van der Laan, L.J. and Huch, M. 2017. Human primary liver cancer-derived organoid cultures for disease modeling and drug screening. *Nat Med.* **23**(12), pp.1424-1435.

Bult CJ, B.J., Smith CL, Kadin JA, Richardson JE, the Mouse Genome Database Group. 2019. 2019. Mouse Genome Database (MGD) 2019. *Nucleic Acids Res.* **8**(47 (D1)), pp.D801–D806.

Burden, N., Chapman, K., Sewell, F. and Robinson, V. 2015. Pioneering better science through the 3Rs: an introduction to the national centre for the replacement, refinement, and reduction of animals in research (NC3Rs). *J Am Assoc Lab Anim Sci.* **54**(2), pp.198-208.

Byrne, J.D., Betancourt, T. and Brannon-Peppas, L. 2008. Active targeting schemes for nanoparticle systems in cancer therapeutics. *Adv Drug Deliv Rev.* **60**(15), pp.1615-1626.

Cadamuro, M., Brivio, S., Stecca, T., Kaffe, E., Mariotti, V., Milani, C., Fiorotto, R., Spirli, C., Strazzabosco, M. and Fabris, L. 2018. Animal models of cholangiocarcinoma: What they teach us about the human disease. *Clin Res Hepatol Gastroenterol.* **42**(5), pp.403-415.

Cadamuro, M., Nardo, G., Indraccolo, S., Dall'olmo, L., Sambado, L., Moserle, L., Franceschet, I., Colledan, M., Massani, M., Stecca, T., Bassi, N., Morton, S., Spirli, C., Fiorotto, R., Fabris, L. and Strazzabosco, M. 2013. Platelet-derived growth factor-D and Rho GTPases regulate recruitment of cancer-associated fibroblasts in cholangiocarcinoma. *Hepatology.* **58**(3), pp.1042-1053.

Castellano-Megias, V.M., Ibarrola-de Andres, C. and Colina-Ruizdelgado, F. 2013. Pathological aspects of so called "hilar cholangiocarcinoma". *World J Gastrointest Oncol.* **5**(7), pp.159-170.

Cavalloni, G., Peraldo-Neia, C., Sassi, F., Chiorino, G., Sarotto, I., Aglietta, M. and Leone, F. 2016. Establishment of a patient-derived intrahepatic cholangiocarcinoma xenograft model with KRAS mutation. *BMC Cancer.* **16**, p90.

Cham, K.K., Baker, J.H., Takhar, K.S., Flexman, J.A., Wong, M.Q., Owen, D.A., Yung, A., Kozlowski, P., Reinsberg, S.A., Chu, E.M., Chang, C.W., Buczkowski, A.K., Chung, S.W., Scudamore, C.H., Minchinton, A.I., Yapp, D.T. and Ng, S.S. 2010. Metronomic gemcitabine suppresses tumour growth, improves perfusion, and reduces hypoxia in human pancreatic ductal adenocarcinoma. *Br J Cancer.* **103**(1), pp.52-60.

Charlesriver. 2019. [Online]. [Accessed 03/10/2019]. Available from: <https://www.criver.com/products-services/find-model/balbc-nude-mouse?region=3671>

Cheal, S.M., Punzalan, B., Doran, M.G., Evans, M.J., Osborne, J.R., Lewis, J.S., Zanzonico, P. and Larson, S.M. 2014. Pairwise comparison of ⁸⁹Zr- and ¹²⁴I-labeled cG250 based on positron emission tomography imaging and nonlinear immunokinetic modeling: in vivo carbonic anhydrase IX receptor binding and internalization in mouse xenografts of clear-cell renal cell carcinoma. *Eur J Nucl Med Mol Imaging.* **41**(5), pp.985-994.

Chen, Wang, Z., Sun, J., Song, Q., He, B., Zhang, H., Wang, X., Dai, W. and Zhang, Q. 2016a. A tenascin C targeted nanoliposome with navitoclax for specifically eradicating of cancer-associated fibroblasts. *Nanomedicine.* **12**(1), pp.131-141.

Chen, F., Ehlerding, E.B. and Cai, W. 2014. Theranostic nanoparticles. *J Nucl Med.* **55**(12), pp.1919-1922.

Chen, G., Roy, I., Yang, C. and Prasad, P.N. 2016b. Nanochemistry and Nanomedicine for Nanoparticle-based Diagnostics and Therapy. *Chem Rev.* **116**(5), pp.2826-2885.

Cheon, D.J. and Orsulic, S. 2011. Mouse models of cancer. *Annu Rev Pathol.* **6**, pp.95-119.

Cherukuri, P. and Curley, S.A. 2010. Use of nanoparticles for targeted, noninvasive thermal destruction of malignant cells. *Methods Mol Biol.* **624**, pp.359-373.

Chiquet-Ehrismann, R. 2004. Tenascins. *Int J Biochem Cell Biol.* **36**(6), pp.986-990.

Chiquet-Ehrismann, R., Mackie, E.J., Pearson, C.A. and Sakakura, T. 1986. Tenascin: an extracellular matrix protein involved in tissue interactions during fetal development and oncogenesis. *Cell.* **47**(1), pp.131-139.

Chiquet-Ehrismann, R. and Tucker, R.P. 2011. Tenascins and the importance of adhesion modulation. *Cold Spring Harb Perspect Biol.* **3**(5).

Cillo, U., Fondevila, C., Donadon, M., Gringeri, E., Mocchegiani, F., Schlitt, H.J., Ijzermans, J.N.M., Vivarelli, M., Zieniewicz, K., Olde Damink, S.W.M. and Groot Koerkamp, B. 2019. Surgery for cholangiocarcinoma. *Liver Int.* **39 Suppl 1**, pp.143-155.

Cisterna, B.A., Kamaly, N., Choi, W.I., Tavakkoli, A., Farokhzad, O.C. and Vilos, C. 2016. Targeted nanoparticles for colorectal cancer. *Nanomedicine (Lond).* **11**(18), pp.2443-2456.

ClinicalTrials.gov. [Online]. [Accessed 30/11/2019]. Available from: <https://ClinicalTrials.gov/show/NCT02862535>

Clinicaltrials.gov. 2019a. [Online]. Available from: <https://clinicaltrials.gov/>

Clinicaltrials.gov. 2019b. [Online]. [Accessed 28/11/2019]. Available from: <https://clinicaltrials.gov/>

Clogston, J.D., Hackley, V.A., Prina-Mello, A., Puri, S., Sonzini, S. and Soo, P.L. 2019. Sizing up the Next Generation of Nanomedicines. *Pharm Res.* **37**(1), p6.

Corcoran, E.B. and Hanson, R.N. 2014. Imaging EGFR and HER2 by PET and SPECT: a review. *Med Res Rev.* **34**(3), pp.596-643.

Croce, A.C., Ferrigno, A., Santin, G., Vairetti, M. and Bottiroli, G. 2014. Bilirubin: an autofluorescence bile biomarker for liver functionality monitoring. *J Biophotonics.* **7**(10), pp.810-817.

Curry, T., Kopelman, R., Shilo, M. and Popovtzer, R. 2014. Multifunctional theranostic gold nanoparticles for targeted CT imaging and photothermal therapy. *Contrast Media Mol Imaging*. **9**(1), pp.53-61.

D'Mello, S.R., Cruz, C.N., Chen, M.L., Kapoor, M., Lee, S.L. and Tyner, K.M. 2017. The evolving landscape of drug products containing nanomaterials in the United States. *Nat Nanotechnol*. **12**(6), pp.523-529.

de Almeida, P.E., van Rappard, J.R. and Wu, J.C. 2011. In vivo bioluminescence for tracking cell fate and function. *Am J Physiol Heart Circ Physiol*. **301**(3), pp.H663-671.

De Minicis, S., Kisseleva, T., Francis, H., Baroni, G.S., Benedetti, A., Brenner, D., Alvaro, D., Alpini, G. and Marziani, M. 2013. Liver carcinogenesis: rodent models of hepatocarcinoma and cholangiocarcinoma. *Dig Liver Dis*. **45**(6), pp.450-459.

De Simone, G. and Supuran, C.T. 2010. Carbonic anhydrase IX: Biochemical and crystallographic characterization of a novel antitumor target. *Biochim Biophys Acta*. **1804**(2), pp.404-409.

de Solorzano, I.O., Prieto, M., Mendoza, G., Sebastian, V. and Arruebo, M. 2020. Triggered drug release from hybrid thermoresponsive nanoparticles using near infrared light. *Nanomedicine (Lond)*. **15**(3), pp.219-234.

Divgi, C.R., Pandit-Taskar, N., Jungbluth, A.A., Reuter, V.E., Gonen, M., Ruan, S., Pierre, C., Nagel, A., Pryma, D.A., Humm, J., Larson, S.M., Old, L.J. and Russo, P. 2007. Preoperative characterisation of clear-cell renal carcinoma using iodine-124-labelled antibody chimeric G250 (124I-cG250) and PET in patients with renal masses: a phase I trial. *Lancet Oncol*. **8**(4), pp.304-310.

Dottermusch, M., Kruger, S., Behrens, H.M., Halske, C. and Rocken, C. 2019. Expression of the potential therapeutic target claudin-18.2 is frequently decreased in gastric cancer: results from a large Caucasian cohort study. *Virchows Arch*. **475**(5), pp.563-571.

Driessen, A., Landuyt, W., Pastorekova, S., Moons, J., Goethals, L., Haustermans, K., Naftoux, P., Penninckx, F., Geboes, K., Lerut, T. and Ectors, N. 2006. Expression of carbonic anhydrase IX (CA IX), a hypoxia-related protein, rather than vascular-endothelial growth factor (VEGF), a pro-angiogenic factor, correlates with an extremely poor prognosis in esophageal and gastric adenocarcinomas. *Ann Surg*. **243**(3), pp.334-340.

Dziawer, L., Majkowska-Pilip, A., Gawel, D., Godlewska, M., Pruszynski, M., Jastrzebski, J., Was, B. and Bilewicz, A. 2019. Trastuzumab-Modified Gold Nanoparticles Labeled with (211)At as a Prospective Tool for Local Treatment of HER2-Positive Breast Cancer. *Nanomaterials (Basel)*. **9**(4).

Ebata, T., Hirano, S., Konishi, M., Uesaka, K., Tsuchiya, Y., Ohtsuka, M., Kaneoka, Y., Yamamoto, M., Ambo, Y., Shimizu, Y., Ozawa, F., Fukutomi, A., Ando,

M., Nimura, Y., Nagino, M. and Bile Duct Cancer Adjuvant Trial Study, G. 2018. Randomized clinical trial of adjuvant gemcitabine chemotherapy versus observation in resected bile duct cancer. *Br J Surg.* **105**(3), pp.192-202.

Edeline, J., Benabdelghani, M., Bertaut, A., Watelet, J., Hammel, P., Joly, J.P., Boudjema, K., Fartoux, L., Bouhier-Leporrier, K., Jouve, J.L., Faroux, R., Guerin-Meyer, V., Kurtz, J.E., Assenat, E., Seitz, J.F., Baumgaertner, I., Tougeron, D., de la Fouchardiere, C., Lombard-Bohas, C., Boucher, E., Stanbury, T., Louvet, C., Malka, D. and Phelip, J.M. 2019. Gemcitabine and Oxaliplatin Chemotherapy or Surveillance in Resected Biliary Tract Cancer (PRODIGE 12-ACCORD 18-UNICANCER GI): A Randomized Phase III Study. *J Clin Oncol.* **37**(8), pp.658-667.

Ehlerding, E.B., Grodzinski, P., Cai, W. and Liu, C.H. 2018. Big Potential from Small Agents: Nanoparticles for Imaging-Based Companion Diagnostics. *ACS Nano.* **12**(3), pp.2106-2121.

Erice, O., Vallejo, A., Ponz-Sarvise, M., Saborowski, M., Vogel, A., Calvisi, D.F., Saborowski, A. and Vicent, S. 2019. Genetic Mouse Models as In Vivo Tools for Cholangiocarcinoma Research. *Cancers (Basel).* **11**(12).

Espinoza, J.A., Riquelme, I., Sagredo, E.A., Rosa, L., Garcia, P., Bizama, C., Apud-Bell, M., Leal, P., Weber, H., Benavente, F., Vargas, S., Romero, D., Kalergis, A.M. and Roa, J.C. 2019. Mucin 5B, carbonic anhydrase 9 and claudin 18 are potential theranostic markers of gallbladder carcinoma. *Histopathology.* **74**(4), pp.597-607.

Estanqueiro, M., Amaral, M.H., Conceicao, J. and Sousa Lobo, J.M. 2015. Nanotechnological carriers for cancer chemotherapy: The state of the art. *Colloids Surf B Biointerfaces.*

Fabris, L., Cadamuro, M., Moserle, L., Dziura, J., Cong, X., Sambado, L., Nardo, G., Sonzogni, A., Colledan, M., Furlanetto, A., Bassi, N., Massani, M., Cillo, U., Mescoli, C., Indraccolo, S., Rugge, M., Okolicsanyi, L. and Strazzabosco, M. 2011. Nuclear expression of S100A4 calcium-binding protein increases cholangiocarcinoma invasiveness and metastasization. *Hepatology.* **54**(3), pp.890-899.

Fang, J., Nakamura, H. and Maeda, H. 2011. The EPR effect: Unique features of tumor blood vessels for drug delivery, factors involved, and limitations and augmentation of the effect. *Adv Drug Deliv Rev.* **63**(3), pp.136-151.

Farazi, P.A., Zeisberg, M., Glickman, J., Zhang, Y., Kalluri, R. and DePinho, R.A. 2006. Chronic bile duct injury associated with fibrotic matrix microenvironment provokes cholangiocarcinoma in p53-deficient mice. *Cancer Res.* **66**(13), pp.6622-6627.

Farges, O., Fuks, D., Le Treut, Y.P., Azoulay, D., Laurent, A., Bachellier, P., Nuzzo, G., Belghiti, J., Pruvot, F.R. and Regimbeau, J.M. 2011. AJCC 7th edition of TNM staging accurately discriminates outcomes of patients with resectable

intrahepatic cholangiocarcinoma: By the AFC-IHCC-2009 study group. *Cancer*. **117**(10), pp.2170-2177.

Farid, S.G., Craven, R.A., Peng, J., Bonney, G.K., Perkins, D.N., Selby, P.J., Rajendra Prasad, K. and Banks, R.E. 2011. Shotgun proteomics of human bile in hilar cholangiocarcinoma. *Proteomics*. **11**(10), pp.2134-2138.

Fausto, N., Campbell, J.S. and Riehle, K.J. 2006. Liver regeneration. *Hepatology*. **43**(2 Suppl 1), pp.S45-53.

Fernandes, A.R., Jesus, J., Martins, P., Figueiredo, S., Rosa, D., Martins, L.M., Corvo, M.L., Carvalheiro, M.C., Costa, P.M. and Baptista, P.V. 2017. Multifunctional gold-nanoparticles: A nanovectorization tool for the targeted delivery of novel chemotherapeutic agents. *J Control Release*. **245**, pp.52-61.

Fisher, S.B., Fisher, K.E., Patel, S.H., Lim, M.G., Kooby, D.A., El-Rayes, B.F., Staley, C.A., 3rd, Adsay, N.V., Farris, A.B., 3rd and Maithel, S.K. 2013. Excision repair cross-complementing gene-1, ribonucleotide reductase subunit M1, ribonucleotide reductase subunit M2, and human equilibrative nucleoside transporter-1 expression and prognostic value in biliary tract malignancy. *Cancer*. **119**(2), pp.454-462.

Foygel, K., Wang, H., Machtaler, S., Lutz, A.M., Chen, R., Pysz, M., Lowe, A.W., Tian, L., Carrigan, T., Brentnall, T.A. and Willmann, J.K. 2013. Detection of pancreatic ductal adenocarcinoma in mice by ultrasound imaging of thymocyte differentiation antigen 1. *Gastroenterology*. **145**(4), pp.885-894 e883.

Frangioni, J.V. 2003. In vivo near-infrared fluorescence imaging. *Curr Opin Chem Biol*. **7**(5), pp.626-634.

Franz, M., Jung, C., Lauten, A., Figulla, H.R. and Berndt, A. 2015. Tenascin-C in cardiovascular remodeling: potential impact for diagnosis, prognosis estimation and targeted therapy. *Cell Adh Migr*. **9**(1-2), pp.90-95.

Frosio, F., Mocchegiani, F., Conte, G., Bona, E.D., Vecchi, A., Nicolini, D. and Vivarelli, M. 2019. Neoadjuvant therapy in the treatment of hilar cholangiocarcinoma: Review of the literature. *World J Gastrointest Surg*. **11**(6), pp.279-286.

Fuhrmann, A., Banisadr, A., Beri, P., Tlsty, T.D. and Engler, A.J. 2017. Metastatic State of Cancer Cells May Be Indicated by Adhesion Strength. *Biophys J*. **112**(4), pp.736-745.

Fujimoto, M., Shiba, M., Kawakita, F., Liu, L., Shimojo, N., Imanaka-Yoshida, K., Yoshida, T. and Suzuki, H. 2016. Deficiency of tenascin-C and attenuation of blood-brain barrier disruption following experimental subarachnoid hemorrhage in mice. *J Neurosurg*. **124**(6), pp.1693-1702.

Gabizon, A. and Papahadjopoulos, D. 1988. Liposome formulations with prolonged circulation time in blood and enhanced uptake by tumors. *Proc Natl Acad Sci U S A.* **85**(18), pp.6949-6953.

Gabriel, E., Gandhi, S., Attwood, K., Kuvshinoff, B., Hochwald, S. and Iyer, R. 2017. Gemcitabine and capecitabine for advanced biliary cancer. *J Gastrointest Oncol.* **8**(4), pp.728-736.

Garcia-Hernandez, V., Quiros, M. and Nusrat, A. 2017. Intestinal epithelial claudins: expression and regulation in homeostasis and inflammation. *Ann N Y Acad Sci.* **1397**(1), pp.66-79.

Garcia, P.L., Miller, A.L., Gamblin, T.L., Council, L.N., Christein, J.D., Arnoletti, J.P., Heslin, M.J., Reddy, S., Richardson, J.H., Cui, X., van Waardenburg, R., Bradner, J.E., Yang, E.S. and Yoon, K.J. 2018. JQ1 Induces DNA Damage and Apoptosis, and Inhibits Tumor Growth in a Patient-Derived Xenograft Model of Cholangiocarcinoma. *Mol Cancer Ther.* **17**(1), pp.107-118.

Gaspersz, M.P., Buettner, S., van Vugt, J.L.A., de Jonge, J., Polak, W.G., Doukas, M., Ijzermans, J.N.M., Koerkamp, B.G. and Willemsen, F. 2019. Evaluation of the New American Joint Committee on Cancer Staging Manual 8th Edition for Perihilar Cholangiocarcinoma. *J Gastrointest Surg.*

Giblin, S.P. and Midwood, K.S. 2015. Tenascin-C: Form versus function. *Cell Adh Migr.* **9**(1-2), pp.48-82.

Gomes, R.V., Rodrigues, M.A., Rodrigues, J., Vidigal, P.T., Damasceno, K.A., Lima, H.A., Gomes, D.A., Machado, C.J. and Resende, V. 2018. Expression of epidermal growth factor receptor (EGFR) in cholangiocarcinomas: predictive factors and survival. *Rev Col Bras Cir.* **45**(3), pe1826.

Gores, G.J., Darwish Murad, S., Heimbach, J.K. and Rosen, C.B. 2013. Liver transplantation for perihilar cholangiocarcinoma. *Dig Dis.* **31**(1), pp.126-129.

Grendar, J., Grendarova, P., Sinha, R. and Dixon, E. 2014. Neoadjuvant therapy for downstaging of locally advanced hilar cholangiocarcinoma: a systematic review. *HPB (Oxford).* **16**(4), pp.297-303.

Gu. 2015a. CA9 overexpression is an independent favorable prognostic marker in intrahepatic cholangiocarcinoma. *Int J Clin Exp Pathol.* **8**(1), pp.862-866.

Gu and Choi, J.H. 2012. Clinicopathological significance of E-cadherin, beta-catenin and epidermal growth factor receptor expression in intrahepatic cholangiocarcinoma. *Hepatogastroenterology.* **59**(116), pp.1241-1244.

Gu, M.J. 2015b. CA9 overexpression is an independent favorable prognostic marker in intrahepatic cholangiocarcinoma. *Int J Clin Exp Pathol.* **8**(1), pp.862-866.

Gulcher, J.R., Nies, D.E., Alexakos, M.J., Ravikant, N.A., Sturgill, M.E., Marton, L.S. and Stefansson, K. 1991. Structure of the human hexabrachion (tenascin) gene. *Proc Natl Acad Sci U S A.* **88**(21), pp.9438-9442.

Hakimzadeh, N., Pinas, V.A., Molenaar, G., de Waard, V., Lutgens, E., van Eck-Smit, B.L.F., de Bruin, K., Piek, J.J., Eersels, J.L.H., Booij, J., Verberne, H.J. and Windhorst, A.D. 2017. Novel molecular imaging ligands targeting matrix metalloproteinases 2 and 9 for imaging of unstable atherosclerotic plaques. *PLoS One.* **12**(11), pe0187767.

Harrison, P.M. 1999. Prevention of bile duct cancer in primary sclerosing cholangitis. *Ann Oncol.* **10 Suppl 4**, pp.208-211.

Hawcroft, G., Volpato, M., Marston, G., Ingram, N., Perry, S.L., Cockbain, A.J., Race, A.D., Munarini, A., Belluzzi, A., Loadman, P.M., Coletta, P.L. and Hull, M.A. 2012. The omega-3 polyunsaturated fatty acid eicosapentaenoic acid inhibits mouse MC-26 colorectal cancer cell liver metastasis via inhibition of PGE2-dependent cell motility. *Br J Pharmacol.* **166**(5), pp.1724-1737.

He, X., Chen, X., Liu, L., Zhang, Y., Lu, Y., Zhang, Y., Chen, Q., Ruan, C., Guo, Q., Li, C., Sun, T. and Jiang, C. 2018. Sequentially Triggered Nanoparticles with Tumor Penetration and Intelligent Drug Release for Pancreatic Cancer Therapy. *Adv Sci (Weinh).* **5**(5), p1701070.

Hicke, B.J., Stephens, A.W., Gould, T., Chang, Y.F., Lynott, C.K., Heil, J., Borkowski, S., Hilger, C.S., Cook, G., Warren, S. and Schmidt, P.G. 2006. Tumor targeting by an aptamer. *J Nucl Med.* **47**(4), pp.668-678.

Hilvo, M., Baranauskiene, L., Salzano, A.M., Scaloni, A., Matulis, D., Innocenti, A., Scozzafava, A., Monti, S.M., Di Fiore, A., De Simone, G., Lindfors, M., Janis, J., Valjakka, J., Pastorekova, S., Pastorek, J., Kulomaa, M.S., Nordlund, H.R., Supuran, C.T. and Parkkila, S. 2008. Biochemical characterization of CA IX, one of the most active carbonic anhydrase isozymes. *J Biol Chem.* **283**(41), pp.27799-27809.

Horiuchi, H., Kawamata, H., Fujimori, T. and Kuroda, Y. 2003. A MEK inhibitor (U0126) prolongs survival in nude mice bearing human gallbladder cancer cells with K-ras mutation: analysis in a novel orthotopic inoculation model. *Int J Oncol.* **23**(4), pp.957-963.

Hughes, D.J., Tiede, C., Penswick, N., Tang, A.A., Trinh, C.H., Mandal, U., Zajac, K.Z., Gaule, T., Howell, G., Edwards, T.A., Duan, J., Feyfant, E., McPherson, M.J., Tomlinson, D.C. and Whitehouse, A. 2017. Generation of specific inhibitors of SUMO-1- and SUMO-2/3-mediated protein-protein interactions using Affimer (Adhiron) technology. *Sci Signal.* **10**(505).

Hughes, N.R., Pairojkul, C., Royce, S.G., Clouston, A. and Bhathal, P.S. 2006. Liver fluke-associated and sporadic cholangiocarcinoma: an immunohistochemical study of bile duct, peribiliary gland and tumour cell phenotypes. *J Clin Pathol.* **59**(10), pp.1073-1078.

Human Protein Atlas. 2019a. [Online]. [Accessed 30/11/2019]. Available from: <https://www.proteinatlas.org/>

Human Protein Atlas. 2019b. [Online]. [Accessed 07/10/2019]. Available from: <https://www.proteinatlas.org/ENSG00000041982-TNC/tissue>

Human Protein Atlas. 2019c. *Human Protein Atlas*. [Online]. [Accessed 30/11/2019]. Available from: <https://www.proteinatlas.org/>

Human Protein Atlas. 2019d. *TNC*. [Online]. [Accessed 07/10/2019]. Available from: <https://www.proteinatlas.org/ENSG00000041982-TNC/tissue>

Huynh, H., Choo, S.P., Toh, H.C., Tai, W.M., Chung, A.Y., Chow, P.K., Ong, R. and Soo, K.C. 2011. Comparing the efficacy of sunitinib with sorafenib in xenograft models of human hepatocellular carcinoma: mechanistic explanation. *Curr Cancer Drug Targets*. **11**(8), pp.944-953.

Huynh, N.T., Passirani, C., Saulnier, P. and Benoit, J.P. 2009. Lipid nanocapsules: a new platform for nanomedicine. *Int J Pharm*. **379**(2), pp.201-209.

Iguchi, T., Yamashita, N., Aishima, S., Kuroda, Y., Terashi, T., Sugimachi, K., Taguchi, K., Taketomi, A., Maehara, Y. and Tsuneyoshi, M. 2009. A comprehensive analysis of immunohistochemical studies in intrahepatic cholangiocarcinoma using the survival tree model. *Oncology*. **76**(4), pp.293-300.

Imanaka-Yoshida, K. 2012. Tenascin-C in cardiovascular tissue remodeling: from development to inflammation and repair. *Circ J*. **76**(11), pp.2513-2520.

Ingram, N., Macnab, S.A., Marston, G., Scott, N., Carr, I.M., Markham, A.F., Whitehouse, A. and Coletta, P.L. 2013. The use of high-frequency ultrasound imaging and biofluorescence for in vivo evaluation of gene therapy vectors. *BMC Med Imaging*. **13**, p35.

Itatsu, K., Sasaki, M., Yamaguchi, J., Ohira, S., Ishikawa, A., Ikeda, H., Sato, Y., Harada, K., Zen, Y., Sato, H., Ohta, T., Nagino, M., Nimura, Y. and Nakanuma, Y. 2009. Cyclooxygenase-2 is involved in the up-regulation of matrix metalloproteinase-9 in cholangiocarcinoma induced by tumor necrosis factor-alpha. *Am J Pathol*. **174**(3), pp.829-841.

Jain, S., Hirst, D.G. and O'Sullivan, J.M. 2012. Gold nanoparticles as novel agents for cancer therapy. *Br J Radiol*. **85**(1010), pp.101-113.

Jo, H.J., Shim, H.E., Han, M.E., Kim, H.J., Kim, K.S., Baek, S., Choi, K.U., Hur, G.Y. and Oh, S.O. 2013. WTAP regulates migration and invasion of cholangiocarcinoma cells. *J Gastroenterol*. **48**(11), pp.1271-1282.

Jokerst, J.V. and Gambhir, S.S. 2011. Molecular imaging with theranostic nanoparticles. *Acc Chem Res.* **44**(10), pp.1050-1060.

Jones, F.S. and Jones, P.L. 2000. The tenascin family of ECM glycoproteins: structure, function, and regulation during embryonic development and tissue remodeling. *Dev Dyn.* **218**(2), pp.235-259.

Jones, L., Richmond, J., Evans, K., Carol, H., Jing, D., Kurmasheva, R.T., Billups, C.A., Houghton, P.J., Smith, M.A. and Lock, R.B. 2017. Bioluminescence Imaging Enhances Analysis of Drug Responses in a Patient-Derived Xenograft Model of Pediatric ALL. *Clin Cancer Res.* **23**(14), pp.3744-3755.

Kamsa-ard, S., Wiangnon, S., Suwanrungruang, K., Promthet, S., Khuntikeo, N., Kamsa-ard, S. and Mahaweerawat, S. 2011. Trends in liver cancer incidence between 1985 and 2009, Khon Kaen, Thailand: cholangiocarcinoma. *Asian Pac J Cancer Prev.* **12**(9), pp.2209-2213.

Kane, S. 2016. *ClinCalc.com*. [Online]. [Accessed 08/11/2019]. Available from: <https://clincalc.com/Stats/SampleSize.aspx>

Kang, J.S., Higuchi, R., He, J., Yamamoto, M., Wolfgang, C.L., Cameron, J.L., Han, Y., Son, D., Lee, S., Choi, Y.J., Byun, Y., Kim, H., Kwon, W., Kim, S.W., Park, T. and Jang, J.Y. 2019. Proposal of the Minimal Number of Retrieved Regional Lymph Nodes for Accurate Staging of Distal Bile Duct Cancer and Clinical Validation of the Three-tier Lymph Node Staging System (AJCC 8(th) edition). *J Hepatobiliary Pancreat Sci.*

Karmani, L., Labar, D., Valembois, V., Bouchat, V., Nagaswaran, P.G., Bol, A., Gillart, J., Leveque, P., Bouzin, C., Bonifazi, D., Michiels, C., Feron, O., Gregoire, V., Lucas, S., Vander Borgh, T. and Gallez, B. 2013. Antibody-functionalized nanoparticles for imaging cancer: influence of conjugation to gold nanoparticles on the biodistribution of ⁸⁹Zr-labeled cetuximab in mice. *Contrast Media Mol Imaging.* **8**(5), pp.402-408.

Kawakita, F., Kanamaru, H., Asada, R. and Suzuki, H. 2019. Potential roles of matricellular proteins in stroke. *Exp Neurol.* **322**, p113057.

Keira, Y., Takasawa, A., Murata, M., Nojima, M., Takasawa, K., Ogino, J., Higashiura, Y., Sasaki, A., Kimura, Y., Mizuguchi, T., Tanaka, S., Hirata, K., Sawada, N. and Hasegawa, T. 2015. An immunohistochemical marker panel including claudin-18, maspin, and p53 improves diagnostic accuracy of bile duct neoplasms in surgical and presurgical biopsy specimens. *Virchows Arch.* **466**(3), pp.265-277.

Kelloff, G.J., Krohn, K.A., Larson, S.M., Weissleder, R., Mankoff, D.A., Hoffman, J.M., Link, J.M., Guyton, K.Z., Eckelman, W.C., Scher, H.I., O'Shaughnessy, J., Cheson, B.D., Sigman, C.C., Tatum, J.L., Mills, G.Q., Sullivan, D.C. and Woodcock, J. 2005. The progress and promise of molecular imaging probes in oncologic drug development. *Clin Cancer Res.* **11**(22), pp.7967-7985.

Kendall, T., Verheij, J., Gaudio, E., Evert, M., Guido, M., Goepfert, B. and Carpino, G. 2019. Anatomical, histomorphological and molecular classification of cholangiocarcinoma. *Liver Int.* **39 Suppl 1**, pp.7-18.

Khaderi, S.A. and Sussman, N.L. 2015. Screening for malignancy in primary sclerosing cholangitis (PSC). *Curr Gastroenterol Rep.* **17**(4), p17.

Khan, S.A., Emadossadaty, S., Ladep, N.G., Thomas, H.C., Elliott, P., Taylor-Robinson, S.D. and Toledano, M.B. 2012. Rising trends in cholangiocarcinoma: is the ICD classification system misleading us? *J Hepatol.* **56**(4), pp.848-854.

Khan, S.A., Tavolari, S. and Brandi, G. 2019. Cholangiocarcinoma: Epidemiology and risk factors. *Liver Int.* **39 Suppl 1**, pp.19-31.

Khan, S.A., Toledano, M.B. and Taylor-Robinson, S.D. 2008. Epidemiology, risk factors, and pathogenesis of cholangiocarcinoma. *HPB (Oxford).* **10**(2), pp.77-82.

Khawar, I.A., Kim, J.H. and Kuh, H.J. 2014. Improving drug delivery to solid tumors: Priming the tumor microenvironment. *J Control Release.*

Kilkenny, C., Browne, W., Cuthill, I.C., Emerson, M., Altman, D.G. and Group, N.C.R.R.G.W. 2010. Animal research: reporting in vivo experiments: the ARRIVE guidelines. *Br J Pharmacol.* **160**(7), pp.1577-1579.

Kirstein, M.M. and Vogel, A. 2016. Epidemiology and Risk Factors of Cholangiocarcinoma. *Visc Med.* **32**(6), pp.395-400.

Ko, H.Y., Choi, K.J., Lee, C.H. and Kim, S. 2011. A multimodal nanoparticle-based cancer imaging probe simultaneously targeting nucleolin, integrin alphavbeta3 and tenascin-C proteins. *Biomaterials.* **32**(4), pp.1130-1138.

Kodiha, M., Wang, Y.M., Hutter, E., Maysinger, D. and Stochaj, U. 2015. Off to the organelles - killing cancer cells with targeted gold nanoparticles. *Theranostics.* **5**(4), pp.357-370.

Komaya, K., Ebata, T., Yokoyama, Y., Igami, T., Sugawara, G., Mizuno, T., Yamaguchi, J. and Nagino, M. 2018. Recurrence after curative-intent resection of perihilar cholangiocarcinoma: analysis of a large cohort with a close postoperative follow-up approach. *Surgery.* **163**(4), pp.732-738.

Koonce, N.A., Quick, C.M., Hardee, M.E., Jamshidi-Parsian, A., Dent, J.A., Paciotti, G.F., Nedosekin, D., Dings, R.P. and Griffin, R.J. 2015. Combination of Gold Nanoparticle-Conjugated Tumor Necrosis Factor-alpha and Radiation Therapy Results in a Synergistic Antitumor Response in Murine Carcinoma Models. *Int J Radiat Oncol Biol Phys.* **93**(3), pp.588-596.

Kumar, A., Tan, A., Wong, J., Spagnoli, J.C., Lam, J., Blevins, B.D., G, N., Thorne, L., Ashkan, K., Xie, J. and Liu, H. 2017. Nanotechnology for

Neuroscience: Promising Approaches for Diagnostics, Therapeutics and Brain Activity Mapping. *Adv Funct Mater.* **27**(39).

Kumar, V., Soni, P., Garg, M., Kamholz, S. and Chandra, A.B. 2018. Emerging Therapies in the Management of Advanced-Stage Gastric Cancer. *Front Pharmacol.* **9**, p404.

Lamb, Y.N. and Scott, L.J. 2017. Liposomal Irinotecan: A Review in Metastatic Pancreatic Adenocarcinoma. *Drugs.* **77**(7), pp.785-792.

Lammers, T., Aime, S., Hennink, W.E., Storm, G. and Kiessling, F. 2011. Theranostic nanomedicine. *Acc Chem Res.* **44**(10), pp.1029-1038.

Lendvai, G., Szekerczes, T., Illyes, I., Dora, R., Kontsek, E., Gogl, A., Kiss, A., Werling, K., Kovalszky, I., Schaff, Z. and Borka, K. 2018. Cholangiocarcinoma: Classification, Histopathology and Molecular Carcinogenesis. *Pathol Oncol Res.*

Leonov, A.P., Zheng, J., Clogston, J.D., Stern, S.T., Patri, A.K. and Wei, A. 2008. Detoxification of gold nanorods by treatment with polystyrenesulfonate. *ACS Nano.* **2**(12), pp.2481-2488.

Leppanen, J., Bogdanoff, S., Lehenkari, P.P., Saarnio, J., Kauppila, J.H., Karttunen, T.J., Huhta, H. and Helminen, O. 2017. Tenascin-C and fibronectin in normal esophageal mucosa, Barrett's esophagus, dysplasia and adenocarcinoma. *Oncotarget.* **8**(40), pp.66865-66877.

Leppanen, J., Lindholm, V., Isohookana, J., Haapasaari, K.M., Karihtala, P., Lehenkari, P.P., Saarnio, J., Kauppila, J.H., Karttunen, T.J., Helminen, O. and Huhta, H. 2019. Tenascin C, Fibronectin, and Tumor-Stroma Ratio in Pancreatic Ductal Adenocarcinoma. *Pancreas.* **48**(1), pp.43-48.

Li, Bouchy, S., Penninckx, S., Marega, R., Fichera, O., Gallez, B., Feron, O., Martinive, P., Heuskin, A.C., Michiels, C. and Lucas, S. 2019. Antibody-functionalized gold nanoparticles as tumor-targeting radiosensitizers for proton therapy. *Nanomedicine (Lond).* **14**(3), pp.317-333.

Li and Chen, X. 2015. Gold nanoparticles for photoacoustic imaging. *Nanomedicine (Lond).* **10**(2), pp.299-320.

Li, F., Zhang, H., He, M., Liao, J., Chen, N., Li, Y., Zhou, S., Palmisano, M., Yu, A., Pai, M.P., Yuan, H. and Sun, D. 2018. Different Nanoformulations Alter the Tissue Distribution of Paclitaxel, Which Aligns with Reported Distinct Efficacy and Safety Profiles. *Mol Pharm.* **15**(10), pp.4505-4516.

Li, M., Peng, F., Li, G., Fu, Y., Huang, Y., Chen, Z. and Chen, Y. 2016. Proteomic analysis of stromal proteins in different stages of colorectal cancer establishes Tenascin-C as a stromal biomarker for colorectal cancer metastasis. *Oncotarget.* **7**(24), pp.37226-37237.

Li, S., Schmitz, K.R., Jeffrey, P.D., Wiltzius, J.J., Kussie, P. and Ferguson, K.M. 2005. Structural basis for inhibition of the epidermal growth factor receptor by cetuximab. *Cancer Cell*. **7**(4), pp.301-311.

Libutti, S.K., Paciotti, G.F., Byrnes, A.A., Alexander, H.R., Jr., Gannon, W.E., Walker, M., Seidel, G.D., Yuldasheva, N. and Tamarkin, L. 2010. Phase I and pharmacokinetic studies of CYT-6091, a novel PEGylated colloidal gold-rhTNF nanomedicine. *Clin Cancer Res*. **16**(24), pp.6139-6149.

Lindsey, M.L. 2018. Assigning matrix metalloproteinase roles in ischaemic cardiac remodelling. *Nat Rev Cardiol*. **15**(8), pp.471-479.

Loeuillard, E., Fischbach, S.R., Gores, G.J. and Rizvi, S. 2019. Animal models of cholangiocarcinoma. *Biochim Biophys Acta Mol Basis Dis*. **1865**(5), pp.982-992.

Longley, D.B. and Johnston, P.G. 2005. Molecular mechanisms of drug resistance. *J Pathol*. **205**(2), pp.275-292.

Lopez-Chaves, C., Soto-Alvaredo, J., Montes-Bayon, M., Bettmer, J., Llopis, J. and Sanchez-Gonzalez, C. 2018. Gold nanoparticles: Distribution, bioaccumulation and toxicity. In vitro and in vivo studies. *Nanomedicine*. **14**(1), pp.1-12.

Lowy, C.M. and Oskarsson, T. 2015. Tenascin C in metastasis: A view from the invasive front. *Cell Adh Migr*. **9**(1-2), pp.112-124.

Lubner, S.J., Mahoney, M.R., Kolesar, J.L., Loconte, N.K., Kim, G.P., Pitot, H.C., Philip, P.A., Picus, J., Yong, W.P., Horvath, L., Van Hazel, G., Erlichman, C.E. and Holen, K.D. 2010. Report of a multicenter phase II trial testing a combination of biweekly bevacizumab and daily erlotinib in patients with unresectable biliary cancer: a phase II Consortium study. *J Clin Oncol*. **28**(21), pp.3491-3497.

Machairas, N., Kostakis, I.D., Tsilimigras, D.I., Prodromidou, A. and Moris, D. 2019. Liver transplantation for hilar cholangiocarcinoma: A systematic review. *Transplant Rev (Orlando)*. p100516.

Mackie, E.J. and Tucker, R.P. 1999. The tenascin-C knockout revisited. *J Cell Sci*. **112 (Pt 22)**, pp.3847-3853.

Madej, T., Lanczycki, C.J., Zhang, D., Thiessen, P.A., Geer, R.C., Marchler-Bauer, A. and Bryant, S.H. 2014. MMDB and VAST+: tracking structural similarities between macromolecular complexes. *Nucleic Acids Res*. **42**(Database issue), pp.D297-303.

Magistri, P., Battistelli, C., Toietta, G., Strippoli, R., Sagnotta, A., Forgiione, A., Di Benedetto, F., Uccini, S., Vittorioso, P., D'Angelo, F., Aurello, P., Ramacciato, G. and Nigri, G. 2019. In vivo Bioluminescence-Based Monitoring of Liver

Metastases from Colorectal Cancer: An Experimental Model. *J Microsc Ultrastruct.* **7**(3), pp.136-140.

Mansour, J.C., Aloia, T.A., Crane, C.H., Heimbach, J.K., Nagino, M. and Vauthey, J.N. 2015. Hilar cholangiocarcinoma: expert consensus statement. *HPB (Oxford)*. **17**(8), pp.691-699.

Maqbool, A., Spary, E.J., Manfield, I.W., Ruhmann, M., Zuliani-Alvarez, L., Gamboa-Esteves, F.O., Porter, K.E., Drinkhill, M.J., Midwood, K.S. and Turner, N.A. 2016. Tenascin C upregulates interleukin-6 expression in human cardiac myofibroblasts via toll-like receptor 4. *World J Cardiol.* **8**(5), pp.340-350.

Martelli, C., Lo Dico, A., Diceglie, C., Lucignani, G. and Ottobrini, L. 2016. Optical imaging probes in oncology. *Oncotarget.* **7**(30), pp.48753-48787.

Martin-Rapun, R., De Matteis, L., Ambrosone, A., Garcia-Embid, S., Gutierrez, L. and de la Fuente, J.M. 2017. Targeted Nanoparticles for the Treatment of Alzheimer's Disease. *Curr Pharm Des.* **23**(13), pp.1927-1952.

Massard, C., Michiels, S., Ferte, C., Le Deley, M.C., Lacroix, L., Hollebecque, A., Verlingue, L., Ileana, E., Rosellini, S., Ammari, S., Ngo-Camus, M., Bahleda, R., Gazzah, A., Varga, A., Postel-Vinay, S., Lorient, Y., Even, C., Breuskin, I., Auger, N., Job, B., De Baere, T., Deschamps, F., Vielh, P., Scoazec, J.Y., Lazar, V., Richon, C., Ribrag, V., Deutsch, E., Angevin, E., Vassal, G., Eggermont, A., Andre, F. and Soria, J.C. 2017. High-Throughput Genomics and Clinical Outcome in Hard-to-Treat Advanced Cancers: Results of the MOSCATO 01 Trial. *Cancer Discov.* **7**(6), pp.586-595.

Matsumoto, K., Nakai, Y., Hoshino, M., Yamazaki, K., Takioto, Y., Takadera, S., Nakagawa, T., Nishimura, R. and Kusakabe, M. 2017. Comprehensive DNA microarray expression profiles of tumors in tenascin-C-knockout mice. *Biosci Biotechnol Biochem.* **81**(10), pp.1926-1936.

McLaughlan, J., Ingram, N., Smith, P.R., Harput, S., Coletta, P.L., Evans, S. and Freear, S. 2013. Increasing the sonoporation efficiency of targeted polydisperse microbubble populations using chirp excitation. *IEEE Trans Ultrason Ferroelectr Freq Control.* **60**(12), pp.2511-2520.

McVeigh, L.E., Wijetunga, I., Ingram, N., Marston, G., Prasad, R., Markham, A.F. and Coletta, P.L. 2019. Development of orthotopic tumour models using ultrasound-guided intrahepatic injection. *Sci Rep.* **9**(1), p9904.

Meng, L., Deschaume, O., Larbanoix, L., Fron, E., Bartic, C., Laurent, S., Van der Auweraer, M. and Glorieux, C. 2019. Photoacoustic temperature imaging based on multi-wavelength excitation. *Photoacoustics.* **13**, pp.33-45.

Mercado, M.A. and Dominguez, I. 2011. Classification and management of bile duct injuries. *World J Gastrointest Surg.* **3**(4), pp.43-48.

Merla, A., Liu, K.G. and Rajdev, L. 2015. Targeted Therapy in Biliary Tract Cancers. *Curr Treat Options Oncol.* **16**(10), p48.

Mertens, J.C., Fingas, C.D., Christensen, J.D., Smoot, R.L., Bronk, S.F., Werneburg, N.W., Gustafson, M.P., Dietz, A.B., Roberts, L.R., Sirica, A.E. and Gores, G.J. 2013. Therapeutic effects of deleting cancer-associated fibroblasts in cholangiocarcinoma. *Cancer Res.* **73**(2), pp.897-907.

Messina, C., Merz, V., Frisinghelli, M., Trentin, C., Grego, E., Veccia, A., Salati, M., Messina, M., Carnaghi, C. and Caffo, O. 2019. Adjuvant chemotherapy in resected bile duct cancer: A systematic review and meta-analysis of randomized trials. *Crit Rev Oncol Hematol.* **143**, pp.124-129.

Mi, H., Muruganujan, A., Ebert, D., Huang, X. and Thomas, P.D. 2019a. PANTHER version 14: more genomes, a new PANTHER GO-slim and improvements in enrichment analysis tools. *Nucleic Acids Res.* **47**(D1), pp.D419-D426.

Mi, H., Muruganujan, A., Huang, X., Ebert, D., Mills, C., Guo, X. and Thomas, P.D. 2019b. Protocol Update for large-scale genome and gene function analysis with the PANTHER classification system (v.14.0). *Nat Protoc.* **14**(3), pp.703-721.

Mi, H., Muruganujan, A. and Thomas, P.D. 2013. PANTHER in 2013: modeling the evolution of gene function, and other gene attributes, in the context of phylogenetic trees. *Nucleic Acids Res.* **41**(Database issue), pp.D377-386.

Mico, V., Charalambous, A., Peyman, S.A., Abou-Saleh, R.H., Markham, A.F., Coletta, P.L. and Evans, S.D. 2017. Evaluation of lipid-stabilised tripropionin nanodroplets as a delivery route for combretastatin A4. *Int J Pharm.* **526**(1-2), pp.547-555.

Midwood, K.S., Chiquet, M., Tucker, R.P. and Orend, G. 2016. Tenascin-C at a glance. *J Cell Sci.* **129**(23), pp.4321-4327.

Midwood, K.S., Hussenet, T., Langlois, B. and Orend, G. 2011. Advances in tenascin-C biology. *Cell Mol Life Sci.* **68**(19), pp.3175-3199.

Midwood, K.S. and Orend, G. 2009. The role of tenascin-C in tissue injury and tumorigenesis. *J Cell Commun Signal.* **3**(3-4), pp.287-310.

Ming, X., Qiu, S., Liu, X., Li, S., Wang, Y., Zhu, M., Li, N., Luo, P., Liang, C. and Tu, J. 2019. Prognostic Role of Tenascin-C for Cancer Outcome: A Meta-Analysis. *Technol Cancer Res Treat.* **18**, p1533033818821106.

Mita, Y., Ajiki, T., Kamigaki, T., Okazaki, T., Hori, H., Horiuchi, H., Hirata, K., Fujita, T., Fujimori, T. and Kuroda, Y. 2007. Antitumor effect of gemcitabine on orthotopically inoculated human gallbladder cancer cells in nude mice. *Ann Surg Oncol.* **14**(4), pp.1374-1380.

Miyamoto, M., Ojima, H., Iwasaki, M., Shimizu, H., Kokubu, A., Hiraoka, N., Kosuge, T., Yoshikawa, D., Kono, T., Furukawa, H. and Shibata, T. 2011. Prognostic significance of overexpression of c-Met oncoprotein in cholangiocarcinoma. *Br J Cancer*. **105**(1), pp.131-138.

Moole, H., Tathireddy, H., Dharmapuri, S., Moole, V., Boddireddy, R., Yedama, P., Dharmapuri, S., Uppu, A., Bondalapati, N. and Duvvuri, A. 2017. Success of photodynamic therapy in palliating patients with nonresectable cholangiocarcinoma: A systematic review and meta-analysis. *World J Gastroenterol*. **23**(7), pp.1278-1288.

Moon, A., Chin, S., Kim, H.K., Kwak, J.J., Koh, E.S., Kim, Y.W. and Jang, K.T. 2016. EGFR, COX2, p-AKT expression and PIK3CA mutation in distal extrahepatic bile duct carcinoma. *Pathology*. **48**(1), pp.35-40.

Morales-Cruz, M., Delgado, Y., Castillo, B., Figueroa, C.M., Molina, A.M., Torres, A., Milian, M. and Griebenow, K. 2019. Smart Targeting To Improve Cancer Therapeutics. *Drug Des Devel Ther*. **13**, pp.3753-3772.

Moris, D., Kostakis, I.D., Machairas, N., Prodromidou, A., Tsilimigras, D.I., Ravindra, K.V., Sudan, D.L., Knechtle, S.J. and Barbas, A.S. 2019. Comparison between liver transplantation and resection for hilar cholangiocarcinoma: A systematic review and meta-analysis. *PLoS One*. **14**(7), pe0220527.

Morizane, C., Ueno, M., Ikeda, M., Okusaka, T., Ishii, H. and Furuse, J. 2018. New developments in systemic therapy for advanced biliary tract cancer. *Jpn J Clin Oncol*. **48**(8), pp.703-711.

Mross, K. and Kratz, F. 2011. Limits of conventional cancer chemotherapy. In: Kratz F, S.P., Steinhagen H ed. *Drug Delivery in Oncology: From Basic Research to Cancer Therapy*. Wiley-VCH, pp.1-31.

Muhamad, N., Plengsuriyakarn, T. and Na-Bangchang, K. 2018. Application of active targeting nanoparticle delivery system for chemotherapeutic drugs and traditional/herbal medicines in cancer therapy: a systematic review. *Int J Nanomedicine*. **13**, pp.3921-3935.

Muko, D., Ikenaga, T., Kasai, M., Rabor, J.B., Nishitani, A. and Niidome, Y. 2019. Imaging mass spectrometry of gold nanoparticles in a tissue section as an immunohistochemical staining mass probe. *J Mass Spectrom*. **54**(1), pp.1-6.

Nagase, H., Visse, R. and Murphy, G. 2006. Structure and function of matrix metalloproteinases and TIMPs. *Cardiovasc Res*. **69**(3), pp.562-573.

Nair, A., Ingram, N., Verghese, E.T., Wijetunga, I., Markham, A.F., Wyatt, J., Prasad, K.R. and Coletta, P.L. 2018. Neutrophil Gelatinase-associated Lipocalin as a Theragnostic Marker in Perihilar Cholangiocarcinoma. *Anticancer Res*. **38**(12), pp.6737-6744.

Neesse, A., Algul, H., Tuveson, D.A. and Gress, T.M. 2015. Stromal biology and therapy in pancreatic cancer: a changing paradigm. *Gut*.

Niimi, T., Nagashima, K., Ward, J.M., Mino, P., Zimonjic, D.B., Popescu, N.C. and Kimura, S. 2001. claudin-18, a novel downstream target gene for the T/EBP/NKX2.1 homeodomain transcription factor, encodes lung- and stomach-specific isoforms through alternative splicing. *Mol Cell Biol.* **21**(21), pp.7380-7390.

Nong, Y., Wu, D., Lin, Y., Zhang, Y., Bai, L. and Tang, H. 2015. Tenascin-C expression is associated with poor prognosis in hepatocellular carcinoma (HCC) patients and the inflammatory cytokine TNF-alpha-induced TNC expression promotes migration in HCC cells. *Am J Cancer Res.* **5**(2), pp.782-791.

O'Farrell, A.C., Shnyder, S.D., Marston, G., Coletta, P.L. and Gill, J.H. 2013. Non-invasive molecular imaging for preclinical cancer therapeutic development. *Br J Pharmacol.* **169**(4), pp.719-735.

Ogo, Y., Nio, Y., Yano, S., Toga, T., Koike, M., Hashimoto, K., Itakura, M. and Maruyama, R. 2006. Immunohistochemical expression of HER-1 and HER-2 in extrahepatic biliary carcinoma. *Anticancer Res.* **26**(1B), pp.763-770.

Okamura, N., Yoshida, M., Shibuya, A., Sugiura, H., Okayasu, I. and Ohbu, M. 2005. Cellular and stromal characteristics in the scirrhous hepatocellular carcinoma: comparison with hepatocellular carcinomas and intrahepatic cholangiocarcinomas. *Pathol Int.* **55**(11), pp.724-731.

Okusaka, T., Nakachi, K., Fukutomi, A., Mizuno, N., Ohkawa, S., Funakoshi, A., Nagino, M., Kondo, S., Nagaoka, S., Funai, J., Koshiji, M., Nambu, Y., Furuse, J., Miyazaki, M. and Nimura, Y. 2010. Gemcitabine alone or in combination with cisplatin in patients with biliary tract cancer: a comparative multicentre study in Japan. *Br J Cancer.* **103**(4), pp.469-474.

Oliveira, I.S., Kilcoyne, A., Everett, J.M., Mino-Kenudson, M., Harisinghani, M.G. and Ganesan, K. 2017. Cholangiocarcinoma: classification, diagnosis, staging, imaging features, and management. *Abdom Radiol (NY).* **42**(6), pp.1637-1649.

Omura, N., Uechi, I. and Yamada, S. 2009. Comparison of plasmonic sensing between polymer- and silica-coated gold nanorods. *Anal Sci.* **25**(2), pp.255-259.

Onodera, M., Zen, Y., Harada, K., Sato, Y., Ikeda, H., Itatsu, K., Sato, H., Ohta, T., Asaka, M. and Nakanuma, Y. 2009. Fascin is involved in tumor necrosis factor-alpha-dependent production of MMP9 in cholangiocarcinoma. *Lab Invest.* **89**(11), pp.1261-1274.

Orend, G. and Chiquet-Ehrismann, R. 2006. Tenascin-C induced signaling in cancer. *Cancer Lett.* **244**(2), pp.143-163.

Padthaisong, S., Thanee, M., Techasen, A., Namwat, N., Yongvanit, P., Liwatthakun, A., Hankla, K., Sangkhamanon, S. and Loilome, W. 2017. Nimotuzumab Inhibits Cholangiocarcinoma Cell Metastasis via Suppression of the Epithelial-Mesenchymal Transition Process. *Anticancer Res.* **37**(7), pp.3591-3597.

Park, W. and Na, K. 2015. Advances in the synthesis and application of nanoparticles for drug delivery. *Wiley Interdiscip Rev Nanomed Nanobiotechnol.*

Park, Y., Kim, K., Paik, J.H., Chie, E.K., Jang, J.Y., Kim, S.W. and Oh, D.Y. 2018. High expression of MMP-9 is associated with better prognosis in extrahepatic bile duct cancer patients. *Eur J Surg Oncol.* **44**(5), pp.638-643.

Pas, J., Wyszko, E., Rolle, K., Rychlewski, L., Nowak, S., Zukiel, R. and Barciszewski, J. 2006. Analysis of structure and function of tenascin-C. *Int J Biochem Cell Biol.* **38**(9), pp.1594-1602.

Pastorekova, S., Parkkila, S., Parkkila, A.K., Opavsky, R., Zelnik, V., Saarnio, J. and Pastorek, J. 1997. Carbonic anhydrase IX, MN/CA IX: analysis of stomach complementary DNA sequence and expression in human and rat alimentary tracts. *Gastroenterology.* **112**(2), pp.398-408.

Patel, T. 2006. Cholangiocarcinoma. *Nat Clin Pract Gastroenterol Hepatol.* **3**(1), pp.33-42.

Patra, C.R., Bhattacharya, R., Mukhopadhyay, D. and Mukherjee, P. 2010. Fabrication of gold nanoparticles for targeted therapy in pancreatic cancer. *Adv Drug Deliv Rev.* **62**(3), pp.346-361.

Patra, C.R., Bhattacharya, R., Wang, E., Katarya, A., Lau, J.S., Dutta, S., Muders, M., Wang, S., Buhrow, S.A., Safgren, S.L., Yaszemski, M.J., Reid, J.M., Ames, M.M., Mukherjee, P. and Mukhopadhyay, D. 2008. Targeted delivery of gemcitabine to pancreatic adenocarcinoma using cetuximab as a targeting agent. *Cancer Res.* **68**(6), pp.1970-1978.

Pelaz, B., Alexiou, C., Alvarez-Puebla, R.A., Alves, F., Andrews, A.M., Ashraf, S., Balogh, L.P., Ballerini, L., Bestetti, A., Brendel, C., Bosi, S., Carril, M., Chan, W.C., Chen, C., Chen, X., Chen, X., Cheng, Z., Cui, D., Du, J., Dullin, C., Escudero, A., Feliu, N., Gao, M., George, M., Gogotsi, Y., Grunweller, A., Gu, Z., Halas, N.J., Hampp, N., Hartmann, R.K., Hersam, M.C., Hunziker, P., Jian, J., Jiang, X., Jungebluth, P., Kadhiresan, P., Kataoka, K., Khademhosseini, A., Kopecek, J., Kotov, N.A., Krug, H.F., Lee, D.S., Lehr, C.M., Leong, K.W., Liang, X.J., Ling Lim, M., Liz-Marzan, L.M., Ma, X., Macchiarini, P., Meng, H., Mohwald, H., Mulvaney, P., Nel, A.E., Nie, S., Nordlander, P., Okano, T., Oliveira, J., Park, T.H., Penner, R.M., Prato, M., Puntès, V., Rotello, V.M., Samarakoon, A., Schaak, R.E., Shen, Y., Sjoqvist, S., Skirtach, A.G., Soliman, M.G., Stevens, M.M., Sung, H.W., Tang, B.Z., Tietze, R., Udugama, B.N., VanEpps, J.S., Weil, T., Weiss, P.S., Willner, I., Wu, Y., Yang, L., Yue, Z., Zhang, Q., Zhang, Q., Zhang, X.E., Zhao, Y., Zhou, X. and Parak, W.J. 2017. Diverse Applications of Nanomedicine. *ACS Nano.* **11**(3), pp.2313-2381.

Pignochino, Y., Sarotto, I., Peraldo-Neia, C., Penachioni, J.Y., Cavalloni, G., Migliardi, G., Casorzo, L., Chiorino, G., Risio, M., Bardelli, A., Aglietta, M. and Leone, F. 2010. Targeting EGFR/HER2 pathways enhances the antiproliferative effect of gemcitabine in biliary tract and gallbladder carcinomas. *BMC Cancer*. **10**, p631.

Plein, S. 2012. [Online]. [Accessed 30/11/2019]. Available from: <https://www.bhf.org.uk/research-projects/gadolinium-labelled-aptamers-as-targeted-contrast-agents-for-use-in-cardiac-mritargeting-tenascin-at-sites-of-cardiac-injury-and-remodelling>

Praet, M.M. and Roels, H.J. 1984. Histogenesis of cholangiomas and cholangiocarcinomas in thioacetamide fed rats. *Exp Pathol*. **26**(1), pp.3-14.

Price, T.J., Tang, M., Gibbs, P., Haller, D.G., Peeters, M., Arnold, D., Segelov, E., Roy, A., Tebbutt, N., Pavlakis, N., Karapetis, C., Burge, M. and Shapiro, J. 2018. Targeted therapy for metastatic colorectal cancer. *Expert Rev Anticancer Ther*. **18**(10), pp.991-1006.

Primrose, J., Fox, R.P., Palmer, D.H., Malik, H.Z., Prasad, R., Mirza, D., Anthony, A., Corrie, P., Falk, S., Finch-Jones, M., Wasan, H., Ross, P., Wall, L., Wadsley, J., Evans, J.T.R., Stocken, D., Prasad, R., Ma, Y.T., Davidson, B., Neoptolemos, J.P., Iveson, T., Raftery, J., Zhu, S., Cunningham, D., Garden, O.J., Stubbs, C., Valle, J.W., Bridgewater, J. and group, B.s. 2019. Capecitabine compared with observation in resected biliary tract cancer (BILCAP): a randomised, controlled, multicentre, phase 3 study. *Lancet Oncol*. **20**(5), pp.663-673.

Public Health England. 2015. *National Cancer Intelligence Network Rare and Less Common Cancers*.

Qi, W., Yang, Z., Li, H., Cui, Y. and Xuan, Y. 2019. The role of Tenascin-C and Twist1 in gastric cancer: cancer progression and prognosis. *APMIS*. **127**(2), pp.64-71.

Raj, S., Khurana, S., Choudhari, R., Kesari, K.K., Kamal, M.A., Garg, N., Ruokolainen, J., Das, B.C. and Kumar, D. 2019. Specific targeting cancer cells with nanoparticles and drug delivery in cancer therapy. *Semin Cancer Biol*.

Rassam, F., Roos, E., van Lienden, K.P., van Hooft, J.E., Klumpen, H.J., van Tienhoven, G., Bennink, R.J., Engelbrecht, M.R., Schoorlemmer, A., Beuers, U.H.W., Verheij, J., Besselink, M.G., Busch, O.R. and van Gulik, T.M. 2018. Modern work-up and extended resection in perihilar cholangiocarcinoma: the AMC experience. *Langenbecks Arch Surg*. **403**(3), pp.289-307.

Razumilava, N. and Gores, G.J. 2013. Classification, diagnosis, and management of cholangiocarcinoma. *Clin Gastroenterol Hepatol*. **11**(1), pp.13-21 e11; quiz e13-14.

Razumilava, N. and Gores, G.J. 2014. Cholangiocarcinoma. *Lancet*. **383**(9935), pp.2168-2179.

Reardon, D.A., Akabani, G., Coleman, R.E., Friedman, A.H., Friedman, H.S., Herndon, J.E., 2nd, Cokgor, I., McLendon, R.E., Pegram, C.N., Provenzale, J.M., Quinn, J.A., Rich, J.N., Regalado, L.V., Sampson, J.H., Shafman, T.D., Wikstrand, C.J., Wong, T.Z., Zhao, X.G., Zalutsky, M.R. and Bigner, D.D. 2002. Phase II trial of murine (131)I-labeled antitenascin monoclonal antibody 81C6 administered into surgically created resection cavities of patients with newly diagnosed malignant gliomas. *J Clin Oncol*. **20**(5), pp.1389-1397.

Reardon, D.A., Akabani, G., Coleman, R.E., Friedman, A.H., Friedman, H.S., Herndon, J.E., 2nd, McLendon, R.E., Pegram, C.N., Provenzale, J.M., Quinn, J.A., Rich, J.N., Vredenburgh, J.J., Desjardins, A., Gururangan, S., Badruddoja, M., Dowell, J.M., Wong, T.Z., Zhao, X.G., Zalutsky, M.R. and Bigner, D.D. 2006a. Salvage radioimmunotherapy with murine iodine-131-labeled antitenascin monoclonal antibody 81C6 for patients with recurrent primary and metastatic malignant brain tumors: phase II study results. *J Clin Oncol*. **24**(1), pp.115-122.

Reardon, D.A., Quinn, J.A., Akabani, G., Coleman, R.E., Friedman, A.H., Friedman, H.S., Herndon, J.E., 2nd, McLendon, R.E., Pegram, C.N., Provenzale, J.M., Dowell, J.M., Rich, J.N., Vredenburgh, J.J., Desjardins, A., Sampson, J.H., Gururangan, S., Wong, T.Z., Badruddoja, M.A., Zhao, X.G., Bigner, D.D. and Zalutsky, M.R. 2006b. Novel human IgG2b/murine chimeric antitenascin monoclonal antibody construct radiolabeled with 131I and administered into the surgically created resection cavity of patients with malignant glioma: phase I trial results. *J Nucl Med*. **47**(6), pp.912-918.

Reardon, D.A., Zalutsky, M.R., Akabani, G., Coleman, R.E., Friedman, A.H., Herndon, J.E., 2nd, McLendon, R.E., Pegram, C.N., Quinn, J.A., Rich, J.N., Vredenburgh, J.J., Desjardins, A., Gururangan, S., Boulton, S., Raynor, R.H., Dowell, J.M., Wong, T.Z., Zhao, X.G., Friedman, H.S. and Bigner, D.D. 2008. A pilot study: 131I-antitenascin monoclonal antibody 81c6 to deliver a 44-Gy resection cavity boost. *Neuro Oncol*. **10**(2), pp.182-189.

Reardon, D.A., Zalutsky, M.R. and Bigner, D.D. 2007. Antitenascin-C monoclonal antibody radioimmunotherapy for malignant glioma patients. *Expert Rev Anticancer Ther*. **7**(5), pp.675-687.

Rienks, M. and Papageorgiou, A.P. 2016. Novel regulators of cardiac inflammation: Matricellular proteins expand their repertoire. *J Mol Cell Cardiol*. **91**, pp.172-178.

Ritelli, R., Ngalani Ngaleu, R., Bontempi, P., Dandrea, M., Nicolato, E., Boschi, F., Fiorini, S., Calderan, L., Scarpa, A. and Marzola, P. 2015. Pancreatic cancer growth using magnetic resonance and bioluminescence imaging. *Magn Reson Imaging*. **33**(5), pp.592-599.

Rizvi, S., Fischbach, S.R., Bronk, S.F., Hirsova, P., Krishnan, A., Dhanasekaran, R., Smadbeck, J.B., Smoot, R.L., Vasmatzis, G. and Gores, G.J.

2018. YAP-associated chromosomal instability and cholangiocarcinoma in mice. *Oncotarget*. **9**(5), pp.5892-5905.

Roach, L., Ye, S., Moorcroft, S.C.T., Critchley, K., Coletta, P.L. and Evans, S.D. 2018. Morphological control of seedlessly-synthesized gold nanorods using binary surfactants. *Nanotechnology*. **29**(13), p135601.

Roll, L. and Faissner, A. 2019. Tenascins in CNS lesions. *Semin Cell Dev Biol*. **89**, pp.118-124.

Sadikot, R.T. and Blackwell, T.S. 2005. Bioluminescence imaging. *Proc Am Thorac Soc*. **2**(6), pp.537-540, 511-532.

Sahai, V., Catalano, P.J., Zalupski, M.M., Lubner, S.J., Menge, M.R., Nimeiri, H.S., Munshi, H.G., Benson, A.B., 3rd and O'Dwyer, P.J. 2018. Nab-Paclitaxel and Gemcitabine as First-line Treatment of Advanced or Metastatic Cholangiocarcinoma: A Phase 2 Clinical Trial. *JAMA Oncol*.

Sahin, U., Koslowski, M., Dhaene, K., Usener, D., Brandenburg, G., Seitz, G., Huber, C. and Tureci, O. 2008. Claudin-18 splice variant 2 is a pan-cancer target suitable for therapeutic antibody development. *Clin Cancer Res*. **14**(23), pp.7624-7634.

Saijyo, S., Kudo, T., Suzuki, M., Katayose, Y., Shinoda, M., Muto, T., Fukuhara, K., Suzuki, T. and Matsuno, S. 1995. Establishment of a new extrahepatic bile duct carcinoma cell line, TFK-1. *Tohoku J Exp Med*. **177**(1), pp.61-71.

Sarr, A., Bre, J., Um, I.H., Chan, T.H., Mullen, P., Harrison, D.J. and Reynolds, P.A. 2019. Genome-scale CRISPR/Cas9 screen determines factors modulating sensitivity to ProTide NUC-1031. *Sci Rep*. **9**(1), p7643.

Sasaki, H., Murakami, Y., Uemura, K., Sudo, T., Hashimoto, Y., Kondo, N. and Sueda, T. 2014. Concurrent analysis of human equilibrative nucleoside transporter 1 and ribonucleotide reductase subunit 1 expression increases predictive value for prognosis in cholangiocarcinoma patients treated with adjuvant gemcitabine-based chemotherapy. *Br J Cancer*. **111**(7), pp.1275-1284.

Sato, A., Klaunberg, B. and Tolwani, R. 2004. In vivo bioluminescence imaging. *Comp Med*. **54**(6), pp.631-634.

Sauerbrei, W., Taube, S.E., McShane, L.M., Cavenagh, M.M. and Altman, D.G. 2018. Reporting Recommendations for Tumor Marker Prognostic Studies (REMARK): An Abridged Explanation and Elaboration. *J Natl Cancer Inst*. **110**(8), pp.803-811.

Schmitz, K.J., Lang, H., Wohlschlaeger, J., Sotiropoulos, G.C., Reis, H., Schmid, K.W. and Baba, H.A. 2007. AKT and ERK1/2 signaling in intrahepatic cholangiocarcinoma. *World J Gastroenterol*. **13**(48), pp.6470-6477.

Schreuder, A.M., Engelsman, A.F., van Roessel, S., Verheij, J., Besselink, M.G., van Gulik, T.M. and Busch, O.R. 2019. Treatment of mid-bile duct carcinoma: Local resection or pancreatoduodenectomy? *Eur J Surg Oncol.* **45**(11), pp.2180-2187.

Sercombe, L., Veerati, T., Moheimani, F., Wu, S.Y., Sood, A.K. and Hua, S. 2015. Advances and Challenges of Liposome Assisted Drug Delivery. *Front Pharmacol.* **6**, p286.

Shafizadeh, N., Grenert, J.P., Sahai, V. and Kakar, S. 2010. Epidermal growth factor receptor and HER-2/neu status by immunohistochemistry and fluorescence in situ hybridization in adenocarcinomas of the biliary tree and gallbladder. *Hum Pathol.* **41**(4), pp.485-492.

Shao, H., Kirkwood, J.M. and Wells, A. 2015. Tenascin-C Signaling in melanoma. *Cell Adh Migr.* **9**(1-2), pp.125-130.

Shi, R.Y., Yang, X.R., Shen, Q.J., Yang, L.X., Xu, Y., Qiu, S.J., Sun, Y.F., Zhang, X., Wang, Z., Zhu, K., Qin, W.X., Tang, Z.Y., Fan, J. and Zhou, J. 2013. High expression of Dickkopf-related protein 1 is related to lymphatic metastasis and indicates poor prognosis in intrahepatic cholangiocarcinoma patients after surgery. *Cancer.* **119**(5), pp.993-1003.

Shinozaki, A., Shibahara, J., Noda, N., Tanaka, M., Aoki, T., Kokudo, N. and Fukayama, M. 2011. Claudin-18 in biliary neoplasms. Its significance in the classification of intrahepatic cholangiocarcinoma. *Virchows Arch.* **459**(1), pp.73-80.

Sia, D., Losic, B., Moeini, A., Cabellos, L., Hao, K., Revill, K., Bonal, D., Miltiadous, O., Zhang, Z., Hoshida, Y., Cornella, H., Castillo-Martin, M., Pinyol, R., Kasai, Y., Roayaie, S., Thung, S.N., Fuster, J., Schwartz, M.E., Waxman, S., Cordon-Cardo, C., Schadt, E., Mazzaferro, V. and Llovet, J.M. 2015. Massive parallel sequencing uncovers actionable FGFR2-PPHLN1 fusion and ARAF mutations in intrahepatic cholangiocarcinoma. *Nat Commun.* **6**, p6087.

Sickmier, E.A., Kurzeja, R.J., Michelsen, K., Vazir, M., Yang, E. and Tasker, A.S. 2016. The Panitumumab EGFR Complex Reveals a Binding Mechanism That Overcomes Cetuximab Induced Resistance. *PLoS One.* **11**(9), pe0163366.

Silsirivanit, A., Sawanyawisuth, K., Riggins, G.J. and Wongkham, C. 2014. Cancer biomarker discovery for cholangiocarcinoma: the high-throughput approaches. *J Hepatobiliary Pancreat Sci.* **21**(6), pp.388-396.

Simbolo, M., Fassan, M., Ruzzenente, A., Mafficini, A., Wood, L.D., Corbo, V., Melisi, D., Malleo, G., Vicentini, C., Malpeli, G., Antonello, D., Sperandio, N., Capelli, P., Tomezzoli, A., Iacono, C., Lawlor, R.T., Bassi, C., Hruban, R.H., Guglielmi, A., Tortora, G., de Braud, F. and Scarpa, A. 2014. Multigene mutational profiling of cholangiocarcinomas identifies actionable molecular subgroups. *Oncotarget.* **5**(9), pp.2839-2852.

Simon, M., Jorgensen, J.T., Norregaard, K. and Kjaer, A. 2020. (18)F-FDG positron emission tomography and diffusion-weighted magnetic resonance imaging for response evaluation of nanoparticle-mediated photothermal therapy. *Sci Rep.* **10**(1), p7595.

Simsek, C., Esin, E. and Yalcin, S. 2019. Metronomic Chemotherapy: A Systematic Review of the Literature and Clinical Experience. *J Oncol.* **2019**, p5483791.

Singh, P., Pandit, S., Mokkapati, V., Garg, A., Ravikumar, V. and Mijakovic, I. 2018. Gold Nanoparticles in Diagnostics and Therapeutics for Human Cancer. *Int J Mol Sci.* **19**(7).

Singh, R. 2019. Nanotechnology based therapeutic application in cancer diagnosis and therapy. *3 Biotech.* **9**(11), p415.

Sirica, A.E. and Gores, G.J. 2014. Desmoplastic stroma and cholangiocarcinoma: clinical implications and therapeutic targeting. *Hepatology.* **59**(6), pp.2397-2402.

Sirica, A.E., Zhang, Z., Lai, G.H., Asano, T., Shen, X.N., Ward, D.J., Mahatme, A. and Dewitt, J.L. 2008. A novel "patient-like" model of cholangiocarcinoma progression based on bile duct inoculation of tumorigenic rat cholangiocyte cell lines. *Hepatology.* **47**(4), pp.1178-1190.

Soejima, Y., Takeuchi, M., Akashi, T., Sawabe, M. and Fukusato, T. 2018. beta4 and beta6 Integrin Expression Is Associated with the Subclassification and Clinicopathological Features of Intrahepatic Cholangiocarcinoma. *Int J Mol Sci.* **19**(4).

Sohal, D.P., Mykulowycz, K., Uehara, T., Teitelbaum, U.R., Damjanov, N., Giantonio, B.J., Carberry, M., Wissel, P., Jacobs-Small, M., O'Dwyer, P.J., Sepulveda, A. and Sun, W. 2013. A phase II trial of gemcitabine, irinotecan and panitumumab in advanced cholangiocarcinoma. *Ann Oncol.* **24**(12), pp.3061-3065.

Sologan, M., Padelli, F., Giachetti, I., Aquino, D., Boccalon, M., Adami, G., Pengo, P. and Pasquato, L. 2019. Functionalized Gold Nanoparticles as Contrast Agents for Proton and Dual Proton/Fluorine MRI. *Nanomaterials (Basel).* **9**(6).

Song, J., Yu, J., Li, Y., Lu, S., Ma, Z. and Shi, H. 2017. MR targeted imaging for the expression of tenascin-C in myocardial infarction in vivo. *J Magn Reson Imaging.* **45**(6), pp.1668-1674.

Song, X., Shao, Z., Han, M. and Liang, H. 2019. A novel mouse model of orthotopic extrahepatic cholangiocarcinoma confirmed with molecular imaging. *Translational Cancer Research.* **8**(2), pp.583-591.

Spence, C., Saupe, F., Midwood, K., Burckel, H., Noel, G. and Orend, G. 2015. Tenascin-C: Exploitation and collateral damage in cancer management. *Cell Adh Migr.* **9**(1-2), pp.141-153.

Stang, A. 2010. Critical evaluation of the Newcastle-Ottawa scale for the assessment of the quality of nonrandomized studies in meta-analyses. *Eur J Epidemiol.* **25**(9), pp.603-605.

Stein, A., Arnold, D., Bridgewater, J., Goldstein, D., Jensen, L.H., Klumpen, H.-J., Lohse, A.W., Nashan, B., Primrose, J., Schrum, S., Shannon, J., Vettorazzi, E. and Wege, H. 2015. Adjuvant chemotherapy with gemcitabine and cisplatin compared to observation after curative intent resection of cholangiocarcinoma and muscle invasive gallbladder carcinoma (ACTICCA-1 trial) - a randomized, multidisciplinary, multinational phase III trial. *BMC Cancer.* **15**(1), p564.

STRING. 2014a. [Online]. [Accessed 30/11/2019]. Available from: <http://string905.embl.de/>

STRING. 2014b. [Online]. Available from: <http://string905.embl.de/>

Suarez-Munoz, M.A., Fernandez-Aguilar, J.L., Sanchez-Perez, B., Perez-Daga, J.A., Garcia-Albiach, B., Pulido-Roa, Y., Marin-Camero, N. and Santoyo-Santoyo, J. 2013. Risk factors and classifications of hilar cholangiocarcinoma. *World J Gastrointest Oncol.* **5**(7), pp.132-138.

Subimerb, C., Pinlaor, S., Khuntikeo, N., Leelayuwat, C., Morris, A., McGrath, M.S. and Wongkham, S. 2010. Tissue invasive macrophage density is correlated with prognosis in cholangiocarcinoma. *Mol Med Rep.* **3**(4), pp.597-605.

Sukowati, C.H., Anfuso, B., Croce, L.S. and Tiribelli, C. 2015. The role of multipotent cancer associated fibroblasts in hepatocarcinogenesis. *BMC Cancer.* **15**, p188.

Sun, Q., Li, F., Sun, F. and Niu, J. 2015. Interleukin-8 is a prognostic indicator in human hilar cholangiocarcinoma. *Int J Clin Exp Pathol.* **8**(7), pp.8376-8384.

Sun, Q., Radosz, M. and Shen, Y. 2012. Challenges in design of translational nanocarriers. *J Control Release.* **164**(2), pp.156-169.

Sun, Q., Sun, X., Ma, X., Zhou, Z., Jin, E., Zhang, B., Shen, Y., Van Kirk, E.A., Murdoch, W.J., Lott, J.R., Lodge, T.P., Radosz, M. and Zhao, Y. 2014a. Integration of nanoassembly functions for an effective delivery cascade for cancer drugs. *Adv Mater.* **26**(45), pp.7615-7621.

Sun, Q., Zhao, C., Xia, L., He, Z., Lu, Z., Liu, C., Jia, M., Wang, J. and Niu, J. 2014b. High expression of matrix metalloproteinase-9 indicates poor prognosis in human hilar cholangiocarcinoma. *Int J Clin Exp Pathol.* **7**(9), pp.6157-6164.

Supuran, C.T. 2018. Carbonic anhydrase inhibitors as emerging agents for the treatment and imaging of hypoxic tumors. *Expert Opin Investig Drugs*. **27**(12), pp.963-970.

Swietach, P., Hulikova, A., Vaughan-Jones, R.D. and Harris, A.L. 2010. New insights into the physiological role of carbonic anhydrase IX in tumour pH regulation. *Oncogene*. **29**(50), pp.6509-6521.

Szklarczyk, D., Gable, A.L., Lyon, D., Junge, A., Wyder, S., Huerta-Cepas, J., Simonovic, M., Doncheva, N.T., Morris, J.H., Bork, P., Jensen, L.J. and Mering, C.V. 2019. STRING v11: protein-protein association networks with increased coverage, supporting functional discovery in genome-wide experimental datasets. *Nucleic Acids Res*. **47**(D1), pp.D607-D613.

Tan, K.X., Pan, S., Jeevanandam, J. and Danquah, M.K. 2019. Cardiovascular therapies utilizing targeted delivery of nanomedicines and aptamers. *Int J Pharm*. **558**, pp.413-425.

Tang, Z., Yang, Y., Meng, W. and Li, X. 2017. Best option for preoperative biliary drainage in Klatskin tumor: A systematic review and meta-analysis. *Medicine (Baltimore)*. **96**(43), pe8372.

Terada, T. and Nakanuma, Y. 1994. Expression of tenascin, type IV collagen and laminin during human intrahepatic bile duct development and in intrahepatic cholangiocarcinoma. *Histopathology*. **25**(2), pp.143-150.

Tian, X., Wang, Q., Li, Y., Hu, J., Wu, L., Ding, Q. and Zhang, C. 2015. The expression of S100A4 protein in human intrahepatic cholangiocarcinoma: clinicopathologic significance and prognostic value. *Pathol Oncol Res*. **21**(1), pp.195-201.

Tiede, C., Bedford, R., Heseltine, S.J., Smith, G., Wijetunga, I., Ross, R., AlQallaf, D., Roberts, A.P., Balls, A., Curd, A., Hughes, R.E., Martin, H., Needham, S.R., Zanetti-Domingues, L.C., Sadigh, Y., Peacock, T.P., Tang, A.A., Gibson, N., Kyle, H., Platt, G.W., Ingram, N., Taylor, T., Coletta, L.P., Manfield, I., Knowles, M., Bell, S., Esteves, F., Maqbool, A., Prasad, R.K., Drinkhill, M., Bon, R.S., Patel, V., Goodchild, S.A., Martin-Fernandez, M., Owens, R.J., Nettleship, J.E., Webb, M.E., Harrison, M., Lippiat, J.D., Ponnambalam, S., Peckham, M., Smith, A., Ferrigno, P.K., Johnson, M., McPherson, M.J. and Tomlinson, D.C. 2017. Affimer proteins are versatile and renewable affinity reagents. *Elife*. **6**.

Tiede, C., Tang, A.A., Deacon, S.E., Mandal, U., Nettleship, J.E., Owen, R.L., George, S.E., Harrison, D.J., Owens, R.J., Tomlinson, D.C. and McPherson, M.J. 2014. Adhiron: a stable and versatile peptide display scaffold for molecular recognition applications. *Protein Eng Des Sel*. **27**(5), pp.145-155.

Tiernan, J.P., Ingram, N., Marston, G., Perry, S.L., Rushworth, J.V., Coletta, P.L., Millner, P.A., Jayne, D.G. and Hughes, T.A. 2015. CEA-targeted nanoparticles allow specific in vivo fluorescent imaging of colorectal cancer models. *Nanomedicine (Lond)*. pp.1-9.

Tucker, R.P. and Chiquet-Ehrismann, R. 2015. Tenascin-C: Its functions as an integrin ligand. *Int J Biochem Cell Biol.* **65**, pp.165-168.

Tucker, R.P., Hammarback, J.A., Jenrath, D.A., Mackie, E.J. and Xu, Y. 1993. Tenascin expression in the mouse: in situ localization and induction in vitro by bFGF. *J Cell Sci.* **104 (Pt 1)**, pp.69-76.

Uhlen, M., Fagerberg, L., Hallstrom, B.M., Lindskog, C., Oksvold, P., Mardinoglu, A., Sivertsson, A., Kampf, C., Sjostedt, E., Asplund, A., Olsson, I., Edlund, K., Lundberg, E., Navani, S., Szgyarto, C.A., Odeberg, J., Djureinovic, D., Takanen, J.O., Hober, S., Alm, T., Edqvist, P.H., Berling, H., Tegel, H., Mulder, J., Rockberg, J., Nilsson, P., Schwenk, J.M., Hamsten, M., von Feilitzen, K., Forsberg, M., Persson, L., Johansson, F., Zwahlen, M., von Heijne, G., Nielsen, J. and Ponten, F. 2015. Proteomics. Tissue-based map of the human proteome. *Science.* **347(6220)**, p1260419.

Valle, J., Wasan, H., Palmer, D.H., Cunningham, D., Anthony, A., Maraveyas, A., Madhusudan, S., Iveson, T., Hughes, S., Pereira, S.P., Roughton, M., Bridgewater, J. and Investigators, A.B.C.T. 2010. Cisplatin plus gemcitabine versus gemcitabine for biliary tract cancer. *N Engl J Med.* **362(14)**, pp.1273-1281.

van der Meel, R., Sulheim, E., Shi, Y., Kiessling, F., Mulder, W.J.M. and Lammers, T. 2019. Smart cancer nanomedicine. *Nat Nanotechnol.* **14(11)**, pp.1007-1017.

van Helden, E.J., Elias, S.G., Gerritse, S.L., van Es, S.C., Boon, E., Huisman, M.C., van Grieken, N.C.T., Dekker, H., van Dongen, G., Vugts, D.J., Boellaard, R., van Herpen, C.M.L., de Vries, E.G.E., Oyen, W.J.G., Brouwers, A.H., Verheul, H.M.W., Hoekstra, O.S. and Menke-van der Houven van Oordt, C.W. 2019. [(89)Zr]Zr-cetuximab PET/CT as biomarker for cetuximab monotherapy in patients with RAS wild-type advanced colorectal cancer. *Eur J Nucl Med Mol Imaging.*

van Oosten, M., Crane, L.M., Bart, J., van Leeuwen, F.W. and van Dam, G.M. 2011. Selecting Potential Targetable Biomarkers for Imaging Purposes in Colorectal Cancer Using TArget Selection Criteria (TASC): A Novel Target Identification Tool. *Transl Oncol.* **4(2)**, pp.71-82.

Vandooren, J., Van den Steen, P.E. and Opdenakker, G. 2013. Biochemistry and molecular biology of gelatinase B or matrix metalloproteinase-9 (MMP-9): the next decade. *Crit Rev Biochem Mol Biol.* **48(3)**, pp.222-272.

Verlingue, L., Hollebecque, A., Boige, V., Ducreux, M., Malka, D. and Ferte, C. 2017a. Matching genomic molecular aberrations with molecular targeted agents: Are biliary tract cancers an ideal playground? *Eur J Cancer.* **81**, pp.161-173.

Verlingue, L., Malka, D., Allorant, A., Massard, C., Ferte, C., Lacroix, L., Rouleau, E., Auger, N., Ngo, M., Nicotra, C., De Baere, T., Tselikas, L., Ba, B.,

Michiels, S., Scoazec, J.Y., Boige, V., Ducreux, M., Soria, J.C. and Hollebecque, A. 2017b. Precision medicine for patients with advanced biliary tract cancers: An effective strategy within the prospective MOSCATO-01 trial. *Eur J Cancer*. **87**, pp.122-130.

Wadsworth, C.A., Dixon, P.H., Wong, J.H., Chapman, M.H., McKay, S.C., Sharif, A., Spalding, D.R., Pereira, S.P., Thomas, H.C., Taylor-Robinson, S.D., Whittaker, J., Williamson, C. and Khan, S.A. 2011. Genetic factors in the pathogenesis of cholangiocarcinoma. *Dig Dis*. **29**(1), pp.93-97.

Wan, J., Wang, J.H., Liu, T., Xie, Z., Yu, X.F. and Li, W. 2015. Surface chemistry but not aspect ratio mediates the biological toxicity of gold nanorods in vitro and in vivo. *Sci Rep*. **5**, p11398.

Wang, D., Meng, L., Fei, Z., Hou, C., Long, J., Zeng, L., Dyson, P.J. and Huang, P. 2018. Multi-layered tumor-targeting photothermal-doxorubicin releasing nanotubes eradicate tumors in vivo with negligible systemic toxicity. *Nanoscale*. **10**(18), pp.8536-8546.

Wang, S., You, Q., Wang, J., Song, Y., Cheng, Y., Wang, Y., Yang, S., Yang, L., Li, P., Lu, Q., Yu, M. and Li, N. 2019. MSOT/CT/MR imaging-guided and hypoxia-manuevered oxygen self-supply radiotherapy based on one-pot MnO₂-mSiO₂@Au nanoparticles. *Nanoscale*. **11**(13), pp.6270-6284.

Wiggers, J.K., Ruys, A.T., Groot Koerkamp, B., Beuers, U., ten Kate, F.J. and van Gulik, T.M. 2014. Differences in immunohistochemical biomarkers between intra- and extrahepatic cholangiocarcinoma: a systematic review and meta-analysis. *J Gastroenterol Hepatol*. **29**(8), pp.1582-1594.

World Cholangiocarcinoma Day. 2019. [Online]. [Accessed 08 Oct 2019]. Available from: <http://worldcholangiocarcinomaday.org/>

Wu, Li, F., Niu, G. and Chen, X. 2013a. PET imaging of inflammation biomarkers. *Theranostics*. **3**(7), pp.448-466.

Wu and Zhou, S.H. 2015a. Nanoparticle-Based Targeted Therapeutics in Head-And-Neck Cancer. *Int J Med Sci*. **12**(2), pp.187-200.

Wu, C., Li, F., Niu, G. and Chen, X. 2013b. PET imaging of inflammation biomarkers. *Theranostics*. **3**(7), pp.448-466.

Wu, L., Merath, K., Farooq, A., Hyer, J.M., Tsilimigras, D.I., Paredes, A.Z., Mehta, R., Sahara, K., Shen, F. and Pawlik, T.M. 2019. Photodynamic therapy may provide a benefit over systemic chemotherapy among non-surgically managed patients with extrahepatic cholangiocarcinoma. *J Surg Oncol*.

Wu, T.T. and Zhou, S.H. 2015b. Nanoparticle-Based Targeted Therapeutics in Head-And-Neck Cancer. *Int J Med Sci*. **12**(2), pp.187-200.

Xu, Li, Z., Jiang, P., Wu, G., Chen, K., Zhang, X. and Li, X. 2015. The co-expression of MMP-9 and Tenascin-C is significantly associated with the progression and prognosis of pancreatic cancer. *Diagn Pathol.* **10**, p211.

Xu, Liu, Z.L., Pan, C., Yang, X.Q., Ning, S.L., Liu, H.D., Guo, S., Yu, J.M. and Zhang, Z.L. 2019. HMGB1 correlates with angiogenesis and poor prognosis of perihilar cholangiocarcinoma via elevating VEGFR2 of vessel endothelium. *Oncogene.* **38**(6), pp.868-880.

Yabluchanskiy, A., Ma, Y., Iyer, R.P., Hall, M.E. and Lindsey, M.L. 2013. Matrix metalloproteinase-9: Many shades of function in cardiovascular disease. *Physiology (Bethesda).* **28**(6), pp.391-403.

Yamada, D., Rizvi, S., Razumilava, N., Bronk, S.F., Davila, J.I., Champion, M.D., Borad, M.J., Bezerra, J.A., Chen, X. and Gores, G.J. 2015. IL-33 facilitates oncogene-induced cholangiocarcinoma in mice by an interleukin-6-sensitive mechanism. *Hepatology.*

Yamamoto, Y., Sugiura, T., Okamura, Y., Ito, T., Ashida, R., Ohgi, K., Nakanuma, Y. and Uesaka, K. 2019. The Evaluation of the Eighth Edition of the AJCC/UICC Staging System for Intrahepatic Cholangiocarcinoma: a Proposal of a Modified New Staging System. *J Gastrointest Surg.*

Yang, X., Wang, W., Wang, C., Wang, L., Yang, M., Qi, M., Su, H., Sun, X., Liu, Z., Zhang, J., Qin, X. and Han, B. 2014. Characterization of EGFR family gene aberrations in cholangiocarcinoma. *Oncol Rep.* **32**(2), pp.700-708.

Ye, S., Benz, F., Wheeler, M.C., Oram, J., Baumberg, J.J., Cespedes, O., Christenson, H.K., Coletta, P.L., Jeuken, L.J., Markham, A.F., Critchley, K. and Evans, S.D. 2016. One-step fabrication of hollow-channel gold nanoflowers with excellent catalytic performance and large single-particle SERS activity. *Nanoscale.* **8**(32), pp.14932-14942.

Ye, S., Brown, A.P., Stammers, A.C., Thomson, N.H., Wen, J., Roach, L., Bushby, R.J., Coletta, P.L., Critchley, K., Connell, S.D., Markham, A.F., Brydson, R. and Evans, S.D. 2019. Sub-Nanometer Thick Gold Nanosheets as Highly Efficient Catalysts. *Adv Sci (Weinh).* **6**(21), p1900911.

Ye, S., Marston, G., McLaughlan, J.R., Sigle, D.O., Ingram, N., Freear, S., J.J., B., Bushby, R.J., Markham, A.F., Critchley, K., Coletta, P.L. and Evans, S.D. 2015. Engineering Gold Nanotubes with Controlled Length and Near-Infrared Absorption for Theranostic Applications. *Advanced Functional Materials.*

Ye, S., Wheeler, M.C., McLaughlan, J.R., Tamang, A., Diggle, C.P., Cespedes, O., Markham, A.F., Coletta, P.L. and Evans, S.D. 2018. Developing Hollow-Channel Gold Nanoflowers as Trimodal Intracellular Nanoprobes. *Int J Mol Sci.* **19**(8).

Yoshikawa, D., Ojima, H., Iwasaki, M., Hiraoka, N., Kosuge, T., Kasai, S., Hirohashi, S. and Shibata, T. 2008. Clinicopathological and prognostic

significance of EGFR, VEGF, and HER2 expression in cholangiocarcinoma. *Br J Cancer*. **98**(2), pp.418-425.

Young, A.L., Prasad, K.R., Toogood, G.J. and Lodge, J.P. 2010. Surgical treatment of hilar cholangiocarcinoma in a new era: comparison among leading Eastern and Western centers, Leeds. *J Hepatobiliary Pancreat Sci*. **17**(4), pp.497-504.

Yu, X., Yang, Y.P., Dikici, E., Deo, S.K. and Daunert, S. 2017. Beyond Antibodies as Binding Partners: The Role of Antibody Mimetics in Bioanalysis. *Annu Rev Anal Chem (Palo Alto Calif)*. **10**(1), pp.293-320.

Zhao, L., Ma, X., Liang, M., Li, D., Ma, P., Wang, S., Wu, Z. and Zhao, X. 2019. Prediction for early recurrence of intrahepatic mass-forming cholangiocarcinoma: quantitative magnetic resonance imaging combined with prognostic immunohistochemical markers. *Cancer Imaging*. **19**(1), p49.

Zhao, Y., Liu, W., Tian, Y., Yang, Z., Wang, X., Zhang, Y., Tang, Y., Zhao, S., Wang, C., Liu, Y., Sun, J., Teng, Z., Wang, S. and Lu, G. 2018. Anti-EGFR Peptide-Conjugated Triangular Gold Nanoplates for Computed Tomography/Photoacoustic Imaging-Guided Photothermal Therapy of Non-Small Cell Lung Cancer. *ACS Appl Mater Interfaces*. **10**(20), pp.16992-17003.

Zheng, X., Chen, B., Wu, J.X., Jia, A.Y., Rong, W.Q., Wang, L.M., Wu, F., Zhao, Y.T., Li, Y.X. and Wang, W.H. 2018. Benefit of adjuvant radiotherapy following narrow-margin hepatectomy in patients with intrahepatic cholangiocarcinoma that adhere to major vessels. *Cancer Manag Res*. **10**, pp.3973-3981.

Zorzi, D., Laurent, A., Pawlik, T.M., Lauwers, G.Y., Vauthey, J.N. and Abdalla, E.K. 2007. Chemotherapy-associated hepatotoxicity and surgery for colorectal liver metastases. *Br J Surg*. **94**(3), pp.274-286.

Appendix 1 Data extraction table

A summary of the 166 candidate biomarkers that met the inclusion/exclusion criteria for systematic review of biomarkers.

Biomarker (Gene)	Year	First Author PMID	Eastern study?	Site of tumour	No: of patients	% high expression	% +	Location of marker	Slide/ TMA	Control group	Expression in normal tissues	Risk of bias
A1AT <i>SERPINA1</i>	2013	Jamnongkan W 23188705	Thailand	CCA	42	57.1%	-	Cytoplasm	S	Inflammatory tissues	Weak +ve normal BD	NR
A1AT <i>SERPINA1</i>	2017	Laohaviroj M (2017) 28618946	Thailand	CCA	354	NR	50%	Cytoplasm	TMA	n=2 normal tissues	NR	2 blinded independent
A1AT <i>SERPINA1</i>	2014	Khenjanta, C 25556446	Thailand	IH-CCA	30	23% (7/30)	NR	Tumour cells	S	n=30, adjacent normal tissue	Weak staining	2 blinded independent observers
AFP <i>AFP</i>	2017	Liu S 28915621	China	IH-CCA	60	-	53.3%	NR	S	N=60 paired normal tissue	NR	NR
Akirin2 <i>AKIRIN2</i>	2019	Leng K 30886152	China	CCA	51	30/51	NR	Nucleus	S	Paired non- tumour n=51	Normal tissue low	NR
Ang1 <i>ANGPT1</i>	2008	Mihara Y -	Japan	EH-CCA	119	-	43.7%	Cytoplasm	S	Normal mucosa n=38	15.8%	2 independent investigators
Ang1 <i>ANGPT1</i>	2006	Tang D 16465407	Japan	CCA (CCC)	33	15.2%	42.4%	Cytoplasm	S	NR	Hepatocytes of adjacent liver tissue	NR
Ang2 <i>ANGPT2</i>	2008	Mihara Y -	Japan	EH-CCA	119	-	42.0%	Cytoplasm	S	Normal mucosa n=38	26.3%	2 independent investigators

Ang2 <i>ANGPT2</i>	2006	Tang D 16465407	Japan	CCA (CCC)	33	15.2%	57.6%	Cytoplasm	S	NR	Hepatocytes of adjacent liver tissue	NR
Ang2 <i>ANGPT2</i>	2014	Voigtlander 24823366	No, Germany	EH-CCA IH-CCA	37 8	Strong induction in tumour vasculature	NR	Tumour vascular endotheliu m	S	PSC	PSC negative.	NR
Aromatase <i>CYP19A1</i>	2018	Kaewlert W 30284180	Thailand	CCA	74	61%	-	Cytoplasm	S	Normal bile duct cells	Lower than CCA	NR
CA9 CA9	2019	Bi C 30849962	China	IH-CCA	113	85.0%	-	NR	S	NR	NR	2 independent pathologists
CA9 CA9	2014	Gu, M 25755787	Korea	IH-CCA	85	NR	44.7%	NR	TMA	n=4 normal liver tissue	NR	NR
Cadherin 17 <i>CDH17</i>	2015	Maeda S 25917007	Japan	EH-CCA	165	-	41%	NR	S	NR	NR	3 observers
CD24 <i>CD24</i>	2006	Su, M-C 16125303	Taiwan	IH-CCA	70	NR	51%	Membrane Cytoplasm	S	Normal liver tissue	-ve	NR
CD24 <i>CD24</i>	2013	Kim, K 23539485	Korea	EH-CCA	84	NR	42.9%	Tumour cells	TMA	None	NR	NR
CD24 <i>CD24</i>	2010	Riener, M-O 20621328	Switzerlan d	IH-CCA EH-CCA	19 59	NR	21% 58%	Cytoplasm	TMA	n=30 normal biliary epithelium of extrahepatic bile ducts	Negative for CD24 expression	NR
CDX2 <i>CDX2</i>	2018	Tang H 29862152	China	IH-CCA	93	-	29.0%	Nucleus	S	NR	NR	NR
CDX2 <i>CDX2</i>	2018	Wang Z No PubMed ID	Japan	IH-CCA	127	-	26.0%	Nucleus	TMA	NR	NR	2 blinded observers

CDX2 <i>CDX2</i>	2019	Ishida K 31401234	Japan	EH-CCA	84	NR	NR	Nucleus	S	NR	NR	3 blinded independent observers
CDX2 <i>CDX2</i>	2007	Chang Y 17295772	Thailand	EH-CCA	49	-	22.5%	Nucleus	S	NR	NR	Single independent pathologist
CDX2 <i>CDX2</i>	2006	Jinawath A 16794828	Thailand	IH-CCA EH-CCA	36 23	-	37.4%	NR	S	NR	NR	NR
CDX2 <i>CDX2</i>	2008	Chiu, C-T 18329969	Taiwan	IH-CCA	30	NR	60%	Nucleus	S	None	NR	NR
CDX2 <i>CDX2</i>	2017	Hass, HG	Germany	IH-CCA	36	NR	25%	Nucleus	S	NR	NR	NR
Claudin 18 <i>CLDN18</i>	2015	Keira Y 25503275	Japan	IH-CCA EH-CCA	27 32	NR	NR	Basolateral membrane	S	NR	non-neoplastic cells -ve	NR
Claudin 18 <i>CLDN18</i>	2011	Shinozaki, A 21607649	Japan	EH-CCA IH-CCA	99 83	NR	90% 43%	Membrane	S	Normal intrahepatic and extrahepatic biliary epithelial	-ve. Inflammatory mucosa basolateral membrane occ. +ve	NR
CTLA4 <i>CTLA4</i>	2017	Lim, YJ 28084572	Korea	EH-CCA	77	79.2% (61/77)	NR	Tumour cells and infiltrating lymphocytes	TMA	None	NR	2 blinded independent observers confirmed the results
CUL4A <i>CUL4A</i>	2017	Huang, G-K 28576144	Taiwan	IH-CCA	105	NR	32.4%	Nucleus	TMA	Normal bile ducts	NR	Two blinded independent observers
CUL4A <i>CUL4A</i>	2017	Zhang, T-J 28428711	China	PH-CCA	72	NR	NR	Nucleus	S	n=12 adjacent normal bile ducts from the 72 patients	Expressed in normal bile ducts	Two blinded independent observers

CXCL12 <i>CXCL12</i>	2019	Miyata, T 31361379	Japan	IH-CCA	127	52% (66/127)	NR	Nucleus and cytoplasm	S	NR	NR	Two blinded independent observers
CXCR2 <i>CXCR2</i>	2014	Sueoka, H 24582495	Japan	IH-CCA	34	64.7% (22/34)	NR	Tumour cells	S	n=30 adjacent normal liver tissue	Weak expression	2 independent observers
CYP39A1 <i>CYP39A1</i>	2014	Khenjanta, C 25556446	Thailand	CCA	30	30% (9/30)	NR	Tumour cells and hepatocytes	S	n=30, adjacent normal tissue	Weak staining	2 blinded independent observers
DKK1 <i>DKK1</i>	2013	Shi RY 23132676	China	IH-CCA	138	-	38.4%	Cytoplasm	TMA	NR	NR	2 observers, 1 blinded
DKK1 <i>DKK1</i>	2016	Shi, X-D 27608843	China	PH-CCA	37	64.9%	NR	Cytoplasm	S	Peritumoral tissue	Very low expression	Two blinded independent observers
EGFR <i>ERBB1</i>	2007	Schmitz 18161916	No, Germany	IH-CCA	61	21.3% 13/61	68.9%	Tumour cell membrane	S	None	NR	2 blinded observers
EGFR <i>ERBB1</i>	2014	Simbolo 24867389	No, Italy	IH-CCA EH-CCA	57 40	NR	49% 18%	Membranous	TMA	None	NR	NR
EGFR <i>ERBB1</i>	2017	Padthaisong S 28668850	Thailand	CCA	94	55%	-	NR	S	NR	NR	NR
EGFR <i>ERBB1</i>	2019	Zhao Li 31307551	China	IH-CCA	47	-	76.6%	NR	S	NR	NR	1 blinded pathologist
EGFR <i>ERBB1</i>	2011	Miyamoto	Japan	IH-CCA	111	-	26.1%	NR	TMA	NR	NR	3 blinded observers
EGFR <i>ERBB1</i>	2010	Pignochino Y 21087480	No, Italy	IH-CCA EH-CCA	17 19	76.5% 26.3%	100% 52.6%	Membrane	S	Normal cholangiocyte and hepatocyte membranes	All positive	NR

EGFR <i>ERBB1</i>	2006	Ogo Y 16739351	Japan	CCA	44	43%	-	Membrane	S	+ control Lung Ca, no normal tissues	+ lung Ca	NR
EGFR <i>ERBB1</i>	2018	Xu YF 30177842	China	PH-CCA	121	45.5%	-	NR	S	NR	NR	NR
EGFR <i>ERBB1</i>	2018	Gomes RV 29995151	No, Brazil	CCA (PH-, IH- &D)	35	-	28.6%	Cell membran e	S	NR	NR	1 blinded experienced pathologist
EGFR <i>ERBB1</i>	2010	Shafizadeh N 20040392	No, USA	IH-CCA EH-CCA	26 19	-	81% 79%	Membrane	S	NR	NR	NR
EGFR <i>ERBB1</i>	2014	Yang, X 24927194	China	IH-CCA EH-CCA	65 110	30.8% (20/65) 20.9% (23/110)	NR	Membrane	TMA	NR	NR	2 blinded independent observers
EGFR <i>ERBB1</i>	2008	Yoshikawa, D. 18087285	Japan	IH-CCA EH-CCA	106 130	NR	27.4% 19.2%	Membrane	S	None	NR	3 Blinded authors
EGFR <i>ERBB1</i>	2012	Gu, MJ 22281980	Korea	IH-CCA	83	NR	55.4%	Membrane	S	None	NR	NR (although no access to full article)
EGFR <i>ERBB1</i>	2016	Moon, A 27020207	Korea	EH-CCA	84	NR	38.1%	Cytoplasm Membrane	TMA	NR	NR	Two authors
EGFR <i>ERBB1</i>	2009	Iguchi T 19262069	Japan	IH-CCA	61	NR	67.2%	Cytoplasm , membran ous	S	None	NR	NR
eNOS <i>NOS3</i>	2017	Suksawat M 27143607	Thailand	CCA	171	100%	50.9%	Epithelial cells	S	Normal bile duct	NR	NR
ER α <i>ESR1</i>	2018	Kaewlert W 30284180	Thailand	CCA	74	78%	-	Cytoplasm and Nucleus	S	Adjacent normal tissue 1. Bile duct epithelial cells 2. Hepatocytes	1. Sig lower 2. High expression in cytoplasm	NR

ERβ <i>ESR2</i>	2018	Kaewlert W 30284180	Thailand	CCA	74	50%	-	Cytoplasm and Nucleus	S	Adjacent normal tissue 1. Bile duct epithelial cells 2. Hepatocytes	1. Sig lower 2. High expression in cytoplasm	NR
Etk/Bmx <i>BMX</i>	2008	Guo L 18270973	China	IH-CCA	57	-	33.3%	Cytoplasm and nucleus	S	Background liver tissue (normal hepatocytes, BD)	Negative	NR
FOXC2 <i>FOXC2</i>	2013	Watanabe A 23919841	Thailand	EH-CCA	77	-	23.3%	Cytoplasm	S	NR	NR	2 independent observers
GLUT-1 <i>SLC2A1</i>	2018	Ikeno y 29642912	Japan	IH-CCA	50	52%	-	Tumour cell memb	S	NR	NR	2 blinded researchers
GLUT-1 <i>SLC2A1</i>	2014	Kubo, Y 24824030	Japan	IH-CCA	149	NR	46.3%	Membrane	S	NR	NR	Two blinded authors
HES1 <i>HES1</i>	2016	Aoki S 27821106	Japan	EH-CCA	132	Unknown	81.8%	Nucleus	TMA	N=8 normal bile duct	Normal bile ducts negative	NR
Hes1 <i>Hes1</i>	2013	Gandou C 23134772	Japan	PH-CCA IH-CCA	25 21	-	84% 62%	Nucleus, cytoplasm	S	Intra-hepatic and extra hepatic BD	Infrequently positive	NR
Hes1 <i>HES1</i>	2012	Igarashi, S 22594685	Japan	PH-CCA	43	NR	35%	NR	S	n=28 normal fetal and adult bile ducts	57% (16/28) Hes1 expression in the Nucleus of lining epithelial	NR
ID2 <i>ID2</i>	2013	Harder J 24409060	No, Germany	IH-CCA EH-CCA	50 45	-	29% 28%	Mainly cytoplasm	S	Normal bile ducts	Low or negative	2 independent blinded observers
IGF-1 <i>IGF1</i>	2012	Ohashi H 22044563	Japan	EH-CCA	30	-	60%	NR	S	NR	NR	NR

IGF-2 <i>IGF2</i>	2012	Ohashi H 22044563	Japan	EH-CCA	30	-	53%	NR	S	NR	NR	NR
IGFBP3 <i>IGFBP3</i>	2006	Jinawath, N 17006947	Thailand	IHCCA	273	NR	55.34 %	Cytoplasm	TMA	Noncancerous liver tissue from n=10 patients with liver metastasis from CRC	Negative expression	Three independent investigators
IL-17 IL17	2015	Asukai K 26228109	Japan	IH-CCA	72	38.9%	-	Cytoplasm membran e	S	Pancreas exocrine tissue +ve control. Peritumoral normal liver	Pancreas +ve, normal liver	NR
IL-6 IL6	2015	Asukai K 26228109	Japan	IH-CCA	72	47%	-	Cytoplasm membran e	S	Appendix +ve control	Appendix +ve	NR
IMP3 <i>IMP3</i>	2014	Gao Y 24745619	China	IH-CCA	72	-	82%	Tumour nests	S	Adjcent normal tissue	No expression	NR
IMP3 <i>IMP3</i>	2009	Riener M-O 19467694	No, Switzerlan d	IH-CCA EH-CCA	19 58	-	36.8% 50.0%	Cytoplasm	TMA	Normal BD (n=36), acute inflammation (n=36), dysplasia (low grade n=9, high grade n=11)	Normal BD, inflammation, low grade dysplasia negative/wea k, high grade all +	3 pathologists
IMP3 <i>IMP3</i>	2014	Lok T 24439226	China	IH-CCA	41	68%	90%	Cytoplasm	S	NR	NR	3 investigators
IMP3 <i>IMP3</i>	2012	Chen Y-L 23246869	Taiwan	IH-CCA	61	-	41.0%	Tumour cells	S	Adjcent normal/ non tumourous liver tissue	Negative	2 blinded independent pathologists
IMP3 <i>IMP3</i>	2013	Kawashima, H 23269460	Japan	EH-CCA	68	NR	74.9%	Cytoplasm	S	n=12 benign	Detected in 1/12 samples	Two independent observes
Laminin 5 <i>LAMA5</i>	2018	Soejima, Y 29584696	Japan	IH-CCA	48	54.2% (26/48)	NR	Cytoplasm of tumour	S	None	NR	NR

								cells and intratumoral stroma				
LEF1 <i>LEF1</i>	2012	Coulouarn, C 22696594	France	CCA	54	NR	32%	Nucleus	TMA	Normal biliary cells	Weak expression?	NR
LI-cadherin <i>CDH17</i>	2009	Takamura M 23852458	Japan	IH-CCA	34	NR	52.9%	NR	S	Non-neoplastic biliary epithelium negative	Non-neoplastic biliary epithelium negative	NR
Lipocalin 1 <i>LCN1</i>	2018	Tian Y AN: 624752303	China	IH-CCA EH-CCA	100 27	44.1%	-	NR	TMA	Adjcent non-tumour liver tissue (n = unknown)	CC > than adjacent normal tissues	2 independent blinded pathologists
MAGE-A1 <i>MAGEA1</i>	2011	Zhou JX 21211023	China	IH-CCA	89	-	29.2%	Cytoplasm	S	NR	NR	NR
MAGE-A3/4 <i>MAGEA3</i> <i>MAGEA4</i>	2011	Zhou JX 21211023	China	IH-CCA	89	-	27.1%	Cytoplasm	S	NR	NR	NR
Matripase <i>ST14</i>	2019	Komatsubara T 30729623	Japan	EH-CCA	256	Cells 48% Stroma 40%	-	Mainly cytoplasm	TMA	Non-malignant epithelial cells	Matriptase + in some tumors	2 blinded indep pathologists
M-CSF <i>CSF1</i>	2015	Oishi 25052379	Japan	IH-CCA	39	NR	35.9%	Cytoplasm	S	Adjacent hepatic paranchyma	None	Single blinded pathologist
Mesothilin <i>MSLN</i>	2012	Kawamata F 23064529	Japan	EH-CCA	61	47.5%	72%	luminal membran e/ cytoplasm	S	NR	NR	3 independent blinded pathologists
MMP7 <i>MMP7</i>	2009	Oka T 19701966	Japan	CCA	30	NR	80%	Cytoplasm	S	None	NR	NR
MMP7	2011	Ohashi H	Japan	EH-CCA	30	-	80%	NR	S	NR	NR	NR

<i>MMP7</i>		22044563										
<i>MMP7</i> <i>MMP7</i>	2016	Shi, X-D 27608843	China	PH-CCA	37	62.2%	NR	Cytoplasm	S	Peritumoral tissue	Very low expression	Two blinded independent observers
<i>MMP9</i> <i>MMP9</i>	2018	Park Y 29422250	Korea	EH-CCA	66	50%	-	NR	S	NR	NR	NR
<i>MMP9</i> <i>MMP9</i>	2014	Sun Q 25337264	China	PH-CCA	58	46.6%	67.2%	Cytoplasm	S	NR	NR	2 independent blinded observers
<i>MMP9</i> <i>MMP9</i>	2009	Itatsu, K 19218340	Japan	EH-CCA IH-CCA	75 35	NR	58%	Cytoplasm	S	Adjacent normal non-neoplastic bile ducts	Faint or absent expression	NR
<i>MMP9</i> <i>MMP9</i>	2015	Tian X 24985031	China	IH-CCA	65	-	53.8%	Cytoplasm	S	NR	NR	2 blinded independent observers
<i>MMP9</i> <i>MMP9</i>	2010	Subimerb	Thailand	IH-CCA EH-CCA	32 18	Overall 6% CCA cells, 44% of TAMs in invasive margin	- -	CCA cells Tumour associated macrophages	S	No control	NR	NR
<i>MMP9</i> <i>MMP9</i>	2015	Sun Q 26339407	China	PH-CCA	62	32.2%	67.7%	Cytoplasm	S	NR	NR	2 independent blinded observers
<i>MMP9</i> <i>MMP9</i>	2013	Shi RY 23132676	China	IH-CCA	138	-	45.6%	Cytoplasm	TMA	NR	NR	2 observers, 1 blinded
<i>MMP9</i> <i>MMP9</i>	2009	Onodera M 19721413	Japan	EH-CCA IH-CCA	55 32	-	47.3% 62.5%	Cytoplasm	S	Non-neoplastic biliary epithelium (n=13)	Negative	2 independent observers
Nanog <i>NANOG</i>	2019	Zhang M-X 30854141	China	IH-CCA	116	61.2%	-	Cytoplasm	TMA	Para-carcinoma tissues	Weak/negative	2 experienced observers

NGF <i>NGF</i>	2014	Yang, X-Q 24744599	China	IH-CCA	83	27.7% (23/83)	NR	Cytoplasm	S	None	NR	NR
Notch4 <i>Notch4</i>	2014	Wu, W-R 25031748	China	IH-CCA	41	NR	34.1%	Nucleus and cytoplasm	S	Adjacent non- tumour liver	Expressed in normal liver tissue	NR
NY-ESO-1 <i>CTAG1B</i>	2011	Zhou JX 21211023	China	IH-CCA	89	-	21.3%	Cytoplasm	S	NR	NR	NR
OPCML <i>OPCML</i>	2011	Sriraksa, R 21448164	Thailand	CCA	92	NR	26%	NR	S	n=29 tumour adjacent normal samples	NR	Two independent observers
p53 <i>TP53</i>	2006	Hughes NR 16679351	Australia & Thailand	IH-CCA EH-CCA Sporadic IH-CCA EH-CCA	27 38 13 34	44% 47% 15% 26%	+ve only if strong stainin g of most cells	Nucleus	S	Normal donor livers n=6, non- neoplastic biliary epithelium	Normal bile ducts and liver negative	NR
P53 <i>TP53</i>	2018	Kim SJ 29309301	Korea	IH-CCA	213	NR	43.7%	Nucleus	TMA	None	NR	NR
P53 <i>TP53</i>	2009	Shen YC 19190145	Taiwan	IH-CCA EH-CCA	74 49	NR	27% 36%	Nucleus	S	NR	NR	NR
P53 <i>TP53</i>	2019	Zhao Li 31307551	China	IH-CCA	47	-	31.9%	NR	S	NR	NR	NR
P53 <i>TP53</i>	2017	Okada R 28508195	Japan	EH-CCA	61	34.4%	-	Nucleus	S	NR	NR	2 observers
P53 <i>TP53</i>	2012	Tan X-P 22783387	China	CCA	69	-	84%	Nucleus	S	No control	NR	2 blinded independent pathologists
P53 <i>TP53</i>	2017	Liu S 28915621	China	IH-CCA	60	-	46.7%	NR	S	N=60 paired normal tissue	NR	NR
p53	2011	Ohashi H	Japan	EH-CCA	30	-	46.7%	NR	S	NR	NR	NR

<i>TP53</i>		22044563										
P53 <i>TP53</i>	2010	Riener, M-O 20621328	Switzerland	IH-CCA EH-CCA	19 59	NR	37% 46%	Nucleus	TMA	n=30 normal biliary epithelium of extrahepatic bile ducts	Negative for p53 expression	NR
P53 <i>TP53</i>	2008	Karamitopoulou, E 18854271	Switzerland	EH-CCA	62	NR	32%	Nucleus staining	TMA	n=24 normal bile ducts	Not expressed in normal tissue	NR
P53 <i>TP53</i>	2013	Kaira, K 24131658	Japan	EH-CCA	89	49.4% (44/89)	NR	Nucleus	S	n=16 benign biliary track lesions	Not expressed in control tissue 0%	2 blinded authors
P53 <i>TP53</i>	2010	Won, HS 20955617	Korea	EH-CCA inc PH-CCA	75	NR	53.3%	Nucleus	TMA	None	NR	Two blinded independent observers
P53 <i>TP53</i>	2006	Liu, X-F 16937443	China	CCA	36	NR	52.8%	Nucleus	S	None	NR	NR
p53 <i>TP53</i>	2013	Hirashima, K 22927259	Japan	EH-CCA	71	NR	39.4%	Nucleus	S	Normal bile duct epithelium of the samples	NR	Two blinded authors
p53 <i>TP53</i>	2015	Vasuri, F 25367684	Italy	IH-CCA	60	NR	38.3%	Nucleus	TMA	N=10 normal liver tissue	NR	NR
p53 <i>TP53</i>	2009	Iguchi T 19262069	Japan	IH-CCA	61	NR	36.1%	Nucleus	S	None	NR	NR
p53 <i>TP53</i>	2015	Keira Y 25503275	Japan	IH-CCA EH-CCA	27 32	NR	NR	Nucleus of adenocarcinomas	S	NR	NR	NR
p53 <i>TP53</i>	2016	Moro CF 27829056	No, Sweden	IH-CCA	97	-	30%	Nucleus	S	NR	NR	2 pathologists
p53 <i>TP53</i>	2017	Bhalla A 28823571	No, USA	IH-CCA	56	-	55.4%	Nucleus	S	Liver with VMC without dysplasia and with LGD	No p53 expression at 10% cut off	NR

p53 <i>TP53</i>	2014	Lee C-T 25245603	China	IH-CCA	54	-	59%	Nucleus	S	NR	NR	2 pathologists
p53 <i>TP53</i>	2013	Park KW 23613672	Korea	EH-CCA PH-CCA IH-CCA	46 41 17	-	52.8% 47.4% 46.2%	Nucleus	TMA	NR	NR	2 blinded independent pathologists
PAI-2 <i>SERPINB2</i>	2018	Utaijaratrasmi P 29347950	Thailand	IH-CCA	72	63%	-	Tumour cell	S	NR	NR	2 blinded independent observers
PBK/TOPK <i>PBK</i>	2010	He F 19954816	China	IH-CCA PH-CCA	51 23	-	91.9%	Cytoplasm, occ membranous	S	N=10 normal donor livers	Expressed in N bile ducts but -ve in hepatocytes	NR
PDGF-D <i>PDGFD</i>	2019	Komatsubara T 30729623	Japan	EH-CCA	256	Cells 32% Stroma 26%	-	Mainly cytoplasm	TMA	Adjacent non-malignant epithelial cells	weak or no staining of PDGF-D	2 blinded indep pathologists
PGF <i>PGF</i>	2006	Jinawath, N 17006947	Thailand	IH-CCA	273	NR	70.83 %	Cytoplasm	TMA	Noncancerous liver tissue from n=10	NR	Three independent investigators
PIWIL2 <i>PIWIL2</i>	2015	Chen YJ 26125915	China	PH-CCA	41	80.5%	-	Cytoplasm	S	Control tissues n=10	90% low or negative	NR
PRL-2 <i>PTP4A3</i>	2010	Xu Y 19757198	China	IH-CCA	102	47.1%	-	Cancer cells	S	Adjcent non-cancerous liver n=102	Negative or low	All sections scored twice
ROS1 <i>ROS1</i>	2016	27136744	Taiwan	IH-CCA	85	-	73%	Cytoplasm	S	NR	NR	2 blinded independent pathologists
ROS1 <i>ROS1</i>	2015	Lee, K-H 26475437	Korea	IH-CCA	194	NR	37.1%	Cytoplasm	TMA	Each TMA had 4 cores of normal tissue	NR	NR
SALL4 <i>SALL4</i>	2015	Deng G 26317546	China	IH-CCA	175	-	58%	Nucleus	S	Adjacent non-tumour tissue	N=28 negative	3 experienced pathologists

SFRP1 <i>SFRP1</i>	2016	Davaadorj 28062160	Japan	IH-CCA	50	NR	60%	NR	S	None	NR	Single blinded pathologist
sFRP1 <i>SFRP1</i>	2014	Kang P 24594839	China	IH-CCA EH-CCA	20 58	-	30% 34.5%	Cytoplasm	S	Normal bile ducts n=36	69.4%	2 blinded independent observers
SHH <i>SHH</i>	2013	Tang L 23493353	China	IH-CCA	108	-	93.5%	Cytoplasm	TMA	Normal liver n=8	Normal bile ducts - ve/weak	NR
SHH <i>SHH</i>	2012	Kim YJ 21946948	Korea	EH-CCA	42	38.1%	85.7%	Cytoplasm	S	Paired normal liver n=42	35.7% normal liver positive	NR
TBX4 <i>TBX4</i>	2013	Zong M 23341740	China	IH-CCA	72	-	52.8%	Nucleus, occ cytoplasm	S	Paired adjacent non-cancerous tissue	2.78% positive	NR
TCF7 <i>TCF7</i>	2019	Liu Z 31248836	China	PH-CCA	103 + 57	-	43.8%	NR	TMA	No control	NR	NR
Tenascin <i>TNC</i>	2009	Iguchi T 19262069	Japan	IH-CCA	61	NR	63.9%	Intra- tumoral stroma	S	None	NR	NR
Tenascin-C <i>TNC</i>	2018	Soejima, Y 29584696	Japan	IH-CCA	48	37.5% (18/48)	NR	Cytoplasm of tumour cells and intratumo ral stroma	S	None	NR	NR
TFF1 <i>TFF1</i>	2007	Thuwajit P 17397518	Thailand	CCA	61	91.8%	98.4%	Cytoplasm , apical biliary epithelium , lumen of BD, stroma	S	Adjcent normal liver	+ large BD but negative hepatocytes and small bile ducts	NR

TFF1 <i>TFF1</i>	2008	Chiu, C-T 18329969	Taiwan	IH-CCA	30	NR	56%	NR	S	None	NR	NR
TFF1 <i>TFF1</i>	2006	Jinawath, N 17006947	Thailand	IH-CCA	273	NR	28.57 %	Cytoplasm	TMA	Noncancerous liver tissue from n=10	NR	Three independent investigators
TFF1 <i>TFF1</i>	2018	Kaewlert W 30284180	Thailand	CCA	74	53%	-	Cytoplasm	S	Adjacent normal bile duct epithelial cells	Negative	NR
TFF2 <i>TFF2</i>	2008	Thuwajit, P 18410610	Thailand	CCA	51	31% (16/51)	NR	Cytoplasm and lumen	S	NR	NR	Two blinded observers
TGF beta 1 <i>TGFB1</i>	2015	Chen Y 25993985	China	IH-CCA	78	29.5%	47.4%	Cytoplasm	S	Normal liver tissue	Hepatocytes and bile ducts -ve	NR
TGFβ1 <i>TGFB1</i>	2018	Soejima, Y 29584696	Japan	IH-CCA	48	45.8% (22/48)	NR	Cytoplasm	S	None	NR	NR
Tie2 <i>TEK</i>	2008	Mihara Y -	Japan	EH-CCA	119	-	774.8 %	Cytoplasm	S	Normal mucosa n=38	23.7%	2 independent investigators
TLR2 <i>TLR2</i>	2016	Liu B 27616304	China	IH-CCA	51	47%	-	NR	S	Paired normal n=51	Significantly lower	NR
Transferrin <i>TF</i>	2017	Jamnongkan W 28671021	Thailand	CCA	49	41%	-	Cytoplasm	S	Cadaveric liver donors n=3	Lower in N BD cells compared to CCA	NR
Twist <i>TWIST1</i>	2014	Nitta T 25077440	Japan	EH-CCA	117	57.3%	-	NR	TMA	NR	NR	2 blinded investigators
Twist <i>TWIST1</i>	2016	Chu C 26479153	China	CCA	54	-	27.7%	NR	S	Choledochal cyst (n=16)	87.5% positive	Single senior pathologist
Twist <i>TWIST1</i>	2014	Duangkumpha, K 24969562	Thailand	CCA	30	30% (9/30)	NR	Nucleus and cytoplasm	S	None	NR	NR

								of tumour cells				
Type IV Collagen a6 <i>COL4A6</i>	2013	Hirashima, K 22927259	Japan	EH-CCA	71	NR	38%	Membrane	S	Normal bile duct epithelium of the samples	Weak expression	Two blinded authors
ULBP1 ULBP1	2016	Tsukagoshi M 26608587	Japan	EH-CCA	82	51.2%	100%	Tumour cells	S	NR	NR	NR
ULBP2 ULBP2	2016	Tsukagoshi M 26608587	Japan	EH-CCA	82	61.0%	76.8%	Tumour cells	S	NR	NR	NR
uPA <i>PLAU</i>	2012	Thummarati P 22294827	Thailand	CCA	174	49.4%	75.3%	Cytoplasm	TMA	NR	NR	NR
VEGF C <i>VEGFC</i>	2008	Aishima 18192971	Japan	IH-CCA	88	NR	30%	Cytoplasm	S	None	NR	Two blinded pathologists
VEGF C	2006	Taniguchi K 16688800	Japan	PH-CCA	34	-	47%	Cancer cells	S	NR	NR	Single blinded pathologist
VEGF C <i>VEGFC</i>	2015	Xu YF 25805932	China	IH-CCA	65	-	49.2%	Cytoplasm	TMA	NR	NR	2 independent blinded observers
VEGFC <i>VEGFC</i>	2017	Suksawat M 27143607	Thailand	CCA	171	100%	66.7%	Cytoplasm and membrane	S	No control	NR	NR
VEGF-C <i>VEGFC</i>	2006	Park BK 16601431	Korea	IH-CCA	36	41.7%	69.5%	Cytoplasm	S	Normal epithelia	Negative	2 blinded observers
VEGF-C <i>VEGFC</i>	2015	Zhao, R 26622616	China	CCA	65	NR	75.4%	NR	S	n=5 normal cholangiolar biopsies	Moderate to low in 5% of BD	NR
VEGF-C <i>VEGFC</i>	2013	Shi RY 23132676	China	IH-CCA	138	-	72.5%	Cytoplasm	TMA	NR	NR	2 observers, 1 blinded

VitD R VDR	2007	Seubwai W 17487855	Thailand	CCA	111	40%	74%	Cytoplasm	S	Normal bile ducts	20% low expression	NR
Wnt3 <i>WNT3</i>	2014	Loilome W 24549785	Thailand	CCA	38	Unknown	42.1%	Tumour cells	S	Cadaveric donor liver. Adjcent non- tumour tissue	Normal BD & hepatocytes - ve.	NR
Wnt3a <i>WNT3A</i>	2014	Loilome W 24549785	Thailand	CCA	38	Unknown	92.1%	Cytoplasm	S	Cadaveric donor liver. Adjcent non- tumour tissue	Normal BD low expression.	NR
Wnt5a <i>WNT5A</i>	2014	Loilome W 24549785	Thailand	CCA	38	Unknown	76.3%	Tumour cells	S	Cadaveric donor liver. Adjcent non- tumour tissue	Normal BD epithelia weak cytoplasm +ve.	NR
Wnt7b <i>WNT7B</i>	2014	Loilome W 24549785	Thailand	CCA	38	34.2%	100%	Cytoplasm	S	Cadaveric donor liver. Adjcent non- tumour tissue	Nucleus +ve hyperplastic BD. +ve	NR
ZNF423 <i>ZNF423</i>	2019	Chaiprasert T 31284679	Thailand	IH-CCA	75	41%	-	NR	S	Adjacent non- cancer areas	NR	NR

Appendix 2 Ethical approval

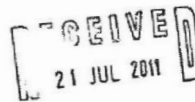
NHS
National Research Ethics Service
NRES Committee Yorkshire & The Humber - Leeds East

Yorkshire and Humber REC Office
First Floor, Millside
Mill Pond Lane
Meanwood
Leeds
LS8 4RA

Tel: 0113 3050108
Fax:

18 July 2011

Mr K R Prasad
Department of HPB & Transplant Surgery
St James' University Hospital
Beckett Street
Leeds
LS9 7TF



Dear Mr Prasad

Study title: Using bile proteomics in the development of diagnostic markers of biliary malignancy
REC reference: 06/Q1206/136
Amendment number: 3
Amendment date: 28 June 2011

The above amendment was reviewed on 14 July 2011 by the Sub-Committee in correspondence.

Ethical opinion

The members of the Committee taking part in the review gave a favourable ethical opinion of the amendment on the basis described in the notice of amendment form and supporting documentation with the condition that the researchers strictly maintain the linked-anonymised format.

Approved documents

The documents reviewed and approved at the meeting were:

Document	Version	Date
Notice of Substantial Amendment (non-CTIMPs)		28 June 2011
Covering Letter		29 June 2011

Membership of the Committee

The members of the Committee who took part in the review are listed on the attached sheet.

This Research Ethics Committee is an advisory committee to the Yorkshire and The Humber Strategic Health Authority
The National Research Ethics Service (NRES) represents the NRES Directorate within
the National Patient Safety Agency and Research Ethics Committees in England

R&D approval

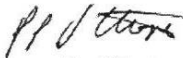
All investigators and research collaborators in the NHS should notify the R&D office for the relevant NHS care organisation of this amendment and check whether it affects R&D approval of the research.

Statement of compliance

The Committee is constituted in accordance with the Governance Arrangements for Research Ethics Committees (July 2001) and complies fully with the Standard Operating Procedures for Research Ethics Committees in the UK.

06/Q1206/136: Please quote this number on all correspondence

Yours sincerely



Alan Ebbutt
Vice Chair

E-mail: jade.thorpe@nhs.net

Enclosures: *List of names and professions of members who took part in the review*

Copy to: *Derek Norfolk, Leeds Teaching Hospitals NHS Trust
N/A. R&D contact/not specified in database.*

NRES Committee Yorkshire & The Humber - Leeds East

Attendance at Sub-Committee of the REC meeting on 14 July 2011

Name	Profession	Capacity
Prof Alan Ebbutt	Statistician	Expert
Ms Emily Griffiths	Deputy Risk Manager	Lay Plus